

Dissertation zur Erlangung des Doktorgrades der Fakultät für Chemie und Pharmazie der Ludwig-Maximilians-Universität München

**Synthesis, characterisation and density-functional calculations:
synthetic progress in the chemistry of the $[\text{Ru}(\text{H}_2\text{O})_6]^{2+}$ cation
from tosylatoruthenium complexes to
hydrogenhyponitrito and diazoniumdiolato complexes**

Daniel Stefan Paul Beck

aus

Augsburg, Deutschland

2019

Dissertation zur Erlangung des Doktorgrades der Fakultät für Chemie und Pharmazie der Ludwig-
Maximilians-Universität München

**Synthesis, characterisation and density-functional calculations:
synthetic progress in the chemistry of the $[\text{Ru}(\text{H}_2\text{O})_6]^{2+}$ cation
from tosylatoruthenium complexes to
hydrogenhyponitrito and diazoniumdiolato complexes**

Daniel Stefan Paul Beck

aus

Augsburg, Deutschland

2019

Erklärung

Diese Dissertation wurde im Sinne von § 7 der Promotionsordnung vom 28.November 2011 von Herrn Prof. Dr. Peter Klüfers betreut.

Eidesstattliche Versicherung

Diese Dissertation wurde eigenständig und ohne unerlaubte Hilfe erarbeitet.

München, den 08.07.2019

Daniel Beck

Dissertation eingereicht am: 11.06.2019

1. Gutachter: Prof. Dr. Peter Klüfers

2. Gutachter: Prof. Dr. Hans-Christian Böttcher

Mündliche Prüfung am: 05.07.2019

Diese Arbeit wurde in der Zeit von Juli 2015 bis Juni 2019 am Department für Chemie der Ludwig-Maximilians-Universität München am Lehrstuhl für Bioanorganische Chemie und Koordinationschemie unter Anleitung von Prof. Dr. Peter Klüfers durchgeführt.

Table of Contents

1 Introduction	1
1.1 Hexaaquaruthenium(II) salts – origin and recent advancements	1
1.2 Sulfonatoruthenium complexes	2
1.3 Phosphanes	4
1.4 Hyponitrite in biology and coordination chemistry	6
1.5 Diazoniumdiolates as ligands	9
2 Aim of this work	12
3 Results.....	13
3.1 Syntheses of hexaaquaruthenium salts	13
3.2 Tosylato- κ^2O,O' ruthenium complexes with phosphane co-ligands	27
3.3 Diaquaruthenium complexes with phosphane co-ligands	34
3.4 Aqua-tosylatoruthenium complexes with phosphane co-ligands.....	38
3.5 Short excursion: bisphosphanes dppbza (21), dpppha (22), dpppra (23).....	44
3.6 Reaction of complexes $[Ru(dppe)_2(tos)]BF_4$ (7) and $[Ru(H_2O)_6](tos)_2$ (1) with NO	45
3.7 Hydrogenhyponitrito and hyponitritoruthenium complexes with bisphosphane co-ligands.....	50
3.8 Short excursion: Synthesis of triphenylstannyl hyponitrite (34).....	65
3.9 Pyrrolidinediazoniumdiolato and benzyldiazoniumdioloruthenium complexes with bisphosphane co-ligands	65
3.10 Short excursion: sodium pyrrolidinediazoniumdiolate (38).....	75
3.11 Short excursion: hydrogen benzyldiazoniumdiolate (42)	75
4 Discussion	77
4.1 Hexaaquaruthenium(II) complexes with different counterions.....	77
4.2 Phosphaneruthenium ligands – between strong σ -donors and σ^* -acceptors.....	80
4.3 Treatment of $[Ru(dppe)(tos)]^{2+}$ (7) with NO.....	83
4.4 Hydrogenhyponitrito and hyponitrito complexes.....	85
— products of salt metathesis	85
4.5 Diazoniumdiolato complexes—a replacement for <i>cis</i> - $N_2O_2^{2-}$	87
5 Summary	90
6 Experimental Part.....	94
6.1 Common working techniques	94
6.2 Analytical methods.....	96
6.3 Reagents and solvents.....	97

Table of Contents

6.4 Syntheses of hexaaquaruthenium(II) salts	99
6.4.1 Preparation of “RuO ₂ ·xH ₂ O”	99
6.4.2 Setup for the synthesis of hexaaquaruthenium(II)	100
6.4.3 Hexaaquaruthenium(II) tosylate (1)	101
6.4.4 Hexaaquaruthenium(II) triflate (2)	103
6.4.5 Hexaaquaruthenium(II) sulfate (3)	105
6.4.6 Hexaaquaruthenium(II) naphthalenedisulfonate (4)	107
6.4.7 Hexaaquaruthenium(II) biphenyldisulfonate (5)	109
6.4.8 Hexaaquaruthenium(II) mesitylsulfonate (6)	110
6.5 Syntheses of phosphane precursor complexes	112
6.5.1 Phosphane complexes with K ² O, O'-tosylato/mesitylsulfonato ligands	112
6.5.2 Phosphane complexes with aqua ligands	124
6.5.3 Borderline complexes between chelate and diaqua coordination	132
6.5.4 Syntheses of bisphosphanes	137
6.6 Reactions with gaseous nitric oxide	140
6.6.1 Bis{bis(diphenylphosphanyl)ethane}hydridonitridoruthenium(0) (24)	140
6.6.2 Bis{bis(diphenylphosphanyl)ethane}nitrosylruthenium tosylate (25)	141
6.6.3 Bis{bis(diphenylphosphanyl)ethane}fluoridonitrosylruthenium tetrafluoroborate (26a)	142
6.6.4 Dinitrosylbis(triphenylphosphane)ruthenium(0) (27) (using NO)	143
6.7 Hydrogenhyponitrito ruthenium complexes and hyponitrite derivatives	144
6.7.1 Bis{bis(diphenylphosphanyl)ethane}hydrogenhyponitridoruthenium(II) tetrafluoroborate (28)	144
6.7.2 Bis{bis(diphenylphosphanyl)propane}hydrogenhyponitridoruthenium(II) tetrafluoroborate (29)	146
6.7.3 Bis{bis(diphenylphosphanyl)ethene}hydrogenhyponitridoruthenium(II) tetrafluoroborate (30)	147
6.7.4 Bis{bis(diphenylphosphanyl)ethane}hyponitridoruthenium(II) (31)	148
6.7.5 Bis{bis(diphenylphosphanyl)propane}hydrogenhyponitridoruthenium(II) tetrafluoroborate (32)	149
6.7.6 Bis{bis(diphenylphosphanyl)ethene}hyponitridoruthenium(II) (33)	150
6.7.7 Bis(triphenylstannyl) hyponitrite (34)	151
6.8 Diazoniumdiolato complexes as models for <i>cis</i> -hyponitrito complexes	153
6.8.1 Bis{bis(diphenylphosphanyl)ethane}pyrrlodinediazoniumdioloruthenium(II) tetrafluoroborate (35)	153
6.8.2 Bis{bis(diphenylphosphanyl)propane}nitrosylruthenium(II) tetrafluoroborate (36)	154
6.8.3 Bis{bis(diphenylphosphanyl)ethene}pyrrlodindiazoniumdioloruthenium(II) tetrafluoroborate (37)	155

Table of Contents

6.8.4 pdd, pyrroldinediazoniumdiolate (38)	156
6.8.5 Bis{bis(diphenylphosphanyl)ethane}benzyldiazoniumdiolatoruthenium(II) tetrafluoridoborate (39)	157
6.8.6 Bis{bis(diphenylphosphanyl)propane}benzyldiazoniumdiolatoruthenium(II) tetrafluoridoborate (40)	158
6.8.7 Bis{bis(diphenylphosphanyl)ethene}benzyldiazoniumdiolatoruthenium(II) tetrafluoridoborate (41)	159
6.8.8 bdd, benzyldiazoniumdiolate (42)	160
7 Appendix	161
7.1 Packing diagrams of the moleculare structures	161
7.2 Crystallographic Tables.....	197
7.3 Safety data sheets (in german).....	209
8 Bibliography	217

List of Figures

Figure 1.1: ORTEP-3 plot of two examples of phosphanesulfonato complexes with a chelating sulfonate group	2
Figure 1.2: ORTEP-3 plot of three examples of complexes with monodentate sulfonato ligands	3
Figure 1.3: Electronic and steric effects of common P donor ligands plotted on a map according to Tolman (ν in cm^{-1})	5
Figure 1.4: Dependency of the orientation of SCN^- ligand of the bite angle of the different phosphane ligands.....	5
Figure 1.5: CCP4MG plot of the nitric oxide reductase of <i>Roseobacter denitrificans</i>	7
Figure 1.6: Ortep-3 plot of the tetranuclear diazoniumdiolatoruthenium complex of Reference 122 on the left	10
Figure 3.1: ^{17}O NMR spectrum of $[\text{Ru}(\text{H}_2\text{O})_6](\text{tos})_2$ (1)	14
Figure 3.2: UV/VIS spectra of $[\text{Ru}(\text{H}_2\text{O})_6](\text{tos})_2$ (1).....	14
Figure 3.3: ORTEP-3 plot (ellipsoids drawn at the 50% probability level at 100 K) of $[\text{Ru}(\text{H}_2\text{O})_6](\text{tos})_2$ (1)	15
Figure 3.4: Mercury packing diagram of $[\text{Ru}(\text{H}_2\text{O})_6](\text{tos})_2$ (1) in the monoclinic space group $P2_1/c$ with view along $[0\ 1\ 0]$	15
Figure 3.5: ORTEP-3 plot (ellipsoids drawn at the 50% probability level at 293 K) of $[\text{Ru}(\text{H}_2\text{O})_6](\text{OTf})_2$ (2)	18
Figure 3.6: Mercury packing diagram of $[\text{Ru}(\text{H}_2\text{O})_6](\text{OTf})_2$ (2) in the monoclinic space group $C2/c$ with view along $[0\ 1\ 0]$	18
Figure 3.7: ORTEP-3 plot (50% probability ellipsoids) of $[\text{Ru}(\text{H}_2\text{O})_6]\text{SO}_4$ (3).....	19
Figure 3.8: Mercury packing diagram of $[\text{Ru}(\text{H}_2\text{O})_6]\text{SO}_4$ (3)	19
Figure 3.9: ORTEP-3 plot (50% probability ellipsoids) of $[\text{Ru}(\text{H}_2\text{O})_6](1,5\text{-NaphDS})$ (4).....	21
Figure 3.10: Mercury packing diagram of $[\text{Ru}(\text{H}_2\text{O})_6](1,5\text{-NaphDS})$ (4) in the monoclinic space group $P2_1/c$ with view along $[0\ 1\ 0]$	21
Figure 3.11: ORTEP-3 plot (50% probability ellipsoids) of $[\text{Ru}(\text{H}_2\text{O})_6](4,4'\text{-BiphenDS})\cdot 2\text{H}_2\text{O}$ (5).....	22
Figure 3.12: Mercury packing diagram of $[\text{Ru}(\text{H}_2\text{O})_6](4,4'\text{-BiphenDS})\cdot 2\text{H}_2\text{O}$ (5)	23
Figure 3.13: ORTEP-3 plot (50% probability ellipsoids) of $[\text{Ru}(\text{H}_2\text{O})_6](\text{Mes})_2$ (6).....	25
Figure 3.14: Mercury packing diagram of $[\text{Ru}(\text{H}_2\text{O})_6](\text{MesSO}_3)_2$ (6) in the monoclinic space group $P2_1/c$ with view along $[1\ 0\ 0]$	25
Figure 3.15: ORTEP-3 plot (ellipsoids drawn at the 50% probability level at 100 K) of the $[\text{Ru}(\text{dppe})_2(\text{tos})]^+$ ion in 7	29
Figure 3.16: The two stretching vibrations of tosylato- $\kappa^2\text{O},\text{O}'$ ruthenium complex 7	30
Figure 3.17: $^{31}\text{P}\{^1\text{H}\}$ NMR spectrum of $[\text{Ru}(\text{dppe})_2(\text{MesSO}_3)]\text{BF}_4$ (11) in CD_2Cl_2 at $0\ ^\circ\text{C}$	31

List of Figures

Figure 3.18: ORTEP-3 plot (ellipsoids drawn at the 50% probability level at 97 K) of the [Ru(dppp) ₂ (tos)] ⁺ ion in 8	31
Figure 3.19: ORTEP-3 plot (ellipsoids drawn at the 50% probability level at 100 K) of the [Ru(dppbza) ₂ (tos)] ⁺ ion in 9	31
Figure 3.20: ORTEP-3 plot (ellipsoids drawn at the 50% probability level at 100 K) of the [Ru(dppe) ₂ (MesSO ₃)] ⁺ ion in 11	32
Figure 3.21: ORTEP-3 plot (ellipsoids drawn at the 50% probability level at 100 K) of [Ru(P ⁱ PrPh ₂) ₂ (tos) ₂] (10).....	33
Figure 3.22: ORTEP-3 plot (ellipsoids drawn at the 50% probability level at 100 K) of [Ru(P ⁱ PrPh ₂)(MesSO ₃) ₂] (12).....	33
Figure 3.23: The three stretching vibrations of ditosylato-κ ² O,O' ruthenium complex 10	34
Figure 3.24: ORTEP-3 plot (ellipsoids drawn at the 50% probability level at 100 K) of the [Ru(dpppha) ₂ (H ₂ O) ₂] ²⁺ ion in 13 cation.....	36
Figure 3.25: ORTEP-3 plot (ellipsoids drawn at the 50% probability level at 100 K) of the [Ru(dppen) ₂ (H ₂ O) ₂] ²⁺ ion in 14	36
Figure 3.26: ORTEP-3 plot (ellipsoids drawn at the 50% probability level at 100 K) of [Ru(dppbz) ₂ (H ₂ O) ₂](BF ₄) ₂ (15).....	36
Figure 3.27: ORTEP-3 plot (ellipsoids drawn at the 50% probability level at 100 K) of the [Ru(dppv) ₂ (H ₂ O) ₂] ²⁺ ion in 16	36
Figure 3.28: ORTEP-3 plot (ellipsoids drawn at the 50% probability level at 100 K) of the [Ru(dpppra) ₂ (H ₂ O)(tos)] ⁺ ion in 17	39
Figure 3.29: Symmetrically and asymmetrically coupled vibrations of aquatosylato complex 17	41
Figure 3.30: ORTEP-3 plot (ellipsoids drawn at the 50% probability level at 100 K) of [Ru(PPh ₃) ₂ (H ₂ O) ₂ (tos) ₂] (18).....	42
Figure 3.31: ORTEP-3 plot (ellipsoids drawn at the 50% probability level at 100 K) of [Ru(PH ^t Bu) ₂ (H ₂ O) ₂ (tos) ₂] (19).....	42
Figure 3.32: ORTEP-3 plot (ellipsoids drawn at the 50% probability level at 293 K) of [Ru(PPh ₂ Bn) ₂ (H ₂ O) ₂ (tos) ₂] (20).....	42
Figure 3.33: Symmetrically and asymmetrically coupled vibrations of aqua and tosylato ligands of compound 19	44
Figure 3.34: ORTEP-3 plot (ellipsoids drawn at the 50% probability level at 100 K) of [Ru(dppe) ₂ (H)(NO ₂)] (24).....	46
Figure 3.35: Difference-Fourier map of 24	46
Figure 3.36: ORTEP-3 plot (ellipsoids drawn at the 50% probability level at 98 K) of the [Ru(dppe) ₂ (NO)] ⁺ ion in 25	47
Figure 3.37: ORTEP-3 plot (ellipsoids drawn at the 50% probability level at 100 K) of [Ru(dppe) ₂ (NO)F] (26).....	47

List of Figures

Figure 3.38: ORTEP-3 plot (ellipsoids drawn at the 50% probability level at 100 K) of [Ru(PPh ₃) ₂ (NO) ₂] (27).....	49
Figure 3.39: ORTEP-3 plot (ellipsoids drawn at the 50% probability level at 100 K) of [Ru(dppe) ₂ (N ₂ O ₂ H)]BF ₄ ·Et ₂ O (28a).....	52
Figure 3.40: ORTEP-3 plot (ellipsoids drawn at the 50% probability level at 100 K) of [Ru(dppe) ₂ (N ₂ O ₂ H)]BF ₄ (28b).....	52
Figure 3.41: ORTEP-3 plot (ellipsoids drawn at the 50% probability level at 100 K) of [Ru(dppp) ₂ (N ₂ O ₂ H)]BF ₄ ·Et ₂ O (29).....	52
Figure 3.42: ORTEP-3 plot (ellipsoids drawn at the 50% probability level at 100 K) of [Ru(dppv) ₂ (N ₂ O ₂ H)]BF ₄ ·0.81TBME (30).....	52
Figure 3.43: The hydrogen-bond network of 33	54
Figure 3.44: ORTEP-3 plot (ellipsoids drawn at the 50% probability level at 100 K) of [Ru(dppe) ₂ (N ₂ O ₂)]·HImiBF ₄ (31).....	54
Figure 3.45: ORTEP-3 plot (ellipsoids drawn at the 50% probability level at 100 K) of [Ru(dppp) ₂ (N ₂ O ₂ H)]BF ₄ ·Imi (32).....	54
Figure 3.46: ORTEP-3 plot (ellipsoids drawn at the 50% probability level at 97 K) of [Ru(dppv) ₂ (N ₂ O ₂)]·HImi ⁺ ·Imi in 33	55
Figure 3.47: Difference-Fourier map of 28a–33	56
Figure 3.48: UV/VIS spectra of [Ru(dppp) ₂ (N ₂ O ₂ H)]BF ₄ ·Et ₂ O (29).....	58
Figure 3.49: Vibrations of the hydrogenhyponitrito ligand of compound 28a	58
Figure 3.50: Vibrations of the hyponitrito ligand of compound 31	59
Figure 3.51: ³¹ P{ ¹ H} NMR spectrum of [Ru(dppe) ₂ (N ₂ O ₂ H)]BF ₄ (28a) in CD ₂ Cl ₂ at RT.....	60
Figure 3.52: ³¹ P{ ¹ H}-MAS NMR spectrum of compound 28a , recorded at 10 kHz rotation in a 4 mm rotor (202 MHz).....	60
Figure 3.53: ³¹ P{ ¹ H}-MAS NMR spectrum of compound 29 , recorded at 10 kHz rotation in a 4 mm rotor (202 MHz) (δ/ppm).....	61
Figure 3.54: ³¹ P{ ¹ H}-MAS NMR spectrum of compound 30 , recorded at 10 kHz rotation in a 4 mm rotor (202 MHz) (δ/ppm).....	61
Figure 3.55: Series of UV/VIS spectra during irradiation with a 365 nm laser of compound 28b	63
Figure 3.56: UV/VIS-Difference plot of signal changes during irradiation of compound 28a	63
Figure 3.57: Series of IR spectra during irradiation with a 365 nm laser in the region of 400–600 cm ⁻¹ of compound 28a	63
Figure 3.58: IR-Difference plot of signal changes during irradiation in the region of 400–600 cm ⁻¹ of compound 28a	63
Figure 3.59: Series of IR spectra during irradiation with a 365 nm laser in the region of 600–900 cm ⁻¹ of compound 28a	63

List of Figures

Figure 3.60: IR-Difference plot of signal changes during irradiation in the region of 600–900 cm ⁻¹ of compound 28a	63
Figure 3.61: Series of IR spectra during irradiation with a 365 nm laser in the region of 900–1500 cm ⁻¹ of compound 28a	64
Figure 3.62: IR-Difference plot of signal changes during irradiation in the region of 900–1500 cm ⁻¹ of compound 28a	64
Figure 3.63: Series of IR spectra during irradiation with a 365 nm laser in the region of 1600–2300 cm ⁻¹ of compound 28a	64
Figure 3.64: IR-Difference plot of signal changes during irradiation in the region of 1600–2300 cm ⁻¹ of compound 28a	64
Figure 3.65: Series of IR spectra during irradiation with a 365 nm laser in the region of 2300–4000 cm ⁻¹ of compound 28a	64
Figure 3.66: IR-Difference plot of signal changes during irradiation in the region of 2300–4000 cm ⁻¹ of compound 28a	64
Figure 3.67: ORTEP-3 plot (ellipsoids drawn at the 50% probability level at 100 K) of the [Ru(dppv) ₂ (pdd)] ⁺ ion in 37	67
Figure 3.68: Vibrations of the pdd (38) ligand in compound 37	68
Figure 3.69: ORTEP-3 plot (ellipsoids drawn at the 50% probability level at 100 K) of [Ru(dppp) ₂ (NO)]BF ₄ (36).....	69
Figure 3.70: ³¹ P{ ¹ H} NMR spectrum of solvated crystals of 36 in CD ₂ Cl ₂ at RT.....	70
Figure 3.71: ORTEP-3 plot (ellipsoids drawn at the 50% probability level at 100 K) of the [Ru(dppe) ₂ (bdd)] ⁺ ion in 39	71
Figure 3.72: ORTEP-3 plot (ellipsoids drawn at the 50% probability level at 100 K) of the [Ru(dppp) ₂ (bdd)] ⁺ ion in 40	71
Figure 3.73: ORTEP-3 plot (ellipsoids drawn at the 50% probability level at 100 K) of the [Ru(dppv) ₂ (bdd)] ⁺ ion in 41	71
Figure 3.74: Vibrations of the bdd (42) ligand in compound 41	72
Figure 3.75: ³¹ P{ ¹ H} NMR spectrum of [Ru(dppe) ₂ (bdd)]BF ₄ (39) in CD ₂ Cl ₂ at RT.....	73
Figure 3.76: ³¹ P{ ¹ H} NMR spectrum of [Ru(dppp) ₂ (bdd)]BF ₄ (40) in CD ₂ Cl ₂ at RT.....	74
Figure 3.77: ³¹ P{ ¹ H} NMR spectrum of [Ru(dppv) ₂ (bdd)]BF ₄ (41) in CD ₂ Cl ₂ at RT.....	74
Figure 4.1: The hydrogen-bond network of [Ru(H ₂ O) ₆](OTf) ₂ (2).....	78
Figure 4.2: Gabedit plot of the frontier orbitals (isovalue 0.02) of [Ru(H ₂ O)(PPh ₃)(tos) ₂] (18).....	81
Figure 4.3: Gabedit plot of the frontier orbitals (isovalue 0.04) of [Ru(dppbza) ₂ (tos)] ⁺ (9).....	82
Figure 4.4: Space-filling models of compounds 28 , 29 , 30 (Gabedit).....	85
Figure 4.5: Comparison between selected bond angles and distances of the labile tosylato ligand of 7 (left) and the hydrogenhyponitrito ligand of 28 (right) which replaces it.....	86

List of Figures

Figure 4.6: Gabedit plot of the frontier orbitals of 28 (isovalue: 0.05).....	86
Figure 4.7: Interaction of the nitrogen lone-pair with the $\sigma^*(\text{N}-\text{O})$ orbital in hyponitrous acid.....	87
Figure 4.8: Gabedit plot of the frontier orbitals (isovalue 0.05) of $[\text{Ru}(\text{dppe})_2(\text{bdd})]^+$ (39).....	87
Figure 4.9: Space-filling model of compounds 37 (Gabedit).....	88
Figure 4.10: Gabedit plot of the HOMO (isovalue 0.04) of $[\text{Ru}(\text{dppv})_2(\text{pdd})]^+$ (37).	89
Figure 5.1: Hexaaquaruthenium tosylate (1); visualisation of the hydrogen bond saturation.	90
Figure 5.2: Examples of complexes obtained from starting complex 8	92
Figure 6.1: Set-up of the apparatus for the synthesis of the $[\text{Ru}(\text{H}_2\text{O})_6]^{2+}$ cation.....	100
Figure 6.2: Set-up plan of the apparatus.	100
Figure 7.1: Mercury packing diagram of $[\text{Ru}(\text{H}_2\text{O})_6](\text{tos})_2$ (1)	161
Figure 7.2: Mercury packing diagram of $[\text{Ru}(\text{H}_2\text{O})_6](\text{OTf})_2$ (2).....	162
Figure 7.3: Mercury packing diagram of $[\text{Ru}(\text{H}_2\text{O})_6]\text{SO}_4$ (3)	163
Figure 7.4: Mercury packing diagram of $[\text{Ru}(\text{H}_2\text{O})_6](1,5\text{-NaphDS})$ (4)	164
Figure 7.5: Mercury packing diagram of $[\text{Ru}(\text{H}_2\text{O})_6](4,4'\text{-BiphenDS})\cdot 2\text{H}_2\text{O}$ (5).....	165
Figure 7.6: Mercury packing diagram of $[\text{Ru}(\text{H}_2\text{O})_6](\text{MesSO}_3)_2$ (6).....	166
Figure 7.7: Mercury packing diagram of $[\text{Ru}(\text{dppe})_2(\text{tos})(\text{BF}_4)]\cdot 0.985\text{CHCl}_3$ (7)	167
Figure 7.8: Mercury packing diagram of $[\text{Ru}(\text{dppp})_2(\text{tos})(\text{BF}_4)]\cdot x\text{Et}_2\text{O}$ (8)	168
Figure 7.9: Mercury packing diagram of $[\text{Ru}(\text{dppbza})_2(\text{tos})(\text{BF}_4)]\cdot 2.9\text{Et}_2\text{O}$ (9)	169
Figure 7.10: Mercury packing diagram of $[\text{Ru}(\text{P}^i\text{PrPh}_2)_2(\text{tos})_2]$ (10)	170
Figure 7.11: Mercury packing diagram of $[\text{Ru}(\text{dppe})_2(\text{MesSO}_3)(\text{BF}_4)]\cdot \text{DCM}$ (11)	171
Figure 7.12: Mercury packing diagram of $[\text{Ru}(\text{P}^i\text{PrPh}_2)_2(\text{MesSO}_3)_2]\cdot 0.826\text{DCM}$ (12)	172
Figure 7.13: Mercury packing diagram of $[\text{Ru}(\text{dpppha})_2(\text{H}_2\text{O})_2](\text{BF}_4)_2\cdot 1.948\text{DCM}$ (13).....	173
Figure 7.14: Mercury packing diagram of $[\text{Ru}(\text{dppen})_2(\text{H}_2\text{O})_2](\text{tos})_2\cdot 1.506\text{DCM}$ (14)	174
Figure 7.15: Mercury packing diagram of $[\text{Ru}(\text{dppbz})_2(\text{H}_2\text{O})_2](\text{BF}_4)_2$ (15)	175
Figure 7.16: Mercury packing diagram of $[\text{Ru}(\text{dppv})_2(\text{H}_2\text{O})_2](\text{BF}_4)_2$ (16)	176
Figure 7.17: Mercury packing diagram of $[\text{Ru}(\text{dpppra})_2(\text{H}_2\text{O})(\text{tos})](\text{tos})\cdot 1.891\text{C}_7\text{H}_8$ (17).....	177
Figure 7.18: Mercury packing diagram of $[\text{Ru}(\text{PPh}_3)_2(\text{H}_2\text{O})_2(\text{tos})_2]\cdot 2\text{C}_4\text{H}_{10}\text{O}$ (18).....	178
Figure 7.19: Mercury packing diagram of $[\text{Ru}(\text{PH}^t\text{Bu}_2)_2(\text{H}_2\text{O})_2(\text{tos})_2]$ (19).....	179
Figure 7.20: Mercury packing diagram of $[\text{Ru}(\text{PPh}_2\text{Bn})_2(\text{H}_2\text{O})_2(\text{tos})_2]\cdot \text{C}_4\text{H}_{10}\text{O}$ (20).....	180
Figure 7.21: Mercury packing diagram of $[\text{Ru}(\text{dppe})_2(\text{H})(\text{NO}_2)]$ (24)	181
Figure 7.22: Mercury packing diagram of $[\text{Ru}(\text{dppe})_2(\text{NO})](\text{tos})\cdot 0.955\text{DCM}$ (25)	182

List of Figures

Figure 7.23: Mercury packing diagram of [Ru(dppe) ₂ (NO)F](SbF ₆) (26)	183
Figure 7.24: Mercury packing diagram of [Ru(PPh ₃) ₂ (NO) ₂] (27)	184
Figure 7.25: Mercury packing diagram of [Ru(dppe) ₂ (N ₂ O ₂ H)]BF ₄ ·Et ₂ O (28a)	185
Figure 7.26: Mercury packing diagram of [Ru(dppe) ₂ (N ₂ O ₂ H)]BF ₄ (28b)	186
Figure 7.27: Mercury packing diagram of [Ru(dppp) ₂ (N ₂ O ₂ H)]BF ₄ ·Et ₂ O·DCM (29)	187
Figure 7.28: Mercury packing diagram of [Ru(dppv) ₂ (N ₂ O ₂ H)]BF ₄ ·0.81TBME·DCM (30)	188
Figure 7.29: Mercury packing diagram of [Ru(dppe) ₂ (N ₂ O ₂)]·HImiBF ₄ (31)	189
Figure 7.30: Mercury packing diagram of [Ru(dppp) ₂ (N ₂ O ₂ H)]BF ₄ ·Imi·0.856DCM (32)	190
Figure 7.31: Mercury packing diagram of [Ru(dppv) ₂ (N ₂ O ₂)]·HImiBF ₄ ·Imi·0.804DCM (33)	191
Figure 7.32: Mercury packing diagram of [Ru(dppp) ₂ (NO)]BF ₄ ·Et ₂ O (36)	192
Figure 7.33: Mercury packing diagram of [Ru(dppv) ₂ (pdd)]BF ₄ ·0.601DCM (37)	193
Figure 7.34: Mercury packing diagram of [Ru(dppe) ₂ (bdd)]BF ₄ (39)	194
Figure 7.35: Mercury packing diagram of [Ru(dppp) ₂ (bdd)]BF ₄ (40)	195
Figure 7.36: Mercury packing diagram of [Ru(dppv) ₂ (bdd)]BF ₄ ·0.867DCM (41)	196

List of Tables

Table 3.1: Distances (<i>d</i>) and angles (α) of hydrogen bonds in 1	16
Table 3.2: Graph set of products 1–6	17
Table 3.3: Distances (<i>d</i>) and angles (α) of hydrogen bonds in 2	18
Table 3.4: Distances (<i>d</i>) and angles (α) of hydrogen bonds in 3	20
Table 3.5: Distances (<i>d</i>) and angles (α) of hydrogen bonds in 4	22
Table 3.6: Distances (<i>d</i>) and angles (α) of hydrogen bonds in 5	24
Table 3.7: Distances (<i>d</i>) and angles (α) of hydrogen bonds in 6	26
Table 3.8: Overview of selected IR, UV/VIS and NMR data of compounds 7a–12	28
Table 3.9: Overview of selected angles (α) and distances (<i>d</i>) of compounds 7–12 and [Ru(NO) ₂ (PPh ₃) ₂ (SO ₄)].....	29
Table 3.10: Overview of selected IR, UV/VIS and NMR data of compounds 13–16	37
Table 3.11: Distances (<i>d</i>) and angles (α) of hydrogen bonds in 13–16	38
Table 3.12: Overview of selected IR, UV/VIS and NMR data of compounds 17–20	40
Table 3.13: Distances (<i>d</i>) and angles (α) of hydrogen bonds in 17–20	43
Table 3.14: Overview of the bond distances (<i>d</i>) and angles (α) of compound 25 and 26 together with [Ru(dppe) ₂ (NO)]BPh ₄ {RuNO} ⁸ and K[Ru(NO)Cl ₃ (mal)] {RuNO} ⁶	48
Table 3.15: Overview of the colour changes before and after the addition of imidazole.....	50
Table 3.16: Overview of bond distances (<i>d</i>) and angles (α) of free hyponitrite fragments from Reference 171 and the products of this work.....	53
Table 3.17: Overview of selected distances (<i>d</i>) and angles (α) the hydrogen bonds formed in the products 5–10	55
Table 3.18: Position and height of the residual density in the absence of the respective hydrogen atom together with the position after the refinement and the temperature factor of the hydrogen atom in 28a–33	57
Table 3.19: UV/VIS values of compounds 28a, 29 and 30	58
Table 3.20: Overview of infrared vibrations $\nu(\text{NO})/\text{cm}^{-1}$ of 28a–33	59
Table 3.21: Selected IR signals of compounds 28b–32	62
Table 3.22: Overview of bond distances (<i>d</i>) and angles (α) of free hyponitrite fragments from Reference 171 and the products of this work.....	67
Table 3.23: Overview of infrared vibrations in cm^{-1} of 37, 39–41	68
Table 3.24: Selected bond distances (<i>d</i>), angles (α) and the N–O stretching vibration of compound [Ru(dppp) ₂ (NO)]BPh ₄ and [Ru(dppp) ₂ (NO)]BF ₄ (36).....	70

List of Tables

Table 3.25: $^{31}\text{P}\{^1\text{H}\}$ NMR signals in DCM at RT and couplings given in parenthesis of compounds 39 and 41	73
Table 4.1: Comparison between published and obtained crystal structure of $[\text{Ru}(\text{H}_2\text{O})_6](\text{tos})_2$ (1).....	80
Table 4.2: Representatives of the hexahydrate mineral group including compound 3	80
Table 4.3: P–Ru–P bite angles in the phosphane complexes 7–20	83
Table 7.1: Crystallographic data of $[\text{Ru}(\text{H}_2\text{O})_6](\text{tos})_2$ (1), $[\text{Ru}(\text{H}_2\text{O})_6](\text{OTf})_2$ (2), $[\text{Ru}(\text{H}_2\text{O})_6](\text{SO}_4)$ (3)....	197
Table 7.2: Crystallographic data of $[\text{Ru}(\text{H}_2\text{O})_6](1,5\text{-NaphDS})$ (4), $[\text{Ru}(\text{H}_2\text{O})_6](4,4'\text{-BiphenDS})\cdot 2\text{H}_2\text{O}$ (5), $[\text{Ru}(\text{H}_2\text{O})_6](\text{MesSO}_3)_2$ (6).....	198
Table 7.3: Crystallographic data of $[\text{Ru}(\text{dppe})_2(\text{tos})]\text{BF}_4\cdot 0.985\text{CHCl}_3$ (7), $[\text{Ru}(\text{dppp})_2(\text{tos})]\text{BF}_4\cdot x\text{Et}_2\text{O}$ (8), $[\text{Ru}(\text{dppbza})_2(\text{tos})]\text{BF}_4\cdot 2.9\text{Et}_2\text{O}$ (9).....	199
Table 7.4: Crystallographic data of $[\text{Ru}(\text{P}^i\text{PrPh}_2)_2(\text{tos})_2]$ (10), $[\text{Ru}(\text{dppe})_2(\text{MesSO}_3)]\text{BF}_4\cdot \text{DCM}$ (11), $[\text{Ru}(\text{P}^i\text{PrPh}_2)_2(\text{MesSO}_3)_2]\cdot 0.826\text{DCM}$ (12).....	200
Table 7.5: Crystallographic data of $[\text{Ru}(\text{dpppha})_2(\text{H}_2\text{O})_2](\text{BF}_4)_2\cdot 1.948\text{DCM}$ (13), $[\text{Ru}(\text{dppen})_2(\text{H}_2\text{O})_2](\text{BF}_4)_2\cdot 1.506\text{DCM}$ (14), $[\text{Ru}(\text{dppbz})_2(\text{H}_2\text{O})_2](\text{BF}_4)_2$ (15).....	201
Table 7.6: Crystallographic data of $[\text{Ru}(\text{dppv})_2(\text{H}_2\text{O})_2](\text{BF}_4)_2$ (16), $[\text{Ru}(\text{dpppra})_2(\text{H}_2\text{O})(\text{tos})](\text{tos})\cdot 1.891\text{C}_7\text{H}_8$ (17), $[\text{Ru}(\text{PPh}_3)_2(\text{H}_2\text{O})_2(\text{tos})_2]\cdot 2\text{C}_4\text{H}_{10}\text{O}$ (18).....	202
Table 7.7: Crystallographic data of $[\text{Ru}(\text{PH}^t\text{Bu})_2(\text{H}_2\text{O})_2(\text{tos})_2]$ (19), $[\text{Ru}(\text{PPh}_2\text{Bn})_2(\text{H}_2\text{O})_2(\text{tos})_2]\cdot \text{C}_4\text{H}_{10}\text{O}$ (20), $[\text{Ru}(\text{dppe})_2(\text{H})(\text{NO}_2)]$ (24).....	203
Table 7.8: Crystallographic data of $[\text{Ru}(\text{dppe})_2(\text{NO})](\text{tos})\cdot 0.955\text{DCM}$ (25), $[\text{Ru}(\text{dppe})_2(\text{NO})\text{F}](\text{SbF}_6)$ (26), $[\text{Ru}(\text{PPh}_3)_2(\text{NO})_2]$ (27).....	204
Table 7.9: Crystallographic data of $[\text{Ru}(\text{dppe})_2(\text{N}_2\text{O}_2\text{H})]\text{BF}_4\cdot \text{Et}_2\text{O}$ (28a), $[\text{Ru}(\text{dppe})_2(\text{N}_2\text{O}_2\text{H})]\text{BF}_4$ (28b), $[\text{Ru}(\text{dppp})_2(\text{N}_2\text{O}_2\text{H})]\text{BF}_4\cdot \text{Et}_2\text{O}\cdot \text{DCM}$ (29).....	205
Table 7.10: Crystallographic data of $[\text{Ru}(\text{dppv})_2(\text{N}_2\text{O}_2\text{H})]\text{BF}_4\cdot 0.81\text{TBME}\cdot \text{DCM}$ (30), $[\text{Ru}(\text{dppe})_2(\text{N}_2\text{O}_2)]\cdot \text{HImiBF}_4$ (31), $[\text{Ru}(\text{dppp})_2(\text{N}_2\text{O}_2\text{H})]\text{BF}_4\cdot \text{Imi}\cdot 0.856\text{DCM}$ (32).....	205
Table 7.11: Crystallographic data of $[\text{Ru}(\text{dppv})_2(\text{N}_2\text{O}_2)]\cdot \text{HImiBF}_4\cdot \text{Imi}\cdot 0.804\text{DCM}$ (33), $[\text{Ru}(\text{dppp})_2(\text{NO})]\text{BF}_4\cdot \text{Et}_2\text{O}$ (36), $[\text{Ru}(\text{dppv})_2(\text{pdd})]\text{BF}_4\cdot 0.601\text{DCM}$ (37).....	207
Table 7.12: Crystallographic data of $[\text{Ru}(\text{dppe})_2(\text{bdd})]\text{BF}_4$ (39), $[\text{Ru}(\text{dppp})_2(\text{bdd})]\text{BF}_4$ (40), $[\text{Ru}(\text{dppv})_2(\text{bdd})]\text{BF}_4\cdot 0.867\text{DCM}$ (41).....	208

List of Schemes

Scheme 1.1: Selected examples of reactions with $[\text{Ru}(\text{H}_2\text{O})_6](\text{tos})_2$ (1) as catalyst.	1
Scheme 1.2: Proposed mechanisms of hyponitrite formation	7
Scheme 1.3: Currently known hyponitrite binding modes	8
Scheme 1.4: Resonance forms of the diazoniumdiolate functional group	9
Scheme 1.5: Simplified syntheses of <i>C</i> - and <i>N</i> -diazoniumdiolate compounds and examples for <i>O</i> and <i>S</i> -diazoniumdiolate anions (Angeli's salt and Pelouze's salt).....	10
Scheme 1.6: Various enzyme inhibitors containing the diazoniumdiolate moiety.	10
Scheme 1.7: Currently known <i>cis</i> -diazoniumdiolato binding modes (excluding the crystal structures with potassium/sodium)	11
Scheme 3.1: Overview of the counterions used.	13
Scheme 3.2: General synthetic procedure for hexa-aqua-ruthenium salts (1–6).....	13
Scheme 3.3: Illustration of the four possible designator patterns (G)	15
Scheme 3.4: Overview of phosphanes used for tosylato- $\kappa^2\text{O},\text{O}'$ ruthenium complexes 7–12	27
Scheme 3.5: General synthetic procedure for tosylato- $\kappa^2\text{O},\text{O}'$ ruthenium complexes 7 and 12	27
Scheme 3.6: Overview of phosphanes used for diaqua-ruthenium complexes 13–16	34
Scheme 3.7: General synthetic procedure for diaqua-ruthenium complexes 13, 15, 16	35
Scheme 3.8: General synthetic procedure for aqua-tosylatoruthenium complexes 17–19 and overview of the phosphane ligands used.....	39
Scheme 3.9: General synthetic procedure for amine bisphosphane ligands dppbza 21 , dpppha 22 , dpppra 23	45
Scheme 3.10: General synthetic procedure for complexes 24–27	46
Scheme 3.11: Formation of the compounds 7–16	51
Scheme 3.12: General synthetic procedure for compound 34	65
Scheme 3.13: General synthetic procedure for compound 41 and 37	65
Scheme 3.14: General synthetic procedure for compound 38	75
Scheme 3.15: General synthetic procedure for 42	75
Scheme 4.1: Qualitative energy-level scheme. Electron distribution of $[\text{Ru}(\text{H}_2\text{O})_6]^{2+}$	79
Scheme 4.2: Qualitative energy level scheme of strong σ -donors on the left side and π -acids capable of π^* -backdonation on the right side.....	81
Scheme 4.3: Reaction pathway from $[\text{Ru}(\text{H}_2\text{O})_6]^{2+}$, over $[\text{Ru}(\text{dppe})_2(\text{tos})]^+$ to different NO derivatives.	84
Scheme 5.1: Possible, simplified formation of a ruthenium hyponitrite complex from compound 27	91

Abbreviations

1,5-NaphDS ²⁻	1,5-naphthalenedisulfonate
4,4'-BiphenDS ²⁻	4,4'-biphenyldisulfonate
bdd	benzyl diazonium diolate
br	broad (NMR)
CShM	continuous shape measure ^[1]
d	doublet
DCM	dichloromethane
dd	doublet of doublets
DFT	density functional theory
dppbz	1,2-bis(diphenylphosphanyl)benzene
dppbza	bis(diphenylphosphanyl)benzylamine
dppe	bis(diphenylphosphanyl)ethane
dppen	1,1'-bis(diphenylphosphanyl)ethene
dppm	bis(diphenylphosphanyl)methane
dppp	bis(diphenylphosphanyl)propane
dpppha	bis(diphenylphosphanyl)phenylamine
dpppra	bis(diphenylphosphanyl)propylamine
dppv	1,2-bis(diphenylphosphanyl)ethene
EA	elemental analysis
EPR	electron paramagnetic resonance
ESI	electron spray ionisation
FAB	fast atom bombardment
HOMO	highest occupied molecular orbital
HRMS	high-resolution mass spectroscopy
Imi	imidazole
IR	infrared
LUMO	lowest unoccupied molecular orbital
m	medium (IR spectroscopy), multiplet (NMR spectroscopy)
MAS	magic angle spinning
NMR	nuclear magnetic resonance

Abbreviations

Tf	trifluoromethanesulfonyl
pdd	pyrrolidindiazoniumdiolate
ppm	parts per million
RT	room temperature
s	strong (IR spectroscopy), singlet (NMR spectroscopy)
sh	shoulder (point)
t	triplet
TBME	<i>tert</i> -butylmethyl ether
tde	tetrakis(dimethylamino)ethylene
th.	theory
THF	tetrahydrofuran
tos ⁻	<i>p</i> -toluenesulfonate
tppts	<i>meta</i> -trisulfonated triphenyl phosphane
UV/VIS	ultraviolet/visible
vs	very strong (IR spectroscopy)
vw	very weak (IR spectroscopy)
w	weak (IR spectroscopy)

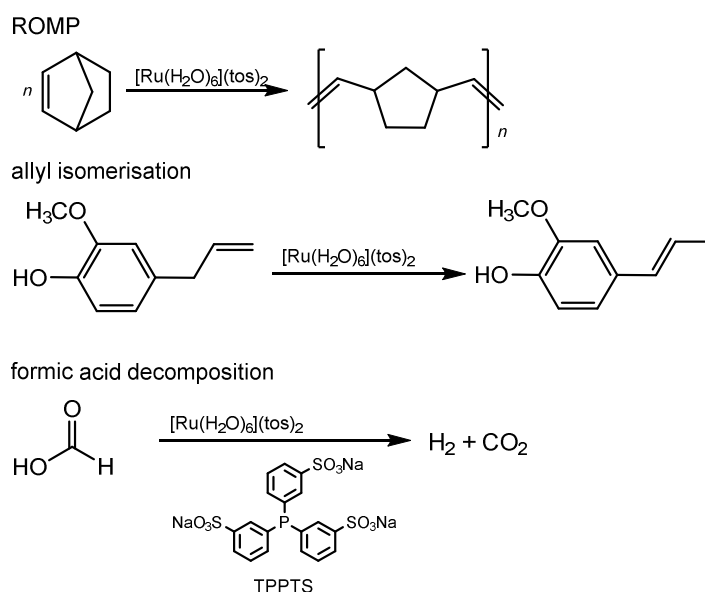
Overview of numbered compounds

1 [Ru(H ₂ O) ₆](tos) ₂	22 dpppha
2 [Ru(H ₂ O) ₆](OTf) ₂	23 dpppra
3 [Ru(H ₂ O) ₆]SO ₄	24 [Ru(dppe) ₂ (H)(NO ₂)]
4 [Ru(H ₂ O) ₆](1,5-NaphDS)	25 [Ru(dppe) ₂ (NO)](tos)·0.955DCM
5 [Ru(H ₂ O) ₆](4,4'-BiphenDS)·2H ₂ O	26 [Ru(dppe) ₂ (NO)F](SbF ₆)
6 [Ru(H ₂ O) ₆](MesSO ₃) ₂	27 [Ru(PPh ₃) ₂ (NO) ₂]
7a [Ru(dppe) ₂ (tos)]BF ₄ ·CH ₂ Cl ₂ ·C ₇ H ₈	28a [Ru(dppe) ₂ (N ₂ O ₂ H)]BF ₄ ·Et ₂ O
7b [Ru(dppe) ₂ (tos)]BF ₄ ·0.985CHCl ₃	28b [Ru(dppe) ₂ (N ₂ O ₂ H)]BF ₄
8 [Ru(dppp) ₂ (tos)]BF ₄ ·xEt ₂ O	29 [Ru(dppp) ₂ (N ₂ O ₂ H)]BF ₄ ·Et ₂ O·DCM
9 [Ru(dppbza) ₂ (tos)]BF ₄ ·2.9Et ₂ O	30 Ru(dppv) ₂ (N ₂ O ₂ H)]BF ₄ ·0.81TBME·DCM
10 [Ru(P ⁱ PrPh ₂) ₂ (tos) ₂]	31 [Ru(dppe) ₂ (N ₂ O ₂)]·HImiBF ₄
11 [Ru(dppe) ₂ (MesSO ₃)]BF ₄ ·DCM	32 [Ru(dppp) ₂ (N ₂ O ₂ H)]BF ₄ ·Imi·0.856DCM
12 [Ru(P ⁱ PrPh ₂) ₂ (MesSO ₃) ₂]·0.826DCM	33 [Ru(dppv) ₂ (N ₂ O ₂)]·HImiBF ₄ ·Imi·0.804DCM
13 [Ru(dpppha) ₂ (H ₂ O) ₂](BF ₄) ₂ ·1.948DCM	34 (Ph ₃ Sn) ₂ N ₂ O ₂
14 [Ru(dppen) ₂ (H ₂ O) ₂](BF ₄) ₂ ·1.506DCM	35 [Ru(dppe)(pdd)]BF ₄
15 [Ru(dppbz) ₂ (H ₂ O) ₂](BF ₄) ₂	36 [Ru(dppp) ₂ (NO)]BF ₄ ·Et ₂ O
16 [Ru(dppv) ₂ (H ₂ O) ₂](BF ₄) ₂	37 [Ru(dppv) ₂ (pdd)]BF ₄ ·0.601DCM
17 [Ru(dpppra) ₂ (H ₂ O)(tos)](tos)·1.891C ₇ H ₈	38 pdd
18 [Ru(PPh ₃) ₂ (H ₂ O) ₂ (tos) ₂]·2C ₄ H ₁₀ O	39 [Ru(dppe) ₂ (bdd)]BF ₄
19 [Ru(PH ^t Bu) ₂ (H ₂ O) ₂ (tos) ₂]	40 [Ru(dppp) ₂ (bdd)]BF ₄
20 [Ru(PPh ₂ Bn) ₂ (H ₂ O) ₂ (tos) ₂]·C ₄ H ₁₀ O	41 [Ru(dppv) ₂ (bdd)]BF ₄ ·0.867DCM
21 dppbza	42 bdd

1 Introduction

1.1 Hexaaquaruthenium(II) salts – origin and recent advancements

While numerous records of binary aqua complexes of iron can be found, they remain rare for ruthenium and have not been identified for osmium yet.^[2-8] In the case of ruthenium two known crystal structures of the hexaaquaruthenium(II) cation have been determined so far, the hexaaquaruthenium tosylate $[\text{Ru}(\text{H}_2\text{O})_6](\text{tos})_2$ synthesised by Bernhard *et al.* (1982) and $[\text{Ru}(\text{H}_2\text{O})_6][\text{RuCl}_3(\text{CO})_3]_2 \cdot 2\text{H}_2\text{O}$ obtained as a side product of a product mixture by Taimisto *et al.* (2003).^[9-10] Apart from these two compounds, only a solid but tentatively microcrystalline form of the trifluoromethane sulfonate salt of hexaaquaruthenium(II) has been obtained by ion-exchange chromatography, yet.^[11] Overall, there have been no synthetic advancements regarding the hexaaquaruthenium(II) cation in almost two decades except for an improved synthesis of the already existent hexaaquaruthenium tosylate in 2010.^[12] Nonetheless, since the standard starting material for most ruthenium chemistry in water is the ill-defined $\text{RuCl}_3 \cdot x\text{H}_2\text{O}$ the hexaaquaruthenium salt as a halogen-free and homogenous compound has gained interest in several fields such as spectroscopy, kinetics, syntheses, computational chemistry and catalytic applications and has been mentioned in an educational study.^[13-18] With respect to catalytic methods, hexaaquaruthenium(II) tosylate offers a broad range of reactions from ring-opening metathesis (ROMP), isomerisation of allyl functionalities and isomerisation of olefins (Scheme 1.1).^[19-21] Hexaaquaruthenium(II) tosylate as precatalyst in the presence of *meta*-trisulfonated triphenylphosphine (TPPTS) enables the selective decomposition of formic acid into hydrogen and carbon dioxide—a viable step in the direction of a regenerative hydrogen storage system.^[17, 22]



Scheme 1.1: Selected examples of reactions with $[\text{Ru}(\text{H}_2\text{O})_6](\text{tos})_2$ (**1**) as catalyst.

Recent advances in using hexaqua ruthenium tosylate as a precursor for new coordination compounds succeeded with phosphanes (e.g. dppe, PPh₃, tppts), small molecules (e.g. N₂, CO, H₂), *N*-heterocycles, arenes and olefines.^[14, 23-30] A special case of complexes obtained from ruthenium compounds including hexaqua ruthenium(II)—the sulfonato complexes—are described in the next subchapter.

1.2 Sulfonatoruthenium complexes

Sulfonato ligands are valued for their weakly coordinating behaviour and for their good leaving-group abilities.^[31-32] Sulfonato ligands coordinate usually labily and tend to be easily replaced by other ligands—a characteristic which is promising for the application in catalysis and synthesis.^[33-38] Bailey *et al.* treated hexaqua ruthenium(II) with phosphane (dppe, PPh₃) ligands and predicted correctly that the previous tosylato counterion coordinated to the ruthenium(II) centre.^[23] A crystal structure of the dppe complex was obtained by this group in 2018 and confirmed a κ^2O, O' coordination of the tosylato ligand (**7**).^[39] A chelate sulfonato ligand in a mononuclear ruthenium complex proven by a crystal structure is a rarity and is known only for two or more chelate phosphanesulfonato co-ligands (Figure 1.1).^[40-42] Nonetheless, tosylato- κ^2O, O' does also appear in dinuclear ruthenium complexes, for example, as bridging ligands.^[43-44]

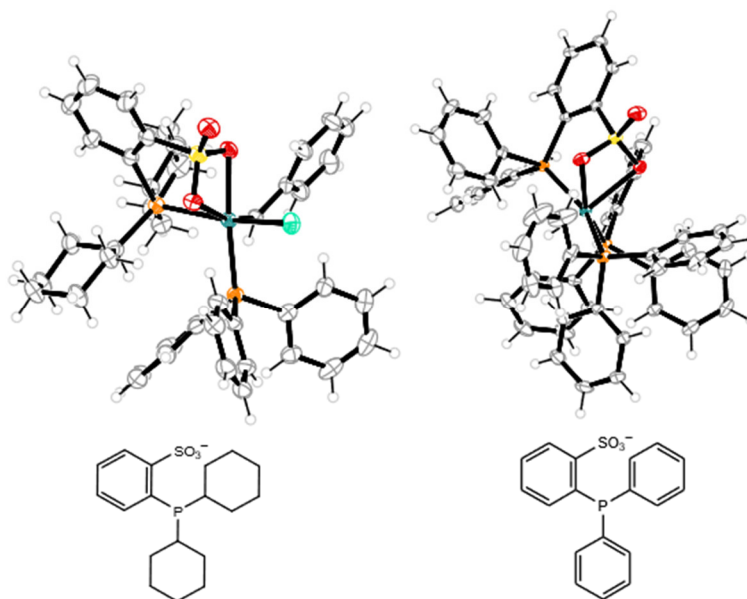


Figure 1.1: ORTEP-3 plot of two examples of phosphanesulfonato complexes with a chelating sulfonato group.^[45] Left: [Ru(CH-Ph)Cl(PPh₃)(P(Cy)₂(-6-SO₃-C₆H₄))]; right: [Ru(H)(PPh₃)₂(P(Ph)₂(-6-SO₃-C₆H₄))].^[41-42]

In contrast, a monodentate sulfonato is not as rare in ruthenium complexes as its weakly coordinating characteristic suggests. Sulfonatoruthenium complexes—similar to the ones synthesised in this work—are known in several coordination forms.^[46-53] A few examples are given in Figure 1.2.

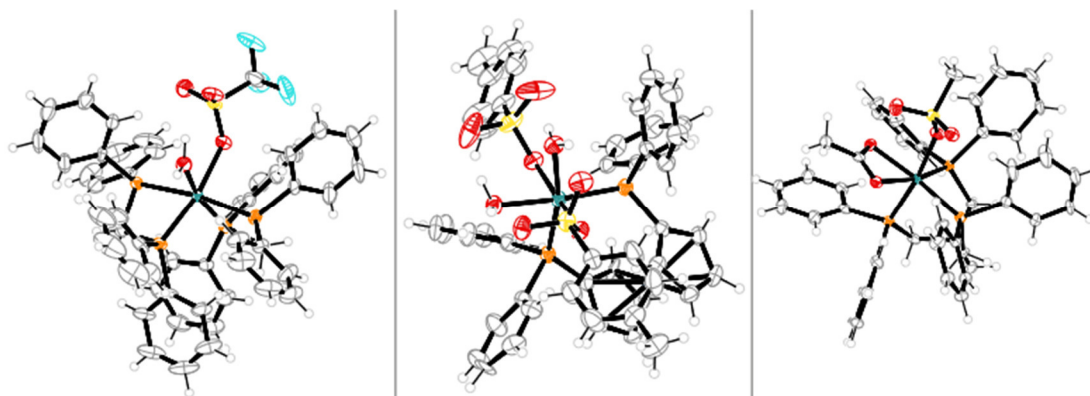


Figure 1.2: ORTEP-3 plot of three examples of complexes with monodentate sulfonato ligands.^[45] Left: $[\text{Ru}(\text{dppe})_2(\text{H}_2\text{O})(\text{OTf})]^+$; centre: $[\text{Os}(\eta^5\text{-C}_5\text{H}_4\text{PPh}_2)_2\text{Ru}(\text{H}_2\text{O})_2(\text{tos})_2]$; right: $[\text{Ru}(\text{CF}_3\text{SO}_3\text{-}\kappa\text{O})(\text{CH}_3\text{COO-}\kappa^2\text{O},\text{O})(\text{triphos})]$, triphos = 1,1,1-tris-(diphenylphosphanylmethyl) ethane.^[38, 49, 54]

The HSAB concept has been the subject of discussion as a possible explanation for the coordination behaviour of aqua and sulfonato ligands.^[50, 55] As coordination centres can be described either as hard or soft, a combination of soft organo ligands and relatively hard aqua ligands do not seem to be favoured.^[28-29, 56] Jørgensen—commenting on the then recently released HSAB principle of Pearson—emphasized that soft ligands flock together in the same complexes (principle of symbiosis).^[57-58] Bjerrum pointed out that mixed complexes of the type MX_aY_b with moderate pairs of ligands such as water and fluoride or water and ammonia are more frequent than the statistical contribution to the higher entropy suggests.^[59] As an example, $[\text{Co}(\text{NH}_3)_5\text{X}]^{2+}$ is more stable for $\text{X} = \text{F}$ than for I , but it is the opposite for $[\text{Co}(\text{CN})_5\text{X}]^{3-}$.^[57] This leads to the question of what standard procedures are used to obtain complexes defying the mentioned observations and principles. The tosylatoruthenium complex with phosphane co-ligands of Peganova *et al.* shown in Figure 1.2 was obtained—as any tosylato complex in this work—through the treatment of $[\text{Ru}(\text{H}_2\text{O})_6](\text{tos})_2$ with the corresponding phosphane.^[39, 49] Triflate ruthenium complexes are gained by silver triflate and ruthenium chlorides, ruthenium(II) hydrides and triflic acid and ruthenium(0) derivatives as well as triflic acid.^[38, 52, 60] The ruthenium hydride route is also established for methanesulfonatoruthenium complexes.^[54] As mentioned before, not only the hexaaquaruthenium salt is catalytically active, but also the phosphane derivatives.^[61] For example, they catalyse the hydrogenation of amides to amines and the transfer hydrohalogenation of organic halides. ($\text{C-Cl} \rightarrow \text{C-H}$).^[54, 62] As green chemistry and water-as-solvent gain interest in synthesis, the catalysts are ideally tolerant towards water and soluble in water.^[51, 63] An example is the Kuntz-Kornils catalyst in Ruhrchemie/Rhône-Poulenc hydroformylation which is a liquid-liquid biphasic catalysis using a water-soluble rhodium catalyst with sulfonated triphenylphosphane co-ligands.^[64] Therefore, to obtain phosphane ruthenium catalysts with similar characteristics, $[\text{Ru}(\text{H}_2\text{O})_6](\text{tos})_2$ was treated with sulfonated triphenylphosphane derivatives in the group of Kovacs *et al.*^[30] This resulted

in catalysts which are capable of formic acid decomposition ($\text{HCOOH} \rightarrow \text{CO}_2 + \text{H}_2$) as previously mentioned in chapter 1.1.^[17, 22, 30]

1.3 Phosphanes

Phosphane ligands are used as stabilisers for metal centres of different oxidation states (+IV to -I). Various substituted chelating phosphanes and polyphosphates can be synthesised. Both their electronic and steric versatility as well as their spectator ligand ability are topics of interest for synthesis and catalysis.^[65] A concept to characterise these versatile ligands was established by Tolman.^[66-67] A Tolman plot shows the infrared carbonyl shift of the model complex $[\text{Ni}(\text{CO})_3\text{X}]$ (X = monophosphane) coordinated with the respective phosphane solved in dichloromethane on the ordinate (electronic effect) and Tolman's cone angle of the monophosphane on the abscissa (steric effect) (Figure 1.3). The electron density donated by the phosphane to the metal centre increases the backbond of the carbonyl ligand through a π^* orbital population. This weakens the C–O bond (lowering the bond order) resulting in an infrared signal shift to lower wavenumbers. In summary, the higher the electron donation of the phosphane, the lower the $\tilde{\nu}(\text{CO})$ stretching vibration. Nonetheless, phosphanes are also σ^* -acceptors due to the empty σ^* -orbital. Accordingly, a part of the metal centres' electron density is withdrawn and the relocation of electron density into a σ^* -orbital strengthens the C–O bond ($\tilde{\nu}(\text{CO})$ shift to higher wavenumbers). Therefore, the actual electronic effect is a result of the competitive effects of σ -donation and σ^* -back donation. The additivity of the substituent contributions enables the prediction of $\tilde{\nu}(\text{CO})$, even if the phosphane was not measured:

$$\text{For } \text{PX}_1\text{X}_2\text{X}_3: \tilde{\nu}(\text{CO}) = 2056.1 + \sum_{i=1}^3 X_i \quad (X = \text{substituent contribution}) \quad (1.1)$$

The cone angle of a space-filling model of $\text{M}(\text{PX}_3)$ is the basis of Tolman's steric parameter. The angle θ of a symmetrically substituted $\text{M}(\text{PX}_3)$ moiety is obtained from a cylindrical cone, which ends in a radius of 2.28 Å from the phosphorus atom. In the presence of internal degrees of freedom, the PR_3 moiety will move in such a manner, that the smallest θ is obtained. For asymmetrical $\text{M}-\text{PX}_1\text{X}_2\text{X}_3$ moieties a formula helps to obtain θ due to additivity of the contributions of the different substituents:

$$\text{For } \text{PX}_1\text{X}_2\text{X}_3: \theta = (2/3) \sum_{i=1}^3 \theta_i / 2 \quad (\theta_i = \text{cone angle of the symmetrically substituted phosphane}) \quad (1.2)$$

Calculated electronic and steric parameters for the monophosphanes PPh_2Bn , PPh_2Pr and P^tHBu_2 are given in Figure 1.3.

Introduction

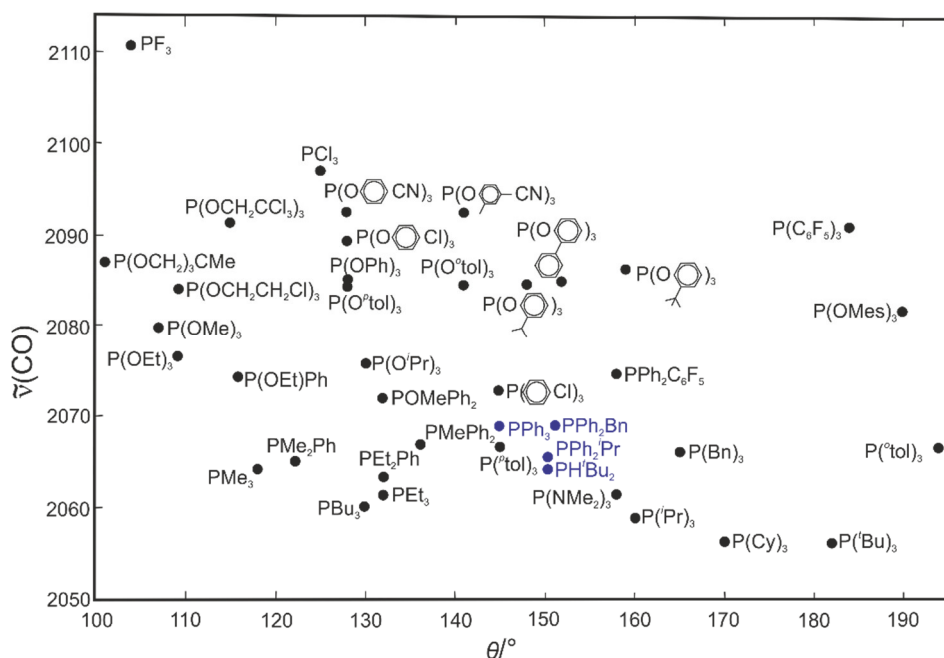


Figure 1.3: Electronic and steric effects of common P donor ligands plotted on a map according to Tolman ($\tilde{\nu}$ in cm^{-1}).^[67] Products obtained in blue: phosphanes, values for PPh_2Bn , PPh_2Pr and $\text{P}^t\text{Bu}_2\text{H}$ calculated by using the listed equations 1.1 and 1.2.

The Tolman plot is applied for monophosphanes as illustrated in Figure 1.3. However, a classification of bisphosphanes according to the used method is problematic as no reliable electronic parameters could be obtained. Therefore, the bite angle of bisphosphanes with its similar electronic characteristics has proven to be a better classification. An example is given for palladium bisphosphane complexes (dppm, dppe, dppp) by Palenik *et al.* which will be discussed shortly.^[68]

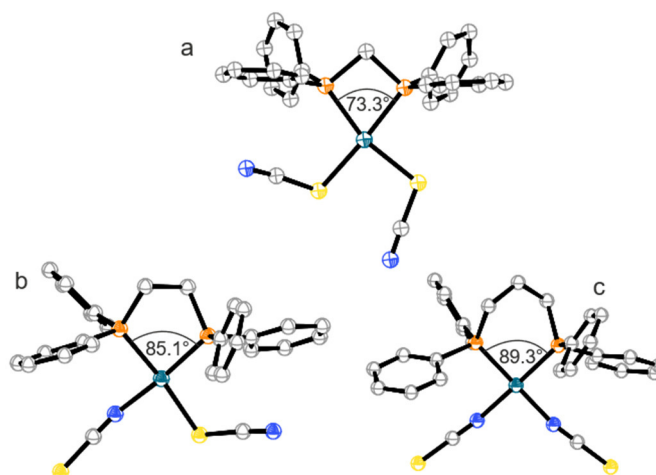


Figure 1.4: Dependency of the orientation of SCN^- ligand of the bite angle of the different phosphane ligands (Palenik). ORTEP-3 plot of a) $[\text{Pd}(\text{dppm})(\text{SCN-}\kappa\text{S})_2]$, b) $[\text{Pd}(\text{dppe})(\text{SCN-}\kappa\text{N})(\text{SCN-}\kappa\text{S})]$, c) $[\text{Pd}(\text{dppp})(\text{SCN-}\kappa\text{N})_2]$.^[45, 68]

As the ligands vary only in terms of their alkyl chain, similar σ -donor and π -acceptor (actually σ^* -acceptor) characteristics are to be expected. There are differences only in steric requirements, as

demonstrated in this work. An increase of steric requirements by the elongation of the alkyl chain and therefore, of the P–Pd–P angle, is evident in Figure 1.4. The rigid phenyl rings are pushed towards the SCN ligands, resulting in a turnover of these only by steric effects. The Pd–S–C angle of 110° compared to 180° of Pd–N–C results in larger steric requirements and, consequently, in an isomerisation. The σ^* -acceptor characteristics were discussed but ultimately discarded by the comparison of Pd–S, Pd–N and Pd–P bond distances with other complexes.^[68] Several structure-reactivity studies followed the shown case.^[69-73] One method to predict chelational preferences was shown by Casey and Whitaker. They introduced the “natural bite angle” and a flexibility range of diphosphane ligands which are a result of molecular mechanics. The “natural bite angle” is the preferred chelate angle determined by the backbone alone, not by the metal valence angles. The flexibility (rigidity of the ligand) was obtained by constraining the P–M–P angle and minimising the structure and calculation of the strain energy which was corrected by the strain energy as a result of the bending of the input bite angle. The obtained potential energy diagrams show a bite angle for bisphosphanes between 90 and 120° resulting in a strain difference of less than 3 kcal mol⁻¹.^[73-74] Nonetheless, a reliable predictability of complex reactivity coordinated by bisphosphanes is still part of lively research.^[75-76]

1.4 Hyponitrite in biology and coordination chemistry

The fixation and release of nitrogen-containing species is realised in the nitrogen cycle. In the process of denitrification, nitrate is reduced by several enzymatic steps to elemental nitrogen ($\text{NO}_3^- \rightarrow \text{NO}_2^- \rightarrow \text{NO} \rightarrow \text{N}_2\text{O} \rightarrow \text{N}_2$).^[77] Not surprisingly, the conversion of the nitrate fertilizer used in agricultural processes is overall unfavourable because of the resulting unavailability of the nutrient for the plants.^[78-79] As an enzyme, the nitric-oxide reductase (NOR) is thereby responsible for the conversion of nitric oxide to nitrous oxide—about 70% of that greenhouse gas is a result of bacterial catabolism releasing nitrogen oxides.^[80-81] Two enzyme types of the diiron metallozyme NOR can be distinguished, the heme/non-heme reductase (NOR) and the non-heme flavodiiron nitric oxide reductase (FNOR).^[82-83] A crystal structure of the nitric oxide reductase (NOR) from *Roseobacter denitrificans* is shown in Figure 1.5.^[84] The forms of bacterial NORs vary, however, all have an electron acceptor for external electron donors (e.g. heme c) and a mediator (e.g. heme b) transporting these electrons to the bimetallic active site (heme b₃ and Fe_b) in common.^[80] Conversely, the active site of FNORs is a nonheme dinuclear iron centre in close range to a redox-active flavin mononucleotide.^[85-86] The reduction step for pathogens like *Neisseria gonorrhoeae* or *N. meningitidis* is essential in order to eliminate the toxic NO molecule which is obtained by the mammalian NO synthase as part of immune defence.^[80, 87-88]

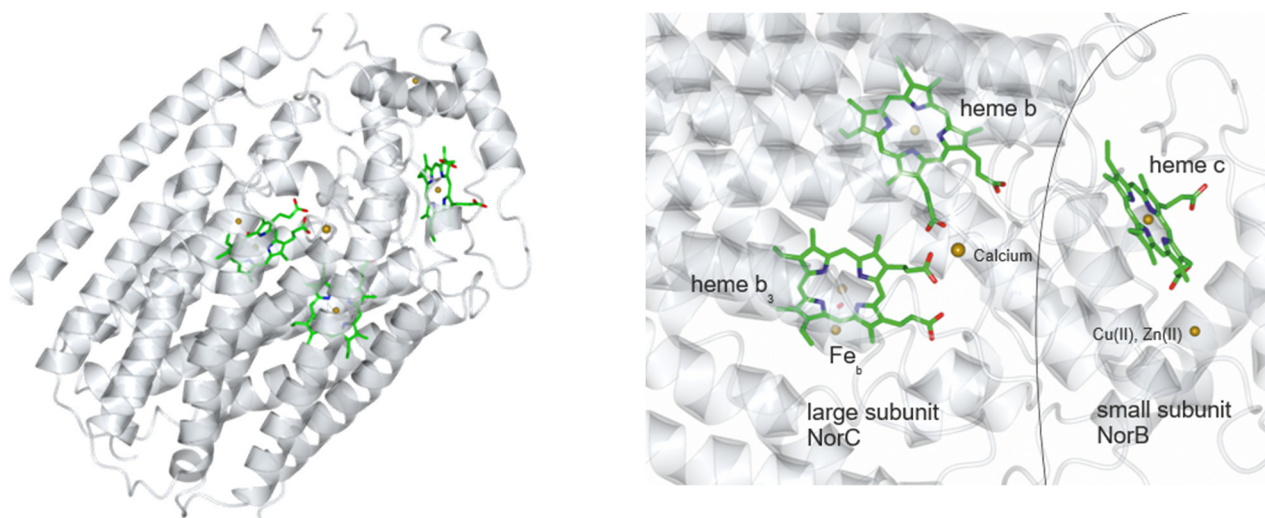
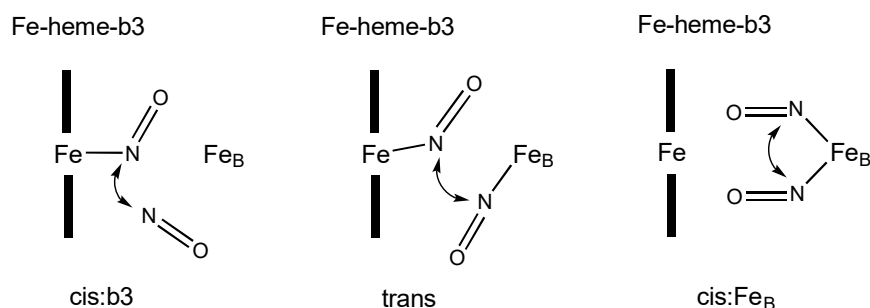


Figure 1.5: CCP4MG plot of the nitric oxide reductase of *Roseobacter dentrificans*.^[89] Left: Overall structure of the RdNorBC complex determined at 2.8 Å resolution. Right: Zoom on the active site heme b_3 and Fe_b , hemebridging calcium, and heme b (mediation of the transfer of electrons) in the large subunit; heme c (accepts electrons from external electron donor) and a unique metal site in the small subunit.^[80, 84]

The mechanism of nitrous oxide generation from nitric oxide is still unclear but it is most likely explained through the formation of a reactive hyponitrite intermediate. Hyponitrite is transformed into nitrous oxide over two protonation steps ($N_2O_2^{2-} + 2H^+ \rightarrow N_2O + H_2O$). Scheme 1.2 shows possible reaction mechanisms for the NO reduction.^[90]

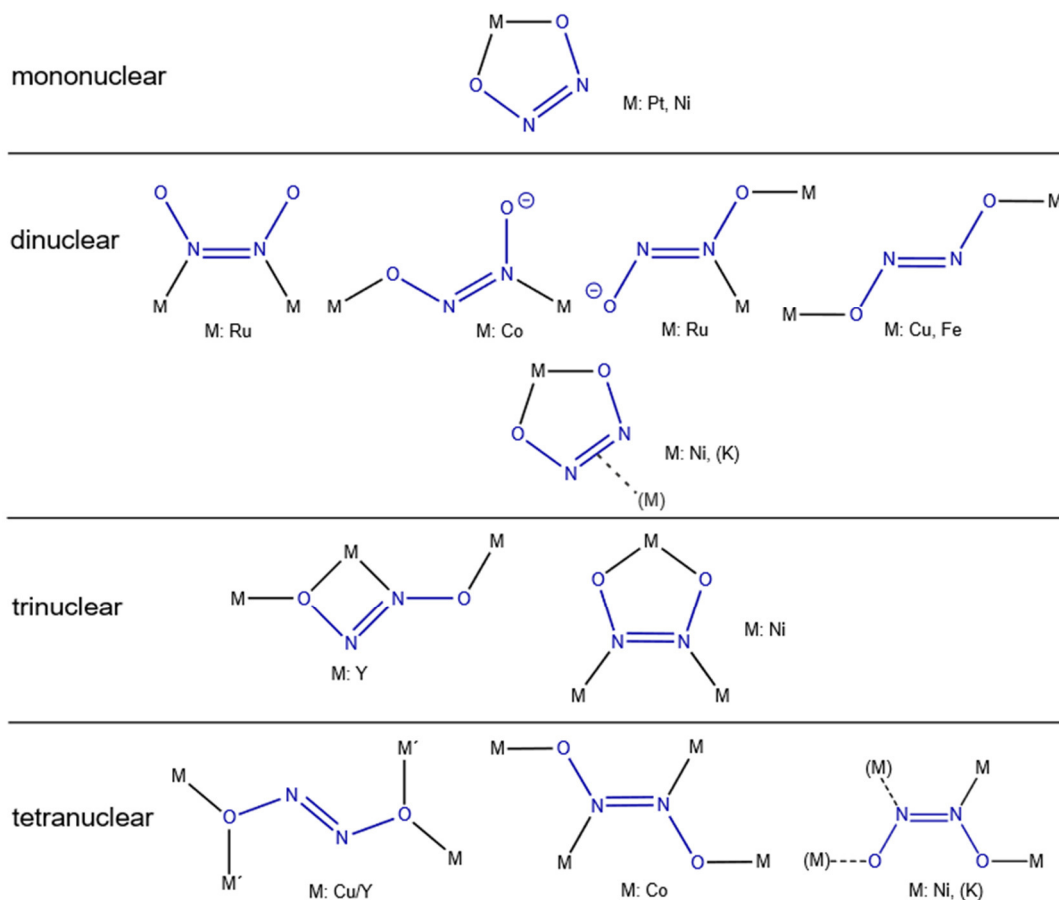


Scheme 1.2: Proposed mechanisms of hyponitrite formation.^[39, 90]

A practical approach on EPR-spectroscopic experiments using freeze-quench techniques suggest the *trans* mechanism to be the most likely. Time-dependent EPR spectral changes show a tentative formation of ferrous Fe_b -NO and ferrous heme- b_3 -NO in the same ratio, which would be a *trans*-mechanism (Scheme 1.2).^[91] Nonetheless, mainly theoretical works indicate energetically unfavourable intermediates of the *trans* mechanism that a so-called *cis:b₃* mechanism seems to be the reasonable choice. Thus, one NO coordinates to the heme-iron centre (Fe - b_3) and gets attacked by a non-coordinating NO. The resulting *cis*-hyponitrite is coordinated to the non-heme iron centre.^[90, 92] Additionally, a theoretical study also supports a *cis*-intermediate in FNORs.^[86] The *cis:Fe_B* mechanism was derived from rules of organometallic chemistry and is, today, without any viable indication of

Introduction

existence in the NOR, of historic interest only.^[93] Consequently, a lack of structural information makes a final conclusion difficult at the moment, especially in terms of binding modes.



Scheme 1.3: Currently known hyponitrite binding modes.^[39]

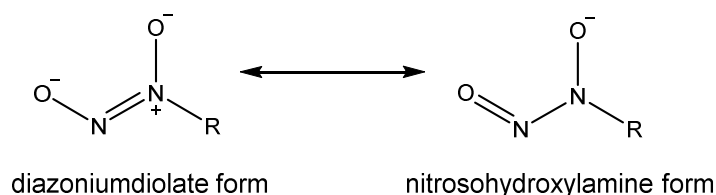
Scheme 1.3 shows that hyponitrite is discussed not only as an intermediate in the enzymatic process of nitric oxide reduction, but is a ligand which attracts attention in other fields of coordination chemistry. So far, eleven coordination modes (except the one from this work) are known for the hyponitrite ligand in its *cis* and *trans* form.^[94-97] Mononuclear complexes are restricted to the *cis* type whereby both isomers are found in polynuclear complexes. In general, hyponitrite is able to bind up to all four via each of its atoms.^[95, 98-101] It is noteworthy that mononuclear *cis*-hyponitrite complexes are obtained only with the group 10 metals, nickel and platinum.^[98, 102] In contrast, cobalt, copper, iron, ruthenium, yttrium and nickel form polynuclear *cis*- and *trans*-hyponitrite complexes.^[95-97, 99-101, 103-105]

Up to now, only one type of coordinated hydrogenhyponitrite complex has been published. Böttcher *et al.* synthesised a diruthenium(I) complex, bridged with sterically demanding phosphide ligands, which is capable of reducing nitric oxide to a bridging hyponitrite ligand according to the following equation: $[\text{Ru}_2(\text{CO})_4(\mu\text{-dppm})(\mu\text{-H})(\mu\text{-P}^t\text{Bu}_2)] + 2\text{NO} \rightarrow [\text{Ru}_2(\text{CO})_4(\mu\text{-dppm})(\mu\text{-H})(\text{ONNO-}1\kappa\text{N:}2\kappa\text{O})(\mu\text{-P}^t\text{Bu}_2)]$. Subsequent protonation led to a hydrogenhyponitrite complex which released nitrous oxide

upon heating.^[39, 99, 105-106] **Please note:** The content was published in Reference 39.

1.5 Diazoniumdiolates as ligands

The name diazoniumdiolate describes the N=N double bond (“diazen”), the formal positive charge (“ium”) and two negatively charged oxygens (“diolate”). Nonetheless, the functional group is known as both diazoniumdiolate (or NONOates) and nitrosohydroxylamine. This is best explained by looking at the resonance forms of these compounds (Scheme 1.4). Additionally, if the compounds were obtained by carbanions and nitric oxide, they are called isonitramines, prepared through the use of nitrosation as nitrosohydroxylamines. To avoid any confusion in nomenclature, the functional group shown in Scheme 1.4 is here referred to only as diazoniumdiolate.^[107-108]

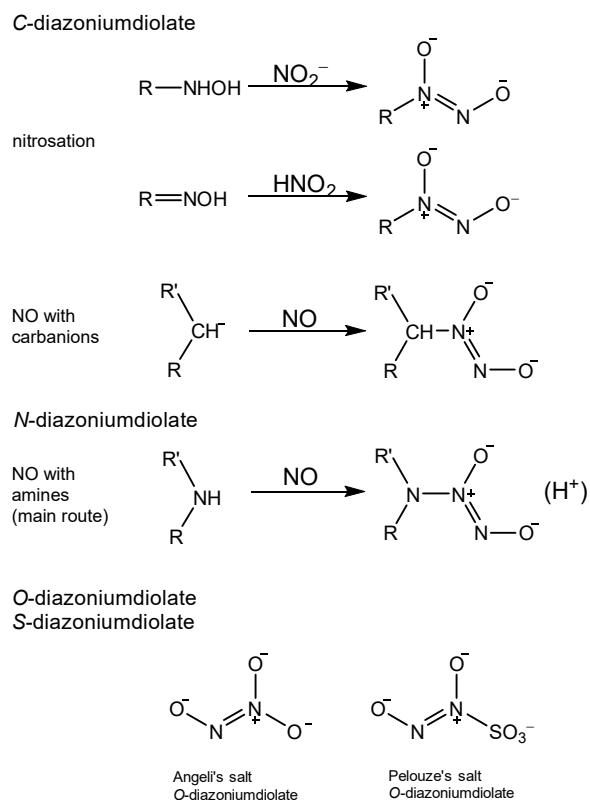


Scheme 1.4: Resonance forms of the diazoniumdiolate functional group.

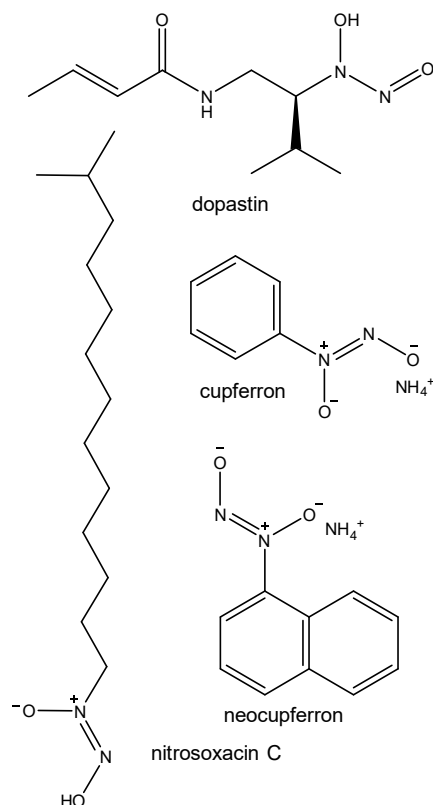
The diazoniumdiolate compounds are distinguished in *C*-diazoniumdiolates and *N*-diazoniumdiolates and smaller inorganic subgroups, whereby the name is determined by the substituent at the nitrogen atom. *C*-Diazoniumdiolate compounds can be prepared by various syntheses, which are—to put it in a nutshell—either a reaction of hydroxylamines or oximes with nitrite or a reaction of nitric oxide in the presence of carbanions. Conversely, *N*-diazoniumdiolates are synthesised by the direct reaction of an amine with nitric oxide (main route). Nonetheless, alternative routes to these compounds are possible and have been investigated.^[107, 109] Beside these two main groups, *O*-diazoniumdiolates (e.g. Angeli’s salt: Na₂N₂O₃), *B*-diazoniumdiolates, *S*-diazoniumdiolates (only known: Pelouze’s salt: O₂N₂–SO₃[−]) were also investigated even though only on a minor scale (summarised in Scheme 1.5).^[107, 110]

In biochemistry, *C*-diazoniumdiolates are most prominent for their enzyme-inhibiting effect in tyrosinases which are copper-containing enzymes.^[111] Further examples are dopastin which is an inhibitor of dopamine-β-monohydroxylase, nitrosoxacin for the 5-lipoxygenase and cupferron for the superoxide dismutase (Scheme 1.6).^[112-114] Furthermore, the diazoniumdiolates can be used as antitumor agents or as killing agents for multi-resistant bacteria.^[115-117] The diazoniumdiolate chelate cupferron is also used in the colorimetric detection of e.g. Cu, Fe or V.^[118-120] In biochemistry, the chelator capability of the diazoniumdiolate function of grambactin—a siderophore of the rhizosphere bacterium *Paraburkholderia graminis*—successfully binds iron over the N₂O₂ moiety.^[121]

Introduction



Scheme 1.5: Simplified syntheses of C- and N-diazoniumdiolate compounds and examples for O- and S-diazoniumdiolate anions (Angeli's salt and Pelouze's salt).



Scheme 1.6: Various enzyme inhibitors containing the diazoniumdiolate moiety.

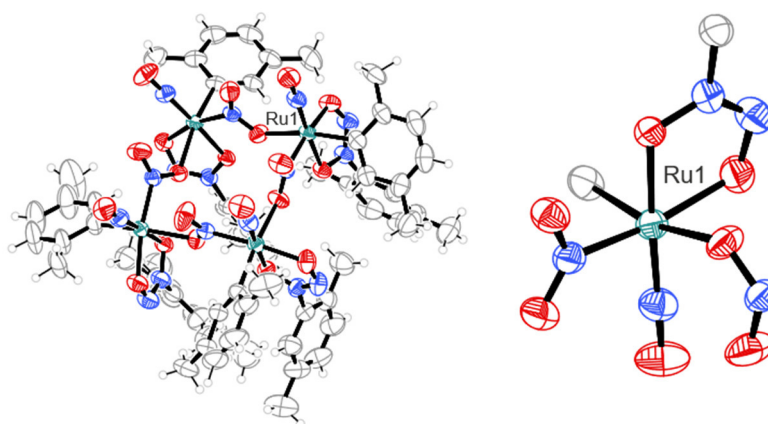
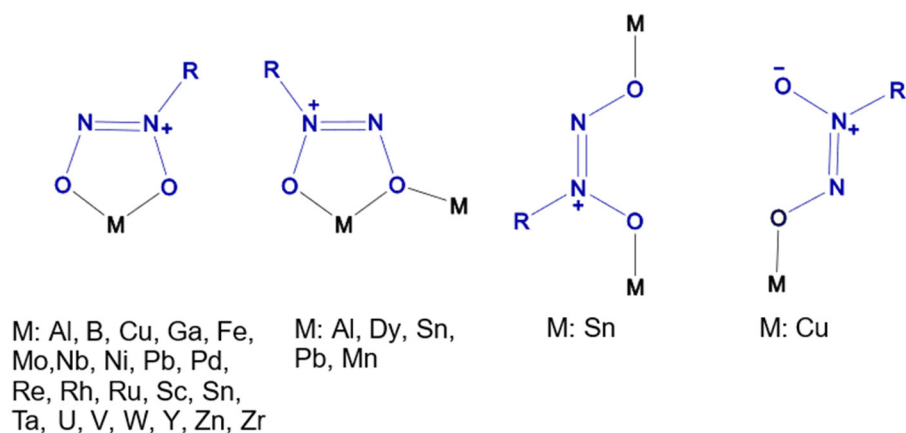


Figure 1.6: Ortep-3 plot of the tetranuclear diazoniumdiolatoruthenium complex of Reference 122 on the left. Right: selected fragment around Ru1.^[45, 122]

Finally, the diazoniumdiolates are capable of releasing nitric oxide (*inter alia* under physiological conditions) which is a desired property in cancer therapy due to the selective antiproliferative activity in tumor cells.^[123] Crystal structures of C-diazoniumdiolates as (chelating) ligands exist for many metals (e.g. Cu, Fe, Rh or Sn), but are also known for N-diazoniumdiolates (Mo, Cu), even though they are not so stable as the corresponding C-compounds.^[108, 124-129] At the current state of research, only one

Introduction

diazoniumdiolato complex is known for ruthenium. A selected fragment of this tetranuclear complex is shown in Figure 1.6. The complex was obtained through the treatment of a tetraaryl ruthenium complex with excess nitric oxide.^[122] An overview of the possible binding modes of the diazoniumdiolato ligand in general is demonstrated in Figure 1.7 followed by an example for each metal in the references. It is worth noting that for the mononuclear chelate form, the dominant coordination motif is (KO,O') beside polynuclear and monocoordinating diazoniumdiolato options.



Scheme 1.7: Currently known *cis*-diazoniumdiolato binding modes (excluding the crystal structures with potassium/sodium).^[110, 122, 127-128, 130-154]

2 Aim of this work

Hence there is only one hexaaquaruthenium salt allowing its effective use in further synthesis, the preparation of alternative hexaaquaruthenium precursors is desired. Intramolecular interactions leading to crystal formation are of special interest, as hydrogen positions were not assigned in the original crystal structure.^[10] Subsequently, the question arises whether its solid and solution species are identical.

As illustrated in the previous chapter, the application of hexaaquaruthenium as the precursor is common in several syntheses, whereby its phosphane chemistry currently undergoes a vivid development for catalytic approaches. In this work, the development of new phosphane complexes—or reevaluation/crystallisation of the already existing complexes with dppe (diphenylphosphanylene) and PPh₃ (triphenylphosphane)—is a step towards their use as precursors.^[23] Furthermore, the collection of good crystallographic data and acceptable yields are intended. The resulting crystal structures will be further contextualised in terms of the ligand's bite angle.

Due to the good leaving group characteristics of the tosylato and aqua ligands, a preferable route towards the synthesis of complexes with rare ligands opens up. The present work focuses on the synthesis of *trans*-hyponitrito complexes where a preparation is characterised by a particular complexity, being rather defined as a matter of luck in the past than of holistic understanding in its reactivity. Nitric oxide reduction and salt metathesis were attempted in the course of this work. The resulting *trans*-hyponitrite compounds were then additionally tested by irradiation and computational calculations elucidating the orbital interactions in these compounds.

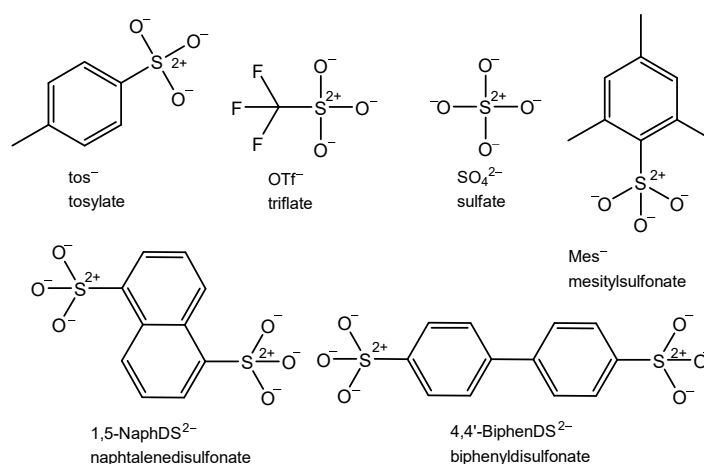
The use of *C*- and *N*-diazoniumdiolato ligands—thereby replacing the explosive *cis*-sodium hyponitrite—have not recognised apart from one exception.^[122] For further analytical investigations, computational calculations were applied on the resulting diazoniumdiolato ruthenium compounds.

In general, for the mentioned complexes an overall analysis including X-ray crystallography (main part), IR, UV/VIS and NMR spectroscopy were conducted. Powder-X-ray diffraction (PXRD), elemental analysis (EA) and high-resolution mass spectroscopy (HRMS) were performed as bulk analyses. Difference-Fourier analysis was further used to assign critical hydrogen positions from crystallographic data.

3 Results

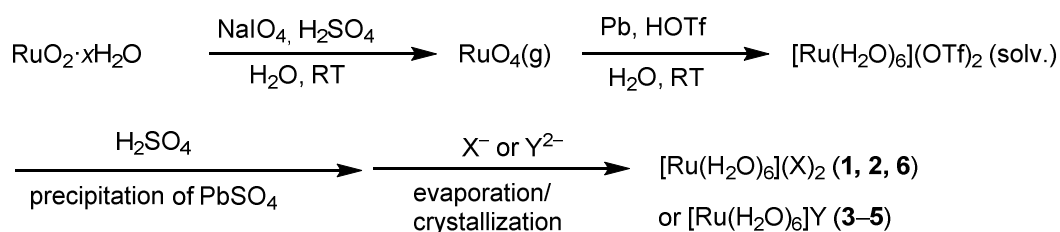
3.1 Syntheses of hexaaquaruthenium salts

In this work the hexaaquaruthenium salts were synthesised according to an altered synthesis of Bernhard *et al.* and Fellay *et al.*^[12] New compounds and crystal structures containing the $[\text{Ru}(\text{H}_2\text{O})_6]^{2+}$ cation were obtained with the following counterions: *p*-toluenesulfonate (tos^-) (**1**), triflate (OTf^-) (**2**), sulfate (SO_4^{2-}) (**3**), 1,5-naphthalenedisulfonate ($1,5\text{-NaphDS}^{2-}$) (**4**), 4,4'-biphenyldisulfonate ($4,4'\text{-BiphenDS}^{2-}$) (**5**) and mesitylsulfonate (MesSO_3^-) (**6**) (Scheme 3.1).



Scheme 3.1: Overview of the counterions used.

The synthetic route was as follows (Scheme 3.2): RuO_2 prepared from $\text{RuCl}_3 \cdot x\text{H}_2\text{O}$ and sodium hydroxide was oxidised with sodium metaperiodate suspended in water with adding sulfuric acid dropwise. The RuO_4 which was poorly soluble in water was transferred by a constant argon flow to a suspension of triflic acid by a constant flow of argon and lead dust resulting in a pink solution of $[\text{Ru}(\text{H}_2\text{O})_6]^{2+}$. The products **1**, **3–6** were obtained by the addition of the respective sulfonic acids, subsequent concentration of the solution and preferential crystallisation at 4 °C. Product **2** was obtained only in the absence of counterions other than triflate.



Scheme 3.2: General synthetic procedure for hexaaquaruthenium salts (**1–6**). X^- : monoanionic sulfonates, Y^{2-} : dianionic sulfonates and sulfate.

Results

The compounds **1–6** have homogenous crystal habits and colours and were analysed by elemental analysis. **1** was additionally analysed by UV/VIS spectroscopy (solution and solid-state) and ^{17}O NMR spectroscopy (coupled) out of historic context (Figure 3.1 and 3.2). The ^{17}O NMR spectrum shows a highfield signal for the ruthenium complex (-189 ppm) and a downfield signal for the SO_3 group of *p*-toluenesulfonate (174 ppm).^[155] The UV/VIS spectra in solution (red: pH 6, green: pH 1) and in solid-state each show two distinctive signals in the region of 390 nm and 529 nm.

Additionally, the crystal structure of $[\text{Ru}(\text{H}_2\text{O})_6](\text{tos})_2$ (**1**) which was originally lacking the exact hydrogen positions of the aqua ligands was reinvestigated by modern methods.^[10] The yields of the compounds were as follows: 59% (**1**), 21% (**2**), 22% (**3**), 37% (**4**), 44% (**5**), 38% (**6**).

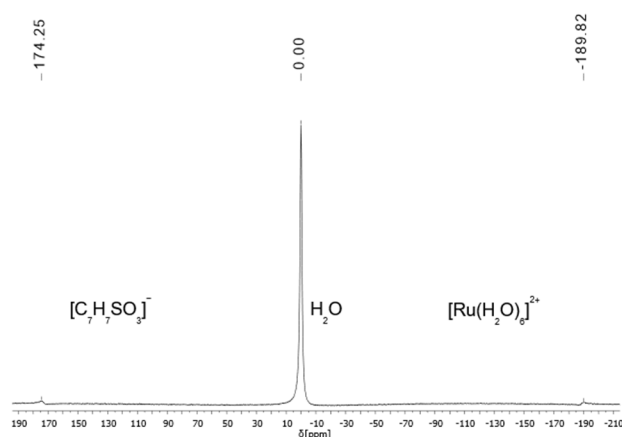


Figure 3.1: ^{17}O NMR spectrum of $[\text{Ru}(\text{H}_2\text{O})_6](\text{tos})_2$ (**1**). Complex is detectable in the high-field (189.8 ppm), the tosylate counterion in the downfield region (174.3 ppm).

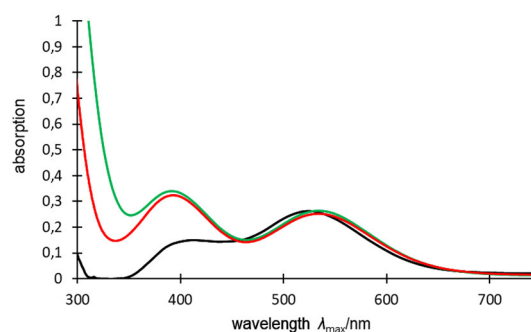


Figure 3.2: UV/VIS spectra of $[\text{Ru}(\text{H}_2\text{O})_6](\text{tos})_2$ (**1**). black: solid-state (388.0, 521.0 nm; y-value (k/s) quadrupled), red: solved in deionised water (pH 6; 391.0, 533.0 nm), green: solved in H-tos solution (pH 1; 392.5, 534.5 nm). In the case of the solid-state spectrum, the Y axis refers to the Kubelka-Munk function ($k/s = (1-R)^2/2R$).^[156]

Crystal structure of $[\text{Ru}(\text{H}_2\text{O})_6](\text{tos})_2$ (**1**)

The structure solution of $[\text{Ru}(\text{H}_2\text{O})_6](\text{tos})_2$ (**1**) succeeded in the monoclinic space group $P2_1/c$. The unit cell contains four formula units (CShM_{OC-6} value: 0.126, asymmetric unit: one molecule). The structure of **1** is shown in Fig. 3.3. The crystal structure can be described as alternate layers of the dicationic complex and the monocationic anion parallel to the *a,b* plane. The sulfonate groups of the tosylate counterion point alternately to the cation sheet above and below. The orientation of the tosyl moiety is orthogonal to the *a,b* plane (Figure 3.4). The hexaaquaruthenium complex is coordinated octahedrally and small deviations are presumably attributable to hydrogen bonds and therefore to crystal-packing effects. The average Ru–O distance is 2.108 Å. The crystal data resembles well with given literature.^[10]

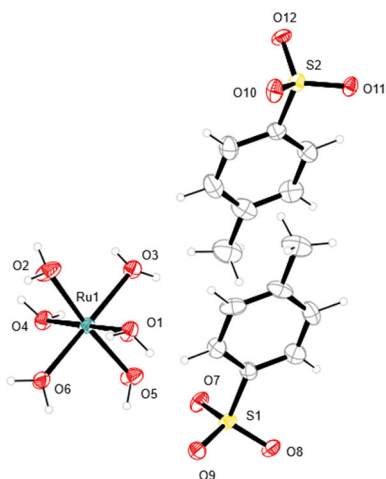
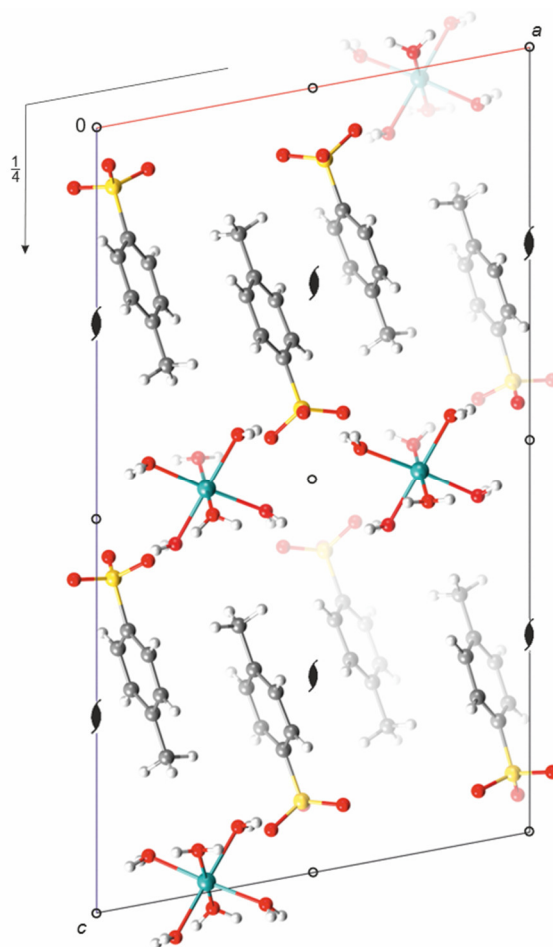
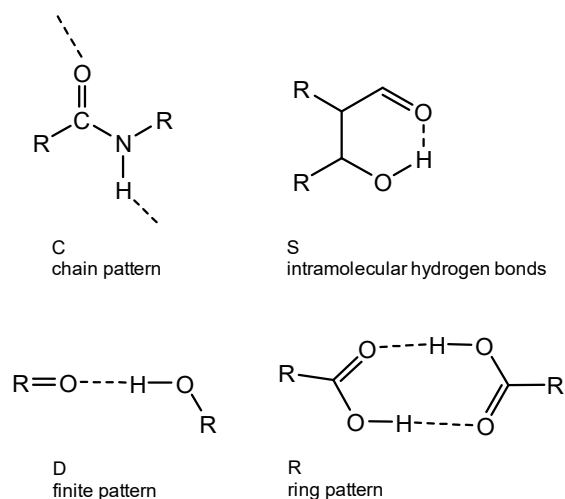


Figure 3.3: ORTEP-3 plot (ellipsoids drawn at the 50% probability level at 100 K) of $[\text{Ru}(\text{H}_2\text{O})_6](\text{tos})_2$ (**1**).^[45] Distances (Å) and angles (°): Ru1–O1 2.102(4), Ru1–O2 2.092(4), Ru1–O3 2.109(4), Ru1–O4 2.113(3), Ru1–O5 2.115(4), Ru1–O6 2.114(3), S1–O7 1.462(4); O8–S1–O7 112.8(2), O1–Ru1–O2 85.31(16), O1–Ru1–O4 179.53(14).

Figure 3.4: Mercury packing diagram of $[\text{Ru}(\text{H}_2\text{O})_6](\text{tos})_2$ (**1**) in the monoclinic space group $P2_1/c$ with view along $[0 \bar{1} 0]$ (on the right side). The symmetry elements of the space group are overlaid. Atoms: carbon (grey), hydrogen (white), oxygen (red), ruthenium (turquoise), sulphur (yellow).



The hydrogen bonds are listed in Table 3.1. There are seven crystallographically independent hydrogen bonds. The resulting hydrogen-bond network was investigated using a graph-set analysis (Table 3.2). A short definition of the designators is given in Scheme 3.3.^[157] In the unary graph set of **1** (looking at one crystallographically independent hydrogen bond) there are four distinguishable ring patterns



Scheme 3.3: Illustration of the four possible designator patterns (G). The designator is defined as follows: $G_d^a(n)$, a number of hydrogen bond acceptors, d number of hydrogen bond donors, n number of atoms in the pattern called degree of pattern. Example: $R_2^2(8)$: ring pattern with two hydrogen bond acceptors, two donors and 8 atoms in total.^[157]

Results

Table 3.1: Distances (d) and angles (α) of hydrogen bonds in **1**. Standard deviations of the last digit are given in parentheses; values without standard deviation are related to hydrogen atoms at calculated positions. D: donor, A: acceptor. Target values of the H...H distance and the O–H distance of the water molecules are restrained to 1.31 Å and 0.82 Å.

D-H...A	$d(\text{D-H})/\text{Å}$	$d(\text{H...A})/\text{Å}$	$d(\text{D-A})/\text{Å}$	$\alpha(\text{D-H...A})/^\circ$
O1–H11...O7	0.82	1.91	2.730(5)	174
O1–H12A...O8 ^I	0.82	1.97	2.791(5)	172
O2–H21...O12 ^{II}	0.82	2.00	2.818(5)	170
O2–H22A...O7 ^I	0.82	1.97	2.766(5)	160
O3–H31...O11 ^{II}	0.82	1.90	2.710(5)	165
O3–H32...O12 ^{II}	0.83	1.95	2.756(5)	162
O4–H41...O11 ^{III}	0.82	1.91	2.734(5)	173
O4–H42...O10 ^{IV}	0.82	1.96	2.768(5)	166
O5–H51...O10 ^{III}	0.82	1.97	2.785(5)	166
O5–H52...O9 ^V	0.82	1.95	2.743(5)	159
O6–H61...O8 ^V	0.83	1.93	2.758(5)	175
O6–H62...O9 ^{VI}	0.82	1.98	2.808(5)	174

^I $[x, y+1, z]$, ^{II} $[-x, y+1/2, -z+1/2]$, ^{III} $[x, -y+1/2, z+1/2]$, ^{IV} $[x, -y+3/2, z+1/2]$,

^V $[-x+1, -y, -z+1]$, ^{VI} $[-x+1, -y+1, -z+1]$.

and three finite patterns. In the binary graph set (two crystallographically independent hydrogen bonds) sixth- or eighth-degree chains are formed with two hydrogen bond acceptors and two donors. A ternary graph set is not possible for **1**. The quarternary graph set consists of tenth-degree ring patterns with either three or two hydrogen-bond acceptors and four hydrogen-bond donors. In summary, the hydrogen-bond donors in **1** are saturated, which means all twelve water hydrogens do form complex hydrogen-bond patterns with the sulfonate groups of the tosylate counterions forming an extended hydrogen-bond network.

Results

Table 3.2: Graph set of products **1–6**. The unary graph set is completely assigned. For the binary, ternary and quaternary graph set an assignment was made as far as possible and shows examples of the patterns obtained.^[157]

	N₁	N₂	N₃	N₄
1	$DR_2^2(8)R_2^2(8)R_2^2(8)DR_2^2(8)D$	$C_2^2(6),$ $C_2^2(8)$	–	$R_4^3(10), R_4^2(10)$
2	$R_2^2(8)DDDD$	$C_2^2(6),$ $C_2^2(8)$	–	$R_4^3(10), R_4^2(10)$
3	$R_2^2(8)DDDDDDDD$	$C_2^2(6),$ $C_2^2(8)$	$C_3^2(6), C_3^3(8)$	$R_4^3(10)$ $N_6: R_6^3(12), R_6^4(14)$
4	$C_1^1(4)R_2^2(8)R_2^2(8)D$	$C_2^1(6),$ $C_2^2(8),$ $C_2^2(6)$	$C_3^2(6), C_3^3(10)$	–
5	$DDDDD$	$C_2^1(6),$ $C_2^2(8),$ $C_2^2(6)$	$C_3^3(8), R_3^3(10)$	$R_4^2(10)$
6	$R_4^3(10)R_2^1(6)R_4^3(12)DDR_2^2(8)$	$C_2^2(8),$ $C_2^2(6)$	–	–

*Crystal structure of $[Ru(H_2O)_6](OTf)_2$ (**2**)*

The structure solution of $[Ru(H_2O)_6](OTf)_2$ (**2**) succeeded in the monoclinic space group $C2/c$. The unit cell contains four formula units (CSHM_{OC-6} value: 0.067, asymmetric unit: half molecule). The structure of **2** is shown in Figure 3.5. The $[Ru(H_2O)_6]^{2+}$ complex is coordinated octahedrally. Small deviations of the Ru–O distances are a tentative result of crystal-packing effects, in particular hydrogen bonds. The average Ru–O distance is 2.105 Å. The packing of the unit cell resembles **1** well. Complex and trifluoromethanesulfonate each form sheets which alternate parallel to the a, b plane. The OTf[–] counterions lay in contrast to to[–] in **1** on a two-fold screw axis (Figure 3.6). The hydrogen bonds are listed in Table 3.3. There are five crystallographically independent hydrogen bonds. The hydrogen-bond network resembles **1** with identical designators for the binary and ternary graph set and an eighth-degree ring pattern with two hydrogen bond acceptors and donors for the unary graph set (Table 3.2).

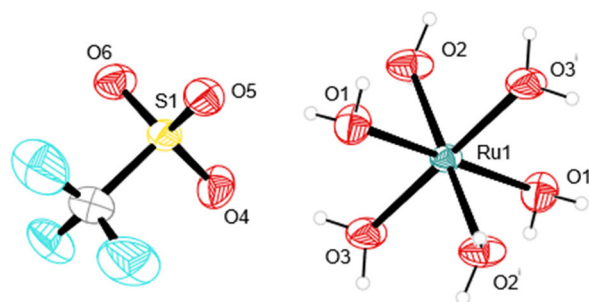


Figure 3.5: ORTEP-3 plot (ellipsoids drawn at the 50% probability level at 293 K) of $[\text{Ru}(\text{H}_2\text{O})_6](\text{OTf})_2$ (**2**).^[45] Distances (Å) and angles (°): Ru1–O1 2.109(2), Ru1–O2 2.111(2), Ru1–O3 2.094(2), S1–O4 1.440(2); O4–S1–O5 114.49(15), O1–Ru1–O2 90.61(10). Symmetry code: $^i-x+3/2, -y+1/2, -z$. *G* site symmetry of the cation.

Figure 3.6: Mercury packing diagram of $[\text{Ru}(\text{H}_2\text{O})_6](\text{OTf})_2$ (**2**) in the monoclinic space group *C2/c* with view along $[0 \bar{1} 0]$ (on the right side). The symmetry elements of the space group are overlaid. Atoms: carbon (grey), hydrogen (white), fluorine (light green), oxygen (red), ruthenium (turquoise), sulphur (yellow).

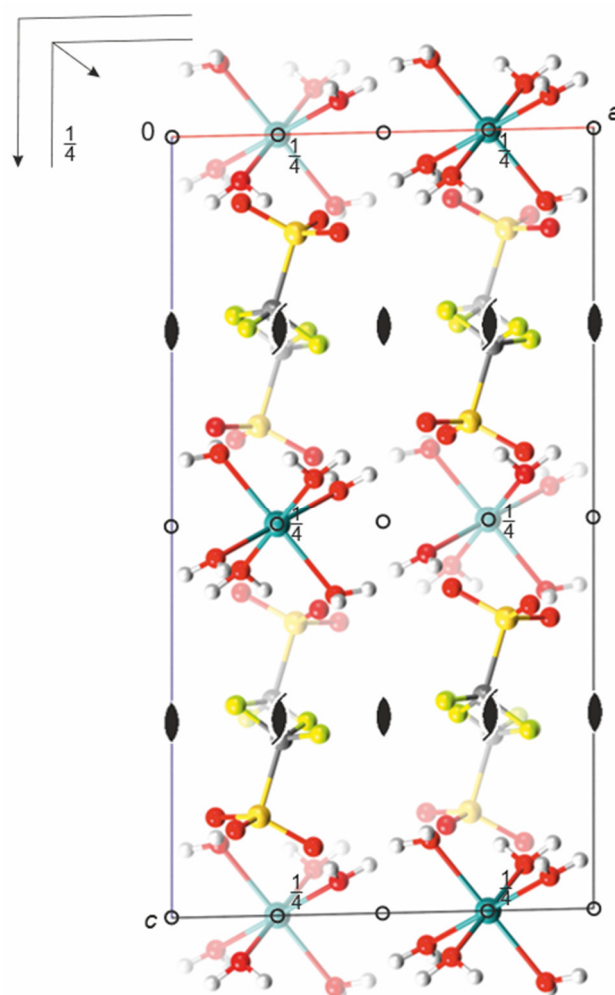


Table 3.3: Distances (*d*) and angles (α) of hydrogen bonds in **2**. Standard deviations of the last digit are given in parentheses; values without standard deviation are related to hydrogen atoms at calculated positions. D: donor, A: acceptor. Target values of the H···H distance and the O–H distance of the water molecules are restrained to 1.31 Å and 0.82 Å.

D–H···A	<i>d</i> (D–H)/Å	<i>d</i> (H···A)/Å	<i>d</i> (D–A)/Å	α (D–H···A)/°
O1–H11···O5	0.82	2.05	2.880(3)	174
O1–H12···O4 ⁱ	0.82	2.02	2.843(3)	172
O2–H21···O6 ⁱⁱ	0.83	2.05	2.836(3)	158
O2–H22···O5 ⁱⁱⁱ	0.83	2.04	2.847(3)	163
O3–H31···O6 ^{iv}	0.82	1.95	2.772(3)	172
O3–H32···O4	0.82	1.95	2.769(3)	172

ⁱ $[x-1/2, y-1/2, z]$, ⁱⁱ $[-x+1/2, -y+3/2, -z+1]$, ⁱⁱⁱ $[-x, -y+1, -z+1]$, ^{iv} $[x+1/2, y-1/2, z]$

Crystal structure of $[\text{Ru}(\text{H}_2\text{O})_6]\text{SO}_4$ (**3**)

The structure solution of $[\text{Ru}(\text{H}_2\text{O})_6]\text{SO}_4$ (**3**) succeeded in the monoclinic space group $C2/c$. The unit cell contains eight formula units (CSHM_{OC-6} value: 0.109, asymmetric unit: one molecule). The structure of **3** is shown in Figure 3.7. The $[\text{Ru}(\text{H}_2\text{O})_6]^{2+}$ complex is coordinated octahedrally whereby small deviations of angles and distances are tentative results of crystal-packing effects. The average Ru–O distance is 2.117 Å (room-temperature measurement). The packing of the unit cell is similar to **1** and **2** (Figure 3.8) with alternating sheets of complex cations and sulphate anions parallel to the a,b plane.

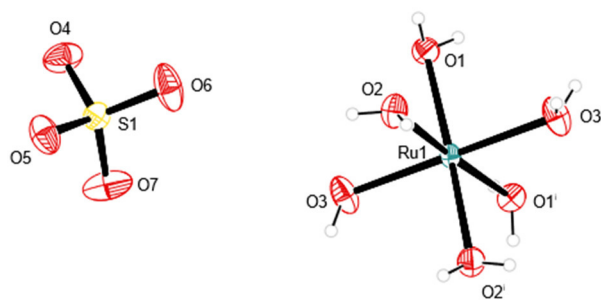
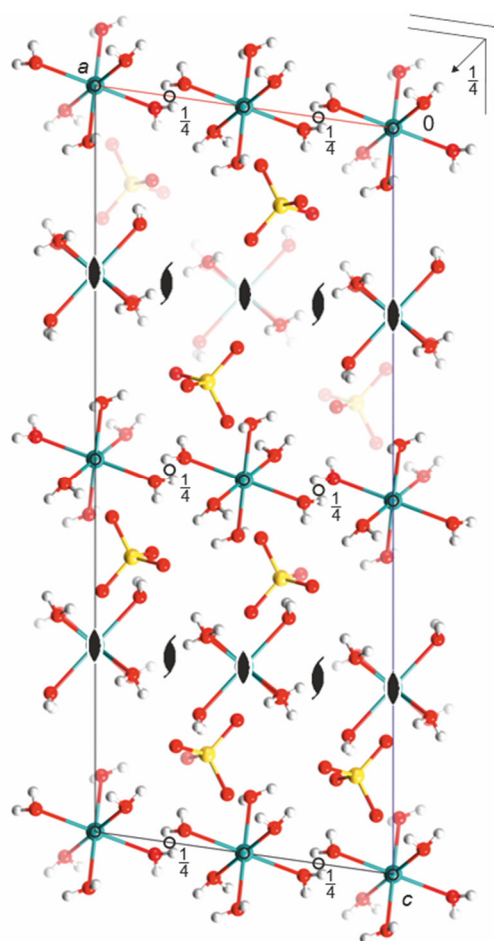


Figure 3.7: ORTEP-3 plot (50% probability ellipsoids) of $[\text{Ru}(\text{H}_2\text{O})_6]\text{SO}_4$ (**3**).^[45] Distances (Å) and angles (°): Ru1–O1 2.1289(16), Ru1–O2 2.1056(17), Ru1–O3 2.1137(18), S1–O4 1.4735(19); O4–S1–O6 108.58(12), O1–Ru1–O2 87.49(7). C_i site symmetry of the cation.

Figure 3.8: Mercury packing diagram of $[\text{Ru}(\text{H}_2\text{O})_6]\text{SO}_4$ (**3**) in the monoclinic space group $C2/c$ with view along $[0\ 1\ 0]$ (on the right side). The symmetry elements of the space group are overlaid. Atoms: hydrogen (white), oxygen (red), ruthenium (turquoise), sulphur (yellow).



The hydrogen bonds are listed in Table 3.4. There are nine crystallographically independent hydrogen bonds. The designators of **1** and **2** are also present in **3**. Additionally, the ternary graph set shows a sixth-degree chain pattern with two hydrogen bond acceptors and three donors and an eighth-degree chain pattern with three hydrogen bond acceptors and three donors. The unusual sextary graph set consists of a twelfth-degree ring pattern with three hydrogen bond acceptors and six donors and a fourteenth-degree ring pattern with four hydrogen bond acceptors and six donors. This is a result of the ability of the oxygens of sulphate to accept three instead two hydrogen bonds (Table 3.2).

Results

Table 3.4: Distances (d) and angles (α) of hydrogen bonds in **3**. Standard deviations of the last digit are given in parentheses; values without standard deviation are related to hydrogen atoms at calculated positions. D: donor, A: acceptor. Target values of the H...H distance and the O–H distance of the water molecules are restrained to 1.31 Å and 0.74 Å.

D-H...A	$d(\text{D-H})/\text{Å}$	$d(\text{H...A})/\text{Å}$	$d(\text{D-A})/\text{Å}$	$\alpha(\text{D-H...A})/^\circ$
O1–H11...O6 ^I	0.74	1.94	2.685(2)	180
O1–H12...O4 ^{II}	0.74	2.00	2.741(2)	168
O2–H21...O6 ^{III}	0.73	2.01	2.747(3)	173
O2–H22...O1 ^{III}	0.74	2.11	2.857(2)	175
O3–H31...O4 ^{IV}	0.73	2.33	2.949(3)	143
O3–H32...O5 ^V	0.74	1.98	2.727(3)	175
O8–H81...O4 ^{IV}	0.73	2.00	2.728(3)	170
O8–H82...O7	0.74	1.96	2.696(3)	172
O9–H91...O5	0.73	2.06	2.780(3)	166
O9–H92...O7 ^{VI}	0.73	2.57	3.065(3)	127
O9–H92...O8 ^{VII}	0.73	2.53	3.186(3)	150
O10–H101...O5 ^{VI}	0.73	2.16	2.877(3)	164
O10–H102...O7 ^{VI}	0.73	1.97	2.696(3)	166
O10–H101...O4 ^{VIII}	0.73	2.61	3.145(3)	131

^I $[-x+1/2, y+1/2, -z+1/2]$, ^{II} $[-x+1, y, -z+1/2]$, ^{III} $[-x+1/2, y-1/2, -z+1/2]$, ^{IV} $[x-1/2, y-1/2, z]$, ^V $[x-1/2, y+1/2, z]$, ^{VI} $[-x+3/2, -y+1/2, -z+1]$, ^{VII} $[x+1/2, y-1/2, z]$, ^{VIII} $[-x+1, -y+1, -z+1]$.

Crystal structure of $[\text{Ru}(\text{H}_2\text{O})_6](1,5\text{-NaphDS})$ (**4**)

The structure solution of $[\text{Ru}(\text{H}_2\text{O})_6](1,5\text{-NaphDS})$ (**4**) succeeded in the monoclinic space group $P2_1/c$. The unit cell contains two formula units (CShM_{OC-6} value: 0.172, asymmetric unit: half molecule). The structure of **4** is shown in Figure 3.9. The $[\text{Ru}(\text{H}_2\text{O})_6]^{2+}$ complex is coordinated octahedrally whereby small deviations of angles and distances are tentative results of crystal-packing effects. The average Ru–O distance is 2.109 Å. The packing diagram of **4** shows the layer structure, but the sheets of dicationic complex and dianionic naphthalenedisulfonate alternate parallel to the c, b plane (Figure 3.10).

Results

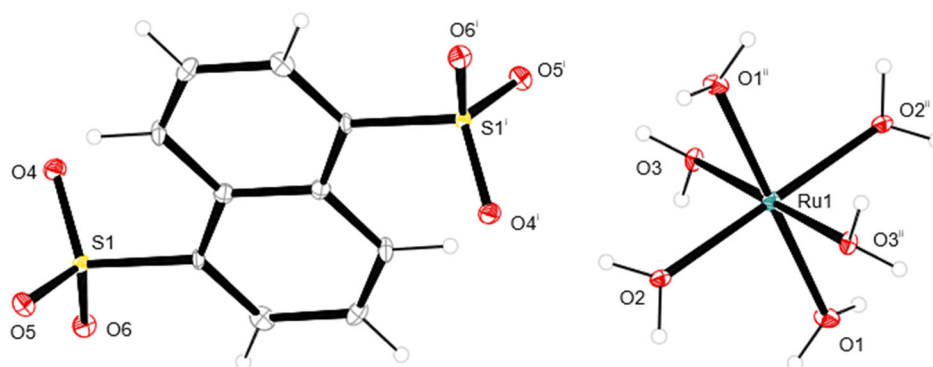


Figure 3.9: ORTEP-3 plot (50% probability ellipsoids) of $[\text{Ru}(\text{H}_2\text{O})_6](1,5\text{-NaphDS})$ (**4**).^[45] Distances (Å) and angles (°): Ru1–O1 2.111(3), Ru1–O2 2.101(3), Ru1–O3 2.115(3), S1–O4 1.448(3); O4–S1–O5 113.09(19), O1–Ru1–O2 93.56(12). *C* site symmetry.

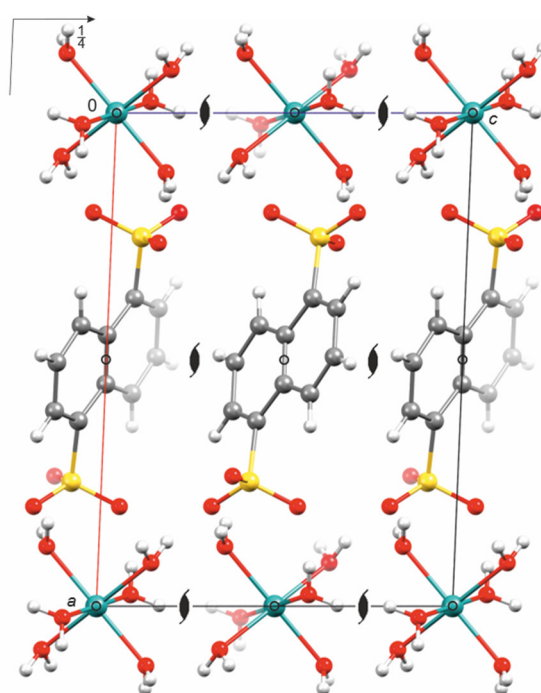


Figure 3.10: Mercury packing diagram of $[\text{Ru}(\text{H}_2\text{O})_6](1,5\text{-NaphDS})$ (**4**) in the monoclinic space group $P2_1/c$ with view along $[0\ 1\ 0]$ (on the right side). The symmetry elements of the space group are overlaid. Atoms: carbon (grey), hydrogen (white), oxygen (red), ruthenium (turquoise), sulphur (yellow).

The hydrogen bonds are listed in Table 3.5. There are four crystallographically independent hydrogen bonds. The unary graph set is a fourth-degree chain pattern with one hydrogen bond acceptor and one donor, and two eighth-degree ring patterns with two acceptors and two donors. The binary graph set shows a sixth-degree ring pattern with one acceptor and two donor positions and eighth- and sixth-degree chain patterns with two acceptors and two donors. The ternary graph set consists of sixth-degree chain patterns with two hydrogen bond acceptors and three donors and tenth-degree chain pattern with three acceptors and three donors (Table 3.2).

Results

Table 3.5: Distances (d) and angles (α) of hydrogen bonds in **4**. Standard deviations of the last digit are given in parentheses; values without standard deviation are related to hydrogen atoms at calculated positions. D: donor, A: acceptor. Target values of the H \cdots H distance and the O–H distance of the water molecules are restrained to 1.31 Å and 0.82 Å.

D–H \cdots A	$d(\text{D–H})/\text{Å}$	$d(\text{H}\cdots\text{A})/\text{Å}$	$d(\text{D–A})/\text{Å}$	$\alpha(\text{D–H}\cdots\text{A})/^\circ$
O1–H11 \cdots O3 ^I	0.82	2.05	2.853(4)	163
O1–H12 \cdots O5 ^{II}	0.82	2.029	2.841(4)	167
O2–H21 \cdots O4 ^{III}	0.83	1.87	2.698(4)	174
O2–H22 \cdots O6 ^{II}	0.82	1.86	2.690(4)	175
O3–H31 \cdots O5 ^{III}	0.82	1.95	2.780(4)	177
O3–H32 \cdots O6 ^{IV}	0.83	1.90	2.726(4)	168

^I $[-x, y+1/2, -z+1/2]$, ^{II} $[-x+1, -y+1, -z+1]$, ^{III} $[-x+1, -y, -z+1]$, ^{IV} $[-x+1, y+1/2, -z+1/2]$.

Crystal structure of $[\text{Ru}(\text{H}_2\text{O})_6](4,4'\text{-BiphenDS})\cdot 2\text{H}_2\text{O}$ (**5**)

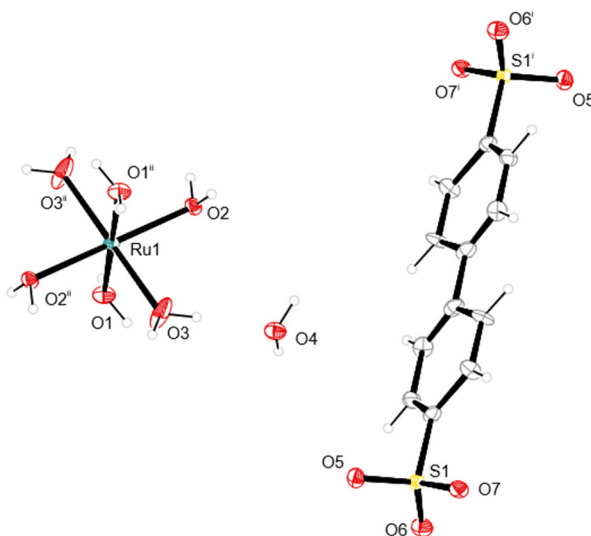


Figure 3.11: ORTEP-3 plot (50% probability ellipsoids) of $[\text{Ru}(\text{H}_2\text{O})_6](4,4'\text{-BiphenDS})\cdot 2\text{H}_2\text{O}$ (**5**).^[45] The structural disorder of the tilted aromatic rings is omitted. Distances (Å) and angles ($^\circ$): Ru1–O1 2.1043(18), Ru1–O2 2.1209(18), Ru1–O3 2.095(2), S1–O5 1.4773(19); O5–S1–O6 111.66(12), O1–Ru1–O2 93.47(8). C_i site symmetry.

Results

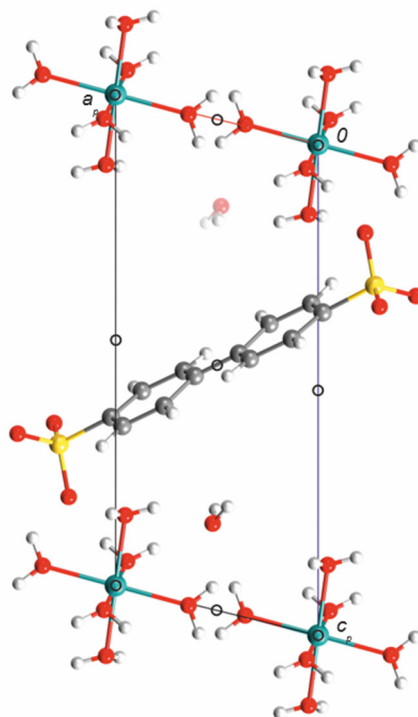


Figure 3.12: Mercury packing diagram of $[\text{Ru}(\text{H}_2\text{O})_6](4,4'\text{-BiphenDS})\cdot 2\text{H}_2\text{O}$ (**5**) in the triclinic space group $P\bar{1}$ with view along $[0\ 1\ 0]$ (on the right). The symmetry elements of the space group are overlaid. Atoms: carbon (grey), hydrogen (white), oxygen (red), ruthenium (turquoise), sulphur (yellow). The disordered part of the biphenyl moiety is omitted.

The structure solution of $[\text{Ru}(\text{H}_2\text{O})_6](4,4'\text{-BiphenDS})\cdot 2\text{H}_2\text{O}$ (**5**) succeeded in the triclinic space group $P\bar{1}$. The unit cell contains one formula unit (CShM_{OC-6} value: 0.228, asymmetric unit: half molecule). The structure of **5** is shown in Figure 3.11. The $[\text{Ru}(\text{H}_2\text{O})_6]^{2+}$ complex is coordinated octahedrally whereby small deviations of angles and distances are tentative results of crystal-packing effects. The biphenyl moiety is disordered (tilted) around the S–S axis. The average Ru–O distance is 2.106 Å. The packing diagram resembles the former layer structures **1–4**, a broad sheet of biphenyldisulfonate and a sheet of $[\text{Ru}(\text{H}_2\text{O})_6]^{2+}$ cations alternating along c_p (Figure 3.12). The hydrogen bonds are listed in Table 3.6. Two molecules of crystal water (O4) are included. The unary graph set consists only of finite patterns (D). The binary graph set consists of a sixth-degree chain pattern (one acceptor, two donors), another sixth-degree chain pattern (two acceptors, two donors) and an eighth-degree chain (two acceptors, two donors). The ternary graph set consists of an eighth-degree chain pattern with three acceptors and three donors and a tenth degree ring pattern with three acceptors and three donors. And the quaternary graph set has a tenth-degree ring pattern with two acceptors and four donors (Table 3.2).

Results

Table 3.6: Distances (d) and angles (α) of hydrogen bonds in **5**. Standard deviations of the last digit are given in parentheses; values without standard deviation are related to hydrogen atoms at calculated positions. D: donor, A: acceptor. Target values of the H...H distance and the O–H distance of the water molecules are restrained to 1.31 Å and 0.82 Å.

D-H...A	$d(\text{D-H})/\text{Å}$	$d(\text{H...A})/\text{Å}$	$d(\text{D-A})/\text{Å}$	$\alpha(\text{D-H...A})/^\circ$
O1–H11...O4 ^I	0.83	1.85	2.685(3)	176
O1–H12...O5 ^I	0.82	2.07	2.874(3)	164
O2–H21...O7 ^{II}	0.82	1.99	2.819(3)	173
O2–H22...O5 ^{III}	0.82	2.03	2.845(3)	165
O3–H31...O5 ^{IV}	0.82	1.97	2.795(3)	175
O3–H32...O4	0.82	1.86	2.689(3)	174
O4–H41...O6 ^{III}	0.82	1.89	2.712(3)	172
O4–H42...O7 ^I	0.82	1.96	2.786(3)	173

^I $[x+1, y, z]$, ^{II} $[x+2, y+1, z]$, ^{III} $[x+1, y+1, z]$, ^{IV} $[-x, -y+1, -z]$

Crystal structure of $[\text{Ru}(\text{H}_2\text{O})_6](\text{MesSO}_3)_2$ (**6**)

The structure solution of $[\text{Ru}(\text{H}_2\text{O})_6](\text{MesSO}_3)_2$ (**6**) succeeded in the monoclinic space group $P2_1/c$. The unit cell contains four formula unit (CShM_{OC-6} value: 0.066, asymmetric unit: one molecule). The structure of **6** is shown in Figure 3.13. The $[\text{Ru}(\text{H}_2\text{O})_6]^{2+}$ complex is coordinated octahedrally whereby small deviations of angles and distances are tentative results of crystal-packing effects as well. The average Ru–O distance is 2.112 Å (room temperature measurement). The packing diagram shows layers of mesitylsulfonate and $[\text{Ru}(\text{H}_2\text{O})_6]^{2+}$ alternating parallel to the a,c plane. The orientation of the mesitylsulfonate counterions is almost parallel to the b,c plane (or orthogonal to the a,c plane) (Figure 3.14). The hydrogen bonds are listed in Table 3.7. There are five crystallographically independent hydrogen bonds. This results in a tenth-degree ring pattern with three hydrogen bond acceptors and four donors, a sixth-degree ring pattern with one acceptor and two donors, a twelfth-degree ring pattern with three acceptors and four donors, and an eighth-degree ring pattern with two hydrogen bond acceptors and two donors for the unary graph set (rest: finite patterns). The binary graph set consists, like **1**, of eighth- and sixth-degree chain patterns with two hydrogen acceptors and two donors (Table 3.2).

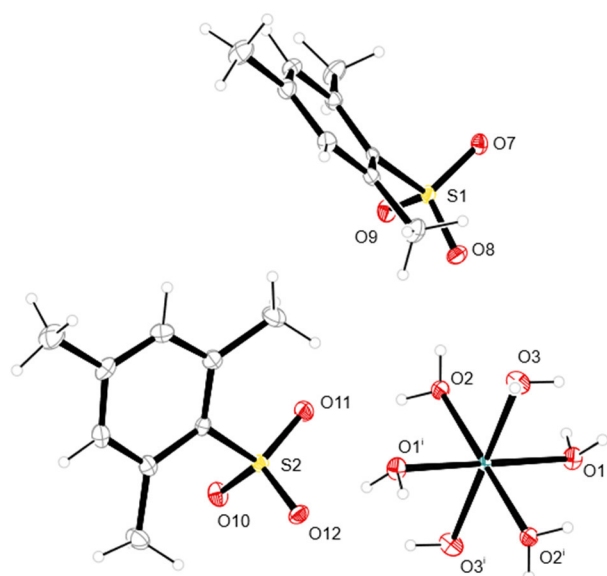
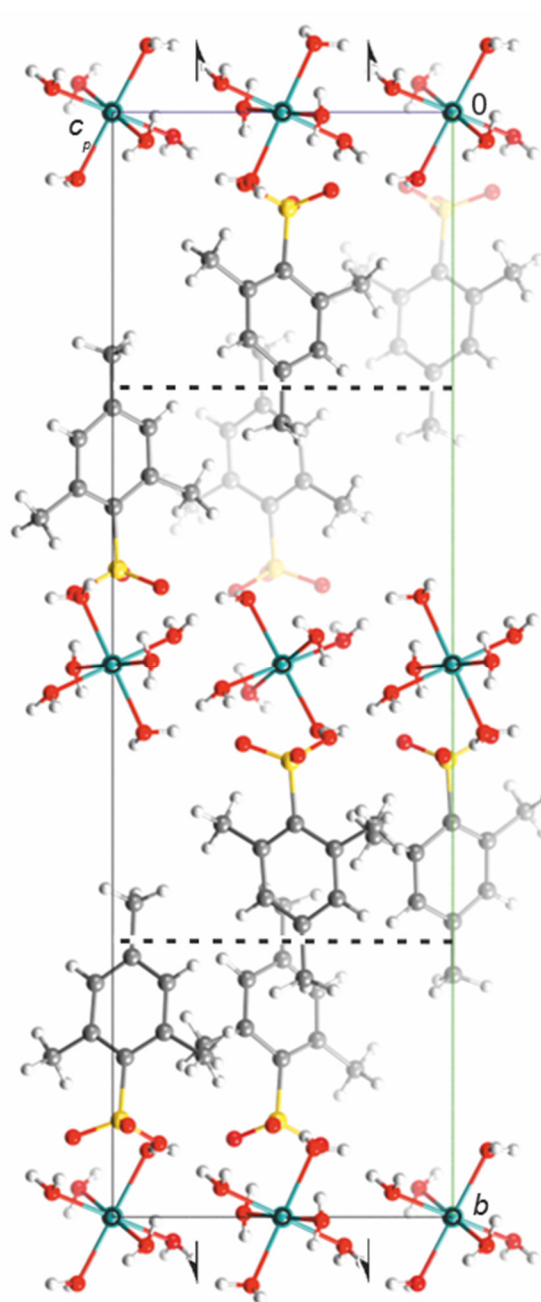


Figure 3.13: ORTEP-3 plot (50% probability ellipsoids) of $[\text{Ru}(\text{H}_2\text{O})_6](\text{Mes})_2$ (**6**).^[45] Distances (\AA) and angles ($^\circ$): Ru1–O1 2.106(2), Ru1–O2 2.112(2), Ru1–O3 2.107(2), S1–O7 1.459(2); O8–S1–O7 111.70(12), O1–Ru1–O2 91.28(8). C_i site symmetry of the cation.

Figure 3.14: Mercury packing diagram of $[\text{Ru}(\text{H}_2\text{O})_6](\text{MesSO}_3)_2$ (**6**) in the monoclinic space group $P2_1/c$ with view along $[1\ 0\ 0]$ (on the right side). The symmetry elements of the space group are overlaid. Atoms: carbon (grey), hydrogen (white), oxygen (red), ruthenium (turquoise), sulphur (yellow).



Results

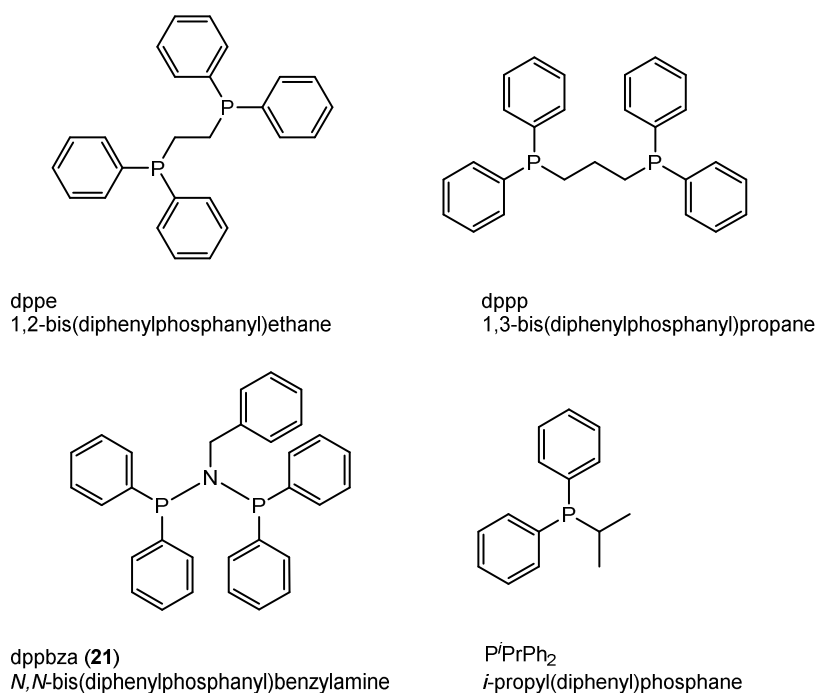
Table 3.7: Distances (d) and angles (α) of hydrogen bonds in **6**. Standard deviations of the last digit are given in parentheses; values without standard deviation are related to hydrogen atoms at calculated positions. D: donor, A: acceptor. Target values of the H...H distance and the O–H distance of the water molecules are restrained to 1.31 Å and 0.82 Å.

D-H...A	$d(\text{D-H})/\text{Å}$	$d(\text{H...A})/\text{Å}$	$d(\text{D-A})/\text{Å}$	$\alpha(\text{D-H...A})/^\circ$
O1–H111...O12 ^I	0.82	1.95	2.772(3)	168
O1–H112...O7 ^{II}	0.82	1.95	2.773(3)	171
O2–H21...O8	0.82	1.99	2.810(3)	171
O2–H22...O11	0.81	1.98	2.799(3)	171
O3–H31...O10 ^{IV}	0.82	1.86	2.664(3)	163
O3–H32...O5 ^{II}	0.82	2.46	2.878(3)	113
O3–H32...O12 ^I	0.82	2.34	3.139(3)	164
O4–H41...O10 ^{III}	0.82	2.57	3.140(3)	127
O4–H41...O12 ^{III}	0.82	2.01	2.819(3)	167
O4–H42...O7 ^{II}	0.82	2.01	2.834(3)	178
O5–H51...O8 ^{II}	0.82	1.90	2.725(3)	177
O5–H52...O9	0.82	1.97	2.791(3)	169
O6–H61...O11	0.82	2.07	2.853(3)	158
O6–H62...O9	0.82	2.00	2.806(3)	163

^I $[-x+1, -y+1, -z+1]$, ^{II} $[-x+1, -y+1, -z]$, ^{III} $[-x+2, -y+1, -z+1]$, ^{IV} $[x-1, y, z]$.

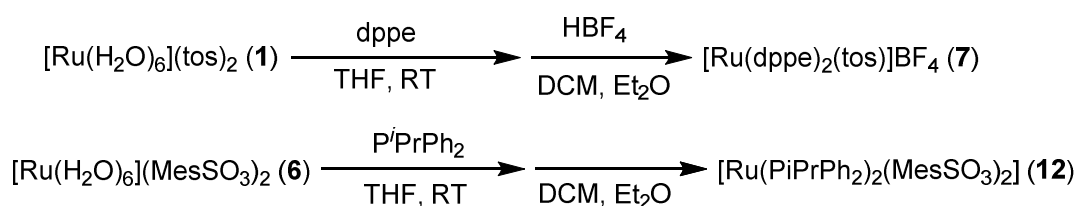
3.2 Tosylato- κ^2O,O' ruthenium complexes with phosphane co-ligands

The synthesis of the tosylatoruthenium complexes in small quantities was accomplished according to a procedure by Bailey *et al.* for $[\text{Ru}(\text{dppe})_2(\text{tos})](\text{tos})$.^[23] Therefore, a broad screening of phosphanes and bisphosphanes was performed, aiming at high quantity and quality crystal yields (chapter 3.2–3.4). The following phosphanes were used for the syntheses of tosylato- κ^2O,O' ruthenium complexes (Scheme 3.4): dppe, dppp, dppbza (**21**) and $P^i\text{PrPh}_2$.



Scheme 3.4: Overview of phosphanes used for tosylato- κ^2O,O' ruthenium complexes **7–12**.

The synthetic route was as follows (Scheme 3.5): A mixture of $[\text{Ru}(\text{H}_2\text{O})_6](\text{tos})_2$ (**1**) or $[\text{Ru}(\text{H}_2\text{O})_6](\text{MesSO}_3)_2$ (**6**) and the proper phosphane was suspended in THF and stirred. For crystallisation the crude was solved in DCM layered with diethyl ether (or trichloromethane-diethyl ether). The products $[\text{Ru}(\text{dppe})_2(\text{tos})]\text{BF}_4$ (**7**), $[\text{Ru}(\text{dppp})_2(\text{tos})]\text{BF}_4$ (**8**), $[\text{Ru}(\text{dppbza})_2(\text{tos})]\text{BF}_4$ (**9**), $[\text{Ru}(\text{dppe})_2(\text{MesSO}_3)]\text{BF}_4$ (**11**) were obtained by addition of tetrafluoroboric acid (in water), $[\text{Ru}(P^i\text{PrPh}_2)_2(\text{tos})_2]$ (**10**), and $[\text{Ru}(P^i\text{PrPh}_2)_2(\text{MesSO}_3)_2]$ (**12**) without additive.



Scheme 3.5: General synthetic procedure for tosylato- κ^2O,O' ruthenium complexes **7** and **12**. The complexes **8–11** were made similarly.

Results

The compounds **7–12** had homogenous crystal habits and colours and were analysed by infrared, UV/VIS and NMR spectroscopy (Table 3.8). Mass spectroscopy, elemental analysis and powder-X-ray diffraction for **7** and **8** were performed as bulk analyses. The yields of the compounds **7–12** were as follows: 94% (**7a**), 82% (**7b**), 89% (**8**), 66% (**9**), 82% (**10**), 90% (**11**), 66% (**12**).

Table 3.8: Overview of selected IR, UV/VIS and NMR data of compounds **7a–12** (***7b** is almost identical to **7a**). ** Expected signals reside in the solvent cut-off region. IR spectrum measured on ATR (attenuated total reflection) unit as solid. NMR spectra measured in CD₂Cl₂ at RT. UV/VIS measured in DCM. *** NMR spectrum measured in CD₂Cl₂ at 0°. The $\hat{\nu}(\text{SO})$ values were taken from quantum chemical calculations, based on DFT.

	IR: $\hat{\nu}_{\text{S-O}}/\text{cm}^{-1}$	IR: $\hat{\nu}_{\text{S-O}}/\text{cm}^{-1}$ calcd.	UV/VIS: $\lambda_{\text{max}}/\text{nm}$	¹³ C{ ¹ H} NMR: δ/ppm (C-CH ₃)	³¹ P{ ¹ H} NMR: δ/ppm
[Ru(dppe) ₂ (tos)]BF ₄ (7a)*	1205, 993	1220, 999	342, 380	142.3	60.3, 46.9
[Ru(dppp) ₂ (tos)]BF ₄ (8)	1191, 1025	1200, 1034	317, 400	142.0	23.1, -2.9
[Ru(dppbza) ₂ (tos)]BF ₄ (9)	1273, 1004	1248, 1004 (945)	–**	135.5	87.7, 66.2
[Ru(P ⁱ PrPh ₂) ₂ (tos) ₂] (10)	1190, 1037, 930	1202, 1042, 935	383, 530	143.3	69.2
[Ru(dppe) ₂ (MesSO ₃)]BF ₄ (11)	1191, 940	1186, 939	341, 379	140.9	60.5, 57.8, 51.4, 42.9***
[Ru(P ⁱ PrPh ₂) ₂ (MesSO ₃) ₂] (12)	≈1200 (sh), 1055, 935	1207, 1058, 935	379, 519	141.0	70.2

Crystal structure of [Ru(dppe)₂(tos)]BF₄ (**7**)

The structure solution [Ru(dppe)₂(tos)]BF₄ (**7**) succeeded in the triclinic space group $P\bar{1}$. The unit cell contains two formula units (CShM_{OC-6} value: 2.293, asymmetric unit: one molecule). The structure of **7** is shown in Figure 3.15. The coordination polyhedron of the cationic complex is best described as distorted-octahedral. Two bisphosphanes and a tosylato- $\kappa^2\text{O},\text{O}'$ ligand which is part of a four-ring chelate coordinate a ruthenium(II) centre.

Results

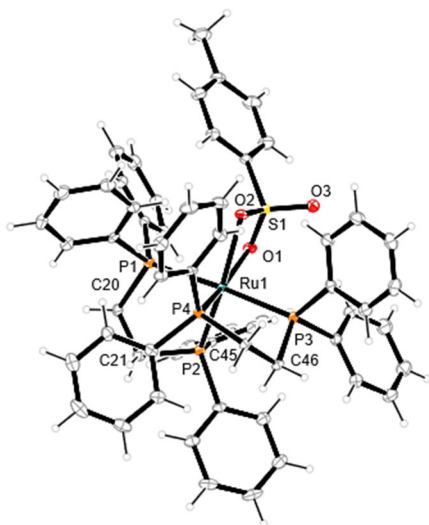


Figure 3.15: ORTEP-3 plot (ellipsoids drawn at the 50% probability level at 100 K) of the $[\text{Ru}(\text{dppe})_2(\text{tos})]^+$ ion in **7** (on the left side).^[45] Selected distances (Å) and angles (°): Ru1–O1 2.267(2), Ru1–O2 2.2914(19), Ru1–P1 2.3815(8), Ru1–P2 2.3031(7), Ru1–P3 2.4481(8), Ru1–P4 2.3034(8), S1–O1 1.486(2), S1–O2 1.489(2), S1–O3 1.441(2); O1–Ru1–O2 62.37(7), O3–S1–O1 112.92(12), O3–S1–O2 115.16(12), O1–S1–O2 105.04(11), S1–O1–Ru1 95.42(10), S1–O2–Ru1 94.33(9). Crystals suitable for X-ray diffraction obtained by layering a chloroform solution with diethyl ether. Crystal solvent (trichloromethane) and tetrafluoridoborate counterion are omitted.^[39]

The four-ring chelate has an acute angle of 62.37° at the central metal (O1–Ru1–O2) and an obtuse angle of 105.04° at the sulphur (O1–S1–O2). The ruthenium-oxygen distance is with 2.267 Å and 2.2914 Å similar to the sulfato- $\kappa^2\text{O},\text{O}'$ ruthenium complex ($[\text{Ru}(\text{NO})_2(\text{PPh}_3)_2(\text{SO}_4)]$) with Ru–O 2.2126 Å (Table 3.9).^[158]

Table 3.9: Overview of selected angles (α) and distances (d) of compounds **7–12** and $[\text{Ru}(\text{NO})_2(\text{PPh}_3)_2(\text{SO}_4)]$.^[158]

	$\alpha(\text{O}-\text{Ru1}-\text{O})/^\circ$	$\alpha(\text{O1}-\text{S1}-\text{O2})/^\circ$	$d(\text{Ru}-\text{O})/\text{Å}$	$d(\text{Ru}-\text{O}')/\text{Å}$
7	62.37(7)	105.0(1)	2.267(2)	2.291(2)
8	62.10(7)	105.0(1)	2.311(2)	2.255(2)
9	64.00(8)	104.7(1)	2.209(2)	2.249(2)
10	64.53(4)/64.16(4)	106.11(7)/105.04(7)	2.301(1), 2.143(1)	2.283(1), 2.165(1)
11	61.64(7)	104.5(1)	2.237(2)	2.340(2)
12	64.34(6)/64.12(6)	104.94(1)/104.73(9)	2.303(2), 2.134(2)	2.295(2), 2.127(2)
$[\text{Ru}(\text{NO})_2(\text{PPh}_3)_2(\text{SO}_4)]$ ^[158]	63.44(9)	100.0(1)	2.212(2)	2.212(2)*

* symmetry generated

The infrared spectrum of **7** shows two bands which can be confirmed by calculation for a coordinated tosylate at 1205 and 999 cm^{-1} . A visualisation is shown in Figure 3.16. The UV/VIS spectrum has two bands at 342 and 380 nm. The signal of the quaternary carbon ($\underline{\text{C}}-\text{CH}_3$) of the tosylate in the $^{13}\text{C}\{^1\text{H}\}$ NMR spectrum (in DCM, RT) can be identified in the literature.^[159-160] The signal appears at 142.3 ppm. The two triplets of the $^{31}\text{P}\{^1\text{H}\}$ NMR spectrum locate at 60.3 and 46.9 ppm and resemble well for *cis*-

Results

dppe chelates.^[23] Elemental analysis confirmed the formation of the complex **7**. The HRMS spectrum shows a peak at $[M]^+$ $m/z = 1069.11$. The calculated powder pattern of the cryogenic single-crystal diffraction measurement (100 K) and the powder pattern of **7** at room temperature agree. Compound **7** is the precursor for compound **28a**, **28b**, **35** and **39**. Due to the similar characteristics of **8–12** compared to **7** the presentation of the complexes is gathered. Important data is summarised in Table 3.8 and Table 3.9.

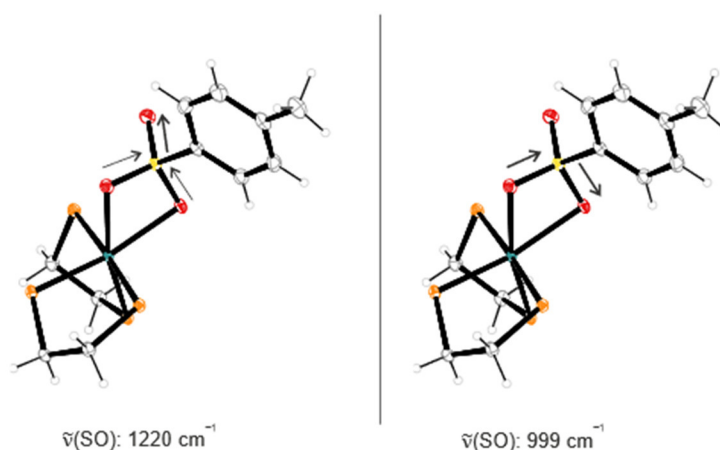


Figure 3.16: The two stretching vibrations of tosylato- κ^2O,O' ruthenium complex **7**. On the left: S–O stretching vibration of the uncoordinated oxygen, weak symmetrically coupled stretching vibration of the coordinated oxygens. On the right: S–O asymmetrically coupled stretching vibration of both coordinated oxygens. $\tilde{\nu}(\text{SO})$ values were taken from quantum-chemical calculations, based on DFT. Similar vibrations are obtained for **8**, **9** and **11**.

*Crystal structure of $[\text{Ru}(\text{dppp})_2(\text{tos})]\text{BF}_4$ (**8**), $[\text{Ru}(\text{dppbza})_2(\text{tos})]\text{BF}_4$ (**9**), $[\text{Ru}(\text{dppe})_2(\text{MesSO}_3)]\text{BF}_4$ (**11**)*

The structure solution of $[\text{Ru}(\text{dppp})_2(\text{tos})]\text{BF}_4$ (**8**) succeeded in the monoclinic space group $P2_1/c$, $[\text{Ru}(\text{dppbza})_2(\text{tos})]\text{BF}_4$ (**9**) in the orthorhombic space group $Fdd2$ and $[\text{Ru}(\text{dppe})_2(\text{MesSO}_3)]\text{BF}_4$ (**11**) in the triclinic space group $P\bar{1}$. The unit cell of **8** contains two formula units, **9** eight and **11** two ($\text{CShM}_{\text{OC}_6}$ value: 1.780 (**8**), 4.018 (**9**), 2.489 (**11**) asymmetric unit: one molecule in **8**, **9**, **11**). The structures of compounds **8**, **9**, **11** are shown in Figures 3.18–3.20. Complexes **8** and **9** are distorted-octahedrally coordinated by two dppp or dppbza chelates and a tosylato ligand. Complex **11** is also distorted-octahedral, but with a mesitylsulfonato ligand and two dppe ligands in *cis*-configuration. The angles and distances of the resulting four-ring chelate of the complexes are almost identical to **7** (Table 3.9). The bulk purity was confirmed by HRMS ($[M]^+$ $m/z = 1027.21$ (**8**), 1310.30 (**9**), $[M]+\text{BF}_4$ 1183.28), by a comparison of a calculated powder pattern of a cryogenic single crystal analysis and a powder pattern at room temperature for **8** and by elemental analysis for **9** and **11**. The formation of **8**, **9**, **11** is also confirmed by IR, UV/VIS and NMR spectroscopy (Table 3.8). Although, the $^{31}\text{P}\{^1\text{H}\}$ NMR spectrum of **11** had to be measured at 0 °C in DCM to obtain four acceptably sharp signals. Two signals (60.6, 57.8 ppm)

Results

in the downfield region can be assigned for the *cis*-standing P atoms. The remaining P atoms have a large *trans*-coupling with roof effect. These signals were analysed as shown in Figure 3.17. The two highfield signals lay at $\nu_A = 51.0$ and $\nu_B = 42.6$ ppm (each two singulets) with a coupling constant of $J_{AB} = 291.6$ Hz (*trans*-coupling).

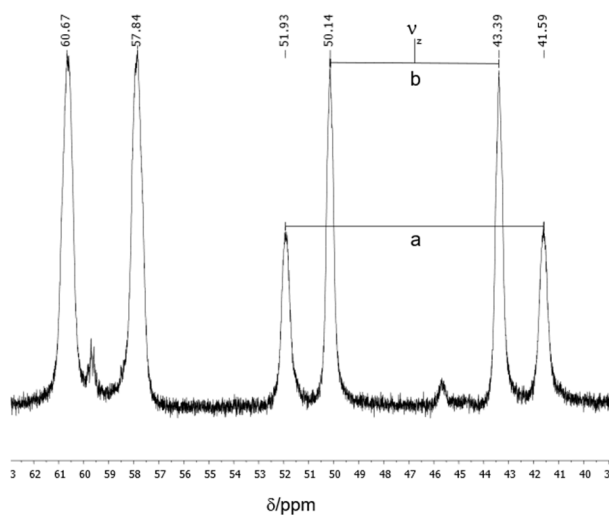


Figure 3.17: $^{31}\text{P}\{^1\text{H}\}$ NMR spectrum of $[\text{Ru}(\text{dppe})_2(\text{MesSO}_3)]\text{BF}_4$ (**11**) in CD_2Cl_2 at 0°C (on the left). Used formulas for the determination of the highfield NMR signals in the spectrum of higher order (on the bottom).

$$\Delta = \sqrt{ab}; J_{AB} = \frac{1}{2}(a - b)$$

$$\nu_A = \nu_z + \frac{1}{2}\Delta$$

$$\nu_B = \nu_z - \frac{1}{2}\Delta$$

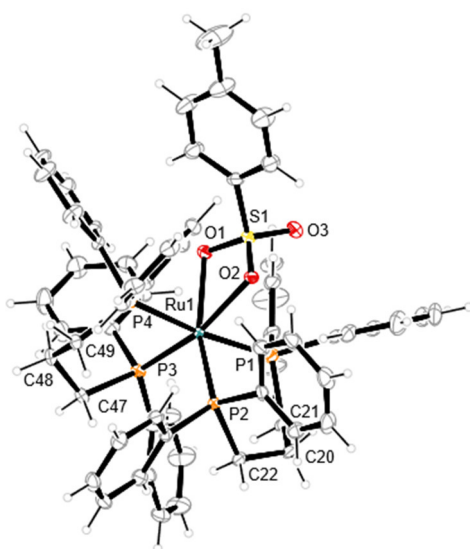


Figure 3.18: ORTEP-3 plot (ellipsoids drawn at the 50% probability level at 97 K) of the $[\text{Ru}(\text{dppp})_2(\text{tos})]^+$ ion in **8**.^[45] Selected distances (\AA) and angles ($^\circ$): Ru1–O1 2.3112(19), Ru1–O2 2.2554(19), Ru1–P1 2.4770(8), Ru1–P2 2.3124(7), Ru1–P3 2.3210(8), Ru1–P4 2.4331(7), S1–O1 1.480(2), S1–O2 1.488(2), S1–O3 1.442(2); O1–Ru1–O2 62.10(7), O3–S1–O1 114.50(13), O3–S1–O2 113.85(12), O1–S1–O2 105.06(11), S1–O1–Ru1 94.32(9), S1–O2–Ru1 96.37(10). Crystal solvent (dichloromethane) and tetrafluoridoborate counterion are omitted.^[39]

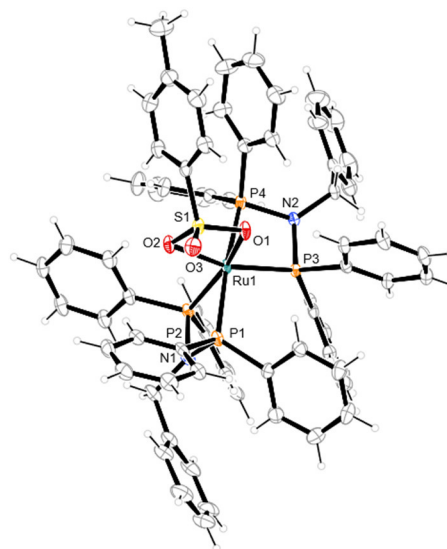


Figure 3.19: ORTEP-3 plot (ellipsoids drawn at the 50% probability level at 100 K) of the $[\text{Ru}(\text{dppbza})_2(\text{tos})]^+$ ion in **9**.^[45] Selected distances (\AA) and angles ($^\circ$): Ru1–O1 2.208(3), Ru1–O2 2.251(3), Ru1–P1 2.3468(11), Ru1–P2 2.2693(10), Ru1–P3 2.2664(10), Ru1–P4 2.3814(11), S1–O1 1.496(3), S1–O2 1.487(3), S1–O3 1.434(3); O1–Ru1–O2 63.97(10), P1–Ru1–P2 69.95(4), O3–S1–O1 113.05(18), O3–S1–O2 115.49(19), O1–S1–O2 104.72(16), S1–O1–Ru1 96.27(14), S1–O2–Ru1 94.74(13). Crystal solvent (dichloromethane) and tetrafluoridoborate counterion are omitted.

Results

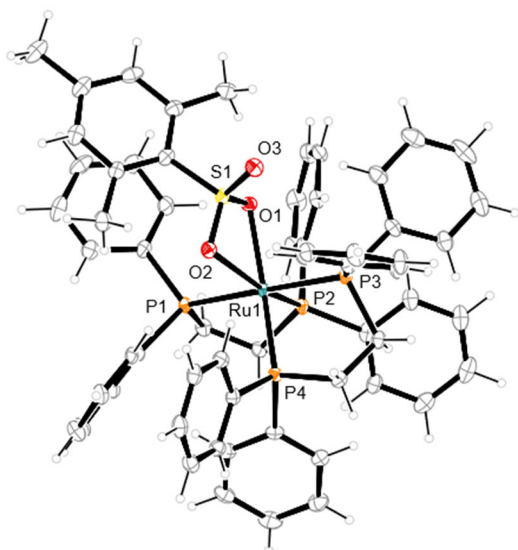


Figure 3.20: ORTEP-3 plot (ellipsoids drawn at the 50% probability level at 100 K) of the $[\text{Ru}(\text{dppe})_2(\text{MesSO}_3)]^+$ ion in **11** (on the left).^[45] Distances (Å) and angles (°): Ru1–O1 2.2373(19), Ru1–O2 2.340(2), Ru1–P1 2.4072(8), Ru1–P2 2.2963(8), Ru1–P3 2.4279(8), Ru1–P4 2.3133(8), S1–O1 1.483(2), S1–O2 1.483(2), S1–O3 1.441(2); O1–Ru1–O2 61.64(7). Crystal solvent (dichloromethane) and tetrafluoroborate counterion are omitted.

Results

Crystal structure of $[\text{Ru}(\text{P}^i\text{PrPh}_2)_2(\text{tos})_2]$ (**10**), $[\text{Ru}(\text{P}^i\text{PrPh}_2)_2(\text{MesSO}_3)_2]$ (**12**)

The structure solutions of $[\text{Ru}(\text{P}^i\text{PrPh}_2)_2(\text{tos})_2]$ (**10**) and $[\text{Ru}(\text{P}^i\text{PrPh}_2)_2(\text{MesSO}_3)_2]$ (**12**) succeeded in the monoclinic space group $P2_1/c$. The unit cell of **10** contains four formula units and of **12** eight ($\text{CShM}_{\text{OC-6}}$ value: 3.106 (**10**), 3.328 (**12**)) asymmetric unit: one molecule in **10**, two molecules in **12**). The structures of **10** and **12** are shown in Figures 3.21 and 3.22. The coordination polyhedron of the cationic complexes is best described as distorted-octahedra. Two diphenyl-*i*-propylphosphanes and two tosylate ligands coordinate the ruthenium centre in **10**, in **12** two phosphanes and two mesitylsulfonate. Both sulfonato ligands form two four-ring chelates. The angles are quite similar to **7**, though the distances differ. Instead of two equidistant Ru–O bonds a long bond ($\approx 2.3 \text{ \AA}$) and a short bond ($\approx 2.1 \text{ \AA}$) are formed in both tosylate and mesitylsulfonate chelates (Table 3.9). In contrast to **7–9**, **11** the di-tosylato complex **10** has three detectable signals/vibrations for the tosylato complex visualised in Figure 3.23. The UV/VIS spectrum of the deep violet compound shows two signals at 383 and 530 nm. The NMR signals of the $^{13}\text{C}\{^1\text{H}\}$ spectrum ($\underline{\text{C}}\text{--CH}_3$ group of the tosylato ligand, 143.3 ppm) and the $^{31}\text{P}\{^1\text{H}\}$ spectrum (a singulett at 69.2 ppm) are as expected. Compound **12** has almost identical analytical values compared to **10** which are listed in Table 3.8. Elemental analysis and HRMS ($m/z = 811.18$ for **10**, 839.21 for **12**) were performed.

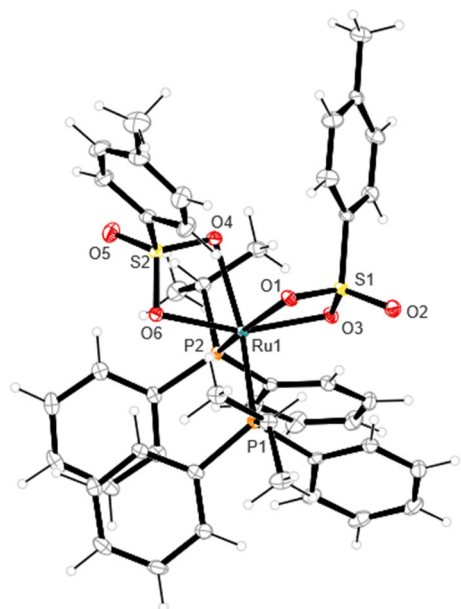


Figure 3.21: ORTEP-3 plot (ellipsoids drawn at the 50% probability level at 100 K) of $[\text{Ru}(\text{P}^i\text{PrPh}_2)_2(\text{tos})_2]$ (**10**).^[45] Distances (\AA) and angles ($^\circ$): Ru1–O1 2.3010(12), Ru1–O3 2.1437(12), Ru1–O4 2.2837(12), Ru1–O6 2.1650(12), Ru1–P1 2.2560(5), Ru1–P2 2.2531(5), S1–O1 1.4760(13), S1–O2 1.4351(13), S1–O3 1.4976(12); O1–Ru1–O3 64.53(4), O4–Ru1–O6 64.16(4).

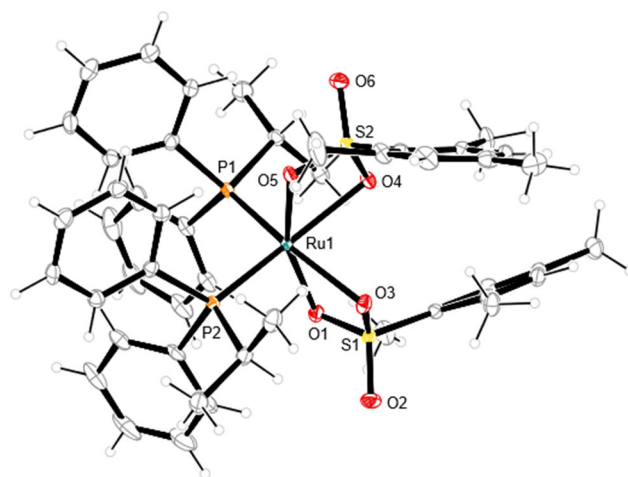


Figure 3.22: ORTEP-3 plot (ellipsoids drawn at the 50% probability level at 100 K) of $[\text{Ru}(\text{P}^i\text{PrPh}_2)_2(\text{MesSO}_3)_2]$ (**12**).^[45] Distances (\AA) and angles ($^\circ$): Ru1–O1 2.1280(17), Ru1–O3 2.2955(17), Ru1–O4 2.3034(16), Ru1–O5 2.1343(17), Ru1–P1 2.2492(6), Ru1–P2 2.2436(6), S1–O1 1.5012(17), S1–O2 1.4391(18), S1–O3 1.4747(18); O1–Ru1–O2 64.35(6), O4–Ru1–O5 64.10(6). Crystal solvent (dichloromethane) is omitted.

Results

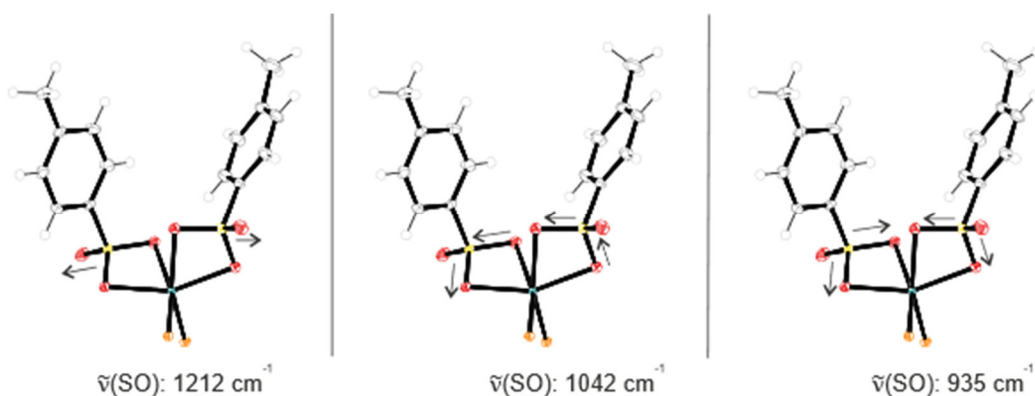
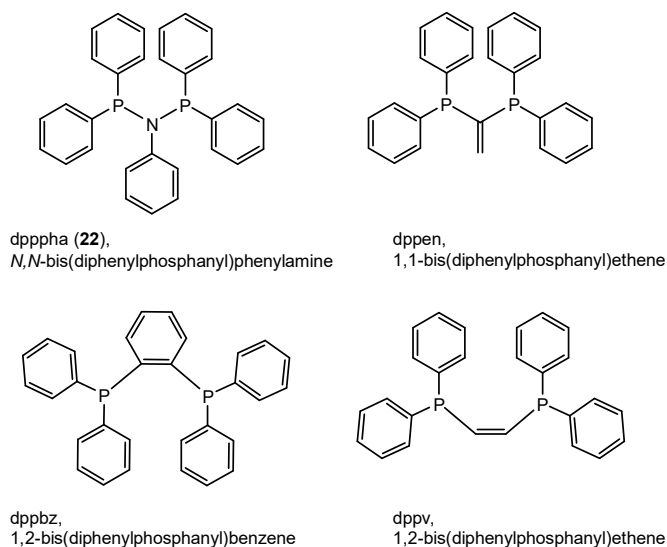


Figure 3.23: The three stretching vibrations of ditosylato- κ^2O,O' ruthenium complex **10**. On the left: stretching vibration of the uncoordinated oxygen (S–O, in phase with second tosylate), in the centre: asymmetrically coupled stretching vibration of the coordinated oxygens (S–O, in phase with second tosylate), on the right: symmetrically coupled stretching vibration of the coordinated oxygens (S–O, in phase with second tosylate).

3.3 Diaquaruthenium complexes with phosphane co-ligands

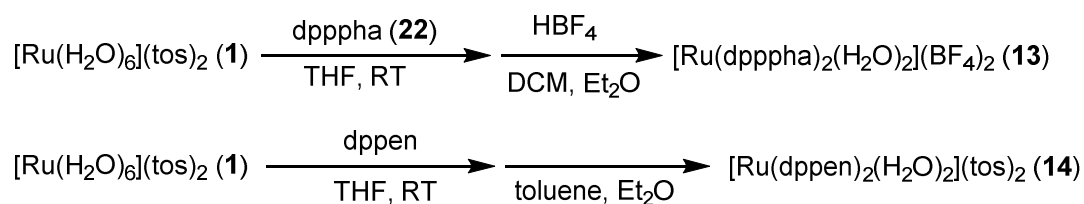
The synthesis of the diaquaruthenium complexes was performed according to a procedure by Bailey *et al.* for $[\text{Ru}(\text{dppe})_2(\text{tos})](\text{tos})$ as previously shown.^[23] The following phosphanes were used for the synthesis of diaqua-ruthenium complexes: dpppha (**22**), dppen, dppbz and dppv (Scheme 3.6).



Scheme 3.6: Overview of phosphanes used for diaquaruthenium complexes **13–16**.

The synthetic route was identical to chapter **3.2**. A mixture of $[\text{Ru}(\text{H}_2\text{O})_6](\text{tos})_2$ **1** and the appropriate phosphane was suspended in THF and stirred. The crude was solved in DCM or toluene and layered with diethyl ether. The compounds $[\text{Ru}(\text{dpppha})_2(\text{H}_2\text{O})_2](\text{BF}_4)_2$ (**13**), $[\text{Ru}(\text{dppen})_2(\text{H}_2\text{O})_2](\text{tos})_2$ (**14**), $[\text{Ru}(\text{dppbz})_2(\text{H}_2\text{O})_2](\text{BF}_4)_2$ (**15**), $[\text{Ru}(\text{dppv})_2(\text{H}_2\text{O})_2](\text{BF}_4)_2$ (**16**) were obtained. For crystallisation the addition of HBF_4 in water was necessary for compounds **13**, **14** and **15** (Scheme 3.7).

Results



Scheme 3.7: General synthetic procedure for diaquaruthenium complexes **13**, **15**, **16**. Compound **14** could only be obtained with tosylate counterions by layering a toluene solution of **14** with diethyl ether.

The crystalline batches of compounds **13**, **14**, **16** had heterogenous crystal habits. More than one crystalline phase can be identified by colour and shape. Compound **15** has a homogenous appearance in colour and shape. The compounds appear as microcrystalline powder most of the time, whereby a single-crystal-diffraction analysis was possible only for one phase. Nonetheless, these compounds can be used as precursors like compound **16**. The compounds were analysed by infrared, UV/VIS and NMR spectroscopy, whereby a “full” characterisation is doubtful as **13**, **14**, **16** are not pure compounds. This fact is emphasised by elemental analyses and a comparison of a calculated powder pattern of a cryogenic single crystal measurement (100 K) and a powder diffractogram at room temperature (**16**). HRMS and UV/VIS spectroscopy was used as proof of reproducibility. **Please note:** The following yields are in the best case an educated guess due to the problem mentioned. Nonetheless, it offers the opportunity to evaluate the approximate requirement for successor reactions. Yields were as follows: $\approx 48\%$ (**13**), $\approx 54\%$ (**14**), 62% , (**15**), $\approx 23\%$ (**16**).

*Crystal structures of [Ru(dpppha)₂(H₂O)₂](BF₄)₂ (**13**), [Ru(dppen)₂(H₂O)₂](tos)₂ (**14**), [Ru(dppbz)₂(H₂O)₂](BF₄)₂ (**15**), [Ru(dppv)₂(H₂O)₂](BF₄)₂ (**16**)*

The structure solutions succeeded in the triclinic space group $P\bar{1}$ for **13** and **16** and in the monoclinic space groups $P2_1/n$ for **14** and $C2/c$ for **15**. The unit cell contains one formula unit in **13** and **16**, two in **14** and four in **15** (CShM_{OC-6} value: 2.486 (**13**), 1.889 (**14**), 0.894 (**15**), 0.820 (**16**), asymmetric unit: half molecule in **13–16**). The structures of **13–16** are shown in Figures 3.24–3.27. The complexes are best described as distorted octahedra, formed by two bisphosphane chelates in equatorial position and two aqua ligands in the axial positions. The Ru–O distance of **16** 2.1252 Å is slightly elongated compared to compound **1** with 2.102 Å. The values of **13–15** resemble well with **16**. The chelate angle of the bisphosphanes ranges from 69° in **13**, over 72° in **14**, to 80 and 82° in **15** and **16**. The hydrogen bonds are listed in Table 3.11.

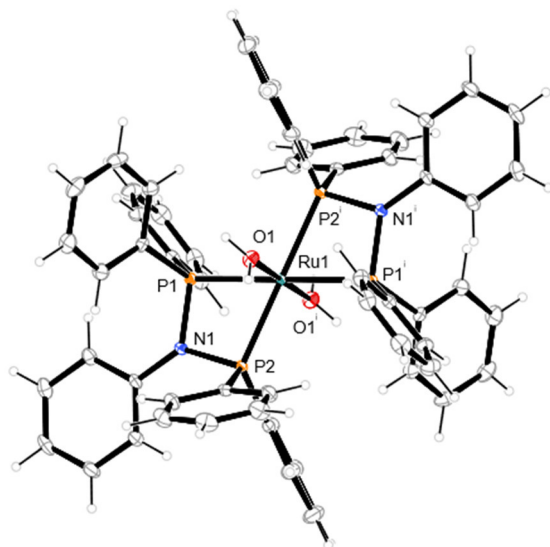


Figure 3.24: ORTEP-3 plot (ellipsoids drawn at the 50% probability level at 100 K) of the $[\text{Ru}(\text{dpppha})_2(\text{H}_2\text{O})_2]^{2+}$ ion in **13** cation.^[45] Selected distances (Å) and angles (°): Ru1–O1 2.1254(13), Ru1–P1 2.3351(4), Ru1–P2 2.3396(4); O1–Ru1–O1ⁱ 180.0, O1–Ru1–P1 88.79(4), O1–Ru1–P2 90.49(4), P1–Ru1–P2 69.023(16). Crystal solvent (dichloromethane) and tetrafluoridoborate counterions are omitted. Symmetry code: $i-x+1, -y+1, -z+1$. *C_i* site symmetry of the cation.

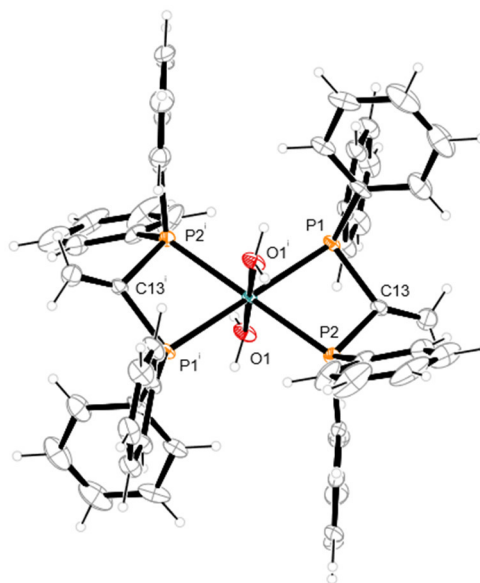


Figure 3.25: ORTEP-3 plot (ellipsoids drawn at the 50% probability level at 100 K) of the $[\text{Ru}(\text{dppen})_2(\text{H}_2\text{O})_2]^{2+}$ ion in **14**.^[45] Selected distances (Å) and angles (°): Ru1–O1 2.122(3), Ru1–P1 2.3598(10), Ru1–P2 2.3560(10); O1–Ru1–O1ⁱ 180.0, O1–Ru1–P1 88.37(9), O1–Ru1–P2 87.99(9), P1–Ru1–P2 72.34(4). Crystal solvent (dichloromethane) and tetrafluoridoborate counterions are omitted. Symmetry code: $i-x, -y+1, -z+1$. *C_i* site symmetry of the cation.

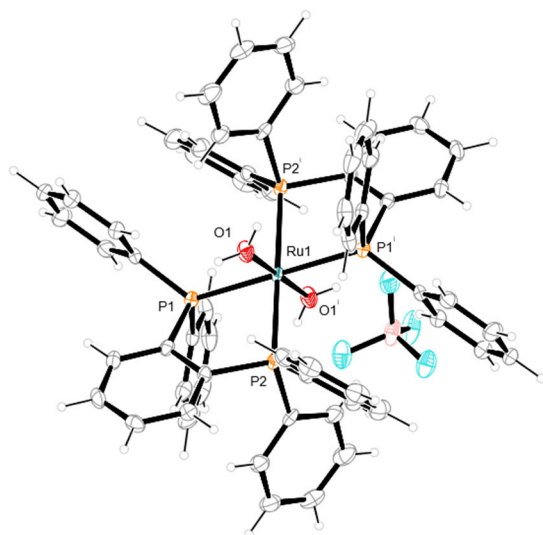


Figure 3.26: ORTEP-3 plot (ellipsoids drawn at the 50% probability level at 100 K) of $[\text{Ru}(\text{dppbz})_2(\text{H}_2\text{O})_2](\text{BF}_4)_2$ (**15**).^[45] Selected distances (Å) and angles (°): Ru1–O1 2.119(2), Ru1–P1 2.3830(8), Ru1–P2 2.119(2); O1–Ru1–O1ⁱ 180.0, O1–Ru1–P1 90.20(7), O1–Ru1–P2 84.87(7), P1–Ru1–P2 80.44(3). Symmetry code: $i-x+1/2, -y+3/2, -z+1$. *C_i* site symmetry of the cation.

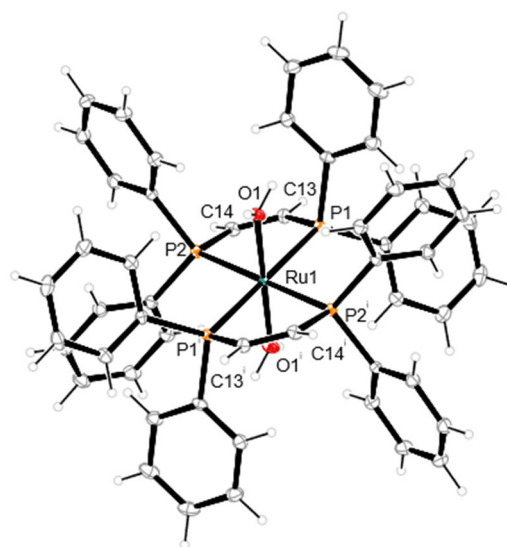


Figure 3.27: ORTEP-3 plot (ellipsoids drawn at the 50% probability level at 100 K) of the $[\text{Ru}(\text{dppv})_2(\text{H}_2\text{O})_2]^{2+}$ ion in **16**.^[45] Selected distances (Å) and angles (°): Ru1–O1 2.1252(12), Ru1–P1 2.3641(4), Ru1–P2 2.3849(4); O1–Ru1–O1ⁱ 180.0, O1–Ru1–P1 87.97(3), O1–Ru1–P2 96.54(4), P1–Ru1–P2 82.342(14). Tetrafluoridoborate counterions are omitted. Symmetry code: $i-x+1, -y+1, -z+1$.^[39] *C_i* site symmetry of the cation.

Results

Table 3.10: Overview of selected IR, UV/VIS and NMR data of compounds **13–16**. IR spectrum measured on ATR (attenuated total reflection) unit as solid. NMR spectra measured in CD₂Cl₂ at RT. UV/VIS measured in DCM. * Shown: Main signals, subsidiary signals mentioned in the experimental section. ** Additional signals in the solvent-cut off region. The $\tilde{\nu}(\text{HOH})$ values were taken from experimental spectra and quantum chemical calculations, based on DFT.

	IR: $\tilde{\nu}_{\text{O-H}}/\text{cm}^{-1}$	IR: $\tilde{\nu}_{\text{O-H}}/\text{cm}^{-1}$ calcd.	UV/VIS: $\lambda_{\text{max}}/\text{nm}$	³¹ P{ ¹ H} NMR: δ/ppm
13	≈3650–3200, 1636 (br)	3508, 3499, 3451, 1630	349, 423	78.7*
14	≈3000–3250 (br), 1586	3452, 3411, 3387, 1584	364, 428	23.1, 3.14*
15	≈3650–3200 (br), 1599	3588, 3587, 3358, 1552	434**	50.7
16	≈3650–3200 (br), 1599	3626, 3382, 1583	360**	69.2, 54.2

Each compound has one crystallographically independent hydrogen bond. The unary graph set is $R_2^2(6)$ for **13–16**. This means, that the BF₄⁻ or to⁻ counterions saturate both hydrogens of the aqua ligands.

The IR signals around 3600–3200 cm⁻¹ and 1580 cm⁻¹ which are vibrations of the aqua ligand indicate the formation of the complexes **13–16**. The dried crystalline compound was measured, therefore, the signals have to be ligand signals. The UV/VIS spectra show similar signal sets to previous phosphane complexes (**7–9**, **11**). The ³¹P{¹H} NMR spectrum shows one and two main signals for **13** and **14** and several subsidiary signals, which indicate at least more than one product. A separation by chromatography was not possible. The powder pattern of crystalline product **16** is clearly not identical to the calculated powder pattern derived from the single-crystal diffractogram. Therefore **16** is a mixture of more than one product in the crystalline form, but, in contrast, the ³¹P{¹H} NMR spectrum shows two defined signals, which indicate one solvent species. Compound **15** is a pure compound with one signal at 50.7 ppm (Table 3.10). HRMS signals could not be assigned correctly (except **16**), but could be reproduced. Elemental analysis which was tried for **15** is probably affected by a phosphorus error, which adds a proportion of the phosphorus onto the carbon value.^[161] Additionally, compound **14** is the *trans*-analogue of the *cis*-[Ru(dppen)₂(H₂O)₂]²⁺ cation synthesised by Bickley *et al.*^[47]

Results

Table 3.11: Distances (d) and angles (α) of hydrogen bonds in **13–16**. Standard deviations of the last digit are given in parentheses; values without standard deviation are related to hydrogen atoms at calculated positions. D: donor, A: acceptor. Target values of the H...H distance and the O–H distance of the water molecules are restrained to 1.31 Å and 0.82 Å.

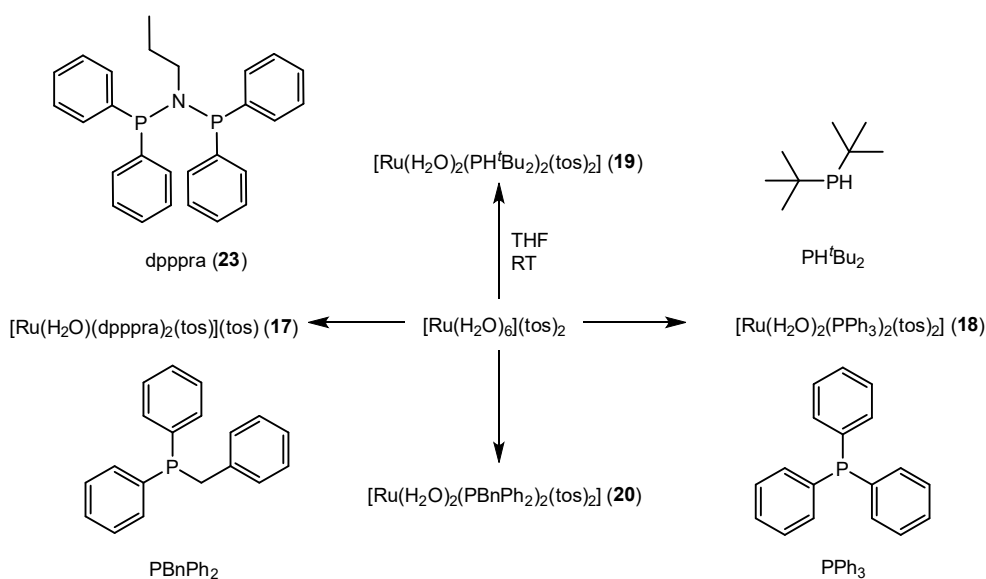
compound	D-H...A	$d(\text{D-H})/\text{Å}$	$d(\text{H...A})/\text{Å}$	$d(\text{D-A})/\text{Å}$	$\alpha(\text{D-H...A})/^\circ$
13	O1-H11...F1 ⁱ	0.823	2.00	2.701(2)	142
	O1-H12...F4 ⁱ	0.82	2.28	2.871(2)	130
14	O1-H11...O2	0.82	2.19	2.793(5)	130
	O1-H12...O3	0.82	1.97	2.691(4)	145
15	O1-H11...F2 ⁱⁱ	0.82	1.84	2.643(3)	160
	O1-H12...F1 ⁱⁱ	0.82	2.25	2.784(3)	122
16	O1-H11...F4	0.831	2.30	2.799(2)	118
	O1-H12...F3	0.828	1.86	2.639(2)	154

ⁱ[-x+1, -y+1, -z+1], ⁱⁱ[-x+1/2, -y+3/2, -z+1]

3.4 Aqua-tosylatoruthenium complexes with phosphane co-ligands

The synthesis of the aqua-tosylatoruthenium complexes were made according to a procedure by Bailey *et al.* for $[\text{Ru}(\text{H}_2\text{O})_2(\text{PPh}_3)_2(\text{tos})_2]$.^[23] The following phosphanes were used for the synthesis of diaquaruthenium complexes: dpppra (**23**), PPh_3 , PH^tBu_2 and PPh_2Bn (Scheme 3.8). For $[\text{Ru}(\text{H}_2\text{O})_2(\text{PPh}_3)_2(\text{tos})_2]$ an elucidation of the crystal structure was desired. The synthetic route was identical to chapter 3.2. A mixture of $[\text{Ru}(\text{H}_2\text{O})_6](\text{tos})_2$ **1** and the appropriate phosphane was suspended in THF and stirred. The crude was solved in DCM and layered with diethyl ether. The compounds $[\text{Ru}(\text{H}_2\text{O})(\text{dpppra})_2(\text{tos})](\text{tos})$ (**17**), $[\text{Ru}(\text{H}_2\text{O})_2(\text{PPh}_3)_2(\text{tos})_2]$ (**18**), $[\text{Ru}(\text{H}_2\text{O})_2(\text{PH}^t\text{Bu}_2)_2(\text{tos})_2]$ (**19**), $[\text{Ru}(\text{H}_2\text{O})_2(\text{PBnPh}_2)_2(\text{tos})_2]$ (**20**) were obtained (Scheme 3.8). The compounds **17–20** had homogenous crystal habits and colours and were analysed by infrared, UV/VIS and NMR spectroscopy (Table 3.12). Mass spectroscopy and elemental analysis were performed as bulk analyses. The yields of the compounds **17–20** were as follows: 44% (**17**), 56% (**18**), 54% (**19**), 35% (**20**).

Results



Scheme 3.8: General synthetic procedure for aqua-tosylatoruthenium complexes **17–19** and overview of the phosphane ligands used.

Crystal structure of $[\text{Ru}(\text{H}_2\text{O})(\text{dpppra})_2(\text{tos})](\text{tos})$ (**17**)

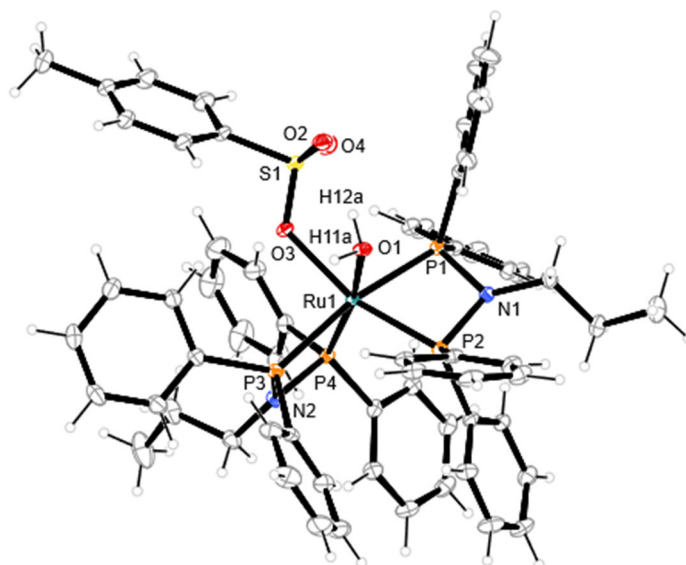


Figure 3.28: ORTEP-3 plot (ellipsoids drawn at the 50% probability level at 100 K) of the $[\text{Ru}(\text{dpppra})_2(\text{H}_2\text{O})(\text{tos})]^+$ ion in **17**.^[45] Distances (Å) and angles (°): Ru1–O1 2.1912(16), Ru1–P1 2.3416(6), Ru1–O3 2.1952(16), O3–S1 1.4939(17), S1–O2 1.4526(19); P1–Ru1–P2 69.60(2), P1–Ru1–O1 88.65(5), P1–Ru1–O3 99.55(5), O1–Ru1–O3 79.00(6), O3–S1–O2 111.04(10). Crystal solvent (toluene) and tosylate counterion are omitted.

The structure solution succeeded in the monoclinic space group $P2_1/n$. The unit cell contains four formula units (CShM_{OC-6} value: 2.831, asymmetric unit: one molecule). The structure is shown in Figure 3.28. The ruthenium(II) centre is coordinated distorted octahedrally by two *cis*-standing

Results

bisphosphane ligands (dpppra (**23**)) and a tosylato ligand tending towards an aqua ligand (hydrogen bridge). The distance Ru–O (tos) with 2.1952 Å and Ru–O (aqua) with 2.1912 Å resemble well with both tosylato and diaqua complexes (Table 3.9 and Figures 3.24–3.27). The chelate angle of the bisphosphane ligand of 70° is in the same range as for the other complexes (**9** and **13**) with diphenylphosphanylamine ligands. The orientation of the tosylato ligand is caused by a hydrogen bond between a sulfonate oxygen and the coordinated aqua ligand ($\cdots\text{H}-\text{OH}$). The tosylato counterion saturates the second hydrogen. The hydrogen bond of compound **17** and the bonds of the following compounds **18–20** are listed in Table 3.13 in the next section. The unary graph set consists of an intramolecular hydrogen bond $S_1^1(6)$ and a finite pattern D (O1–H11a \cdots O5').

Table 3.12: Overview of selected IR, UV/VIS and NMR data of compounds **17–20**. IR spectrum measured on ATR (attenuated total reflection) unit as solid. NMR spectra measured in CD_2Cl_2 at RT. UV/VIS measured in DCM. The $\tilde{\nu}(\text{SO})$ and $\tilde{\nu}(\text{HOH})$ values were taken from experimental spectra and quantum chemical calculations, based on DFT.

	IR: $\tilde{\nu}_{\text{O-H}}/\text{cm}^{-1}$, $\tilde{\nu}_{\text{S-O}}/\text{cm}^{-1}$	IR: $\tilde{\nu}_{\text{O-H}}/\text{cm}^{-1}$, $\tilde{\nu}_{\text{S-O}}/\text{cm}^{-1}$ calcd.	UV/VIS: $\lambda_{\text{max}}/\text{nm}$	$^{31}\text{P}\{^1\text{H}\}$ NMR: δ/ppm
17	3350–3057, 1623, 1200(sh), 1011, \approx 950 (sh)	3688, 2965, 1612, 1220, 1016, 952	306, 362	83.6, 62.2
18	3349 (br), 1111, 1024, 858	3539, 3505, 3356, 3291, 1109, 1057, 859	372, 474	52.6
19	3328 (br), 1126, 1087, 1025, 920	3395, 3381, 3334, 1147, 1113, 1058, 940	377, 516	75.0
20	\approx 3400 (br), 3376 (br), 1180, 1151, 1025, 917	3442, 3324, 3274, 1180, 1143, 1058, 939	360, 463***	59.8

There are both aqua and tosylato ligand signals detectable in the IR spectrum Table 3.12. An illustration of the vibrations is given in Figure 3.29. The UV/VIS signals are in the same range as for previous complexes (**7–9**, **11**, **13–16**). Two triplets are detectable for **17** in the $^{31}\text{P}\{^1\text{H}\}$ NMR spectrum as

Results

expected for two *cis*-standing bisphosphane ligands (dpppra) in this complex. Elemental analysis succeeded and HRMS with $m/z = 1127.24$ and 1209.29 are repeatable mass peaks for this complex.

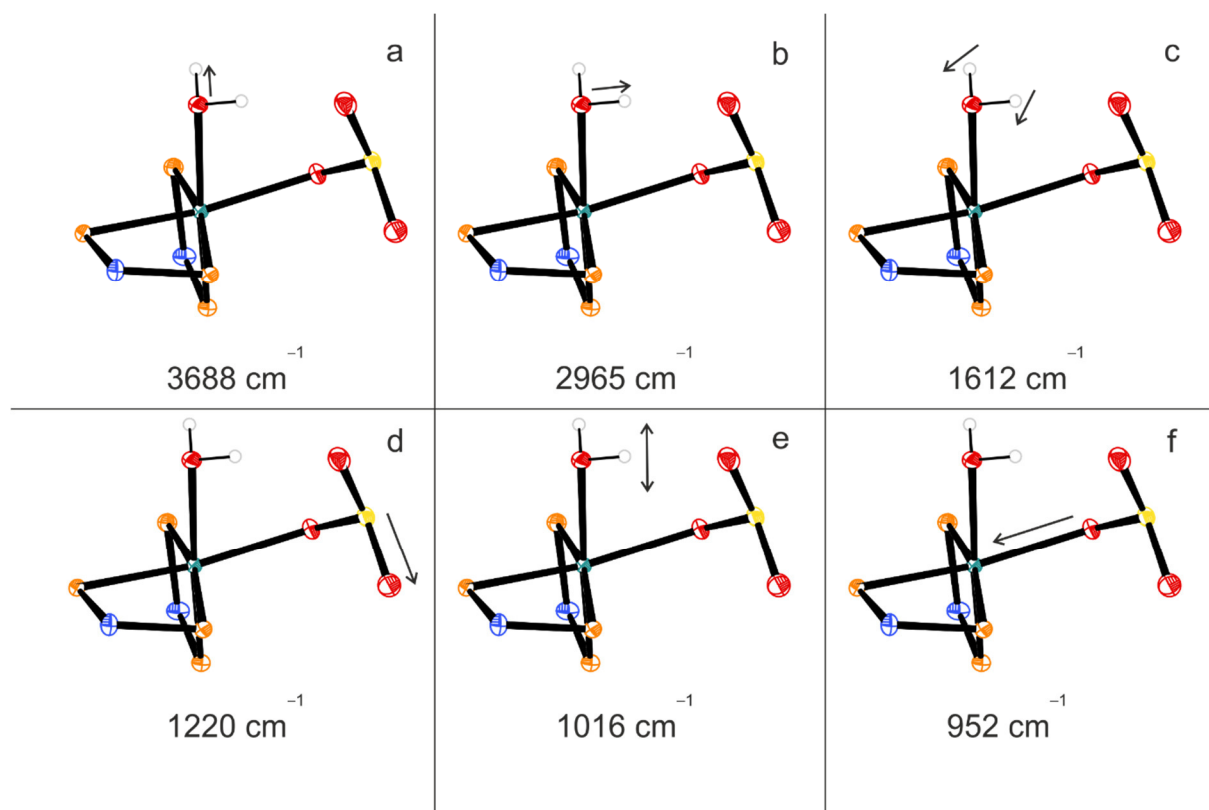


Figure 3.29: Symmetrically and asymmetrically coupled vibrations of aquatosylato complex **17**. a) Stretching vibration of the hydrogen of the aqua ligand pointing away from the tosylato ligand, b) stretching vibration of the hydrogen pointing toward the tosylato ligand, c) scissoring of the aqua ligand, d) S–O stretching vibration of the uncoordinated oxygen of the tosylato ligand pointing away from the aqua ligand, e) wagging of the hydrogen of the aqua ligand pointing towards the tosylato ligand, f) S–O stretching vibration of the oxygen of the tosylato ligand coordinated to the ruthenium centre. The values of the different vibrations were taken from quantum-chemical calculations based on DFT.

Crystal structure of $[Ru(H_2O)_2(PPh_3)_2(tos)_2]$ (**18**), $[Ru(H_2O)_2(PH^tBu_2)_2(tos)_2]$ (**19**), $[Ru(H_2O)_2(PBnPh_2)_2(tos)_2]$ (**20**)

The structure solutions succeeded in the triclinic space group $P\bar{1}$ for **18**, and in the monoclinic space groups $C2/c$ and $P2_1/n$ for **19** and **20**. The unit cells contain two formula units in **18** and four formula units each in **19** and **20** (CShM_{OC-6} value: 0.563 (**18**), 0.677 (**19**), 0.534 (**20**)) asymmetric unit: one molecule in **18** and **20**, half molecule in **19**. The crystal structures are shown in Figures 3.30–3.32. The ruthenium centre in **18–20** is coordinated octahedrally by two, *cis*-standing phosphane ligands (equatorial), two *trans*-standing tosylato ligands (axial) oriented towards two *cis*-standing aqua ligands (equatorial). The distances between the tosylato ligands and the ruthenium centre are shorter (≈ 2.12 Å) compared to tosylato- κ^2O,O' complexes (**7–9**) (≈ 2.26 Å), while the aqua ruthenium distance is

Results

slightly longer ($\approx 2.21 \text{ \AA}$ (**18–20**) $\leftrightarrow 2.11 \text{ \AA}$ (**13–16**)). The formed hydrogen bonds are listed in Table 3.13. In compound **18** and **19** the hydrogen bond network is exclusively intramolecular (between tosylato and aqua ligand), while in compound **20** an intermolecular hydrogen bond between two complexes is formed additionally. Since all four hydrogen bonds are crystallographically dependent, a ring pattern is formed ($N_1 = R_4^4(12)$ in **18**. In **19**, the unary is $N_1 = DD$ and the binary graph set $N_2 = R_2^2(10)$. In **20**, the unary graph set consists of a ring pattern and a finite pattern $N_1 = R_4^4(12)D$. The binary graph set regarding the intermolecular bond between two complex molecules consists of a ring pattern $R_2^2(4)$.

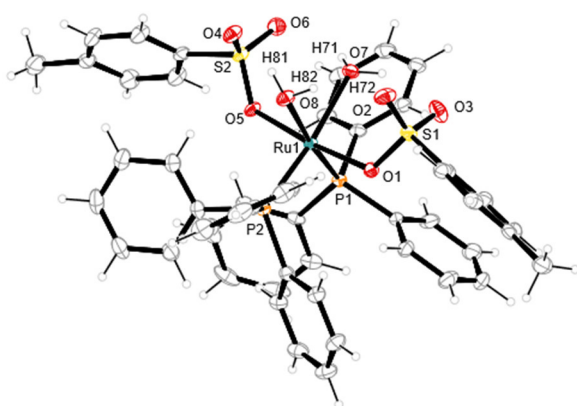


Figure 3.30: ORTEP-3 plot (ellipsoids drawn at the 50% probability level at 100 K) of [Ru(PPh₃)₂(H₂O)₂(tos)₂] (**18**).^[45] Distances (Å) and angles (°): Ru1–O1 2.1261(17), Ru1–P1 2.2753(7), Ru1–O7 2.2158(18), O1–S1 1.4927(18), S1–O2 1.453(2); P1–Ru–O7 93.98(5), P1–Ru1–O1 94.28(5), O1–Ru1–O7 90.87(7), O1–S1–O3 111.26(11). Crystal solvent (diethyl ether) is omitted.

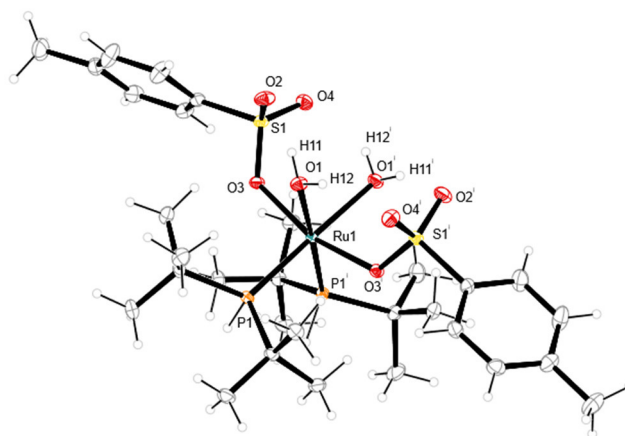


Figure 3.31: ORTEP-3 plot (ellipsoids drawn at the 50% probability level at 100 K) of [Ru(PH^tBu)₂(H₂O)₂(tos)₂] (**19**).^[45] Distances (Å) and angles (°): Ru1–O1 2.2245(12), Ru1–P1 2.2933(4), Ru1–O3 2.1416(11), O3–S1 1.4904(12), S1–O2 1.4570(13); P1–Ru–O1 89.60(3), P1–Ru1–O3 97.82(3), O1–Ru1–O3 85.98, O3–S1–O2 112.51(7). Symmetry code: ⁱ $-x+1, y, -z+1/2$. C_i site symmetry.

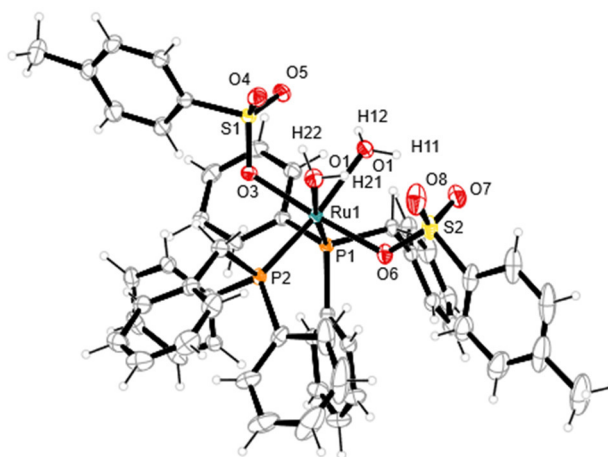


Figure 3.32: ORTEP-3 plot (ellipsoids drawn at the 50% probability level at 293 K) of [Ru(PPh₂Bn)₂(H₂O)₂(tos)₂] (**20**) (On the left side).^[45] Distances (Å) and angles (°): Ru1–O1 2.1993(16), Ru1–P1 2.2586(6), Ru1–O3 2.1248(15), O3–S1 1.4887(16), S1–O5 1.4506(17); P1–Ru1–O1 91.59(5), P1–Ru1–O3 93.84(5), O1–Ru1–O3 91.36(6), O3–S1–O5 111.83(10). Crystal solvent (diethyl ether) is omitted.

Results

The IR spectrum shows a broad signal at around 3350 cm^{-1} for the aqua ligands and distinctive signals in the area around $1180\text{--}858\text{ cm}^{-1}$ for the tosylato ligands (Table 3.12). A visualisation and description of the different vibrations for **19** are shown in Figure 3.33. The UV/VIS signals of **18–20** are in the same range as for previous complexes (**7–9**, **11**, **13–16**) and one singulett is detectable in a $^{31}\text{P}\{^1\text{H}\}$ NMR spectrum confirming the *cis*-standing, chemically equivalent phosphane ligands. Elemental analysis confirmed the formation of complexes **18–20**. HRMS was performed and shows reproducible peaks at $m/z = 838.12$ for **18**, 606.19 for **19** and 866.16 for **20**.

Table 3.13: Distances (d) and angles (α) of hydrogen bonds in **17–20**. Standard deviations of the last digit are given in parentheses; values without standard deviation are related to hydrogen atoms at calculated positions. D: donor, A: acceptor. Target values of the H \cdots H distance and the O–H distance of the water molecules are restrained to 1.31 \AA and 0.82 \AA .

compound	D–H \cdots A	$d(\text{D–H})/\text{\AA}$	$d(\text{H}\cdots\text{A})/\text{\AA}$	$d(\text{D–A})/\text{\AA}$	$\alpha(\text{D–H}\cdots\text{A})/^\circ$
17	O1–H11a \cdots O5 ^I	0.83	1.79	2.621(3)	174
	O1–H12a \cdots O2	0.83	1.90	2.720(2)	169
18	O7–H71 \cdots O6	0.82	2.11	2.803(3)	140
	O7–H72 \cdots O3	0.83	2.112	2.760(3)	135
	O8–H81 \cdots O4	0.83	1.940	2.711(3)	154
	O8–H82 \cdots O2	0.83	2.00	2.781(3)	155
19	O1–H11 \cdots O2	0.822	1.89	2.658(2)	154
	O1–H12 \cdots O4 ^{II}	0.821	2.05	2.793(2)	150
20	O2–H21 \cdots O8	0.823	1.99	2.754(3)	154
	O2–H22 \cdots O4	0.827	2.02	2.795(3)	155
	O1–H11 \cdots O7	0.822	2.02	2.769(3)	150
	O1–H12 \cdots O5	0.818	2.26	2.808(2)	125
	O1–H12 \cdots O5 ^{III}	0.818	2.08	2.832(2)	151

^I[$-x+1, -y+1, -z+1$], ^{II}[$-x+1, y, -z+1/2$], ^{III}[$-x, -y+2, -z+1$]

Results

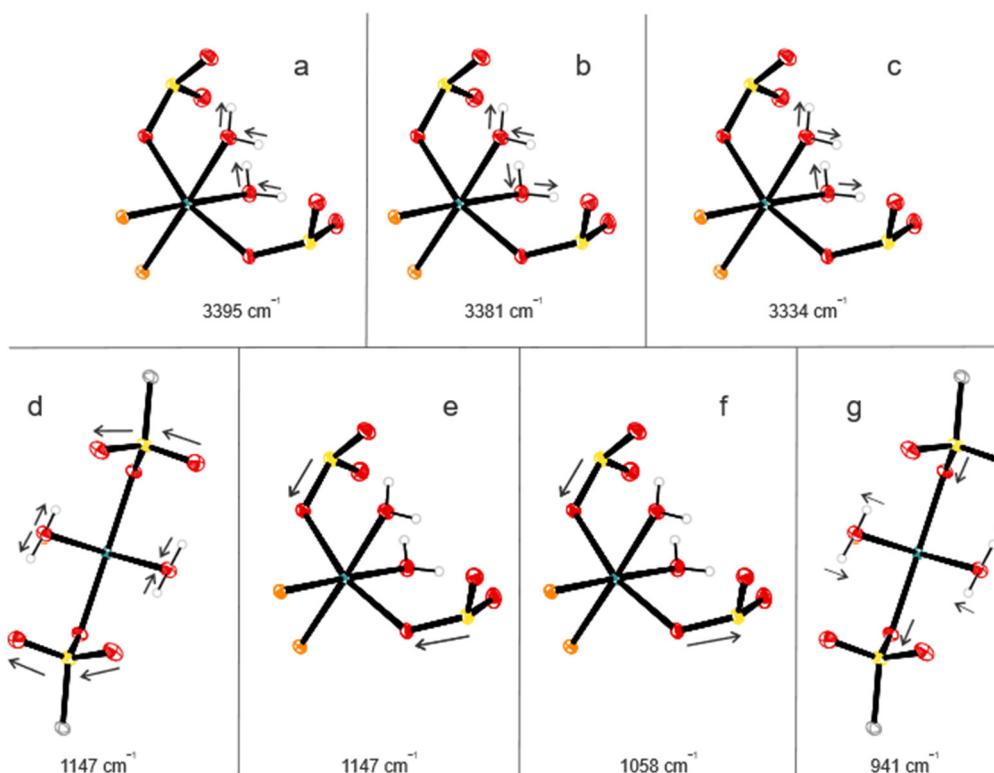
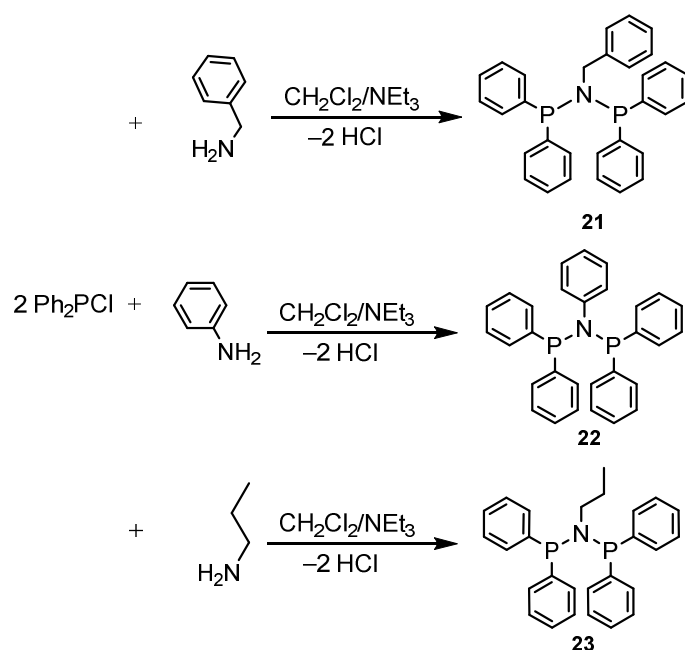


Figure 3.33: Symmetrically and asymmetrically coupled vibrations of aqua and tosylato ligands of compound **19**. a) asymmetrically coupled stretching vibration of the aqua ligands (in phase), b) asymmetrically coupled stretching vibration (aphasic) of the aqua ligands, c) symmetrically coupled stretching vibration (in phase) of the aqua ligands, d) asymmetrically coupled stretching vibration of the uncoordinated S–O oxygens, asymmetrically coupled scissoring of the hydrogens of the aqua ligands, e) S–O stretching vibration (in phase), f) S–O stretching vibration (aphasic), g) S–O stretching vibration (aphasic), asymmetrically coupled twisting of the hydrogens of the aqua ligands. The values of the different vibrations were taken from quantum-chemical calculations based on DFT. Vibrations of **18** and **20** are similar.

3.5 Short excursion: bisphosphanes dppbza (**21**), dpppha (**22**), dpppra (**23**)

The bisphosphanes dppbza (**21**), dpppha (**22**), dpppra (**23**) were reproduced from literature.^[162-164] Chlorodiphenylphosphane was solved in DCM and treated with one equivalent of benzylamine, aniline or propylamine in presence of triethylamine. After addition of a second equivalent, stirring overnight and evaporation of the solvent, the residue was resolved in DCM and crystallised by layering with acetonitrile (Scheme 3.9). The yields were as follows: 36% (**21**), 71% (**22**), 61% (**23**). Elemental analysis and HRMS (for **23**: $m/z = 428.16$ ($[M-H]^+$, $C_{27}H_{28}NP_2$)) were performed as bulk analyses. Decoupled $^{13}C\{^1H\}$ - and $^{31}P\{^1H\}$ NMR spectra (THF-d8) confirm the published ppm values.^[165]

Results



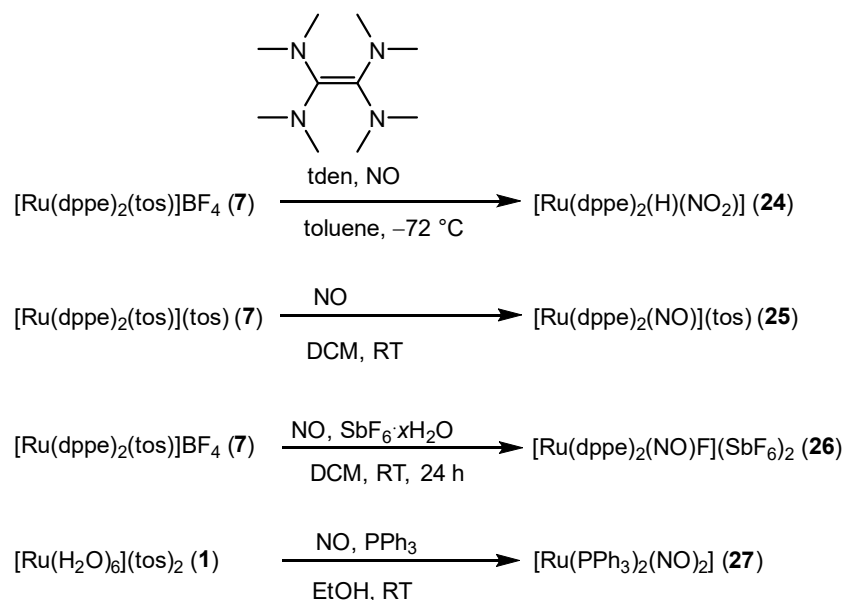
Scheme 3.9: General synthetic procedure for amine bisphosphane ligands dppbza **21**, dpppha **22**, dpppra **23**.

3.6 Reaction of complexes $[\text{Ru}(\text{dppe})_2(\text{tos})]\text{BF}_4$ (**7**) and $[\text{Ru}(\text{H}_2\text{O})_6](\text{tos})_2$ (**1**) with NO

The previously shown phosphaneruthenium complexes were treated with NO gas to investigate their reaction behaviour in terms of hyponitrite formation. **Please note:** Despite only four complexes obtained, most of the phosphane complexes (**7–20**) were tested, whereby either a nitrosyl complex or even a hyponitrite complex was aim of this reaction. Complexes that did not crystallise or reactions in which the phosphorus of the phosphane was oxidised are not discussed in this work.

The general procedure was as follows: The starting complex was solved in a suitable solvent (DCM or EtOH) and treated in absence of oxygen with nitrogen monoxide. For **24** a reducing agent (tden) was added previously to investigate, whether a reductive coupling of NO was possible. Using different counterions (tos^- and BF_4^-) and a different reaction time resulted in complexes **25** and **26**. And by adding PPh_3 to the process in excess to **1** compound **27** was formed. A detailed discussion of the reaction pathways is given in chapter 4.3. After removal of the solvent, the crude was solved in DCM and layered with diethyl ether. The compounds $[\text{Ru}(\text{dppe})_2(\text{H})(\text{NO}_2)]$ (**24**), $[\text{Ru}(\text{dppe})_2(\text{NO})](\text{tos})$ (**25**), $[\text{Ru}(\text{dppe})_2(\text{NO})\text{F}]\text{SbF}_6$ (**26**), $[\text{Ru}(\text{PPh}_3)_2(\text{NO})_2]$ (**27**) were obtained (Scheme 3.10). Compound **25** was originally synthesized by Townsend *et al.* and the crystal structure described by Pierpont *et al.*^[166] Compound **27** was synthesised by Gaughan *et al.* using a different synthetic method.^[167] In contrast to standard synthetic procedures, complex **27** was formed by reaction of a ruthenium complex with

gaseous NO. The crystals of compounds **24–27** had homogenous habits and colours in presence of powdery side products. As far as possible the complexes were analysed by infrared and NMR spectroscopy. Mass spectroscopy and elemental analysis were performed as bulk analyses. The yields of the compounds **24–27** were as follows: few crystals (**24**), few crystal agglomerates (**25**), 45% (**26**), 30% (**27**). In general, the nitrosyl complexes are described using the Enemark-Feltham notation.^[168]



Scheme 3.10: General synthetic procedure for complexes **24–27**.

*Crystal structure of $[\text{Ru}(\text{dppe})_2(\text{H})(\text{NO}_2)]$ (**24**)*

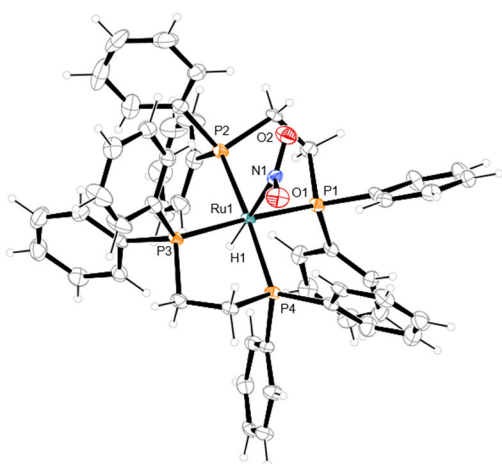


Figure 3.34: ORTEP-3 plot (ellipsoids drawn at the 50% probability level at 100 K) of $[\text{Ru}(\text{dppe})_2(\text{H})(\text{NO}_2)]$ (**24**).^[45] Distances (Å) and angles (°): Ru1–N1 2.193(3), Ru1–H1 1.49(4), Ru1–P1 2.3329(11), Ru1–P2 2.3363(11), N1–O1 1.251(4), N1–O2 1.214(4); H1–Ru1–N1 179.4(17), P1–Ru1–P2 82.31(4), O1–N1–O2 119.0(3), Ru1–N1–O1 118.9(2).

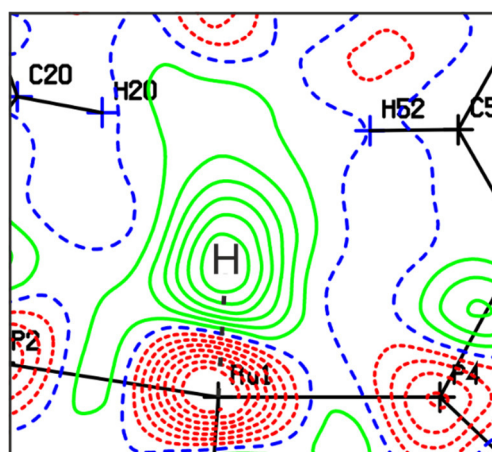


Figure 3.35: Difference-Fourier map of **24**. Shown: ΔF analysis, prior to the H atom's assignment (H1), in terms of the residual density's height and position along the tentative H–Ru bond: difference Fourier peak ($0.82\text{ e } \text{\AA}^{-3}$), distance from Ru1 (1.237 \AA), refined distance ($1.49(4)\text{ \AA}$), U_{iso} ($0.025(11)\text{ \AA}^2$).

Results

The structure solution succeeded in the monoclinic space group $P2_1/n$. The unit cell contains four formula units (CShM_{OC-6} value: 2.634, asymmetric unit: one molecule). The structure is shown in Figure 3.34. The complex is a distorted octahedron. The ruthenium centre is coordinated equatorially by two dppe ligands, while the two axial positions are occupied by a nitrito-κN and a hydrido ligand. Due to almost immediate dissolution of the crystals when taken out of the mother liquor, further analytics were not possible. Nonetheless, the X-ray method allows a particularly reliable assignment of the tentative hydrogen (H1) on basis of a data set of very good quality. The Difference-Fourier map including the relevant data of the tentative hydrogen bond is shown in Figure 3.35, whereby a Ru–H bond is evident. The occurrence of this complex correlates always with the occurrence of compound **25**. If an apparatus is used with nearly complete water exclusion (i.e. without wash bottles, using dried solvent etc.) compound **24** could not be obtained.

Crystal structure of $[Ru(dppe)_2(NO)](tos)$ (**25**) $[Ru(dppe)_2(NO)F]SbF_6$ (**26**)

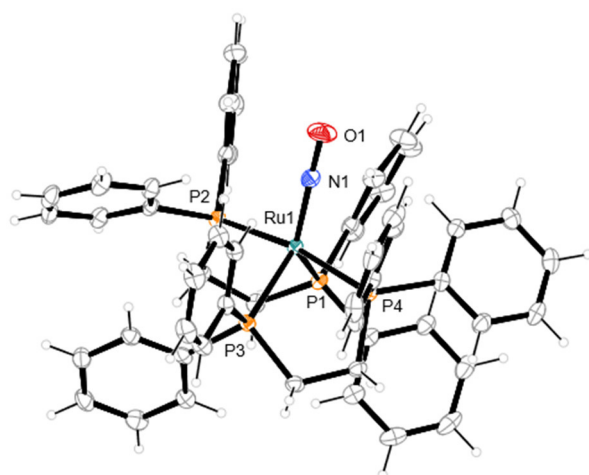


Figure 3.36: ORTEP-3 plot (ellipsoids drawn at the 50% probability level at 98 K) of the $[Ru(dppe)_2(NO)]^+$ ion in **25**.^[45] Distances (Å) and angles (°): Ru1–N1 1.7926(16), N1–O1 1.190(2), Ru1–P1 2.3366(5), Ru1–P2 2.3619(5), Ru1–P3 2.3583(5); Ru1–N1–O1 177.59(16), P1–Ru1–P2 78.097(17), P1–Ru1–P3 103.880(18). Crystal solvent (dichloromethane) and tosylate counterion are omitted.

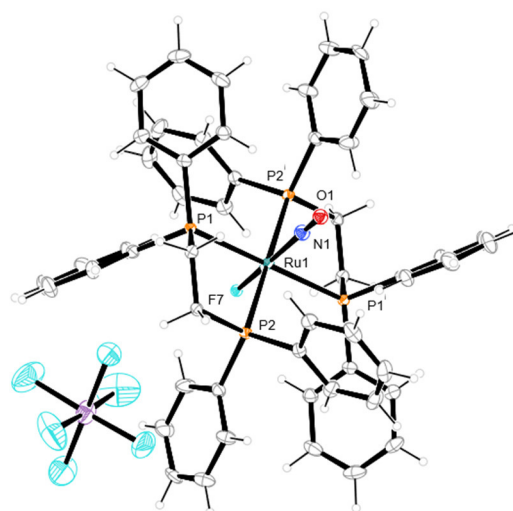


Figure 3.37: ORTEP-3 plot (ellipsoids drawn at the 50% probability level at 100 K) of $[Ru(dppe)_2(NO)F]$ (**26**).^[45] Distances (Å) and angles (°): Ru1–N1 2.02(2)*, N1–O1 1.02(2), Ru1–F7 1.774(10), Ru1–P1 2.4361(12), Ru1–P2 2.4452(12); Ru1–N1–O1 178.9(14), F1–Ru1–N1 178.6(7), P1–Ru1–P2 81.33(4). Symmetry code: $^1-x+2, -y+1, -z$ (substitutional disorder of F7 and N1–O1 omitted for reasons of clarity).

The structure solutions succeeded in the triclinic space group $P\bar{1}$ for **25** and **26**. The unit cells contain two and one formula units for **25** and **26** (CShM_{TBPY-5} value: 1.180, CShM_{OC-6} value: 1.964, asymmetric unit: one molecule in **25**, half molecule in **26**). The structures are shown in Figures 3.36 and 3.37. The complex cation in **25** is coordinated in a distorted trigonal-bipyramidal fashion in accordance with

Results

literature.^[166] The bisphosphane ligands occupy both axial positions and one equatorial position. The NO ligand is in the remaining position. The Ru–N–O moiety is almost linear with 177.59° and is described best as {RuNO}⁸, most likely a d⁸ Ru(0) NO⁺ complex. This is emphasised by a N–O bond length of 1.190 Å and a Ru–N bond length of 1.7926 Å. The crystallographic data is similar to the previously given literature (Table 3.14).^[166] A shortened Ru–N bond indicates for **25** a back donation from the ruthenium centre into π* orbitals of the nitrosyl ligand. The values for compound **26** are not reliable in terms of distances and angles regarding the F–Ru–N–O axis due to a disorder of the F and NO position on an inversion centre. Nonetheless, a {RuNO}⁶ complex is a reasonable choice to describe this distorted octahedrally coordinated complex. Two dppe ligands coordinate equatorially, while a NO and a fluorido ligand occupy the axial positions (occupation: N–O 50% - F 50%). In comparison to K[Ru(NO)Cl₃(mal)] (mal: maltol) the NO distance is shortened, the Ru–N distance is elongated and the R–N–O angle is quite similar.^[169] Therefore, to confirm the oxidation state of complex **26** spectroscopic analysis has to be performed.

Table 3.14: Overview of the bond distances (*d*) and angles (*α*) of compound **25** and **26** together with [Ru(dppe)₂(NO)]BPh₄ {RuNO}⁸ and K[Ru(NO)Cl₃(mal)] {RuNO}⁶.^[169] IR spectrum measured on ATR (attenuated total reflection) unit as solid. NMR spectra measured in CD₂Cl₂ at RT.

	<i>d</i> (N–O)/Å	<i>d</i> (Ru–N)/Å	<i>α</i> (Ru–N–O)/°	$\tilde{\nu}$ (NO)/cm ⁻¹	³¹ P{ ¹ H} NMR δ/ppm
[Ru(dppe) ₂ (NO)]BPh ₄ ^[166]	1.20 (1)	1.74(1)	174 (1)	1673	–
[Ru(dppe) ₂ (NO)](tos) (25)	1.190(2)	1.792(2)	177.5(2)	1665	61.4, 31.8
K[Ru(NO)Cl ₃ (mal)] (mal: maltol) ^[169]	1.149(4)	1.735(3)	174.4(2)	1857	–
[Ru(dppe) ₂ (NO)F]SbF ₆ (26)*	1.02(2)	2.02(2)	178.6(7)	1846	41.5 (d, J = 34.6 Hz)

* disorder of F and N–O on an inversion centre. Reduced reliability of the given values.

A comparison of the NO stretching vibrations shown in Table 3.14 between compound **25**, **26** with literature values confirms the proposed oxidation states. A comparison of the compounds among themselves makes the differentiation between a {RuNO}⁸ and {RuNO}⁶ even clearer. The ³¹P{¹H} NMR spectra show two signals for the chemically independent phosphorus atoms for compound **25** and one duplet for the four chemical dependent phosphorus atoms coupled with the ¹⁹F ligand for compound **26** which emphasises the coordination of only one fluorido and a nitrosyl ligand. Compound **25** is exclusively formed in the absence of a reductive agent or a BF₄ counterion. Compound **26** is formed from **25** after a period of time by consumption of parts of the BF₄ or SbF₆ counterions, visible through

Results

colour change from red-brown **25** to citron yellow **26**. High resolution mass spectroscopy confirmed the formation of the complexes ($m/z = 928.17$ (**25**), 1052.15 . (**26**)).

Crystal structure of $[Ru(PPh_3)_2(NO)_2]$ (**27**)

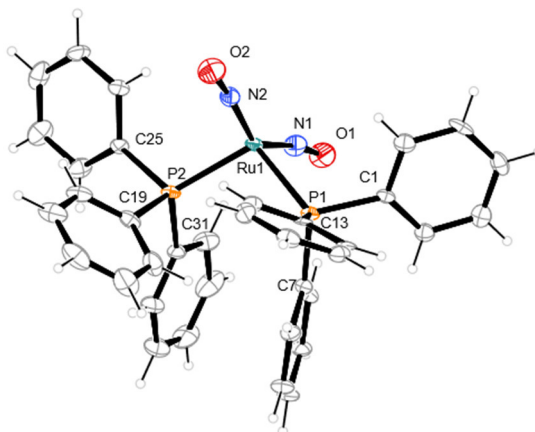


Figure 3.38: ORTEP-3 plot (ellipsoids drawn at the 50% probability level at 100 K) of $[Ru(PPh_3)_2(NO)_2]$ (**27**).^[45] Distances (Å) and angles (°): Ru1–N1 1.797(5), N1–O1 1.183(7), Ru1–N2 1.802(5), N2–O2 1.177(6), Ru1–P1 2.3367(15), Ru1–P2 2.3415(15); N1–Ru1–N2 141.9(2), Ru1–N1–O1 169.9(5), Ru1–N2–O2 172.8(5), P1–Ru1–P2 104.87(5).

The structure solution succeeded in the monoclinic space group $P2_1/n$. The unit cell contains four formula units (CShM_{T-4} value: 2.131, asymmetric unit: one molecule). The structure is shown in Figure 3.38. Compound **27** is coordinated distorted tetrahedrally by two triphenylphosphane and two nitrosyl ligands. A comparison of the bond lengths and angles of compound **27** are almost identical to published values.^[158, 167] The Ru–N–O angle is 170° and 173° therefore, the nitrosyl ligands bind nearly linear. The NO ligands point away from each other. A shortened NO distance indicates a back donation of the ruthenium centre in the π^* orbitals of the nitrosyl ligand. The infrared bands at 1651 ($\tilde{\nu}(NO)_{sym}$) and 1605 ($\tilde{\nu}(NO)_{asym}$) and the $^{31}P\{^1H\}$ NMR signal of the chemically equivalent phosphorus atoms at 54.8 ppm resemble well with already published values of the $\{Ru(NO)_2\}^{10}$ complex.^[158] An elemental analysis validates the formation. Bhaduri *et al.* obtained originally the crystal structure of **27**.^[170]

3.7 Hydrogenhyponitrito and hyponitritoruthenium complexes with bisphosphane co-ligands

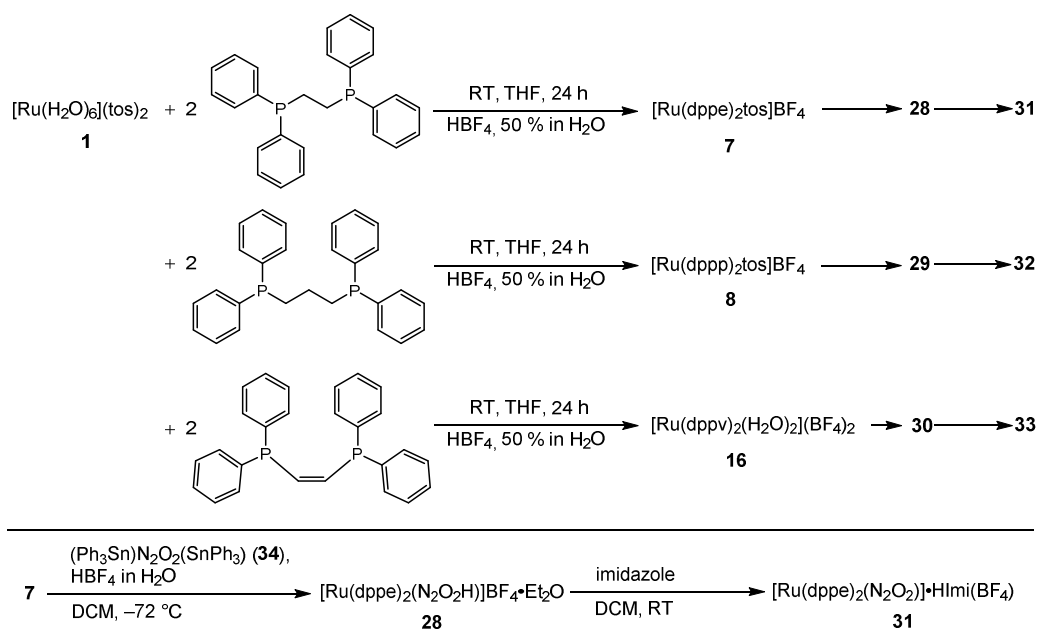
After a reductive coupling of two nitrogen monoxide molecules was not possible a different approach for hyponitrito complexes was performed. To obtain hydrogenhyponitrito compounds the crude of the respective phosphane complexes (**7**, **8**, **16**) were solved in DCM and under cryogenic conditions ($-72\text{ }^{\circ}\text{C}$) triphenylstannylhyponitrite (**34**) solved in DCM was added. After addition of tetrafluoroboric acid (in water) and intensive stirring tentative stannyl derivatives precipitated, while the hydrogenhyponitrito complex remained in solution. Evaporation of the main volume of the solvent, filtration and layering with diethyl ether leads to crystal growth beside another precipitation of tentative stannyl derivatives. The grown crystals were then big enough to pick them manually (Scheme 3.11). The procedure was tested with more compounds than **7**, **8**, **16** but these syntheses did not succeed. The compounds $[\text{Ru}(\text{dppe})_2(\text{N}_2\text{O}_2\text{H})]\text{BF}_4\cdot\text{Et}_2\text{O}$ (**28a**), $[\text{Ru}(\text{dppe})_2(\text{N}_2\text{O}_2\text{H})]\text{BF}_4$ (**28b**), $[\text{Ru}(\text{dppp})_2(\text{N}_2\text{O}_2\text{H})]\text{BF}_4\cdot\text{Et}_2\text{O}$ (**29**), $[\text{Ru}(\text{dppv})_2(\text{N}_2\text{O}_2\text{H})]\text{BF}_4\cdot\text{TBME}$ (**30**) were obtained. Preparation of hyponitrito complexes from this reaction set-up (for example by leaving out tetrafluoroboric acid) was not possible. A reaction with sodium hyponitrite or silver hyponitrite was not possible as well and leads to decomposition of the hyponitrite precursors. The yields were as follows: 80% (**28a**), 78% (**29**), 24% (**30**). The hydrogenhyponitrito complexes (**28–30**) were analysed by IR, UV/VIS (solution and solid-state), NMR (solution and solid-state) spectroscopy. HRMS was performed as bulk analysis.

To obtain the corresponding hyponitrito complexes compounds **28–30** were solved in DCM and treated with imidazole (Imi) as amine base. The deprotonation was indicated by a colour change (Table 3.15). The solution was then layered with diethyl ether and crystallised (Scheme 3.11). Compounds $[\text{Ru}(\text{dppe})_2(\text{N}_2\text{O}_2)]\cdot\text{HImi}(\text{BF}_4)$ (**31**), $[\text{Ru}(\text{dppp})_2(\text{N}_2\text{O}_2\text{H})]\text{BF}_4\cdot\text{Imi}$ (**32**) and $[\text{Ru}(\text{dppv})_2(\text{N}_2\text{O}_2)]\cdot\text{HImi}(\text{BF}_4)\cdot\text{Imi}$ (**33**) were obtained, whereby **32** was not deprotonated by imidazole. A reaction with diisopropylethylamine (DPEA, Hünig's base) and diazabicycloundecene (DBU) is possible, but only crystal structures with disorder in the amine cation were obtained. The yields of the compounds were as follows: 83% (**31**), 72% (**32**), 91% (**33**). These compounds were analysed by IR and UV/VIS spectroscopy and HRMS was performed as bulk analysis. Complexes **28–33** are the first mononuclear *trans*-hyponitrito/hydrogenhyponitrito complexes synthesised.

Table 3.15: Overview of the colour changes before and after the addition of imidazole.^[39]

28 → 31	red-orange → yellow
29 → 32	brown-red → brown-red
30 → 33	yellow → pale yellow

Results



Scheme 3.11: Formation of the compounds **7–16** and their usage as precursor for the hydrogenhyponitrito compounds **28–30**, followed by the formation of the hyponitrito compounds **31–33**. On the bottom: formation of **28** and **31** starting with precursor **7**. The reaction using **8** and **16** are identical.^[39]

Crystal structure of $[\text{Ru(dppe)}_2(\text{N}_2\text{O}_2\text{H})]\text{BF}_4 \cdot \text{Et}_2\text{O}$ (**28a**), $[\text{Ru(dppe)}_2(\text{N}_2\text{O}_2\text{H})]\text{BF}_4$ (**28b**), $[\text{Ru(dppp)}_2(\text{N}_2\text{O}_2\text{H})]\text{BF}_4 \cdot \text{Et}_2\text{O}$ (**29**), $[\text{Ru(dppv)}_2(\text{N}_2\text{O}_2\text{H})]\text{BF}_4 \cdot \text{TBME}$ (**30**)

The structure solution succeeded in the orthorhombic space group *Pbca* for **28a**, the monoclinic space group *P2₁/n* for **28b** and **29** and the monoclinic space group *P2₁/c* for **30**. The unit cells contain eight formula units for **28a** and four formula units each for **28b**, **29** and **30** (CShM_{OC-6} value: 3.622 (**28a**), 3.442 (**28b**), 2.711 (**29**), 2.775 (**30**), asymmetric unit: one molecule in **28a–30**). The structures are shown in Figures 3.39–3.42. The complexes are best described as distorted octahedra. The ruthenium centres are coordinated by two *cis*-standing bisphosphane ligands and a hydrogenhyponitrite which coordinates $\kappa^2\text{N,O}$ forming a chelate four-ring. The bond distances and angles are listed in Table 3.16. The hydrogenhyponitrito ligand resembles *trans*-H₂N₂O₂ and the *trans*-N₂O₂²⁻ anion in the sodium salt in terms of bond distances, whereas the angles about the nitrogen atoms are enlarged for the hydroxy-bonding N, and diminished for the chelate-N. The dominant motif of the crystal structures shown is the hydrogen bond between a hydrogenhyponitrite unit and an ether acceptor (diethyl ether or TBME). If **28** is crystallised from DCM/toluene (a solvent free from acceptor positions) the tetrafluoridoborate counterion forms a hydrogen bond with the hydrogenhyponitrite donor (see **28b**). The hydrogen bonds of compounds **28–33** are listed in Table 3.17. An example of a hydrogen bond between a tetrafluoridoborate counterion or a carbonyl co-ligand and a ligand is known for the dinuclear hydrogenhyponitrito complexes of Böttcher *et al.*^[99, 106]

Results

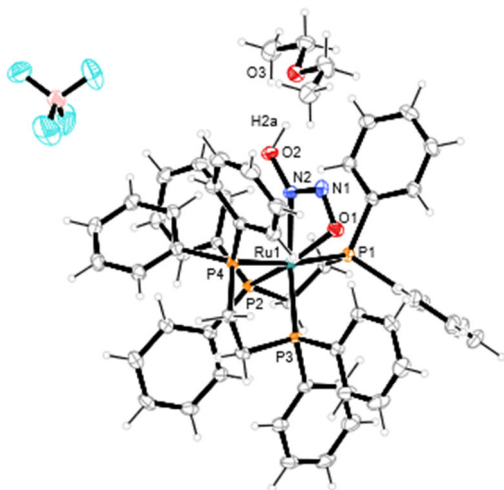


Figure 3.39: ORTEP-3 plot (ellipsoids drawn at the 50% probability level at 100 K) of $[\text{Ru}(\text{dppe})_2(\text{N}_2\text{O}_2\text{H})]\text{BF}_4 \cdot \text{Et}_2\text{O}$ (**28a**).^[45] Distances (Å) and angles (°): Ru1–N2 2.151(2), Ru1–O1 2.1728(17), Ru1–P1 2.3875(6), Ru1–P2 2.3357(6), Ru1–P3 2.3229(6), Ru1–P4 2.3725(6), N1–N2 1.258(3), N1–O1 1.309(3), N2–O2 1.384(3); N2–Ru1–O1 56.92(7), N2–N1–O1 106.77(19), N1–O1–Ru1 96.77(13), N1–N2–O2 115.72(19), N1–N2–Ru1 99.53(15), O2–N2–Ru1 144.55(15).^[39]

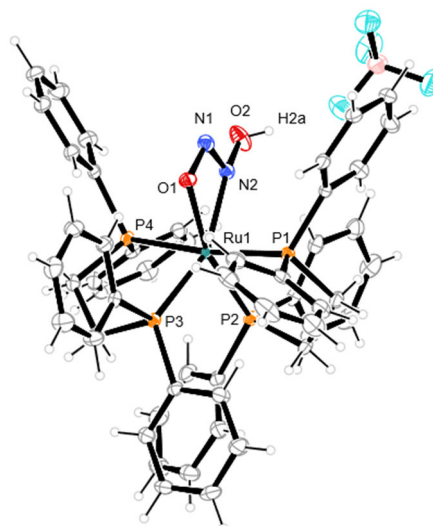


Figure 3.40: ORTEP-3 plot (ellipsoids drawn at the 50% probability level at 100 K) of $[\text{Ru}(\text{dppe})_2(\text{N}_2\text{O}_2\text{H})]\text{BF}_4$ (**28b**).^[45] Distances (Å) and angles (°): Ru1–N2 2.150(2), Ru1–O1 2.1624(18), Ru1–P1 2.3710(7), Ru1–P2 2.3259(7), Ru1–P3 2.3513(7), Ru1–P4 2.3709(7), N1–N2 1.269(3), N1–O1 1.329(3), N2–O2 1.392(3); N2–Ru1–O1 57.38(8), N2–N1–O1 105.7(2), N1–O1–Ru1 97.05(14), N1–N2–O2 112.0(2), N1–N2–Ru1 99.68(16), O2–N2–Ru1 145.69(18).^[39]

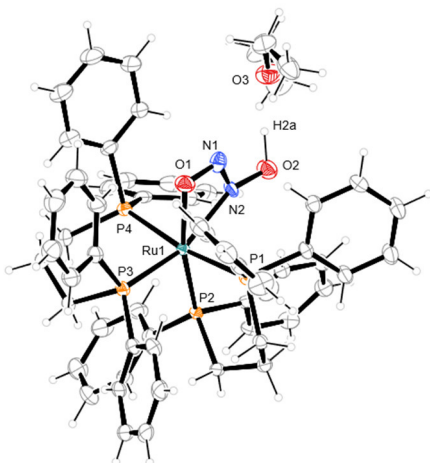


Figure 3.41: ORTEP-3 plot (ellipsoids drawn at the 50% probability level at 100 K) of $[\text{Ru}(\text{dppp})_2(\text{N}_2\text{O}_2\text{H})]\text{BF}_4 \cdot \text{Et}_2\text{O}$ (**29**).^[45] Distances (Å) and angles (°): Ru1–N2 2.201(3), Ru1–O1 2.137(2), Ru1–P1 2.4144(9), Ru1–P2 2.3404(8), Ru1–P3 2.3183(9), Ru1–P4 2.4112(9), N1–N2 1.236(4), N1–O1 1.307(4), N2–O2 1.380(4); N2–Ru1–O1 56.99(11), N2–N1–O1 109.0(3), N1–O1–Ru1 97.4(2), N1–N2–O2 113.3(3), N1–N2–Ru1 96.6(2), O2–N2–Ru1 150.1(2). Crystal solvent (dichloromethane) and tetrafluoridoborate counterion are omitted.^[39]

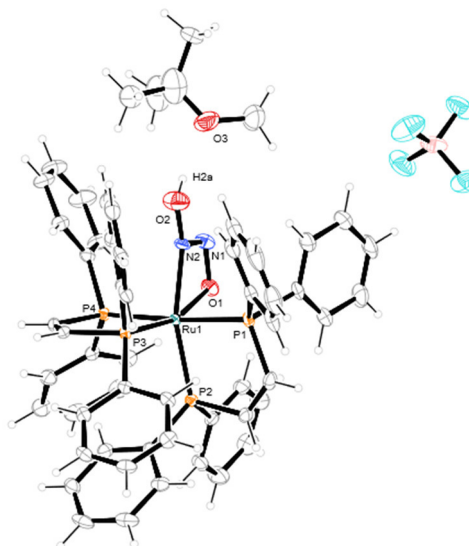


Figure 3.42: ORTEP-3 plot (ellipsoids drawn at the 50% probability level at 100 K) of $[\text{Ru}(\text{dppv})_2(\text{N}_2\text{O}_2\text{H})]\text{BF}_4 \cdot 0.81\text{TBME}$ (**30**).^[45] Distances (Å) and angles (°): Ru1–N2 2.120(3), Ru1–O1 2.163(3), Ru1–P1 2.3465(11), Ru1–P2 2.3025(11), Ru1–P3 2.2885(10), Ru1–P4 2.3510(11), N1–N2 1.287(5), N1–O1 1.346(5), N2–O2 1.343(5); N2–Ru1–O1 58.68(13), N2–N1–O1 105.7(3), N1–O1–Ru1 95.8(2), N1–N2–O2 113.6(3), N1–N2–Ru1 99.8(3), O2–N2–Ru1 146.5(3). Crystal solvent (dichloromethane) is omitted.^[39]

Results

Table 3.16: Overview of bond distances (d) and angles (α) of free hyponitrite fragments from Reference 171 and the products of this work.^[39, 171]

compound	fragment/ ligand	$d(\text{N-N})/\text{\AA}$	$d(\text{N-O})/\text{\AA}$	$\alpha(\text{N-N-O})/^\circ$
[HEt ₂ NCH ₂ CH ₂ NEt ₂ H]	H ₂ N ₂ O ₂	1.226(4)	1.363(3)	109.9(3)
[N ₂ O ₂ H]·H ₂ N ₂ O ₂ ^[171]	HN ₂ O ₂ ⁻	1.232(3)	1.371(3) (-O ⁻)	110.1(2) (-O ⁻)
			1.402(3) (-OH)	108.2(2) (-OH)
Na ₂ N ₂ O ₂ ·5H ₂ O ^[171]	N ₂ O ₂ ²⁻	1.256(2)	1.3622(11)	112.14(9)
protonated compounds				
28a	HN ₂ O ₂ ⁻	1.258(3)	1.309(3) (-O-Ru)	106.77(19) (-O-Ru)
			1.384(3) (-OH)	115.72(19) (-OH)
29	HN ₂ O ₂ ⁻	1.236(4)	1.307(4) (-O-Ru)	109.0(3) (-O-Ru)
			1.380(4) (-OH)	113.3(3) (-OH)
30	HN ₂ O ₂ ⁻	1.287(5)	1.346(5) (-O-Ru)	105.7(3) (-O-Ru)
			1.343(5) (-OH)	113.6(3) (-OH)
32	HN ₂ O ₂ ⁻	1.263(3)	1.348(3) (-O-Ru)	105.74(18) (-O-Ru)
			1.370(3) (-OH)	113.72(18) (-OH)
deprotonated compounds				
31	N ₂ O ₂ ²⁻	1.260(3)	1.369(3) (-O-Ru)	104.7(2) (-O-Ru)
			1.345(3) (-O ⁻)	116.0(2) (-O ⁻)
33	N ₂ O ₂ ²⁻	1.268(3)	1.383(2) (-O-Ru)	105.71(17) (-O-Ru)
			1.323(2) (-O ⁻)	117.06(18) (-O ⁻)

Crystal structure of [Ru(dppe)₂(N₂O₂)]·HImi(BF₄) (**31**), [Ru(dppp)₂(N₂O₂H)]BF₄·Imi (**32**) and [Ru(dppv)₂(N₂O₂)]·HImi(BF₄)·Imi (**33**)

The structure solutions succeeded in the orthorhombic space group $P2_12_12_1$ for **31** and the monoclinic space group $P2_1/n$ for **32** and **33**. The unit cells contain four formula units for **31–33** each. (CShM_{OC-6} value: 3.309 (**31**), 2.671 (**32**), 2.849 (**33**), asymmetric unit: one molecule in **31–33**). The crystal structures are shown in Figures 3.44–3.46. The coordination form is identical to compounds **28–30**. A ruthenium centre is coordinated by two bisphosphane ligands (dppe, dppp, dppv) and a hyponitrito (hydrogenhyponitrito for **32**) ligand which forms a four-ring chelate. Protonated imidazole (HImi) replaces the ether-hydrogen-bond acceptor (or BF₄⁻-acceptor) in compound **31** and **33**. In compound **32** the hydrogenhyponitrite moiety is not deprotonated by imidazole. Nonetheless, imidazole replaces also the ether acceptor. In **33**, a complex H-bond system was formed by imidazolium and imidazole

Results

(Figure 3.43). In contrast, **31** was a fragment of **32** forming only one H-bond (N4–H7···O1). The hydrogen bonds of the compounds **31–33** are listed in Table 3.17. The bond distances and angles are almost unaltered after deprotonation and resemble exceptional well with the previous protonated compounds **28–30**, the free hyponitrous acid and its hyponitrito fragments (Table 3.16).

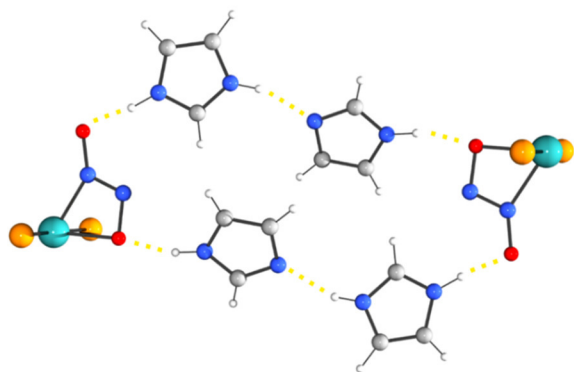


Figure 3.43: The hydrogen-bond network of **33**. Reduced illustration of the complex cation. Grey: carbon, blue: nitrogen, white: hydrogen, cyan: ruthenium, orange: phosphorus.^[39]

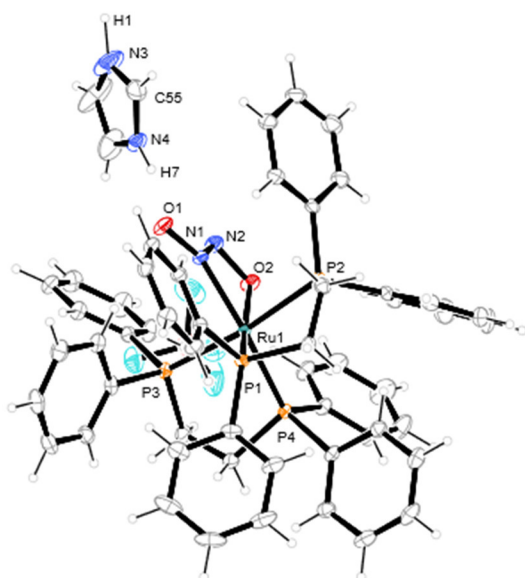


Figure 3.44: ORTEP-3 plot (ellipsoids drawn at the 50% probability level at 100 K) of $[\text{Ru}(\text{dppe})_2(\text{N}_2\text{O}_2)] \cdot \text{HImiBF}_4$ (**31**).^[45] Distances (Å) and angles (°): Ru1–N1 2.125(2), Ru1–O2 2.1440(18), Ru1–P1 2.3402(7), Ru1–P2 2.3712(7), Ru1–P3 2.3708(7), Ru1–P4 2.3351(7), N1–N2 1.260(3), N1–O1 1.345(3), N2–O2 1.369(3); N1–Ru1–O2 58.40(8), N2–N1–O1 105.7(3), O1–N1–Ru1 95.8(2), N2–N1–O1 116.0(2), N2–N1–Ru1 100.71(17), O1–N1–Ru1 142.90(17), N1–N2–O2 104.7(2).^[39]

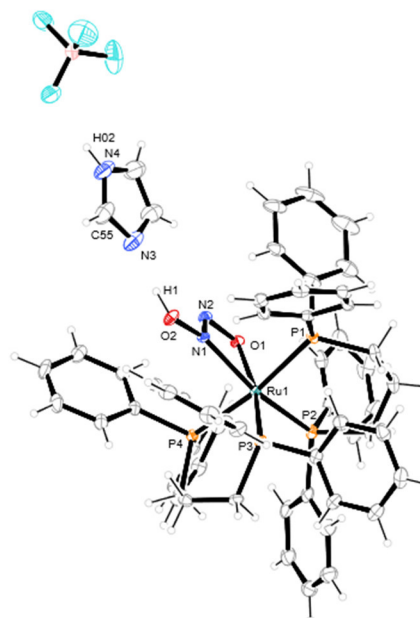


Figure 3.45: ORTEP-3 plot (ellipsoids drawn at the 50% probability level at 100 K) of $[\text{Ru}(\text{dppp})_2(\text{N}_2\text{O}_2\text{H})]\text{BF}_4 \cdot \text{Imi}$ (**32**).^[45] Distances (Å) and angles (°): Ru1–N1 2.1940(19), Ru1–O1 2.1353(16), Ru1–P1 2.4147(6), Ru1–P2 2.3100(6), Ru1–P3 2.3513(6), Ru1–P4 2.4062(6), N1–N2 1.263(3), N1–O2 1.370(3), N2–O1 1.348(3); N1–Ru1–O1 57.48(7), N2–N1–O2 113.72(18), N2–O1–Ru1 98.40(12), N1–N2–O1 105.74(18), N2–N1–Ru1 98.38(14), O2–N1–Ru1 147.86(15). Crystal solvent (dichloromethane) is omitted.^[39]

Results

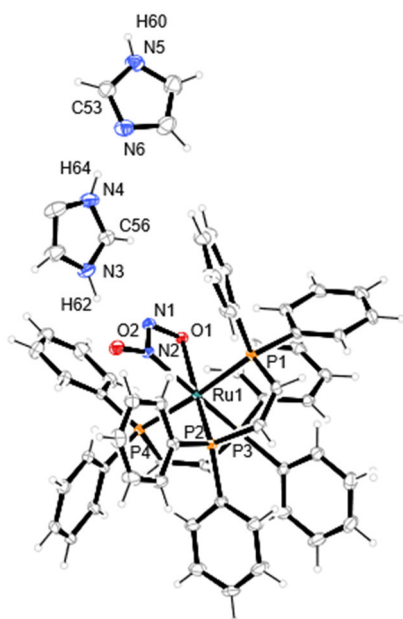


Figure 3.46: ORTEP-3 plot (ellipsoids drawn at the 50% probability level at 97 K) of $[\text{Ru}(\text{dppv})_2(\text{N}_2\text{O}_2)] \cdot \text{HImi}^+ \cdot \text{Imi}$ in **33**.^[45] Distances (Å) and angles (°): Ru1–N2 2.1240(18), Ru1–O1 2.1487(15), Ru1–P1 2.3402(6), Ru1–P2 2.3036(6), Ru1–P3 2.2846(6), Ru1–P4 2.3469(6), N1–N2 1.268(3), N1–O1 1.383(2), N2–O2 1.323(2); N2–Ru1–O1 59.31(7), N2–N1–O1 105.71(17), N1–O1–Ru1 95.01(11), N1–N2–O2 117.06(18), N1–N2–Ru1 99.94(13), O2–N2–Ru1 142.54(15). Crystal solvent (dichloromethane) and tetrafluoridoborate counterion are omitted.^[39]

Table 3.17: Overview of selected distances (d) and angles (α) the hydrogen bonds formed in the products **5–10** by the hydrogen hyponitrite moiety and an ether, a tetrafluoridoborate anion or imidazole.^[39]

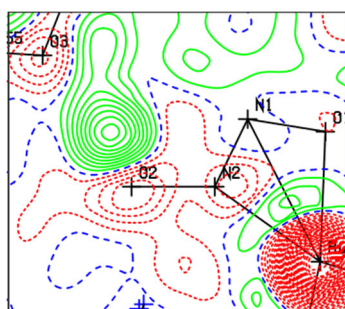
compound	D–H \cdots A	$d(\text{D–H})/\text{Å}$	$d(\text{H}\cdots\text{A})/\text{Å}$	$d(\text{D–A})/\text{Å}$	$\alpha(\text{D–H}\cdots\text{A})/^\circ$
protonated compounds:					
28a	O2–H2A \cdots O3	1.05(3)	1.63(3)	2.639(3)	159(3)
29	O2–H2A \cdots O3	1.12(5)	1.62(5)	2.663(4)	151(4)
30	O2–H2A \cdots O3	0.93(2)	1.80(4)	2.629(6)	148(6)
32	O2–H1 \cdots N3	0.99(4)	1.66(4)	2.6929(3)	165(4)
	N4–H2 \cdots F2	0.88(5)	1.90(5)	2.768(3)	172(4)
28b	O2–H2A \cdots F1	0.74(5)	2.01(5)	2.674(3)	150(6)
deprotonated compounds:					
31	N4–H7 \cdots O1	0.88 ^a	1.66	2.520(3)	166.2
32	N3–H62 \cdots O2	0.92(2) ^b	1.65(2)	2.567(3)	174(4)
	N4–H64 \cdots N6	0.88 ^a	1.95	2.801(3)	161.1
	N5–H60 \cdots O1 ^l	0.91(2) ^b	1.92(2)	2.800(3)	164(4)

^l $-x + 1, -y + 1, -z + 2$. ^a constraint refinement ^b restraint refinement

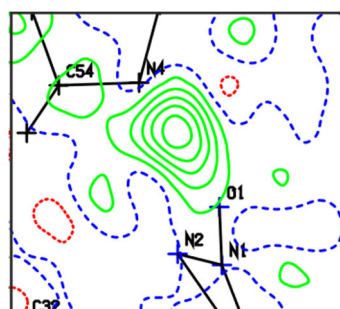
Results

Difference-Fourier Analysis

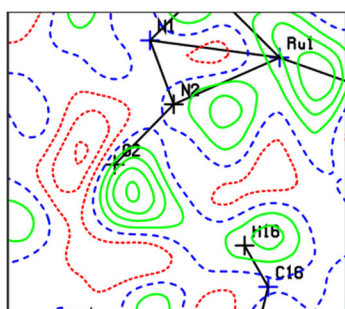
Though the determination of a hydrogen position in a standard X-ray analysis is subject to methodological limitations, a Difference-Fourier analysis can be used to visualise residual electron density prior to the H atom's assignment. The results of the ΔF analysis, in terms of the residual density's height and position along the tentative hydrogen bond are shown in Fig. 3.47. As shown the assignment of a hydrogen atom at the oxygen (O2) of hydrogenhyponitrite is evident for **28a–30, 32**.



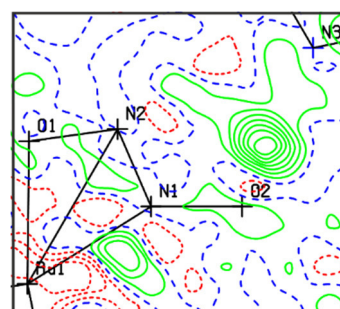
[Ru(dppe)₂(N₂O₂H)]BF₄·Et₂O (**28a**)



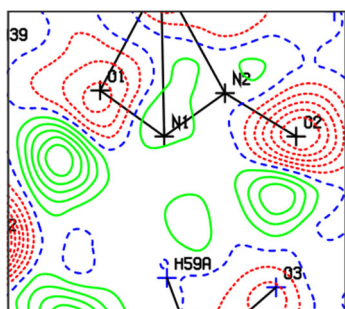
[Ru(dppe)₂(N₂O₂)]·HImi(BF₄) (**31**)



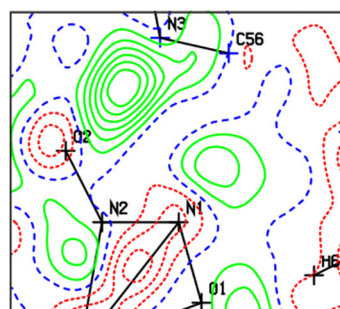
[Ru(dppe)₂(N₂O₂H)]BF₄ (**28b**)



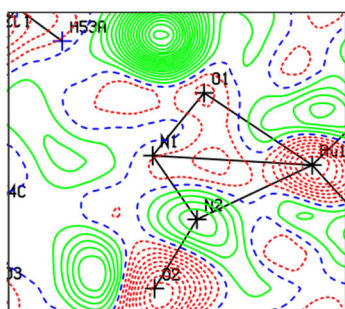
[Ru(dppp)₂(N₂O₂H)]BF₄·Imi (**32**)



[Ru(dppp)₂(N₂O₂H)]BF₄·Et₂O (**29**)



[Ru(dppv)₂(N₂O₂)]·HImi(BF₄)·Imi (**33**)



[Ru(dppv)₂(N₂O₂H)]BF₄·TBME (**30**)

Figure 3.47: Difference-Fourier map of **28a–33**, around the hydrogenhyponitrite/ ether (or tetrafluoroborate; on the left) or the hyponitrite/imidazole couple (on the right).^[39]

Results

Nonetheless, for compounds **29** and **30** residual densities are also located at the O1 atom indicating a possible O–H bond ($0.80 \text{ e } \text{\AA}^{-3}$ (**29**), $1.31 \text{ e } \text{\AA}^{-3}$ (**30**)), but both a missing hydrogen bond acceptor and a proposed bond distance of around 1.3 \AA which is too large for an O–H bond lead to the conclusion, that these are mere artefacts. A comparison with compounds **32** and **33** emphasises this conclusion since the residual density at the O1 atom is greatly reduced. Table 3.18 shows the result of the subsequent least-squares refinement with the positional parameters and an individual isotropic temperature parameter of the hydrogen atom as the refined parameters as far as possible.

Table 3.18: Position and height of the residual density in the absence of the respective hydrogen atom together with the position after the refinement and the temperature factor of the hydrogen atom in **28a–33**. If necessary, an afix constraint for O–H or N–H was applied.^[39]

	difference Fourier peak in $\text{e } \text{\AA}^{-3}$	distance from O/N $d/\text{\AA}$	refined distance $d/\text{\AA}$	$U_{\text{iso}}/\text{\AA}^2$
28a	0.58	0.962 (O–H)	1.05(3)	0.035 ^b
28b	0.60	0.705 (O–H)	0.74(5)	0.09(2)
29	0.54	0.981 (O–H)	1.12(5)	0.049 ^b
30	0.31	1.035 (O–H)	0.93(2)	0.064 ^b
31	0.36	0.913 (N–H)	0.88 ^a	0.07(2)
32	0.77	0.947 (O–H)	0.994(4)	0.05(1)
33	0.74	0.996 (N–H)	0.92(2)	0.05(1)

^aconstraint: afix 43 (fixed distance, riding model), ^bconstraint: afix 148 (refinement of OH-distance)

Further analytics of compounds **28a–33**

Both the hydrogenhyponitrito and the hyponitrito complexes **28a–33** were confirmed by high resolution mass spectroscopy. Using the FAB (fast atom bombardment) method the complex cation can be observed intact. The mass peaks are as follows: $m/z = 959.18$ ($\text{C}_{52}\text{H}_{49}\text{N}_2\text{O}_2\text{P}_4^{102}\text{Ru}$, **28**), 987.21 ($\text{C}_{54}\text{H}_{53}\text{N}_2\text{O}_2\text{P}_4^{102}\text{Ru}$, **29**), 955.15 ($\text{C}_{52}\text{H}_{45}\text{N}_2\text{O}_2\text{P}_4^{102}\text{Ru}$, **30**), 961.18 ($\text{C}_{52}\text{H}_{49}\text{N}_2\text{O}_2\text{P}_4^{102}\text{Ru}$, **31**), 987.21 ($\text{C}_{54}\text{H}_{53}\text{N}_2\text{O}_2\text{P}_4^{102}\text{Ru}$, **32**), 957.14 ($\text{C}_{52}\text{H}_{48}\text{O}_2\text{P}_4\text{Ru}$, ESI+, **33**). A comparison of solid-state and solution UV/VIS (in DCM) was done for **28a**, **29**, **30**. As seen in Figure 3.48 the solution and solid-state spectra of compound **29** are similar to each other which indicates that solid-state species and solution species are probably the same. This is similar for compound **28a** and **30**. The later described comparison between solution and solid-state NMR spectra emphasise this observation. UV/VIS values are listed in Table 3.19.

Results

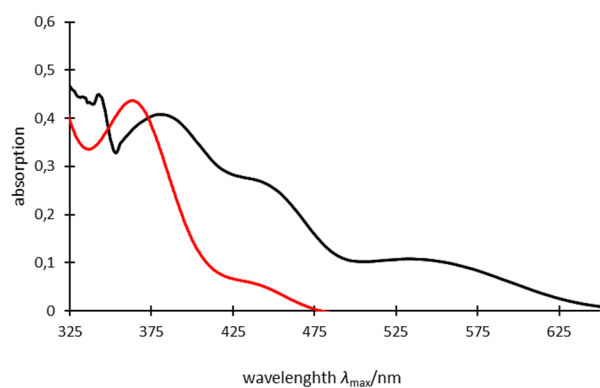


Figure 3.48: UV/VIS spectra of $[\text{Ru}(\text{dppp})_2(\text{N}_2\text{O}_2\text{H})]\text{BF}_4 \cdot \text{Et}_2\text{O}$ (**29**) (on the left): black: solid-state (386.0, 445.3, 545.3 nm; y-value (k/s) tripled); red: solution in DCM (371.5, 453.2 nm). In the case of the solid-state spectrum, the Y axis refers to the Kubelka-Munk function ($k/s = (1-R)^2/2R$).^[156]

Table 3.19: UV/VIS values of compounds **28a**, **29** and **30** obtained from solution (DCM) and solid-state measurements.

	UV/VIS peaks in solution (DCM) $\lambda_{\text{max}}/\text{nm}$	UV/VIS peaks in solid-state $\lambda_{\text{max}}/\text{nm}$
$[\text{Ru}(\text{dppe})_2(\text{N}_2\text{O}_2\text{H})]\text{BF}_4 \cdot \text{Et}_2\text{O}$ (28a)	357.6	378.0, 532.9
$[\text{Ru}(\text{dppp})_2(\text{N}_2\text{O}_2\text{H})]\text{BF}_4 \cdot \text{Et}_2\text{O}$ (29)	371.5, 453.2	386.0, 445.3, 545.3
$[\text{Ru}(\text{dppv})_2(\text{N}_2\text{O}_2\text{H})]\text{BF}_4 \cdot \text{TBME}$ (30)	358	≈ 388

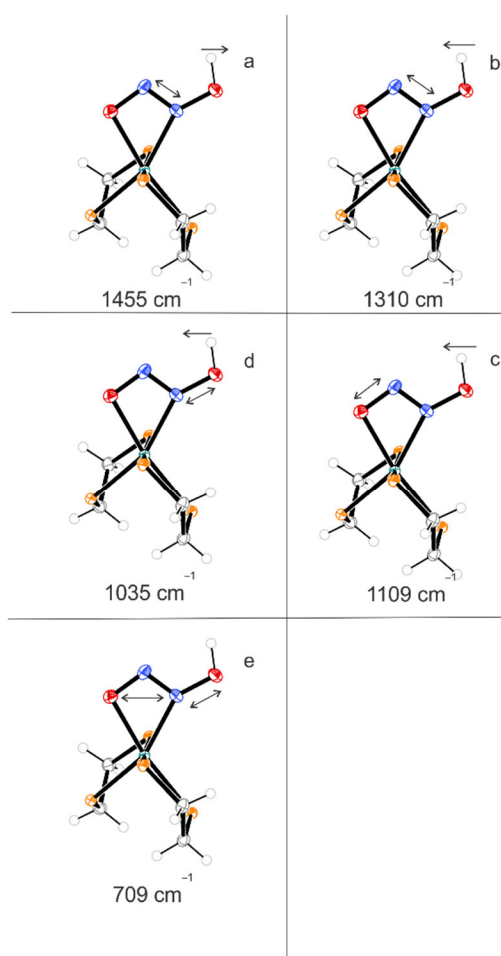


Figure 3.49: Vibrations of the hydrogenhyponitrito ligand of compound **28a**. a) stretching vibration of the N–N bond, bending of the O–H pointing away at the greatest extent of the N–N vibration, b) stretching vibration of the N–N bond, bending of the O–H pointing away at the smallest extent of the N–N vibration, c) stretching vibration of the coordinated O–N bond, bending of the O–H pointing inward at the greatest extent of the O–N vibration, d) stretching vibration of the uncoordinated O–N bond, bending of the O–H pointing inward at the greatest extent of the O–N vibration, e) symmetrically coupled stretching vibration of the uncoordinated O–N bond with scissoring of the O–N–N moiety. The values of the different vibrations were taken from quantum-chemical calculations based on DFT. Vibrations of **29** and **30** are similar.

IR vibrational frequencies of **28a–33** are given in Table 3.20. A visualisation of the hydrogenhyponitrite/ hyponitrite vibrations is shown in Figures 3.49 and 3.50. A comparison of calculated and experimental signals confirms the formation of compounds **28a–33**.

Results

Table 3.20: Overview of infrared vibrations $\tilde{\nu}(\text{NO})/\text{cm}^{-1}$ of **28a–33**. The IR frequencies were taken from quantum chemical calculations, based on DFT.^[39]

	$\tilde{\nu}(\text{N-O})/\text{cm}^{-1}$			$\tilde{\nu}(\text{N-N})/\text{cm}^{-1}$	
	found	calculated	assignment	found	calculated
	protonated compounds:				
$[\text{Ru}(\text{dppe})_2(\text{N}_2\text{O}_2\text{H})]\text{BF}_4$ (28a)	715 1032 1100	709 1035 1109	$\text{O} \leftrightarrow \text{N-N}$ $\text{O} \leftrightarrow \text{N-N}$ $\text{N} \leftrightarrow \text{O-Ru}$	1311 1450	1310 1455
$[\text{Ru}(\text{dppp})_2(\text{N}_2\text{O}_2\text{H})]\text{BF}_4$ (29)	730 1023 1115	715 1022 1122	$\text{O} \leftrightarrow \text{N-N}$ $\text{O} \leftrightarrow \text{N-N}$ $\text{N} \leftrightarrow \text{O-Ru}$	1313 1453	1314 1453
$[\text{Ru}(\text{dppv})_2(\text{N}_2\text{O}_2\text{H})]\text{BF}_4$ (30)	718 1035 1112	707 1035 1112	$\text{O} \leftrightarrow \text{N-N}$ $\text{O} \leftrightarrow \text{N-N}$ $\text{N} \leftrightarrow \text{O-Ru}$	1313	1307 1453
$[\text{Ru}(\text{dppp})_2(\text{N}_2\text{O}_2\text{H})]\text{BF}_4$ (32)	734 1020 1131	714 1027 1131	$\text{O} \leftrightarrow \text{N-N}$ $\text{O} \leftrightarrow \text{N-N}$ $\text{N} \leftrightarrow \text{O-Ru}$	1313 1453	1313 1451
deprotonated compounds:					
$[\text{Ru}(\text{dppe})_2(\text{N}_2\text{O}_2)] \cdot (\text{HImi})\text{BF}_4$ (31)	717 943	730 943	$\text{O} \leftrightarrow \text{N-N}$ $\text{N} \leftrightarrow \text{O-Ru}$	1252 1390	1252 1386
$[\text{Ru}(\text{dppv})_2(\text{N}_2\text{O}_2)] \cdot (\text{HImi})\text{BF}_4$ (32)	716 935	716 939	$\text{O} \leftrightarrow \text{N-N}$ $\text{N} \leftrightarrow \text{O-Ru}$	1253 1385	1253 1385

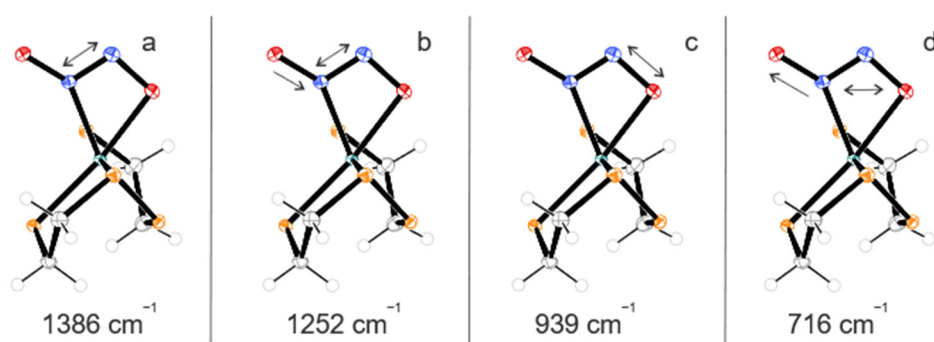


Figure 3.50: Vibrations of the hyponitrito ligand of compound **31**. a) stretching vibration of the N–N bond, b) symmetrically coupled stretching vibration of the N–N bond, stretching vibration of uncoordinated N–O, c) stretching vibration of the coordinated O–N bond, d) symmetrically coupled stretching vibration of the uncoordinated O–N bond with scissoring of the O–N–N moiety. The values of the different vibrations were taken from quantum-chemical calculations based on DFT. Vibrations of **32** and **33** are similar.

Results

$^{31}\text{P}\{^1\text{H}\}$ NMR spectroscopy of compound **28a**

A reliable determination of the phosphorus signals in the $^{31}\text{P}\{^1\text{H}\}$ NMR spectrum of compound **28a** in solution is difficult in the region around 56, 54 and 52 ppm (Figure 3.51). Though there are computational programs to separate these signals, a different approach was made by using $^{31}\text{P}\{^1\text{H}\}$ NMR spectroscopy (Figures 3.52–3.54).

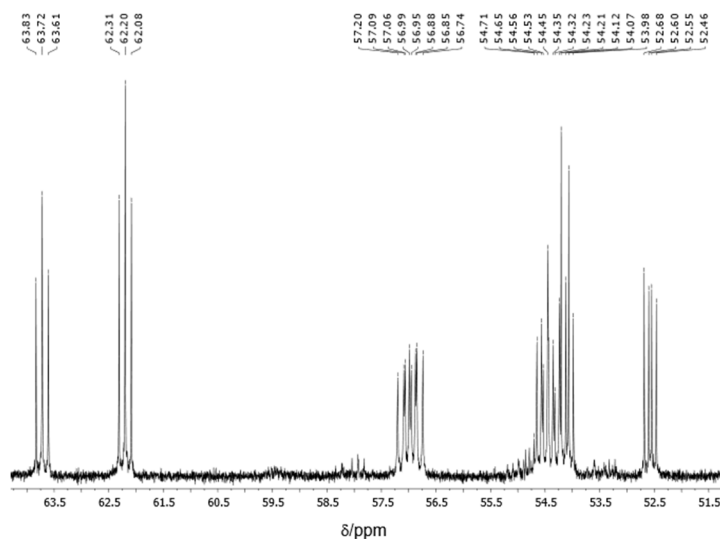


Figure 3.51: $^{31}\text{P}\{^1\text{H}\}$ NMR spectrum of $[\text{Ru}(\text{dppe})_2(\text{N}_2\text{O}_2\text{H})]\text{BF}_4$ (**28a**) in CD_2Cl_2 at RT.

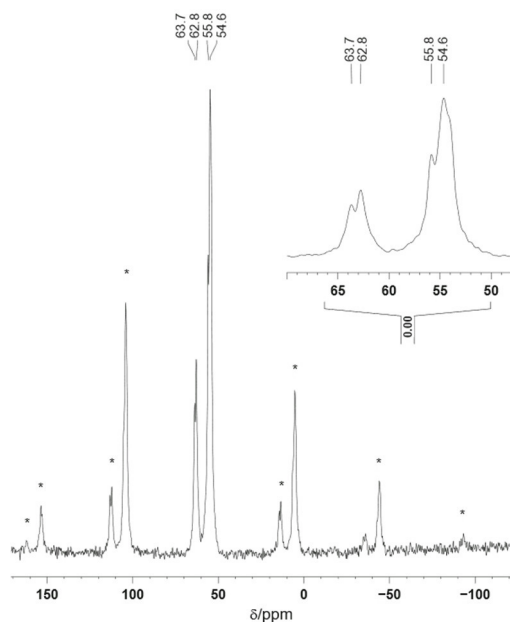


Figure 3.52: $^{31}\text{P}\{^1\text{H}\}$ -MAS NMR spectrum of compound **28a**, recorded at 10 kHz rotation in a 4 mm rotor (202 MHz). Rotation bands are marked with an asterisk.^[39]

Additionally, the recording of solid-state NMR spectra of compounds **28a–30** emphasise the formation of the said compounds (Figures 3.52–3.54). The chemically independent phosphorus atoms show four signals, whereby the signals of the spectrum of compound **29** is shifted to the highfield region

Results

compared to **28a** and **30** probably indicating a higher electron density at the phosphorus atoms of the dppp ligand. An additional splitting of the signals as in the solution spectrum of compound **28a** was not observed.

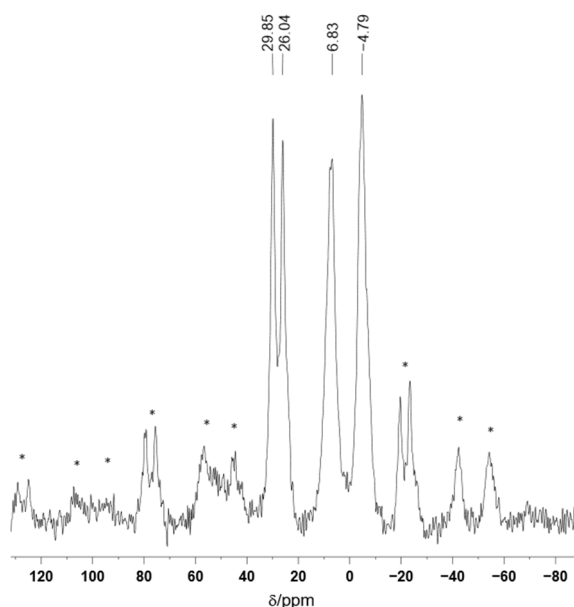


Figure 3.53: $^{31}\text{P}\{^1\text{H}\}$ -MAS NMR spectrum of compound **29**, recorded at 10 kHz rotation in a 4 mm rotor (202 MHz). Rotation bands are marked with an asterisk.^[39]

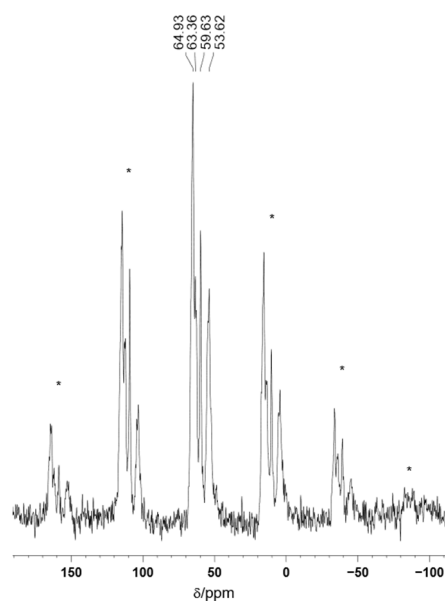


Figure 3.54: $^{31}\text{P}\{^1\text{H}\}$ -MAS NMR spectrum of compound **30**, recorded at 10 kHz rotation in a 4 mm rotor (202 MHz). Rotation bands are marked with an asterisk.^[39]

Photochemical reactions of protonated and deprotonated compounds **28–33**

The measurements described in this subchapter were performed by Prof. Dr. Dominik Schaniel (*Université de Lorraine*). The compounds were irradiated with a laser of 365 nm wavelengths (70 mW) over a period of 2–180 min. Due to great resemblance of the hydrogenhyponitrite complexes to each other $[\text{Ru}(\text{dppe})_2(\text{N}_2\text{O}_2\text{H})]\text{BF}_4$ **28b** is shown as best example. During the irradiation process the colour of compound **28b** changed from yellow orange to a darker red-brownish colour. A darkening of the colour of compounds **28a–30** is also observed. An observable, continuous increase of absorption in the UV/VIS spectrum over time is evident in Figure 3.55. A difference plot visualises the growth of signals at 525, 420 and 312 nm (Figure 3.56). In the region of 400–600 cm^{-1} a remarkable decrease at 526 cm^{-1} (calculated $\tilde{\nu}(\text{N}_2\text{O}_2\text{H}) \approx 506 \text{ cm}^{-1}$) is detectable and an increase 546 cm^{-1} indicating the tentative formation of a nitrosyl complex (probably $[\text{Ru}(\text{dppe})_2\text{NO}]\text{BF}_4$) stretching vibration of Ru–N or a scissoring of Ru–N–O (Figures 5.57 and 5.58), whereby the calculated value for a rather small Ru–N–O scissoring vibration lays at 539 cm^{-1} and for a significant Ru–N stretch at 559 cm^{-1} . A summary of the experimental and calculated values is given in Table 3.21. In the region of 600–900 cm^{-1} a signal at 730 increases significantly, while several signals, for example 650, 674, 815 and 875 cm^{-1} decrease. A concrete assignment for the signals is not possible, but a rearrangement of the co-ligands (dppe) is

Results

plausible, more precisely several phenyl group vibrations are likely (Figure 3.59–3.60). In the region of 900–1500 cm^{-1} a signal increase is detectable at 1157, 1463 and probably 1049 cm^{-1} and a signal decrease at 992, 1074 cm^{-1} . The signal increase in this region is a result of the scissoring and twisting vibrations of the CH_2 -groups (calcd.: 1049, 1157 cm^{-1}) and rocking of a phenyl-group (calcd.: 1441 cm^{-1}). Nonetheless, as the signal at 992 cm^{-1} is probably also a vibration of CH_2 or phenyl groups (calcd.: 993–999 cm^{-1}) the decrease of the signal at 1074 cm^{-1} is an indicator for the tentative transformation of the hydrogenhyponitrito ligand (calcd.: 1027 cm^{-1}) (Figures 3.61–3.62). In contrast to the fingerprint area, the area around 1500–2300 cm^{-1} is much more significant for the characterization of NO and N_2O gas and derivatives. The increase at 1676 cm^{-1} and on a smaller scale at 1589 and 1610 cm^{-1} show the formation of a NO complex. A comparison with experimental values of $[\text{Ru}(\text{dppe})_2(\text{NO})]\text{BF}_4$ from this work (1665 cm^{-1}) and the value of the original literature (1675 cm^{-1}) confirm the formation of a $[\text{Ru}(\text{dppe})(\text{NO})]^+$ complex similar/identical to **25**.^[166] Also, there is a temporary signal increase 2195 and 2220 cm^{-1} , whereby the latter signal increases at expense of the first (Figures 3.63–3.64). The signals of gaseous N_2O are in this region and would be in accordance with an aqua complex (3385 cm^{-1}) formed by N_2O release and protonation of the resulting hydroxide ligand of the hydrogenhyponitrito ligand ($\text{HN}_2\text{O}_2^- + \text{H}^+ \rightarrow \text{H}_2\text{O} + \text{N}_2\text{O}$) (Figures 3.65–3.66).^[172-173] In combination with the formation of a NO complex and therefore NO gas which could not be detected undoubtedly ($\text{HN}_2\text{O}_2^- \rightarrow \text{NO} + \text{NO} + \text{H}^+$) a reaction of the formed aqua complex and a gaseous NO molecule seems reasonable ($\text{Ru}-\text{H}_2\text{O} + \text{NO} \rightarrow \text{H}_2\text{O} + \text{Ru}-\text{NO}$). Such a reaction would explain the diminishing, tentative water signal. Analyses for **29** and **30** and **32** were similar (Table 3.21). The corresponding hyponitrito compound **31** shows no difference to **28a**. Compound **33** was not synthesised at this time and was therefore not analysed with this method.

Table 3.21: Selected IR signals of compounds **28b–32** obtained by irradiation with a 365 nm laser after a certain amount of time.^[166]

	$\tilde{\nu}(\text{Ru}-\text{N}-\text{O})/\text{cm}^{-1}$ scissoring, $\tilde{\nu}(\text{Ru}-\text{N})/\text{cm}^{-1}$ (calcd.)	$\tilde{\nu}(\text{N}-\text{O})/\text{cm}^{-1}$ (calcd.)	$\tilde{\nu}(\text{N}_2\text{O})/\text{cm}^{-1}$	$\tilde{\nu}(\text{H}_2\text{O})/\text{cm}^{-1}$
28b	546 (539, 559)	1676 (1665*, 1675 ^[166] , calcd. 1648)	2195, 2220	3385
29	548 (522, 557)	1660 (1656*, calcd. 1657)	2221	3421
30	526, 538 (**)	1690	2220	3420
31	– (only decrease)	1676	2220	3410
32	548	1660	2220	3400

* results of this work, compounds **25** and **36**, ** not obtained

Results

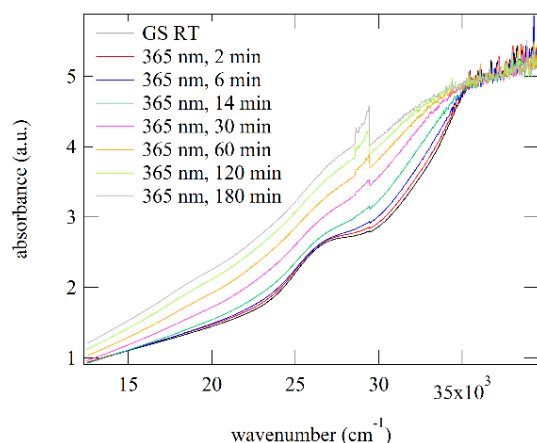


Figure 3.55: Series of UV/VIS spectra during irradiation with a 365 nm laser of compound **28b**.

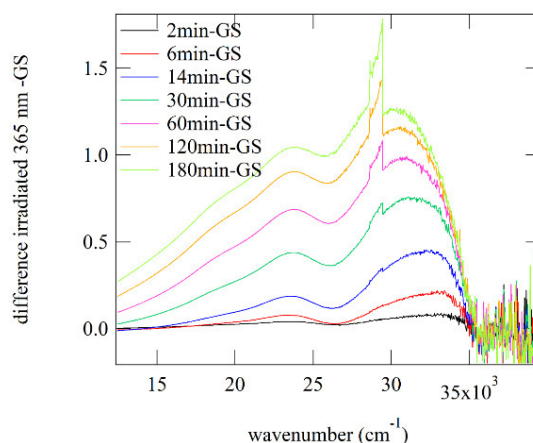


Figure 3.56: UV/VIS-Difference plot of signal changes during irradiation of compound **28a**.

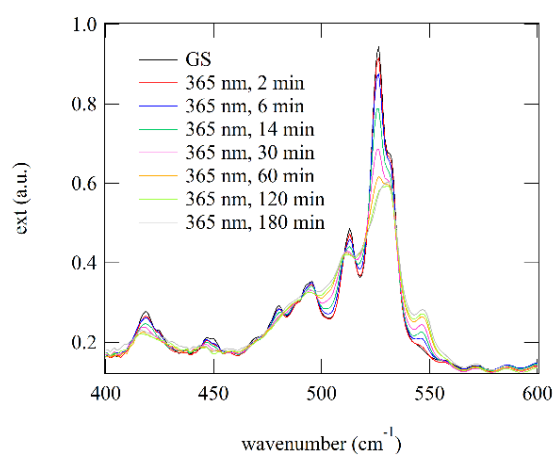


Figure 3.57: Series of IR spectra during irradiation with a 365 nm laser in the region of 400–600 cm^{-1} of compound **28a**.

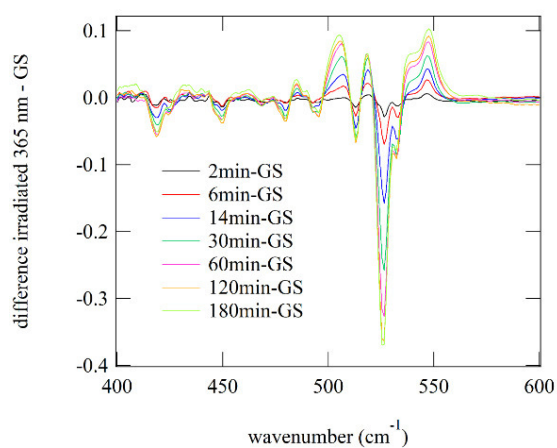


Figure 3.58: IR-Difference plot of signal changes during irradiation in the region of 400–600 cm^{-1} of compound **28a**.

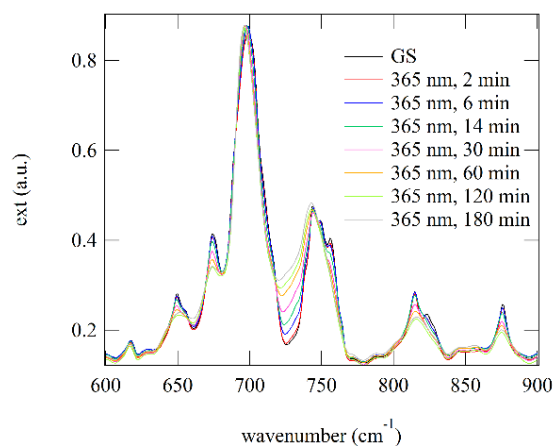


Figure 3.59: Series of IR spectra during irradiation with a 365 nm laser in the region of 600–900 cm^{-1} of compound **28a**.

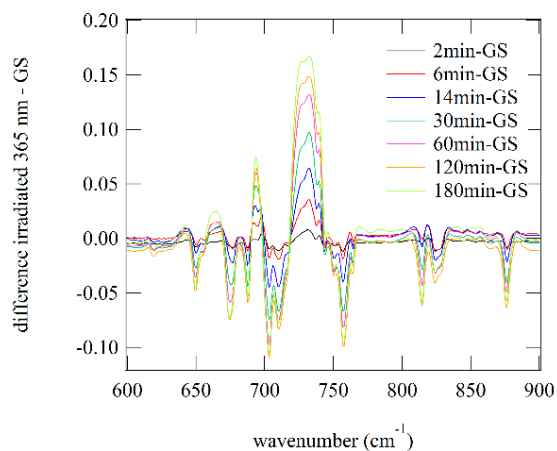


Figure 3.60: IR-Difference plot of signal changes during irradiation in the region of 600–900 cm^{-1} of compound **28a**.

Results

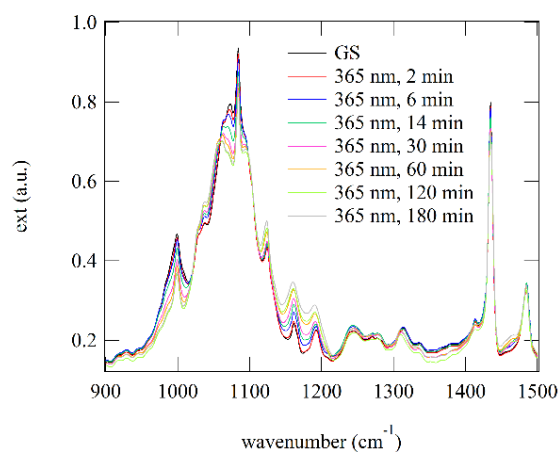


Figure 3.61: Series of IR spectra during irradiation with a 365 nm laser in the region of 900–1500 cm⁻¹ of compound **28a**.

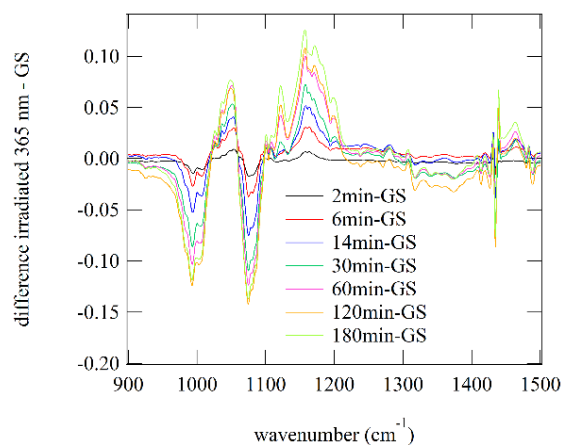


Figure 3.62: IR-Difference plot of signal changes during irradiation in the region of 900–1500 cm⁻¹ of compound **28a**.

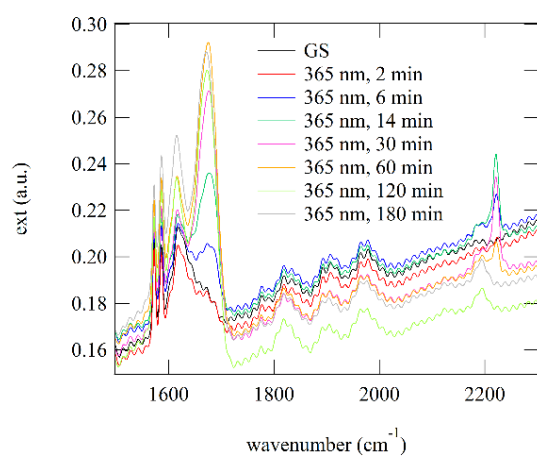


Figure 3.63: Series of IR spectra during irradiation with a 365 nm laser in the region of 1600–2300 cm⁻¹ of compound **28a**.

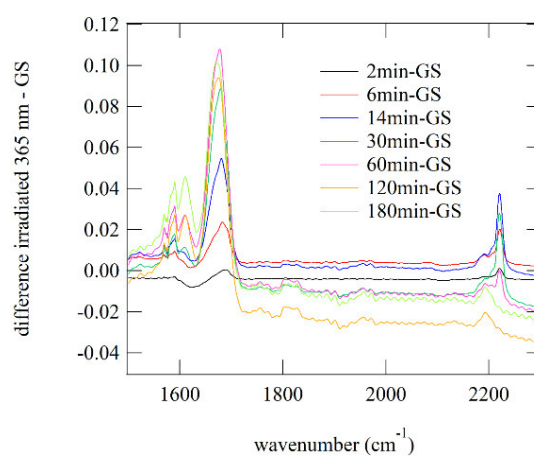


Figure 3.64: IR-Difference plot of signal changes during irradiation in the region of 1600–2300 cm⁻¹ of compound **28a**.

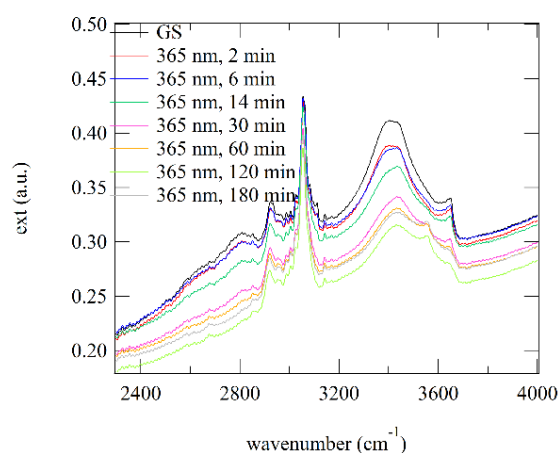


Figure 3.65: Series of IR spectra during irradiation with a 365 nm laser in the region of 2300–4000 cm⁻¹ of compound **28a**.

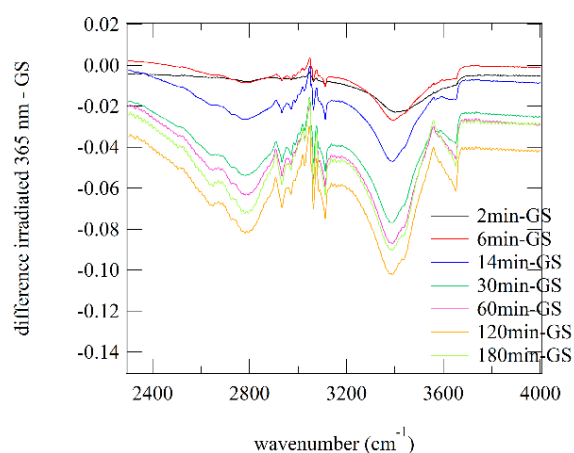
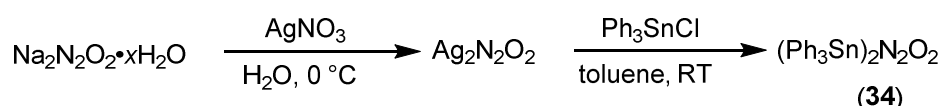


Figure 3.66: IR-Difference plot of signal changes during irradiation in the region of 2300–4000 cm⁻¹ of compound **28a**.

3.8 Short excursion: Synthesis of triphenylstannyl hyponitrite (**34**)

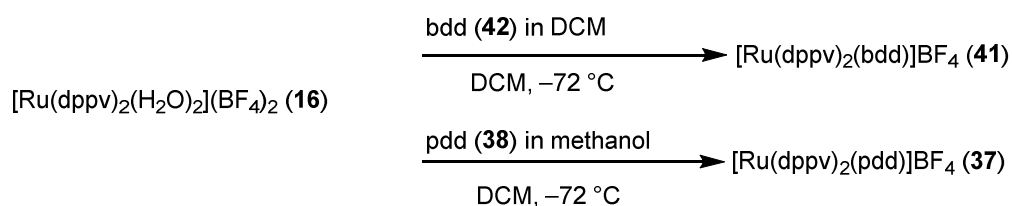


Scheme 3.12: General synthetic procedure for compound **34**.

Triphenylstannyl hyponitrite (**34**) was synthesised from literature.^[174-175] Commercially obtainable *trans*-sodium hyponitrite was treated with silver nitrate cooled by an ice bath under exclusion of light. The solid was washed with ethanol, dried and used without further analytics. The green-yellow *trans*-silver hyponitrite was suspended with two equivalents triphenylstannyl chloride in toluene and stirred for 18-20 hours. The reaction finished, when no coloured silver compound was left. After evaporation of the solvent, the crystalline slurry was recrystallised from toluene/*i*-hexane. (Scheme 3.12) The obtained colourless compound *trans*-((Ph₃Sn)₂N₂O₂) **34** was dried and used for compounds **28a–33**. The yield of ca. 350 mg was directly solved in DCM and used for the subsequent reactions. Compound **34** was analysed by IR and ¹¹⁹Sn{¹H} NMR spectroscopy (singulett: -87.9 ppm). As bulk analyses HRMS (*m/z* = 715.9 [M⁺-N₂O]⁺) and elemental analysis were performed. The obtained values resemble very well with the values given in literature.^[165]

3.9 Pyrrolidinediazoniumdiolato and benzyldiazoniumdioloruthenium complexes with bisphosphane co-ligands

The acquisition of *cis*-hyponitrito complexes was not possible and was avoided due to its explosive behaviour and its sensitivity to substitution. A form of *cis*-Ag₂N₂O₂ and *cis*-((Ph₃Sn)₂N₂O₂) was not obtainable due to decomposition. As suitable replacement of *cis*-hyponitrite *N*-diazoniumdiolate and *C*-diazoniumdiolate compounds were tested, especially to investigate whether a *cis*-hyponitrite ligand would fit in the two coordination sites of the chelate-tosylato ligand of compounds **7** and **8** in terms of distances and angles. For compound **33** a similar reaction behaviour was expected. Reactions of the *N*-sulfonatodiazoniumdiolate did not succeed due to poor solubility in organic solvents.



Scheme 3.13: General synthetic procedure for compound **41** and **37**.

Results

The *N*-diazoniumdiolato complexes were synthesised similarly to the procedure for **28a–33** (Scheme 3.13). The starting compounds **7**, **8**, **16** were solved in DCM and cooled using an *i*-propanol/dry-ice bath. The sodium *N*-pyrrolidindiazoniumdiolate **38** was solved in MeOH and added dropwise. After stirring for 1 h, evaporation of the solvent and recrystallisation from DCM/diethyl ether, two *N*-diazoniumdiolato complexes ($[\text{Ru}(\text{dppe})_2(\text{pdd})]\text{BF}_4$ (**35**), $[\text{Ru}(\text{dppv})_2(\text{pdd})]\text{BF}_4$ (**37**)) and one nitrosyl complex ($[\text{Ru}(\text{dppp})_2(\text{NO})]\text{BF}_4$ (**36**)) could be obtained. The yields were as follows: 46% (**35**), 23% (**36**), 32% (**37**). The *N*-diazoniumdiolate (**38**) is subject to steady decomposition (brown gas, yellowish solid), therefore the given yield can vary. The complexes were analysed by IR, UV/VIS and $^{31}\text{P}\{^1\text{H}\}$ spectroscopy. HRMS was performed as bulk analysis.

The procedure for *C*-diazoniumdiolato complexes is almost identical compared to *N*-diazoniumdiolato complexes (Scheme 3.13). Compounds **7**, **8**, **16** were solved in DCM and cooled using an *i*-propanol/dry-ice bath. The sodium hydrogenbenzylidiazoniumdiolate (**42**, Hbdd) was solved in DCM and added dropwise. After stirring for 1 h and evaporation of the solvent, recrystallisation of the crude from DCM/diethyl ether lead to the compounds $[\text{Ru}(\text{dppe})_2(\text{bdd})]\text{BF}_4$ (**39**), $[\text{Ru}(\text{dppp})_2(\text{bdd})]\text{BF}_4$ (**40**) and $[\text{Ru}(\text{dppv})_2(\text{bdd})]\text{BF}_4$ (**41**). The yields were as follows: 74% (**39**), 80% (**40**), 56% (**41**). The complexes **35–37** and **39–41** were analysed by IR, UV/VIS and $^{31}\text{P}\{^1\text{H}\}$ spectroscopy. HRMS was performed as bulk analysis.

*Crystal structure of $[\text{Ru}(\text{dppv})_2(\text{pdd})]\text{BF}_4$ (**37**) (and analytics of $[\text{Ru}(\text{dppe})_2(\text{pdd})]\text{BF}_4$ (**35**))*

The structure solution of **37** succeeded in the monoclinic space group $P2_1/c$. The unit cell contains 2 formula units (CShM_{OC-6} value: 1.368, asymmetric unit: one molecule). The structure is shown in Figure 3.67. The complex is best described as distorted octahedron. The ruthenium centre is coordinated by two *cis*-standing dppv units and a pyrrolidindiazoniumdiolato- κ^2O,O ligand (pdd, **38**) filling up the remaining coordination sites and are forming a chelate five-ring. Please note, that the crystal structure was obtained with a $R(F_{\text{obs}})$ of 0.0567 and $R_w(F^2)$ of 0.1469, but it is clearly visible that the pyrrolidine moiety is unsatisfactorily solved in terms of crystallography. Different crystallisation methods (including a variation of the used solvents) did not succeed in a better crystal quality and therefore in a better data set. Crystals of **35** were obtained, but the quality of the data set was not suitable to solve this structure.

Results

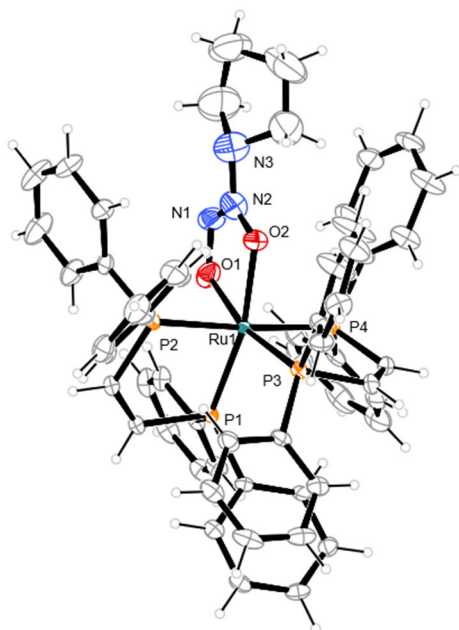


Figure 3.67: ORTEP-3 plot (ellipsoids drawn at the 50% probability level at 100 K) of the $[\text{Ru}(\text{dppv})_2(\text{pdd})]^+$ ion in **37** (on the left).^[45] Distances (Å) and angles (°): Ru1–O1 2.119(3), Ru1–O2 2.119(4), O1–N1 1.317(6), O2–N2 1.262(7), N1–N2 1.205(7), N2–N3 1.446(8), Ru1–P1 2.2816(10), Ru1–P2 2.3637(11); O1–Ru1–O2 73.3(2), O1–N1–N2 116.8(5), N1–N2–O2 125.2(5), N1–N2–N3 122.9(6), N1–O1–Ru1 113.3(3), N2–O2–Ru1 111.3(4), P1–Ru1–P2 84.49(4), P1–Ru1–P3 93.12(4). Crystal solvent (diethyl ether) and tetrafluoridoborate counterion are omitted.

The Ru–O distance of **37** of 2.119 Å is in accordance with the *trans*-hydrogenhyponitrito complexes **28a–30** (averaged: 2.159 Å). A comparison with a crystal structure of *cis*-sodium hyponitrite and the compounds **39–41** is given in Table 3.22.^[171] The resemblance of the distances of the *cis*-hyponitrite salt compared to product **37** is in an acceptable range. Both N–O distances are shorter than the uncoordinated salt and the N–O distance of the substituted nitrogen is remarkably shorter than of the unsubstituted nitrogen which is a tentative result of the pyrrolidine substituent. In contrast, the accordance of the angles between the N=N–O moieties is evident.

Table 3.22: Overview of bond distances (d) and angles (α) of free hyponitrite fragments from Reference 171 and the products of this work.

	$d(\text{N}=\text{N})/\text{Å}$	$d(\text{N}-\text{O}')/\text{Å}$	$d(\text{N}-\text{O}'')/\text{Å}$	$\alpha(\text{O}'-\text{N}=\text{N})/^\circ$	$\alpha(\text{O}''-\text{N}=\text{N})/^\circ$
$\text{Na}_2\text{N}_2\text{O}_2$ ^[171]	1.20(3)	1.40(3)	1.41(3)	117.6(4)	120.8(4)
$[\text{Ru}(\text{dppv})_2(\text{pdd})]\text{BF}_4$ (37)	1.205(7)	1.317(6)	1.262(7)	116.8(5)	125.2(5)
$[\text{Ru}(\text{dppe})_2(\text{bdd})]\text{BF}_4$ (39)	1.270(4)	1.330(4)	1.312(4)	114.9(3)	124.7(3)
$[\text{Ru}(\text{dppp})_2(\text{bdd})]\text{BF}_4$ (40)	1.270(3)	1.328(3)	1.311(3)	114.4(2)	124.3(2)
$[\text{Ru}(\text{dppv})_2(\text{bdd})]\text{BF}_4$ (41)	1.262(5)	1.343(4)	1.306(4)	115.0(3)	125.5(3)

Results

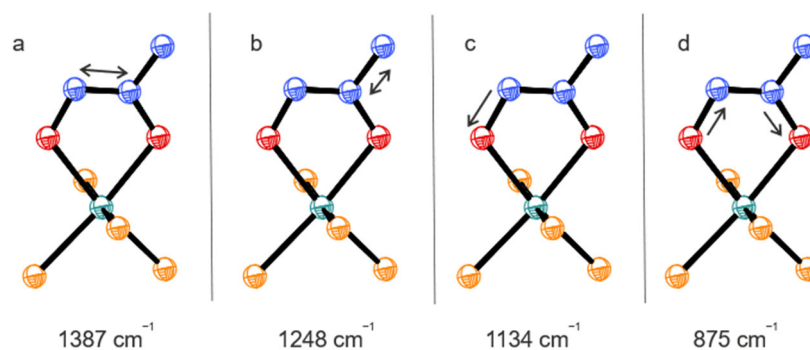


Figure 3.68: Vibrations of the pdd (**38**) ligand in compound **37**. a) stretching vibration of the N=N double bond b) stretching vibration of the N–N bond, c) stretching vibration of the unsubstituted O–N d) asymmetrically coupled stretching vibrations of the O–N bonds, whereby the vibration of the O–N bond of the substituted nitrogen is dominant. The values of the different vibrations and the xyz-file were taken from quantum-chemical calculations based on DFT.

A comparison of experimental and calculated IR signals of **37** and **35** is listed in Table 3.23. An illustration of the IR vibrations of compound **37** obtained from DFT calculations is given in Figure 3.68. The UV/VIS spectra of both complexes have a signal in the ultraviolet region with 371 (**35**) and 364 nm (**37**) in good accordance with the hydrogenhyponitrite complexes **28a–30**. $^{31}\text{P}\{^1\text{H}\}$ NMR spectra of **35** and **37** were recorded which are spectra of higher order, but an assignment of the signals without an NMR-solving program due to their complexity was not possible at the time. Nonetheless, HRMS spectra of the complexes show the formation of the desired compounds with $m/z = 944.17$ ($\text{C}_{52}\text{H}_{48}\text{O}_2\text{NP}_4\text{Ru}$), 1024.21 ($\text{C}_{56}\text{H}_{52}\text{O}_2\text{N}_3\text{P}_4\text{Ru}$).

Table 3.23: Overview of infrared vibrations in cm^{-1} of **37**, **39–41**. The IR frequencies were taken from quantum chemical calculations, based on DFT.

	$\tilde{\nu}(\text{N-O})/\text{cm}^{-1}$		$\tilde{\nu}(\text{N-C/N-N}_{\text{pyr}})/\text{cm}^{-1}$		$\tilde{\nu}(\text{N=N})/\text{cm}^{-1}$	
	experimental	calculated	experimental	calculated	experimental	calculated
N-diazoniumdiolato compounds						
35	874, 1167, 1190	–	1257	–	1378	–
37	885, \approx 1140, 1187	875, 1134, –	\approx 1240	1248	\approx 1400	1387
C-diazoniumdiolato compounds						
39	923, 1146, 1192	919, 1134, 1181	1217	1203	1408(sh)	1406

Results

40	933, 1142, 1197	930, 1144, 1192	–	1204	1410(sh)	1403
41	910, 1146, 1191	909, 1132, 1181	1209	1201	1400(sh)	1398
[Fe(bdd) ₃] ^[176]	958	–	–	–	1373	–
bdd ^[176]	953	–	–	–	1376	–
Et ₂ N– N ₂ O ₂ Na ^[109]	952	925*	–	–	1384	1353*

* values derived from literature.^[109]

Crystal structure of [Ru(dppp)₂(NO)]BF₄ (**36**)

The structure solution succeeded in the monoclinic space group $P2_1$. The unit cell contains two formula units (CShM_{TBPY-5} value: 2.041, asymmetric unit: one molecule). The structure is shown in Figure 3.69. The trigonal-bipyramidal complex is coordinated by two bisphosphane ligands (dppp) occupying each an axial and an equatorial position. The nitrosyl ligand resides on the remaining position. The Ru–N–O moiety is almost linear with 170.8° and is best described as {RuNO}⁸, most likely a d⁸ Ru(0)–NO⁺ complex. This is emphasised by a N–O bond length of 1.169 Å and a Ru–N bond length of 1.795 Å. The crystallographic data resembles well to the given literature (Table 3.24).^[177-178] A synthesis for the tetraphenylborate complex was not given in 177, nevertheless several preparations of the complex cation are known.^[178-179] A shortened Ru–N bond indicates for **36** a back donation from the ruthenium centre into π* orbitals of the nitrosyl ligand.

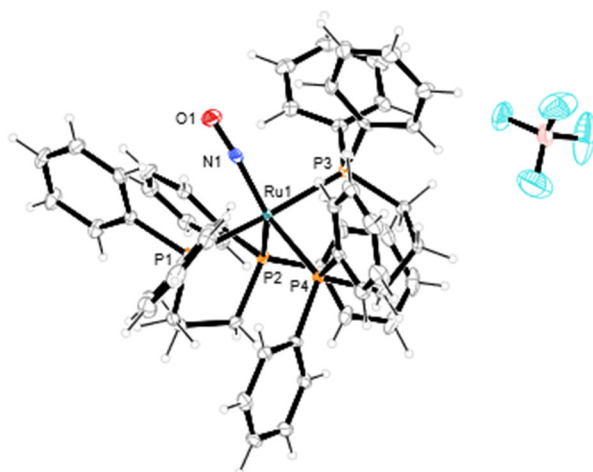


Figure 3.69: ORTEP-3 plot (ellipsoids drawn at the 50% probability level at 100 K) of [Ru(dppp)₂(NO)]BF₄ (**36**) (on the left).^[45] Distances (Å) and angles (°): Ru1–N1 1.795(3), N1–O1 1.169(4), Ru1–P1 2.4006(9), Ru1–P2 2.3441(10), Ru1–P3 2.4046(10); Ru1–N1–O1 170.7(3), P1–Ru1–P2 89.58(4), P1–Ru1–P3 176.01(4). Crystal solvent (diethyl ether) is omitted.

Results

Table 3.24: Selected bond distances (d), angles (α) and the N–O stretching vibration of compound [Ru(dppp)₂(NO)]BPh₄ and [Ru(dppp)₂(NO)]BF₄ (**36**).^[177-178]

	$d(\text{N-O})/\text{\AA}$	$d(\text{Ru-N})/\text{\AA}$	$\alpha(\text{Ru-N-O})/^\circ$	$\tilde{\nu}(\text{NO})/\text{cm}^{-1}$
[Ru(dppp) ₂ (NO)]BPh ₄ ^[177]	1.23(3)	1.72(2)	169.5(2.5)	1670 (KBr) ^[178]
[Ru(dppp) ₂ (NO)]BF ₄ (36)	1.169(4)	1.795(3)	170.7(3)	1656 (ATR)

The $\tilde{\nu}(\text{NO})$ stretching vibration of compound **36** is also in good accordance with the given literature and is in the region of {RuNO}⁸ complexes as shown for compound **25**.^[178] The UV/VIS spectrum of the brown crystals shows three signals at 373, 432, 573 nm. The ³¹P{¹H} NMR spectrum shows three different isomers, a tentative result of the flexibility of the dppp ligand in solution (Figure 3.70). Six triplets are identified and can be divided in three signal sets (**a**: $J = 39.1$ Hz, **b**: $J = 31.0$ Hz, **c**: $J = 32.4$ Hz) of the three isomers. According to the integrals isomer **a** has a percentage share of 80.65%, **b** of 16.13% and **c** of 3.22%.

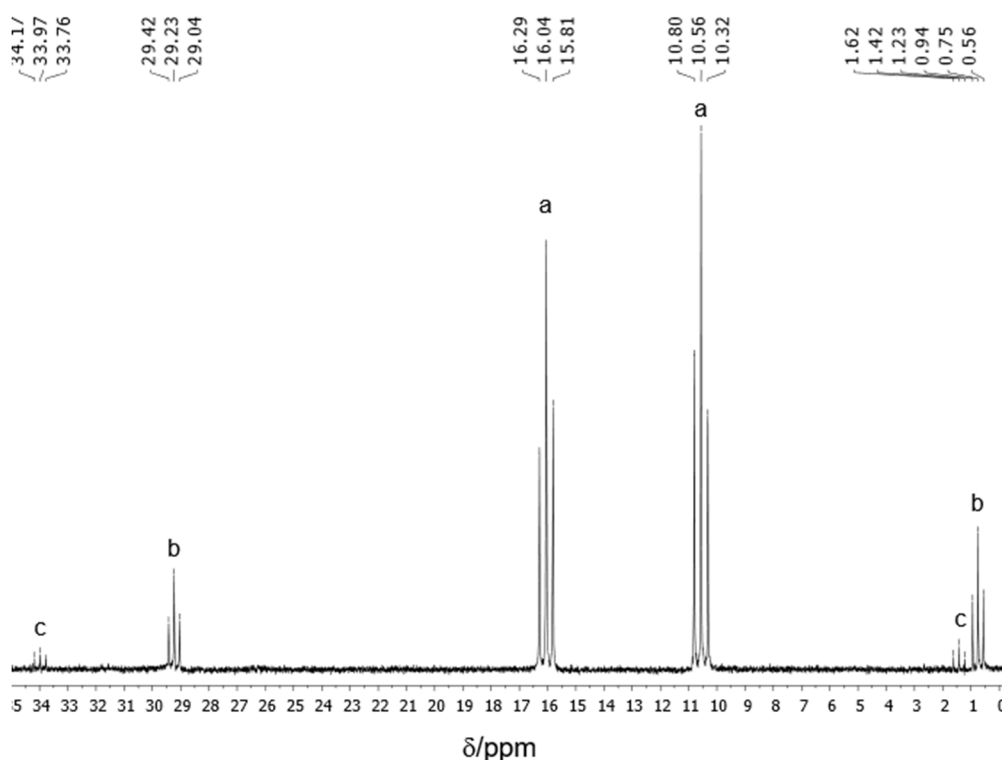


Figure 3.70: ³¹P{¹H} NMR spectrum of solvated crystals of **36** in CD₂Cl₂ at RT.

Results

Crystal structures of $[Ru(dppe)_2(bdd)]BF_4$ (**39**), $[Ru(dppp)_2(bdd)]BF_4$ (**40**) and $[Ru(dppv)_2(bdd)]BF_4$ (**41**)

The structure solutions succeeded in the monoclinic space groups $P2_1$ for **39** and $P2_1/n$ for **40** and **41**. The unit cell contains two formula units in **39** and four each in **40** and **41**. (CShM_{OC-6} value: 1.436 (**39**), 0.971 (**40**), 1.076 (**41**), asymmetric unit: one molecule in **39–41**). The structures are shown in Figures 3.71–3.73.

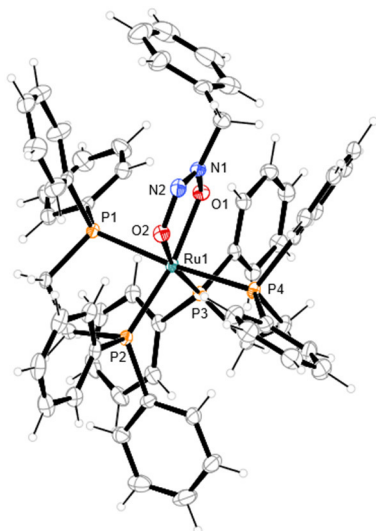


Figure 3.71: ORTEP-3 plot (ellipsoids drawn at the 50% probability level at 100 K) of the $[Ru(dppe)_2(bdd)]^+$ ion in **39**.^[45] Distances (Å) and angles (°): Ru1–O1 2.097(3), Ru1–O2 2.122(2), O1–N1 1.330(4), O2–N2 1.312(4), N1–N2 1.270(4), N1–C1 1.463(5), Ru1–P1 2.3902(9), Ru1–P2 2.3239(9); O1–Ru1–O2 75.47(10), O1–N1–N2 124.7(3), N1–N2–O2 114.9(3), N2–N1–C1 118.7(3), N1–O1–Ru1 110.1(2), N2–O2–Ru1 114.7(2), P1–Ru1–P2 83.62(3), P1–Ru1–P3 100.03(3). Tetrafluoridoborate counterion is omitted.

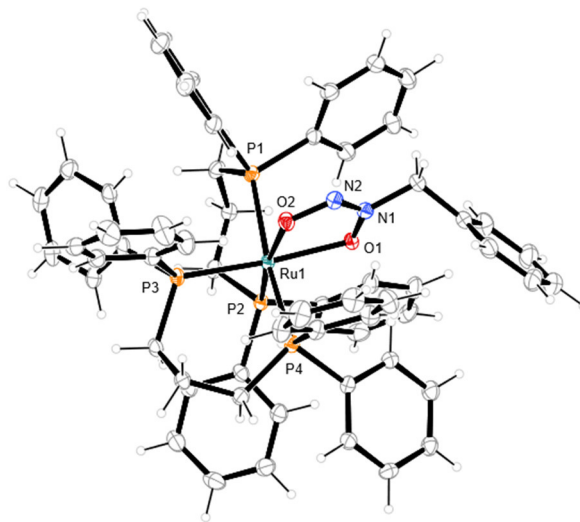


Figure 3.72: ORTEP-3 plot (ellipsoids drawn at the 50% probability level at 100 K) of the $[Ru(dppp)_2(bdd)]^+$ ion in **40**.^[45] Distances (Å) and angles (°): Ru1–O1 2.1447(17), Ru1–O2 2.1239(18), O1–N1 1.328(3), O2–N2 1.311(3), N1–N2 1.270(3), N1–C1 1.479(3), Ru1–P1 2.4216(7), Ru1–P2 2.3420(7); O1–Ru1–O2 73.81(7), O1–N1–N2 124.3(2), N1–N2–O2 114.4(2), N2–N1–C1 117.5(2), N1–O1–Ru1 110.20(14), N2–O2–Ru1 116.53(15), P1–Ru1–P2 91.05(2), P1–Ru1–P3 94.34(2). Tetrafluoridoborate counterion is omitted.

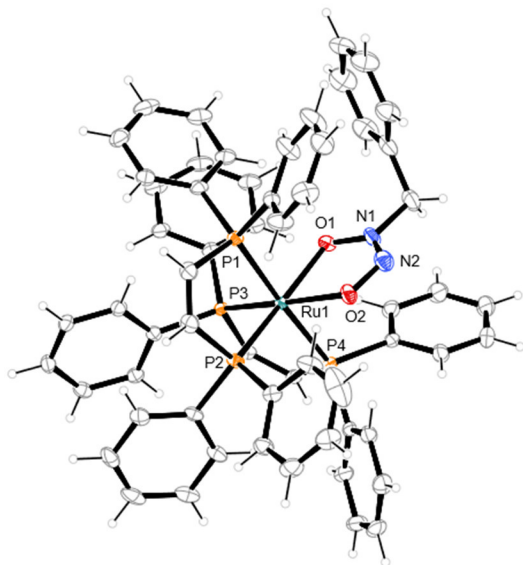


Figure 3.73: ORTEP-3 plot (ellipsoids drawn at the 50% probability level at 100 K) of the $[Ru(dppv)_2(bdd)]^+$ ion in **41** (on the left side).^[45] Ru1–O1 2.121(2), Ru1–O2 2.134(2), O1–N1 1.343(4), O2–N2 1.306(4), N1–N2 1.262(5), N1–C1 1.484(5), Ru1–P1 2.3565(9), Ru1–P2 2.3017(9); O1–Ru1–O2 75.12(10), O1–N1–N2 125.5(3), N1–N2–O2 115.0(3), N2–N1–C1 118.6(3), N1–O1–Ru1 109.1(2), N2–O2–Ru1 115.2(2), P1–Ru1–P2 83.69(3), P1–Ru1–P3 96.15(3). Crystal solvent (dichloromethane) and tetrafluoridoborate counterion are omitted.

Results

The ruthenium centre of compounds **39–41** is coordinated octahedrally by two bisphosphane co-ligands and a benzyldiazoniumdiolate (bdd). A comparison of bond angles and distances of sodium *cis*-hyponitrite and these compounds is given in Table 3.22. The N=N distance is clearly longer than the 1.2 Å of the *cis*-hyponitrite, while the N–O distances diminish. The N=N–O' and N=N–O'' angle resemble in an acceptable range with the *cis*-hyponitrite salt and pdd-compound **37** as well.

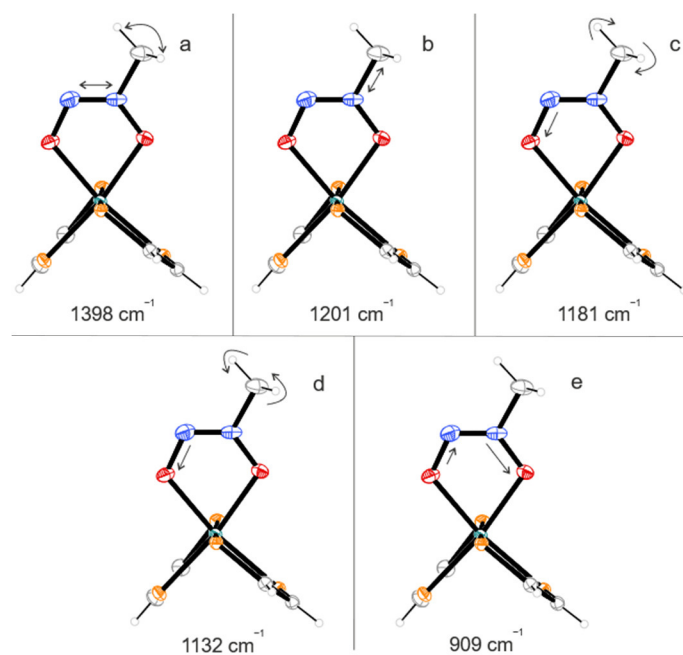


Figure 3.74: Vibrations of the bdd (**42**) ligand in compound **41**. a) asymmetrically coupled stretching vibration of the N–N double bond with scissoring of the CH₂ group b) stretching vibration of the C–N bond, c) symmetrically coupled stretching vibration of the unsubstituted O–N bond with twisting of the CH₂ group d) asymmetrically coupled stretching vibration of the unsubstituted O–N bond with twisting of the CH₂ group e) asymmetrically coupled stretching vibrations of the O–N bonds, whereby the vibration of the O–N bond of the substituted nitrogen is dominant. The values of the different vibrations were taken from quantum-chemical calculations based on DFT. Vibrations of **39** and **40** are similar.

The calculated and experimental IR signals of the bdd ligand of compounds **39–41** are very similar and are given in Table 3.23. The illustration of these vibrations is given in Figure 3.74. The UV/VIS spectra show one signal at 370 nm for **39**, 379 nm for **40** and 365 nm for **41**. These signals are accordance with the pdd compounds **35** and **37** and the hydrogenhyponitrito compounds **28a–30** which are also in the ultraviolet region. The ³¹P{¹H} NMR spectra of **39** and **41** are similar to compound **11** and to the solution spectrum of **28a** (Figures 3.75 and 3.77). The spectra of higher order are analysed as shown for compound **11**, summarised in Table 3.25. The spectrum of compound **40** is shown in Figure 3.76 whose overlapping signals prevent a comparable analysis as for **39** and **41**, but a resemblance is nevertheless detectable. HRMS confirms the formation of the compounds (*m/z* = 1049.23 (C₅₉H₅₅O₂N₂P₄Ru, **39**), 1077.26 (C₆₁H₅₉O₂N₂P₄Ru, **40**), 1045.20 (C₅₉H₅₁O₂N₂P₄Ru, **41**).

Results

Table 3.25: $^{31}\text{P}\{^1\text{H}\}$ NMR signals in DCM at RT and couplings given in parenthesis of compounds **39** and **41**.

	P'		P''		P'''		P''''	
39	55.8 (dd, 11.6 Hz, 21.1 Hz)	55.6 (dd, 11,7 Hz, 21.1 Hz)	55.1 (dd, 13.3 Hz, 21.1 Hz)	54.9 (dd, 13.3 Hz, 21.1 Hz)	50.3 (dd, 11.7 Hz, 21.9 Hz)	48.3 (dd, 11.6 Hz, 21.9 Hz)	44.6 (dd, 13.3 Hz, 21.2 Hz)	42.6 (dd, 13.3 Hz, 21.1 Hz)
					$\nu_{\text{A}} = 49.1 \text{ ppm}, J_{\text{AB}} = 332.1 \text{ Hz (trans-coupling)}$		$\nu_{\text{B}} = 43.8 \text{ ppm}, J_{\text{AB}} = 332.1 \text{ Hz (trans-coupling)}$	
41	66.1 (dd, 6.7 Hz, 19.9 Hz)	65.9 (dd, 7.0 Hz, 19.6 Hz)	65.5 (dd, 8.3 Hz, 20.1 Hz)	65.3 (dd, 8.1 Hz, 20.3 Hz)	56.3 (dd, 6.9 Hz, 20.2 Hz)	54.1 (dd, 6.8 Hz, 20.3 Hz)	53.3 (dd, 8.1 Hz, 19.8 Hz)	51.2 (dd, 8.2 Hz, 19.6 Hz)
					$\nu_{\text{A}} = 54.8 \text{ ppm}, J_{\text{AB}} = 348.3 \text{ Hz (trans-coupling)}$		$\nu_{\text{B}} = 52.8 \text{ ppm}, J_{\text{AB}} = 348.3 \text{ Hz (trans-coupling)}$	

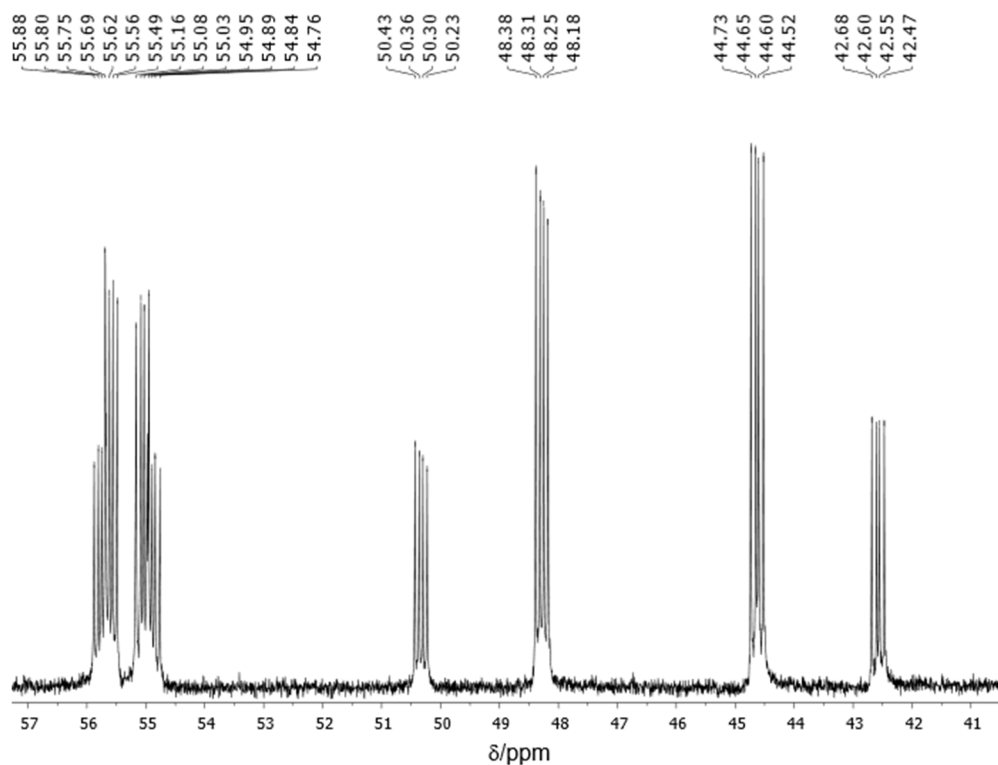


Figure 3.75: $^{31}\text{P}\{^1\text{H}\}$ NMR spectrum of $[\text{Ru}(\text{dppe})_2(\text{bdd})]\text{BF}_4$ (**39**) in CD_2Cl_2 at RT.

Results

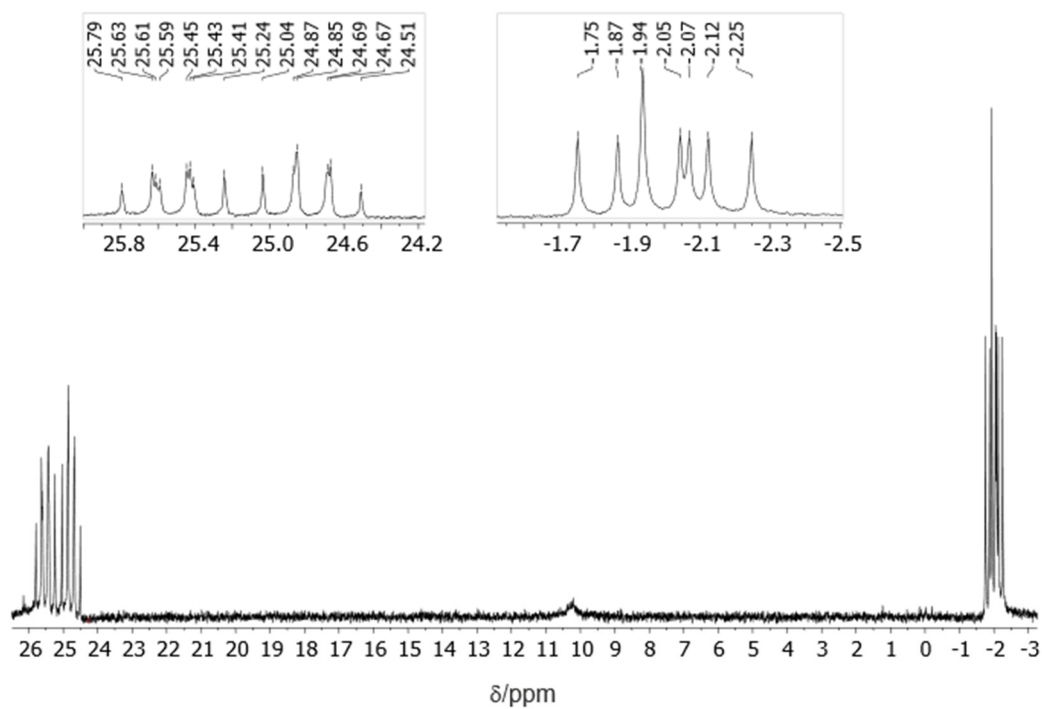


Figure 3.76: $^{31}\text{P}\{^1\text{H}\}$ NMR spectrum of $[\text{Ru}(\text{dppp})_2(\text{bdd})]\text{BF}_4$ (**40**) in CD_2Cl_2 at RT.

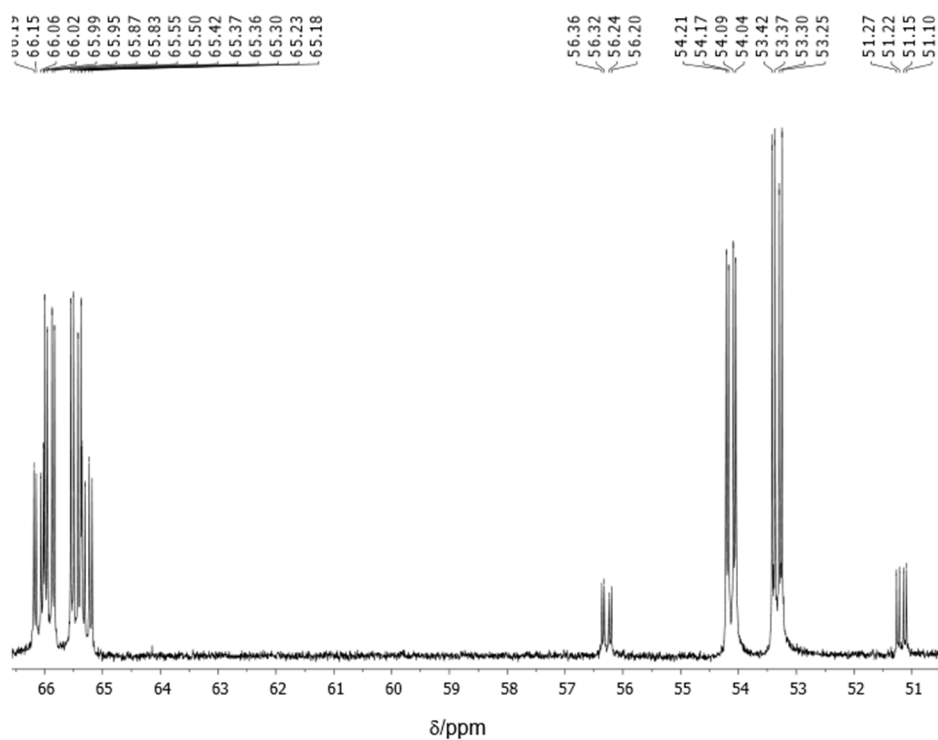
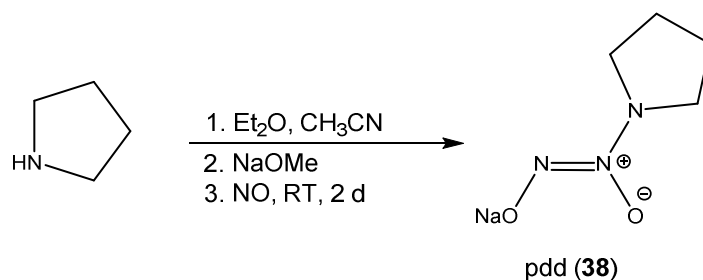


Figure 3.77: $^{31}\text{P}\{^1\text{H}\}$ NMR spectrum of $[\text{Ru}(\text{dppv})_2(\text{bdd})]\text{BF}_4$ (**41**) in CD_2Cl_2 at RT.

3.10 Short excursion: sodium pyrrolidinediazoniumdiolate (38)

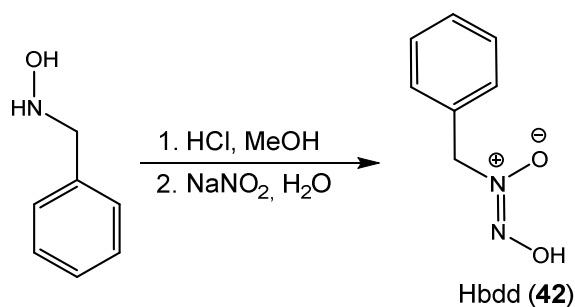
Sodium pyrrolidinediazoniumdiolate was synthesised using the synthesis of Saavedra *et al.*^[180] Freshly prepared sodium methanolate was mixed with pyrrolidine in a pressure flask which was flushed with argon. The mixture was treated with nitrous oxide under intensive stirring. After precipitation of the diolate, the colourless slurry was filtered and washed with diethyl ether and dried *in vacuo* (Scheme 3.14). Even strict evasion of air and especially water and storage at $-4\text{ }^{\circ}\text{C}$ does not prevent the slow decomposition of the product (brown gas, yellowish solid). Therefore, only an ill-defined product was used directly for the synthesis of compounds **35–37**. HRMS and elemental analysis were performed, but did not succeed.



Scheme 3.14: General synthetic procedure for compound **38**.

3.11 Short excursion: hydrogen benzyldiazoniumdiolate (42)

Hydrogen benzyldiazoniumdiolate (**42**) was prepared using the synthesis of Maskill *et al.*^[181] Sodium nitrate solved in water was added dropwise to an ice-cold solution of *N*-benzylhydroxylamine hydrochloride which was solved in methanol and acidified with hydrochloric acid (2M). The resulting fluffy, colourless solid was filtered off, washed with ice-cold water and dried *in vacuo* (Scheme 3.15).



Scheme 3.15: General synthetic procedure for **42**.

Results

Elemental analysis and HRMS ($m/z = 151.05$ ($C_7H_7O_2N_2$)) confirm the formation of this compound. A comparison of the IR spectrum of 42 and the corresponding ruthenium complexes 39–41 emphasise this result (N–O stretching vibration: 947, 1159, 1186 cm^{-1} ; N–C stretching vibration: 1211 cm^{-1} ; N–N stretching vibration: 1395 cm^{-1}). The comparison of the IR spectrum done in this thesis with the spectrum of Kovalchu *et al.* shows resemblance.^[176]

4 Discussion

This subchapter will deal with the crystallographical conditions of the hexaaquaruthenium salts, their classification in terms of the HSAB principle and crystal field model. In the second subchapter the frontier orbitals of the phosphane complexes are analysed. Their reaction mechanism with gaseous nitric oxide is then set up with a focus on the missing hyponitrite compound. The main part of this chapter deals with the *trans*-hydrogenhyponitrito/hyponitrito compounds, especially their preparation, reaction behaviour and their classification in terms of the spectrochemical series. Finally, a similar approach is made for the diazoniumdiolato complexes including their ability to substitute the *cis*-hyponitrite moiety. Most complexes in this work have OC-6 symmetry (IUPAC polyhedral). To simplify the orbital considerations the orbitals are named as for the O_h case (t_{2g} , e_g etc.).

4.1 Hexaaquaruthenium(II) complexes with different counterions

Studies on the hexaaquaruthenium cation were performed for a long time only in dilute solutions.^[26, 182-184] The crystallisation and the resulting crystal structure enabled reactions on a larger scale and an understanding of which attractive interactions enable crystal formation in general.^[10, 28] Essentially, the formation of hydrogen bonds represents the main driving force of the crystallisation of hexaaquaruthenium(II) salts, whereby the tosylato and complex ions are oriented in layers, a motif that is more or less identical for all hexaaqua compounds (**1–6**) in this work. Since, in the original crystal structure of hexaaquaruthenium tosylate from Bernhard *et al.*, no hydrogen positions were determined, but the crystal structure obtained in this work revealed that the hydrogen-bond network saturates the aqua ligands (twelve hydrogen atoms → twelve hydrogen bonds).^[10] This principle is evidently valid for the new synthesised compounds **2–6** (Figure 4.1). In $[\text{Ru}(\text{H}_2\text{O})_6]\text{SO}_4$ (**3**) the sulphate anion can support three instead of two hydrogen bonds which leads to the situation of six donors : twelve hydrogens : four acceptors (SO_4^{2-})—a known characteristic in literature.^[185] Compound **5** which includes a sterically demanding biphenyldisulfonate anion compensates this fact with two molecules of crystal water. Additionally, the graph-set analysis elucidates the tight hydrogen-bond network over the different layers of cationic complexes and the counterions in compounds **1–6**. The Ru–O average distance and the angles between the aqua ligands and the ruthenium centre (O–Ru–O') are almost unaltered, whereby higher values for distances are obtained, as expected, for room temperature measurements instead of cryogenic ones. ^{17}O NMR measurements confirmed the given value for $[\text{Ru}(\text{H}_2\text{O})_6]^{2+}$ and showed, additionally, the signal for the tosylate counter-ion.^[186] UV/VIS studies showed that, both in solid-state and in solution, independent of the pH in the acidic area, the hexaaquaruthenium complex is present as shown in Figure 4.1.^[11]

Discussion

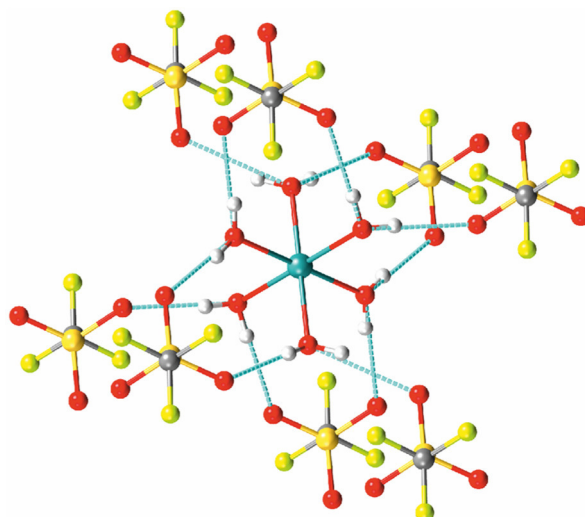
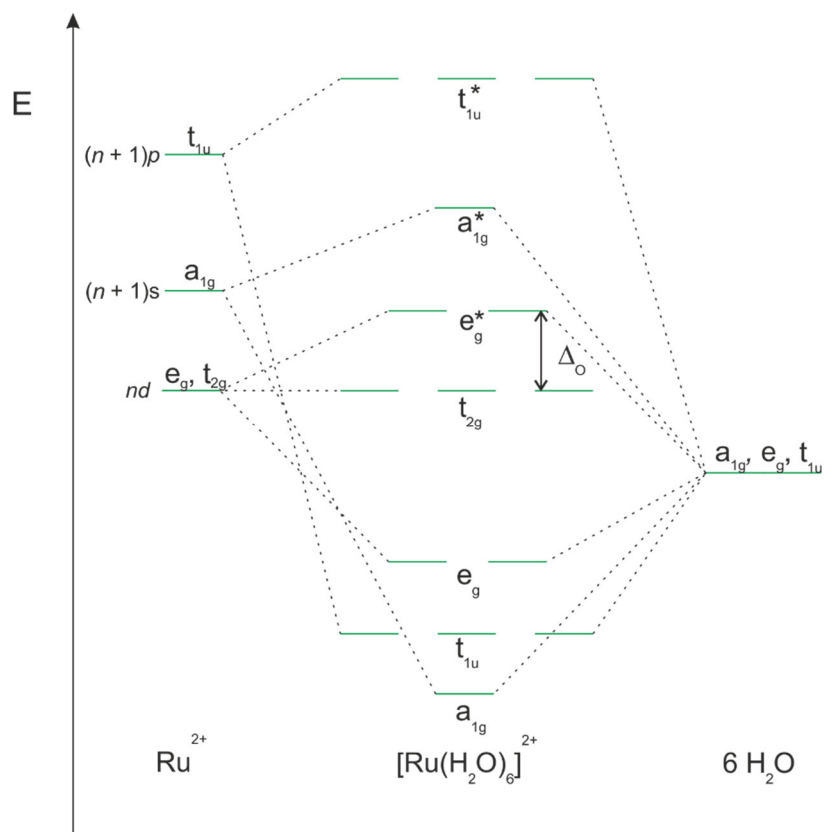


Figure 4.1: The hydrogen-bond network of $[\text{Ru}(\text{H}_2\text{O})_6](\text{OTf})_2$ (**2**). Grey: carbon, white: hydrogen, cyan: ruthenium, green-yellow: fluorine, blue lines: hydrogen bonds.

Regarding Pearson's HSAB concept, a combination of hard (high charge density, small atomic radius, less polarisable) and soft (low charge density, big atomic radius, easy polarisable) Lewis acids and bases is disfavoured in terms of reactivity and bond strength than the soft-soft (covalent case) and hard-hard (ionic case) combination.^[58] Nonetheless, this empirical concept has limitations as for example the reaction of the hard acid H^+ and the soft base H^- shows ($\text{H}^+ + \text{H}^- \rightarrow \text{H}_2$). Modern explanations emphasise the importance to considerate the acidity/basicity beside the hardness/softness of the components, as well.^[187] In coordination chemistry, large ligands with low charge and low electronegativity stabilise metal centres in low oxidation states, whereby high-valent metal centres are stabilised by the contrary.^[58] Therefore, it is not surprising that the synthesis of $[\text{Ru}(\text{H}_2\text{O})_6]^{2+}$ with a soft ruthenium(II) centre and has to be done in the strict absence of potential ligands other than sulfonic acid and water. Chloride impurities, for example, react immediately with the hexaaqua ion forming tentative chlorido complexes which are thermodynamically more favoured (brown colour of the otherwise pink solution). Nonetheless, it should be mentioned that $[\text{Ru}(\text{H}_2\text{O})_6]^{2+}$ can be prepared—as previously described—in diluted form using chlorido products, but only by the strict separation of the chlorido-product derivatives *via* ion exchange.^[26, 182] Also, the elucidation of the reaction pathway with small molecules and the kinetics delivers a valid explanation for the reaction behaviour of the complex.^[14] Aebischer *et al.* discovered that complex formation starts with a Ru–O bond rupture (dissociative interchange mechanism) which is, therefore, the rate-determining step.^[14, 155] Strong π -acceptor ligands clearly decrease the activity of the *cis*-standing aqua ligand, but increase it for the *trans*-standing one. Each step of water substitution slows down the reaction.^[14, 188] With a rate constant of $1.8 \cdot 10^{-2} \text{ s}^{-1}$ for water exchange of the first coordination sphere (inner-sphere interchange rate constant) for $[\text{Ru}(\text{H}_2\text{O})_6]^{2+}$,

the fast reaction with amines and halogens can be explained. If the Ru–O bond breaks as the first step, the vacant coordination site can easily be occupied by a π -base halogen or a σ -donor amine.^[189] An octahedral complex with an unoccupied coordination site due to ligand dissociation has fewer negative point charges which repulse the d-electrons of ruthenium. The now diminished crystal-field splitting ($\downarrow\Delta_o$) results in a reduced ligand field stabilisation energy. The energy loss can be assigned as the activation energy of the ligand substitution and its magnitude is directly correlated to the ligand exchange rate, independent of the thermodynamics of the newly formed bond. In the case of $[\text{Ru}(\text{H}_2\text{O})_6]^{2+}$ the t_{2g} orbitals which are non-bonding for pure σ -donors are filled with six electrons resulting in a ligand-field stabilisation energy of $-2.4 \Delta_o$. In the case of an aqua-ligand-bond dissociation the relative Δ_o is reduced (Scheme 4.1).^[190] This leads to the second subchapter, the reaction of hexaaquaruthenium(II) phosphanes with diverse phosphanes.



Scheme 4.1: Qualitative energy-level scheme. Electron distribution of $[\text{Ru}(\text{H}_2\text{O})_6]^{2+}$: $a_{1g}^2 t_{1u}^6 e_g^4 t_{2g}^6$.

The crystal structure of **1** resulted in a different crystal system and, therefore, in another space group compared to the former crystal structure of $[\text{Ru}(\text{H}_2\text{O})_6](\text{tos})_2$ (Table 4.1).^[10] In addition to the previously mentioned characteristics, compound **3** is the first 4d representative of the hexahydrate mineral group. As shown in Table 4.2, the unit-cell parameters and the number of units in the unit cell are in good accordance with the given values.

Table 4.1: Comparison between published and obtained crystal structure data of $[\text{Ru}(\text{H}_2\text{O})_6](\text{tos})_2$ (**1**).^[10]

$[\text{Ru}(\text{H}_2\text{O})_6](\text{tos})_2$		
	Reference 10	obtained 1
space group	$\bar{1}$	$C2/c$
$a/\text{\AA}$	6.318(1)	14.0088(7)
$b/\text{\AA}$	7.287(2)	6.2999(3)
$c/\text{\AA}$	12.423(4)	24.9685(14)
$\alpha/^\circ$	92.22(2)	90
$\beta/^\circ$	94.82(2)	100.545(5)
$\gamma/^\circ$	107.13(2)	90
$V/\text{\AA}^3$	527.9(4)	2166.3(2)

Table 4.2: Representatives of the hexahydrate mineral group including compound **3**. (crystallographic information files obtained from the ICSD database). The mentioned structures were solved in the $C2/c$ space group.

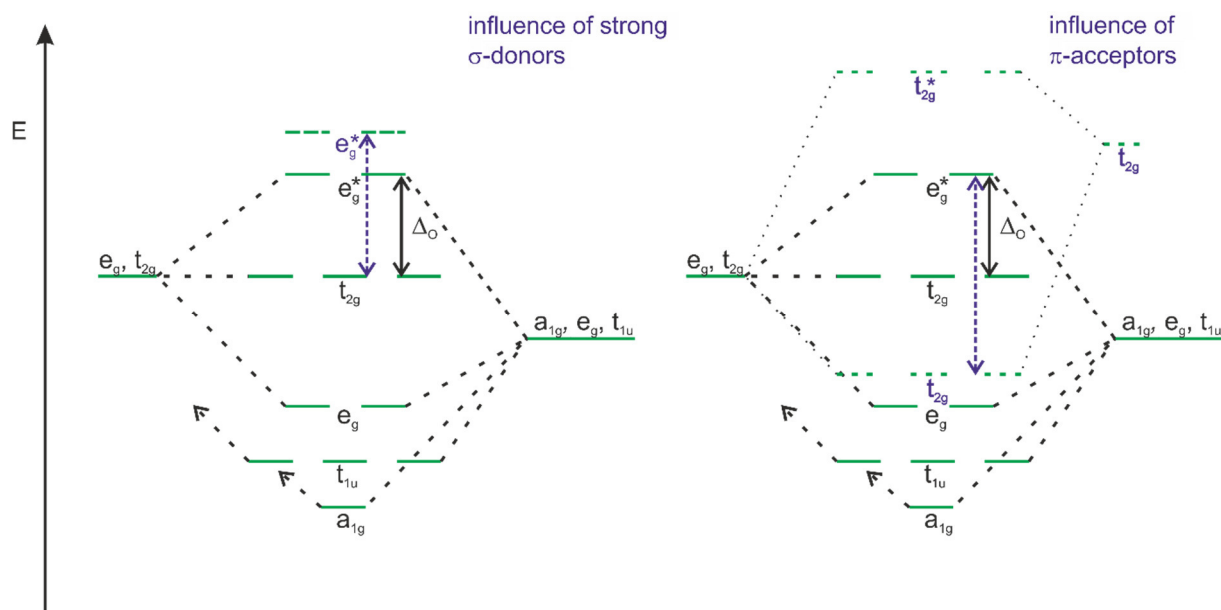
chemical formula	common name	$a/\text{\AA}$	$b/\text{\AA}$	$c/\text{\AA}$	$\beta/^\circ$	Z
$[\text{Mg}(\text{H}_2\text{O})_6]\text{SO}_4$ ^[191]	Hexahydrate	10.11(5)	7.212(4)	24.41(1)	98.30(5)	8
$[\text{Co}(\text{H}_2\text{O})_6]\text{SO}_4$ ^[192]	Moorhouseite	10.022(3)	7.217(2)	24.224(3)	98.42(2)	8
$[\text{Ni}(\text{H}_2\text{O})_6]\text{SO}_4$ ^[193]	Nickelhexahydrate	9.878(2)	7.214(2)	24.065(6)	98.37(2)	8
$[\text{Zn}(\text{H}_2\text{O})_6]\text{SO}_4$ ^[194]	Bianchite	9.981(2)	7.250(9)	24.280(3)	98.45(7)	8
$[\text{V}(\text{H}_2\text{O})_6]\text{SO}_4$ ^[195]	–	10.081(3)	7.286(2)	24.445(7)	98.78(2)	8
$\text{FeSO}_4 \cdot 6(\text{H}_2\text{O})$ ^{[196] a)}	Ferrohexahydrate	10.08	7.28	24.59	98.37	8
$[\text{Ru}(\text{H}_2\text{O})_6]\text{SO}_4$ (3)	–	9.6832(4)	7.3250(3)	24.023(1)	98.113(1)	8

a) cif without standard deviation

4.2 Phosphaneruthenium ligands – between strong σ -donors and σ^* -acceptors

As described in the introduction, phosphanes are capable of either σ^* -back donation or strong covalent contributions, resulting in two different energy level schemes shown in Scheme 4.2. It is unlikely that a triphenylphosphane complex with no strong acceptors attached to the phenyl rings is capable of π -backbonding, more likely this and similar ligands interact as σ -donors with the metal centre. This argument is supported by DFT calculations. Since PPh_3 mainly classified as σ -donor, the HOMO orbitals of the complex $[\text{Ru}(\text{H}_2\text{O})_2(\text{PPh}_3)_2(\text{tos})_2]$ (**18**) display metal-centred non-bonding t_{2g} orbitals (Figure 4.2).^[187] An observation of metal-ligand π -bonds and intraligand π -antibonds which would indicate a

π -acid activity is not made. The σ -donor activity is similarly observed for the phosphanes and bisphosphanes with pure carbon moieties attached to the phosphorus atom.^[187] In contrast, the bisphosphanes with nitrogen moieties show a substantial amount of σ^* -backbonding (Figure 4.3).



Scheme 4.2: Qualitative energy level scheme of strong σ -donors on the left side and π -acids capable of π^* -backdonation on the right side. For strong σ -donors the splitting of e_g and e_g^* is increased, while for π -acids the previous non-bonding t_{2g} orbitals are split due to interaction with the empty π^* -orbitals (σ^* -orbitals) of the ligand. The electron distribution of e.g. $[\text{Ru}(\text{dppe})_2(\text{tos})]^{2+}$ is $a_{1g}^2 t_{1u}^6 e_g^4 t_{2g}^6$, therefore in both cases only the energetically is favoured t_{2g} orbital occupied.

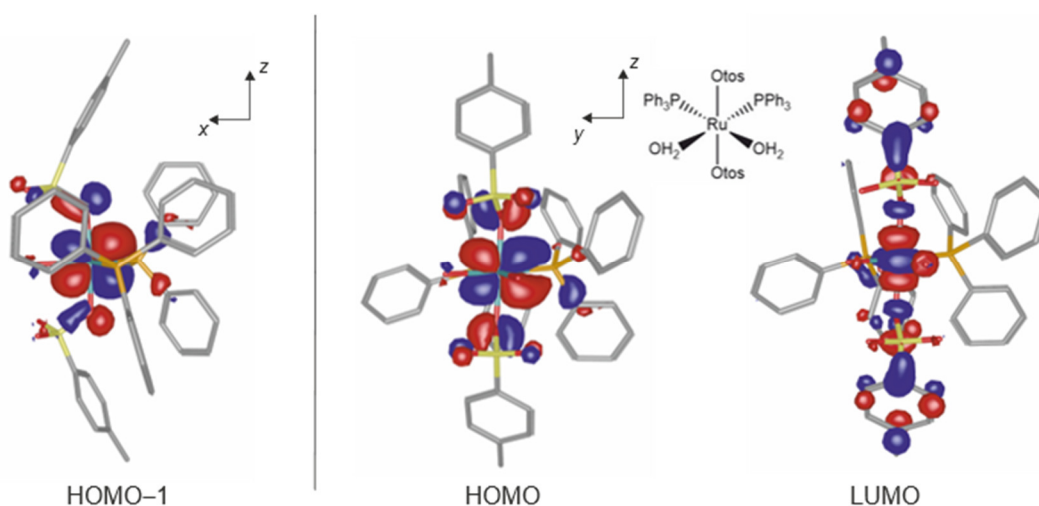


Figure 4.2: Gabedit plot of the frontier orbitals (isovalue 0.02) of $[\text{Ru}(\text{H}_2\text{O})_2(\text{PPh}_3)_2(\text{tos})_2]$ (**18**).^[197] HOMO-1 (xz) and HOMO (yz) as part of the t_{2g} molecular orbital set. LUMO (unoccupied, z^2) as part of the virtual e_g orbitals. The occupied orbitals show mainly metal-centred, non-bonding orbital lobes.

Discussion

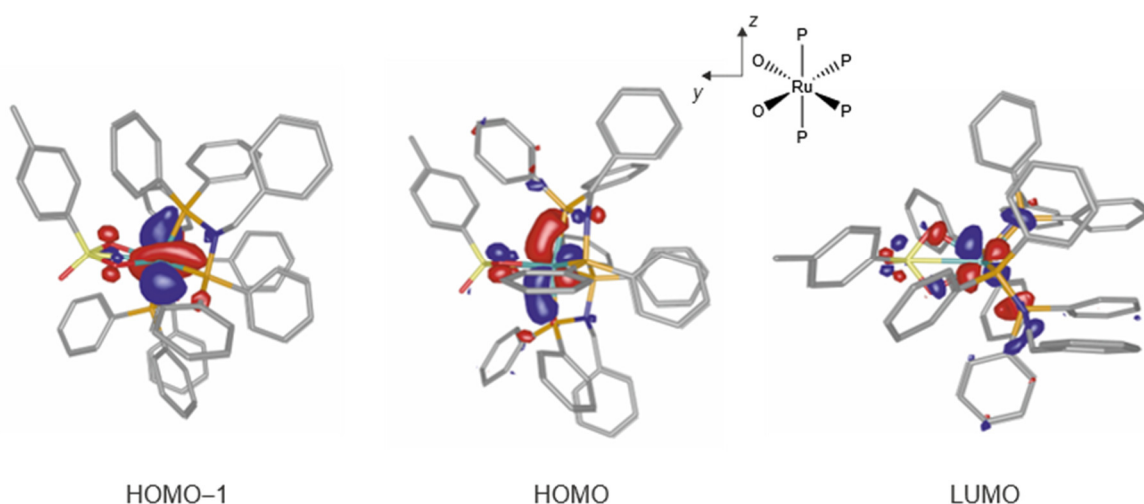


Figure 4.3: Gabbit plot of the frontier orbitals (isovalue 0.04) of $[\text{Ru}(\text{dppbza})_2(\text{tos})]^+$ (**9**).^[197] HOMO-1 (z^2 -like shaped) and HOMO (yz) as part of the t_{2g} molecular orbital set. LUMO (unoccupied, xy) as part of the virtual e_g orbitals. The occupied orbitals show metal-ligand π -bonds with intraligand π -antibonding.

It is evident that the occupied HOMO and HOMO-1 orbitals show π -bonding between the ruthenium centre and the bisphosphane (dppbz, **21**) ligand. The LUMO which is part of the virtual e_g orbitals has a metal-centred orbital that is antibonding to the phosphane ligand. A similar behaviour can be expected for the complexes with the other aminophosphane ligands dpppha (**22**) and dpppra (**23**) as σ^* -acceptors. As in Scheme 4.2, an increased Δ_0 and therefore an increased LFSE is the result of both strong σ -donors and σ^* -acceptors. A classification using the bite angle P-Ru-P is not significant (Table 4.3). Even though a classification of the complexes obtained is desirable, the combination of electronic and steric effects (bite angle and steric hindrance) of the phosphane ligands are not suitable for an overall explanation of the complex formation of **7-20**. Nonetheless, these complexes can be used as powerful precursors due to the labile water and tosylato ligands they bear.

Table 4.3: P–Ru–P bite angles in the phosphane complexes **7–20**.

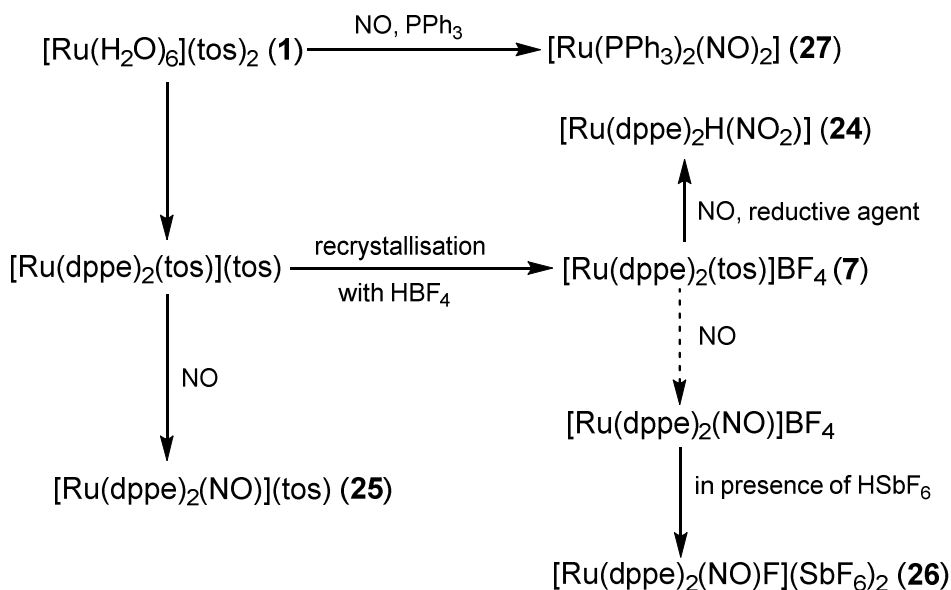
	sulfonato- κ^2O,O' complexes			disulfonato- κ^2O,O' complexes		
	7	8	10	11	12	
P–Ru–P angle	81.42(3),	88.55(3),	81.44(3),	96.66(2)	95.85(2)	
	81.80(3)	89.40(3)	82.07(3)			
$\alpha/^\circ$	diaqua complexes			aqua-tosylato- κO complexes		
	14	15	16	18	19	
	72.34(4)	80.44(3)	82.34(1)	98.05(2)	88.71(2)	
	20		aminephosphane complexes:			
			9 (sulfonato- κ^2O,O')	13 (diaqua)	17 (aqua-tosylato- κO)	
			69.96(3), 69.24(3)	69.02(2)	69.60(2), 69.34(2)	
	97.92(2)					

4.3 Treatment of $[\text{Ru}(\text{dppe})(\text{tos})]^{2+}$ (**7**) with NO

Since there is a broad interest in literature for reductive coupling of nitric oxide at model complexes of the nitric oxide reductase, the previously mentioned phosphane complexes were treated with NO.^[95, 97, 103, 198] Compound $[\text{Ru}(\text{dppe})_2(\text{tos})]^{2+}$ (**7**) was chosen as the model complex, whereby the two other compounds (**8** and **16**) that are capable of binding a hydrogenhyponitrito or hyponitrito ligand (chapter 4.4) were treated with nitric oxide as well. However, they did not crystallise which was necessary for a deeper and profound understanding of the reaction pathways.

As previously shown, in the absence of a reductive agent, two products form over time. Compound $[\text{Ru}(\text{dppe})_2(\text{NO})(\text{tos})]$ (**25**) which is obtained in the absence of a BF_4^- anion and $[\text{Ru}(\text{dppe})_2(\text{NO})\text{F}](\text{SbF}_6)_2$ (**26**) which is obtained in the presence of BF_4^- or SbF_6^- . It is clearly evident, that compound **26** is a derivative of **25**, as the latter is obtained exclusively in the absence of a fluoride donor. It is likely that the remaining NO acts thereby as oxidant, but since the amount of complex consumed is small and the reaction itself lengthy, no spectroscopic evidence was found. In the presence of a reductive agent, compound $[\text{Ru}(\text{dppe})_2(\text{H})(\text{NO}_2)]$ (**24**) is formed, but only in the simultaneous presence of water. Different apparatuses with and without wash bottles were used, whereby **24** was obtained only with the first and **25** in the latter. It is likely that the H_2O impurities are deprotonated by the tetrakisdimethylaminoethylene (tden) reductive agent and the hydroxide ion reacts as nucleophile with the NO^+ ligand of the ruthenium complex as known in literature.^[199] The vacant *trans* position of

the nitrite ligand is then occupied by a hydrido ligand, which can be confirmed by a Difference-Fourier analysis. An overview of the tentative, simplified reaction mechanism is given in Scheme 4.3.



Scheme 4.3: Reaction pathway from $[\text{Ru}(\text{H}_2\text{O})_6]^{2+}$, over $[\text{Ru}(\text{dppe})_2(\text{tos})]^+$ to different NO derivatives.

Finally, the question arises, whether there is a hyponitrito ligand present or not. Since both a hydrogenhyponitrito and a hyponitrito complex could be obtained, the characteristic orange/yellow colour of such compounds was not visible at any time. Additionally, the crystalline products (with powdery residue) showed no sign of hyponitrite in the respective IR spectra. No crystallisation occurred beside the previously mentioned products, although the hydrogenhyponitrito/hyponitro complexes are stable and tend to crystallise easily. Nonetheless, as there is no negative proof, it is only an indication of the absence of a hyponitrite moiety. In literature, the metal-centred reduction of nitric oxide is favoured. Most of the time, two low-valent metal centres provide two electrons for the reductive coupling of gaseous nitric oxide.^[95, 97, 103] The ruthenium centre of the phosphane complexes used in this work is probably too stable in the oxidation state of +II, especially since the examples of hyponitrite formation using gaseous nitric oxide at ruthenium centres were Ru(I) complexes.^[99, 105]

As shown in Scheme 4.3, the reactivity towards NO is also given for hexaaquaruthenium which forms in the presence of PPh_3 and NO the $\{\text{Ru}(\text{NO})_2\}^{10}$ complex $[\text{Ru}(\text{PPh}_3)_2(\text{NO})_2]$. In terms of its electronic status the formation of a hyponitrito ligand is possible ($[\text{Ru}(\text{PPh}_3)_2(\text{NO})_2] \rightarrow [\text{Ru}(\text{PPh}_3)_2(\text{N}_2\text{O}_2)]$) as shown for $[\text{Pt}(\text{PPh}_3)_2(\text{N}_2\text{O}_2)]$, but it is evidently not favoured.^[98] It has to be mentioned that in general, the reactivity of the phosphane complexes and $[\text{Ru}(\text{H}_2\text{O})_6]^{2+}$ towards NO is of a rather chaotic nature. A broad range of products was obtained which are not displayed in this work due to rather poor data sets. This concerns dinitrosyl complexes with or without oxidised phosphane ligands (*e.g.* with PPh_3 or P^tBuPh_2), and mononitrosyl complexes (*e.g.* with dpppha).

4.4 Hydrogenhyponitrito and hyponitrito complexes

— products of salt metathesis

To avoid product mixtures which are hard to purify for obtaining hyponitrito complexes, a different approach was taken. As already shown, silver hyponitrite or hyponitrous acid were successfully used to generate hyponitrito complexes.^[103-104] Therefore, the triphenylstannyl hyponitrite compounds which were originally synthesised by Beck *et al.*, reacted well with the phosphane complexes in this work (**7**, **8**, **16**), but only with these three.^[175,200] Experiments with the remaining phosphane complexes were unsuccessful. Nonetheless, the hydrogenhyponitrito complexes are exceptionally stable and can flexibly be protonated and deprotonated. A tentative reason for this could be the sterically demanding phenyl groups which form, thereby, a protective pocket that encases the hydrogenhyponitrite/hyponitrite moiety (Figure 4.4).

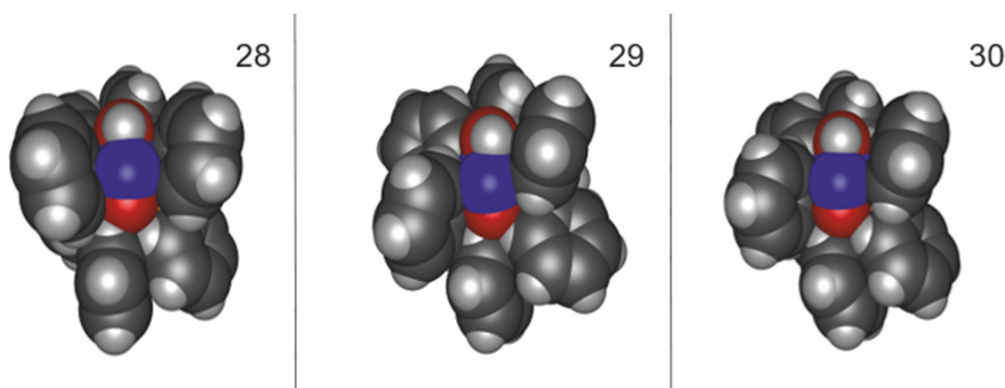


Figure 4.4: Space-filling models of compounds **28**, **29**, **30** (Gabedit).^[39, 197]

Additionally, the “pocket” is visualised by a comparison between the starting complex and the hydrogenhyponitrite product. As seen in Figure 4.5, the hydrogenhyponitrito and tosylato ligands are, in terms of bond distances and angles, similar. Also, the hydrogenhyponitrito and hyponitrite complexes (**28–33**) form hydrogen bond networks as seen in Figure 4.5, which are discussed in literature as key components for the formation of hyponitrito complexes in general.^[103, 201] It is likely that this combination of steric protection, steric similarity and hydrogen bond networks favours the formation and crystallisation of these complexes.

A classification of the hyponitrite moiety as weak-field or strong-field ligand was part of our publication.^[39] The frontier orbitals show characteristics of σ -donors and π -bases. Figure 4.6, in which z lays on the P–Ru–P axis (left), shows the LUMO (centre) and the HOMO (right). The virtual LUMO consists of the e_g -derived N/O–Ru σ -antibond and the Ru- $d(x^2-y^2)$ orbital as the metal part. Two of the three occupied frontier MOs, specifically the HOMO–1 and the HOMO–2, show mainly Ru- d -character in agreement with the σ -character of the Ru–P interactions. The HOMO is made up from the HOMO–1 of the free hydrogenhyponitrito ligand in an antibond to the remaining t_{2g} -derived orbital. Specifically,

with the axes chosen in Figure 4.6 (left), the HOMO was a linear combination of $d(xz)$ and $d(yz)$ (Figure 4.6, right). Thus, with its antibond between the metal orbital and an occupied ligand-MO, the HOMO reflects π -donor properties of the HN_2O_2^- ligand. The intraligand- π -MO contribution to the HOMO is N–N bonding but has nodes to both participating oxygen-p-AOs.).^[39]

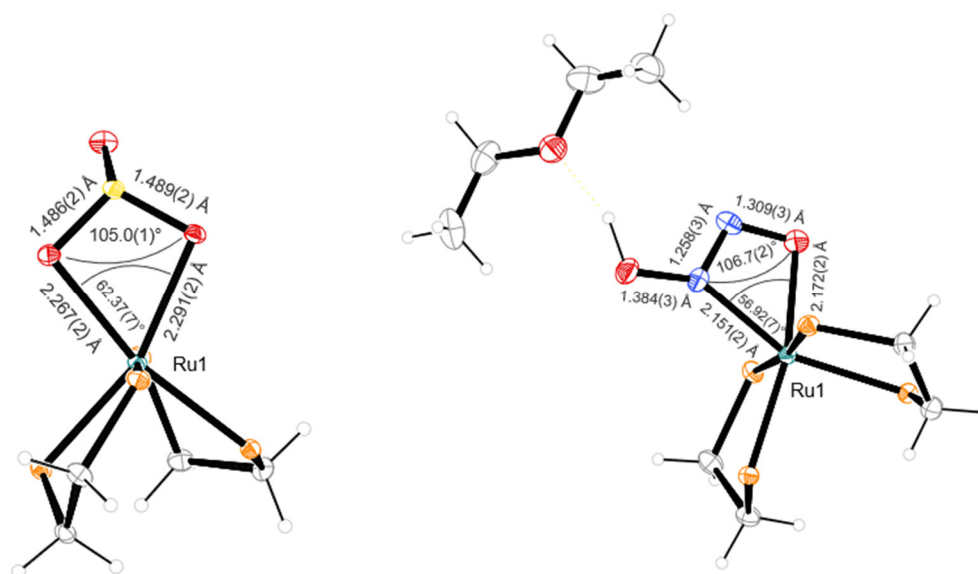


Figure 4.5: Comparison between selected bond angles and distances of the labile tosylato ligand of **7** (left) and the hydrogenhyponitrito ligand of **28** (right) which replaces it.

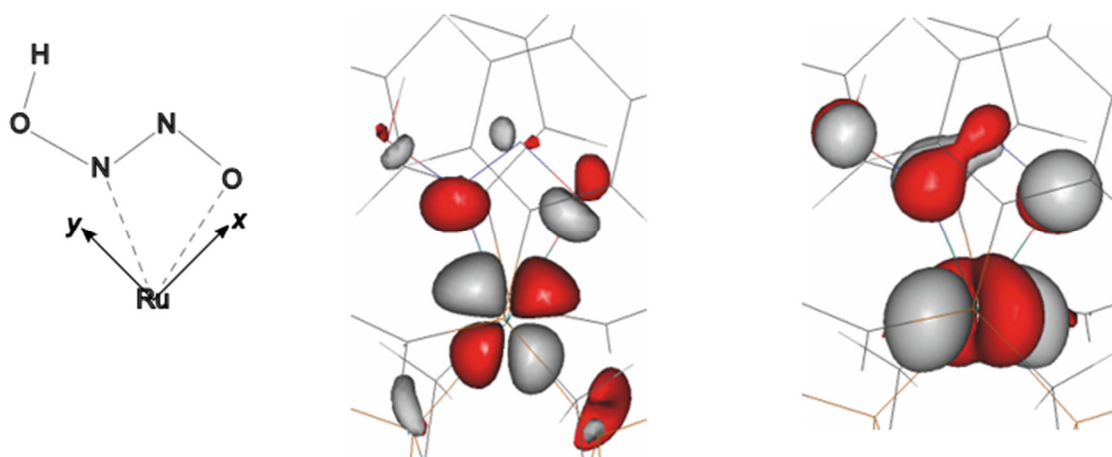


Figure 4.6: Gabedit plot of the frontier orbitals of **28** (isovalue: 0.05).^[197] Top: choice of the Cartesian axes (z towards the observer); centre: the LUMO; bottom: the HOMO.^[39]

The irradiation of the hyponitrite complexes **28**, **29**, **30** and their corresponding hyponitrite complexes **31** and **32** with ultraviolet light showed that these complexes can react to a nitric oxide species (confirmed by the crystallised compounds **25**, **36**) and release N_2O as well. The proposed mechanism described previously reveals a plausible pathway. Therefore, the compounds react on the one hand like *trans*-hyponitrite salts which release N_2O if irradiated (investigated by Chacón Villalba *et al.*) and, on the other hand, like diazoniumdiolates that release NO under the same conditions.^[202-204]

4.5 Diazoniumdiolato complexes—a replacement for *cis*-N₂O₂²⁻

Due to orbital interactions the *cis*-hyponitrous acid is less stable than the *trans* analogue. As seen in Figure 4.7, the donation of the nitrogen lone pair into the $\sigma^*(\text{N}-\text{O})$ lowers kinetic stability due to the weakening of the N–O bond favouring N₂O release.^[94]

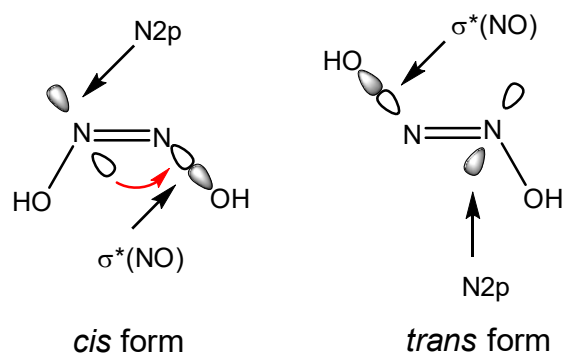


Figure 4.7: Interaction of the nitrogen lone-pair with the $\sigma^*(\text{N}-\text{O})$ orbital in hyponitrous acid.^[94, 201]

As a consequence of this intramolecular lability, *cis*-hyponitrite salts exhibit explosive behaviour which is probably triggered by impact or shock. Also, there are no substituted derivatives of *cis*-hyponitrite known.^[94] Therefore, a safer method for using diazoniumdiolato ligands was performed to get insight to see whether a *cis*-hyponitritoruthenium complex is possible.

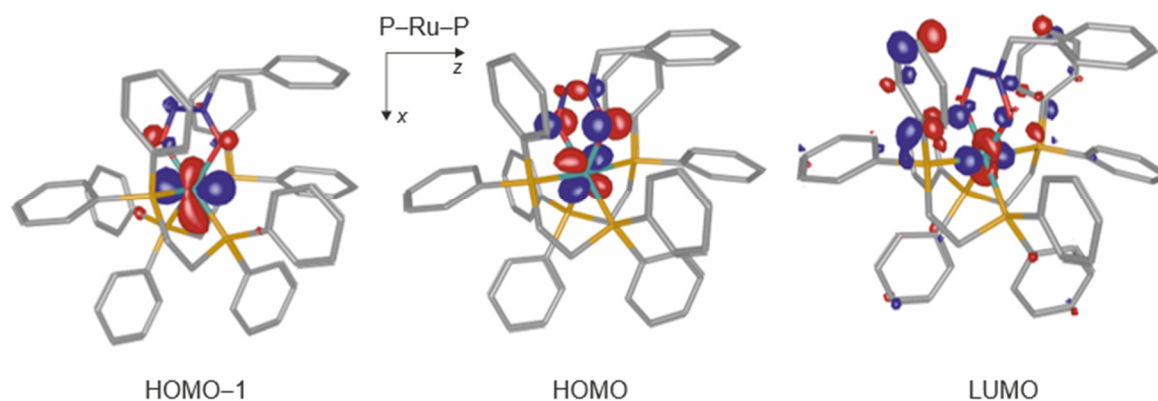


Figure 4.8: Gabbit plot of the frontier orbitals (isovalue 0.05) of [Ru(dppe)₂(bdd)]⁺ (**39**).^[197] HOMO-1 (x^2-y^2 -like shaped) and HOMO (xz) as part of the t_{2g} molecular orbital set. LUMO (unoccupied, z^2 -like shaped) as part of the virtual e_g orbitals.

A classification of the diazoniumdiolato ligand, as made for *trans*-hyponitrite, is given in Figure 4.8. The occupied orbitals are metal-centred with metal-ligand π -antibonds as well. Any π -acceptor characteristics are not observable. Similar observations are made for compounds **37**, **40**, **41**. Therefore, the diazoniumdiolato ligands can be characterised as mainly σ -donors with π -donor capability (weak-field ligands).

Discussion

Most *C*- and *N*-diazoniumdiolates are formed under basic conditions due to instant decomposition under acidic conditions.^[107] In general, the decomposition of diazoniumdiolates can be accomplished either by photoexcitation or by the addition of an electron pair acceptor such as H⁺ for example.^[203, 205] Therefore, the reaction and crystallisation of the starting complexes **7**, **8**, **16** was successful only, if these compounds were crystallised before in the presence of tetrafluoroboric acid. In comparison, *C*-diazoniumdiolates are far more stable than *N*-diazoniumdiolates due to the better stabilisation of the N₂O₂ moiety. Also, the substitution of the terminal oxygen atoms is more established with even protonated *C*-diazoniumdiolates obtainable as in compound **42**.^[107, 206] In contrast to their unstable behaviour in their salt form, the *N*-diazoniumdiolato ligands are as stable in their corresponding complexes (**35**, **37**) as their *C*-diazoniumdiolato counterparts (**39–41**), which could also result from the phenylgroup protection (Figure 4.9).

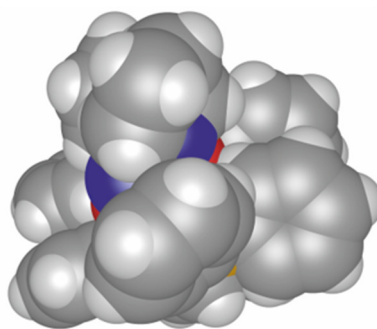


Figure 4.9: Space-filling model of compounds **37** (Gabedit).^[197]

With the dppp co-ligand, compound [Ru(dppp)₂(NO)]BF₄ (**36**) was obtained instead of the *N*-diazoniumdiolato complex. Nitric-oxide release of diazoniumdiolates is well known in literature, but formation of a nitrosyl complex after adding a diazoniumdiolato ligand probably represents a novelty.^[117, 204] The reactivity of compound **8** towards the *N*-diazoniumdiolato **38** is probably explained best by the higher σ -donor capability as indicated by the high-field-shifted ³¹P{¹H} NMR signals compared to **7** and **16**. The higher electron density presumably promotes the reverse reaction from pyrrolidinediazoniumdiolate back to nitric oxide (pdd → 2NO + pyrrolidine). The involved antibonding orbitals of the N=N double bond of compound **37** (as model for **36**) which have to be occupied are part of the LUMO+3 and therefore, as a tentative part of the energetically disfavoured *t*_{1u}* orbital sets, unavailable. Shaik *et al.* emphasised the stabilisation of the N₂O₂-moiety through the substituent on the nitrogen and the bond cleavage as the rate-determining step for the decomposition.^[205] Therefore, it is more likely that the antibonding orbitals between the pyrrolidine and the N₂O₂ moiety which are part of the HOMO of **37** (Figure 4.10) are affected by the previously mentioned higher basicity of the dppp ligand, resulting in a borderline situation between the dppe and dppv compounds **35**, **37** and NO

Discussion

compound **36**. The remaining N_2O_2 moiety decomposes and the emitted nitric oxide coordinates to the ruthenium centre.

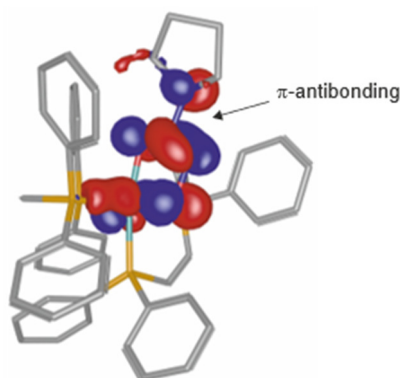


Figure 4.10: Gbedit plot of the HOMO (isovalue 0.04) of $[\text{Ru}(\text{dppv})_2(\text{pdd})]^+$ (**37**).^[197]

5 Summary

The first part of this work deals with the descriptive analysis of hexaaquaruthenium salts. An alteration of the original work made a synthesis possible which is best described as an avoidance of the ion-chromatography step in order to obtain $[\text{Ru}(\text{H}_2\text{O})_6](\text{tos})_2$ (**1**).^[10] A reproduction of the ^{17}O NMR signal of the complex cation was possible whereby the signal of the tosylate anion was added. A comparison of solid-state and solution UV/VIS spectroscopy—in solution with or without toluenesulfonic-acid addition—revealed that in all three cases the hexaaquaruthenium cation is present as shown in Figure 5.1.

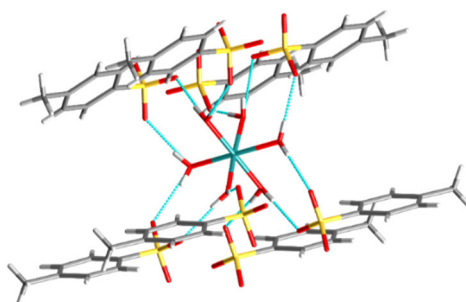


Figure 5.1: Hexaaquaruthenium tosylate (**1**); visualisation of the hydrogen bond saturation.

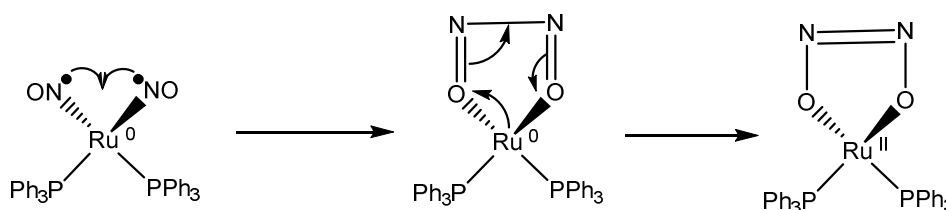
Five new hexaaquaruthenium compounds **2–6** such as the highly soluble hexaaquaruthenium triflate (**2**) and hexaaquaruthenium sulphate (**3**) being the first 4d version of the hexahydrate mineral group have been synthesised. Graph-set analysis revealed similar patterns for the hexaaquaruthenium compounds confirming the assumption on full occupation of all hydrogen bond positions. The mesitylsulfonate compound **6** was tested beside compound **1** for two phosphane complexes and resulted with respect to the coordination in identical complexes (**7** and **10, 11, 12**).

The treatment of hexaaquaruthenium tosylate (**1**) (or **6**) as a precursor resulted in six phosphane compounds with tosylato- $\kappa^2\text{O},\text{O}'$ ligand (**7–12**), four diaquaphosphane complexes (**13–16**) and four borderline complexes with aqua and tosylato ligands (**17–20**). As introduced, compounds **7–12** are the first crystal structures of tosylato- $\kappa^2\text{O},\text{O}'$ ruthenium complexes synthesised representing the rare compounds with chelating sulfonato ligands in general. It was possible to obtain two mononuclear ruthenium compounds (**10** and **12**) with two chelating tosylato ligands which had been unknown in this coordination form. Compound **14**, the *trans*-diaqua form of the originally published *cis*- $[\text{Ru}(\text{dppen})_2(\text{H}_2\text{O})_2]$ by Bickley *et al.* was obtained as a tosylate salt.^[47] Compounds **13, 15, 16** are tetrafluoridoborate salt analogues of **14**. Apart from X-ray-crystallographic analysis, the comparison between calculated and empirical IR spectra confirmed the formation of all these compounds and

Summary

made an illustration of the respective vibrations possible. $^{31}\text{P}\{^1\text{H}\}$ NMR and UV/VIS spectroscopy were further used to complete the analytic data for the newly synthesised compounds.

The synthesis of hyponitrito complexes by the treatment of compound **7** as the model complex with nitric oxide was not possible in the context of the experiments shown. The $\{\text{RuNO}\}^8$ complex $[\text{Ru}(\text{dppe})_2(\text{NO})]\text{BF}_4$ (**25**) is the main derivative of this reaction and is formed independently of the NO concentration. In the presence of excess nitric oxide and a fluoride donor, compound **26** is formed. Compound **24** was obtained by adding a reducing agent to the mentioned NO set-up whereby this nitrite hydride complex emerges. Compound **24** is obtained solely in the presence of traces of water indicating a reaction taking place of both, hydroxide with the NO^+ ligand and a reaction of the ruthenium centre as hydride catalyst with the resulting hydrogen. A reaction of the more reactive hexaaquaruthenium with nitric oxide in the presence of PPh_3 results in a $\{\text{Ru}(\text{NO})_2\}^{10}$ compound **27**, which is theoretically able to form a hyponitrite complex in terms of the electronic state (Scheme 5.1) such as the reaction of $[\text{Pt}(\text{PPh}_3)_2(\text{NO})_2]$ to $[\text{Pt}(\text{PPh}_3)_2(\text{N}_2\text{O}_2)]$.^[98] A Difference-Fourier analysis was performed for compound **24** to ensure the assignment of the hydrido ligand. For compounds **25–27** IR spectroscopy and $^{31}\text{P}\{^1\text{H}\}$ NMR spectroscopy complete the analytical data of the compounds.



Scheme 5.1: Possible, simplified formation of a ruthenium hyponitrite complex from compound **27**.

In contrast to the previous reactions, it was possible to obtain the first mononuclear *trans*-hydrogenhyponitrito ruthenium compounds with dppe (bis(diphenylphosphanyl)ethane), dppp (bis(diphenylphosphanyl)propane) and dppv (bis(diphenylphosphanyl)ethene) (**28a–30**) by using salt metathesis and subsequent protonation (example **29** in Figure 3.41 and 5.2 left). The previously formed four-ring-tosylato chelate is substituted by a *trans*-hydrogenhyponitro ligand. The deprotonation with imidazole led to two hyponitrito compounds (**28a→31**, **30→33**). The deprotonation of compound **29** using imidazole was not possible resulting in compound **32** with a hydrogenhyponitrito imidazole hydrogen bridge. The imidazole/imidazolium replaces, thereby, the diethyl ether/TBME (*tert*-butylmethyl ether) moiety. X-ray diffraction analysis was performed as the main analysis. Difference-Fourier analyses of the very good crystallographic data enabled the assignment of the hydrogenhyponitrito hydrogen and its migration to the imidazole in case of deprotonation. A comparison of solid-state and solution UV/VIS spectra of **28a–30** confirmed that the chromophore is, in both cases, identical. Solid-state $^{31}\text{P}\{^1\text{H}\}$ NMR spectroscopy confirmed the

formation of the complexes delivering a tentative explanation for the unaltered protonation of compound **29** due to higher basicity of the dppp ligands indicated by a high-field shift. The comparison of calculated and empirical IR spectra made an assignment of the hyponitrito-ligand vibrations possible which were then illustrated. The computational calculations (RI-DFT level using def2-TZVP basis sets and the functionals BP-86 which is used for the calculations in general in this thesis) made a classification of the hydrogenhyponitrito/hyponitrito ligand as a weak-field ligand possible using orbital considerations. These obtained results were published.^[39] Irradiation experiments in the ultraviolet region (365 nm) broke down compounds **28a–32** resulting in both N₂O release and the formation of nitrosyl complexes regardless whether the hyponitrite was protonated or deprotonated. Compounds **25** and **36** were identified by comparing IR vibrations as likely decomposition products, *i.e.* nitrosyl products obtained in the process of irradiation for compounds **28a,b/31** and **29/32**. A reasonable, irradiation induced reaction pathway could be assigned.

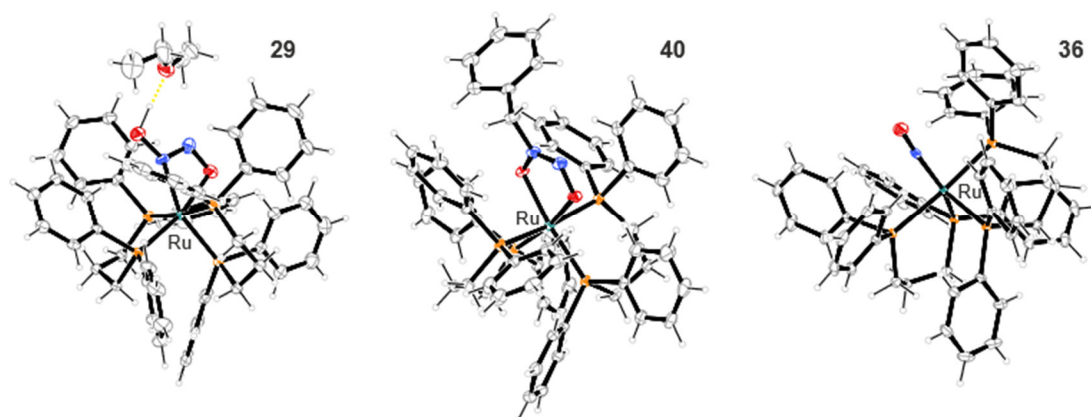


Figure 5.2: Examples of complexes obtained from starting complex **8** (ORTEP-3 plot). Left: complex cation [Ru(dppp)₂(N₂O₂H)]⁺ in **29** with hydrogen bridge to diethyl ether; centre: complex cation [Ru(dppp)₂(bdd)]⁺ in **40**; right: complex cation [Ru(dppp)₂(NO)]⁺ in **36**.

Due to the explosive behaviour of *cis*-sodium hyponitrite, *C*- and *N*-diazoniumdiolates (benzyldiazoniumdiolate (bdd, **42**) and pyrrolidinediazoniumdiolate (pdd, **38**)) were both used as replacements. The main reason for this was to prove that *cis*-hyponitrite can bind to the starting complexes **7**, **8**, **16** with respect to bond distances and angles. It was possible to obtain three *C*-diazoniumdiolato ruthenium compounds (**39–41**) including their crystal structures with the co-ligands dppe, dppp and dppv of **28–30** (see example **40** in Figure 5.2). Also, the two *N*-diazoniumdiolato compounds **35** and **37** were obtained, whereby **37** was identified by X-ray diffractometry. In general, a comparison of calculated and empirical infrared spectra made an assignment of the diazoniumdiolato vibrations possible, which were then illustrated. UV/VIS and ³¹P{¹H} NMR spectroscopy complete the analytic information. Apart from the one example of a diazoniumdiolatoruthenium complex shown in chapter 1.5, all illustrated compounds are the first diazoniumdiolatoruthenium complexes synthesised

Summary

with these ligand forms ever. Compound **36** $[\text{Ru}(\text{dppp})_2(\text{NO})]\text{BF}_4$ is a nitrosyl complex obtained when the starting complex **8** is treated with pdd (Figure 5.2). Both the complex cation $[\text{Ru}(\text{dppe})_2(\text{NO})]^+$ (**25**) and $[\text{Ru}(\text{dppp})_2(\text{NO})]^+$ (**36**) were already published, but their synthetic routes are different.^[166, 177] The supposed mechanism of the reaction provides an explanation for compound **36**, whose existence was confirmed by infrared and $^{31}\text{P}\{^1\text{H}\}$ NMR spectroscopy.

Future work should include intensive testing of the newly synthesised hexaaquaruthenium compounds as already shown for compound **6** on a minor scale. As already stated in this work, the phosphane complexes (especially **7**, **8** and **16**) are able to stabilise the hyponitrite ligand and diazoniumdiolato complexes as well. Even if these complexes are incapable of metal centred reduction of nitric oxide, the phosphane complexes are able to serve as crystallisation-anchor complexes for ligands which are unstable or whose crystallisation is difficult. The reactivity of diazoniumdiolato ruthenium complexes remains unexplored. Therefore, the question of whether or not an irradiation of these compounds leads to nitrosyl complexes such as compound **36** is of particular interest.

6 Experimental Part

6.1 Common working techniques

All reactions, as far as not explicitly described otherwise, were carried out under inert-gas atmosphere using standard Schlenk techniques.

The syringes and cannulas which were used to transfer reagents and solvents, were purged three times with argon prior to use. Diethyl ether which was used for the purification of the raw products was dried by heating to reflux, cooled and stored under argon flow over 4 Å molecular sieves. The solvents, as well as the air-sensitive phosphanes, were stored under argon atmosphere.

For crystallisation, several techniques were applied: hexa-aqua-ruthenium(II) salts were obtained by concentrating the solution with different sulfonic acids. As far as possible, the phosphane-precursor complexes were obtained by layering a methylene chloride or chloroform solution with the corresponding antisolvent (toluene, diethyl ether, cyclohexane). The hydrogenhyponitrite, hyponitrite and diazoniumdiolate complexes were obtained in the same manner layering DCM solutions with diethyl ether, TBME and cyclohexane. Adjusting of various concentrations enhanced the crystal quality and yield. Additional rinsing with diethyl ether is obligatory in the case of the hydrogen hyponitrite complexes to obtain a clean product.

As far as possible, high-resolution mass spectra were recorded. In other cases, data of elemental analysis and powder-X-ray diffraction are shown.

The absorption bands of the infrared spectra were reported in wave numbers (cm^{-1}).

NMR spectra were recorded on solutions in:^[207]

D₂O: residual water: δ 4.79 for ¹H NMR; δ 0.0 ppm for ¹⁷O NMR

CD₂Cl₂: residual dichloromethane: δ 5.32 ppm for ¹H NMR; δ 53.84 ppm for ¹³C{¹H} NMR

CDCl₃: residual chloroform: δ 7.26 ppm for ¹H NMR; δ 77.16 ppm for ¹³C{¹H} NMR

THF-d₈: residual THF: δ 3.58, 1.72 ppm for ¹H NMR, δ 67.21, 25.31 ppm for ¹³C{¹H} NMR

CD₃OD: residual methanol: δ 3.31 ppm for ¹H NMR; δ 49.00 ppm for ¹³C{¹H} NMR

Chemical shifts were reported as δ values in ppm relative to the solvent peak, if possible.

Solid-state NMR were recorded from finely powdered material using a 4 mm rotor (rotation around the "magic angle" of 54.74° with respect to the external magnetic field).

Experimental Part

Crystallography

Crystals were selected using a Leica MZ6 polarisation microscope. Suitable crystals were measured with Bruker D8 Venture diffractometer and Oxford XCalibur 3 using Mo-K α irradiation ($\lambda = 0.71073 \text{ \AA}$). Multi-scan-absorption correction was applied. The structure solutions were carried out by direct methods using SHELXT. The structures were refined by full-matrix least-squares calculations on F^2 using SHELXL-2014.^[39, 208-209]

Computational chemistry

All quantum-chemical calculations at the DFT level were performed with Orca4 (version 4.0.1). Initial geometries were taken from crystal-structure analyses. Wave functions were calculated at the multipole-accelerated RI-DFT level using def2-TZVP basis sets and the functional BP86; dispersion correction was applied by using Grimme's DFT-D3 with BJ-damping as implemented in Orca4.^[210] Frequency analyses were done numerically.^[39]

6.2 Analytical methods

Analytic method	equipment
Elemental analysis	<i>Elementar</i> vario EL (C, H, N content)
Infrared spectrometer	<i>Jasco</i> FT/IR-4600 Fourier-Transform Infrared spectrometer with ATR Diamond plate
Crystal selection	microscope <i>Leica</i> MZ6 with polarisation filter
NMR spectrometer	<i>Jeol</i> ECX 400 MHz <i>Jeol</i> GSX 270 <i>Bruker</i> Avance III HD 400 MHz
Solid-state NMR spectrometer	<i>Bruker</i> Avance III 500 MHz
X-ray diffractometer	<i>Bruker</i> D8 venture TXS <i>Oxford</i> XCalibur3 <i>STOE</i> Stadi P powder diffractometer
UV/VIS spectrophotometer	<i>Varian</i> Cary 50
Scales	<i>Mettler Toledo</i> AG204 <i>Sartorius</i> BP410S <i>Sartorius</i> ED124S
Mass spectrometer	<i>Jeol</i> JMS 700, <i>Thermo</i> Finnigan MAT 95, FAB <i>Thermo</i> Finnigan LTQ FT, IonMax ion source, ESI

6.3 Reagents and solvents

chemicals	purity	company
Ba(OH) ₂	≥98%	Fluka
<i>N</i> -benzylhydroxylamine hydrochloride	<i>puriss.</i> , ≥99%	Aldrich
chloroform	99%	Kraft
DCM	99.9%	Kraft
diethyl ether	99.5%	Kraft
dppbz	>98%	TCI
dppe	99%	ABCR
dppen	98%	Aldrich
dppp	≥98%	ABCR
dppv	97%	ABCR
ethanol	<i>pA</i>	—
ethyl acetate	<i>purum</i>	—
H ₂ (1,5-NaphDS)	>98%	TCI
H ₂ (4,4'-BiphenDS)	>98%	TCI
H ₂ O	de-ionised	house installation
H ₂ SiF ₆	33.5–35%	Aldrich
H ₂ SO ₄	96%	—
HOTf	99%	ABCR
HSbF ₆ ·6H ₂ O	—	Aldrich
<i>i</i> -hexane	<i>purum</i>	—
imidazole	99%	ABCR
MesSO ₃ ·2H ₂ O	97%	Aldrich

Experimental Part

methanol (dried over molecular sieve)	99.8%	Aldrich
$\text{Na}_2\text{N}_2\text{O}_2 \cdot x\text{H}_2\text{O}$	–	Aldrich
NaIO_4	–	Normapur
NaNO_2	<i>pA</i>	Grüssing
NaOH	<i>puriss.</i>	ABCR
nitric oxide	99.5%	Air Liquide
<i>n</i> -pentane	<i>puriss.</i>	–
Pb	≥99%	Aldrich
PBnPh_2	99%	Alfa Aesar
PPh_2Pr	99%	ABCR
PPh_3	99%	Acros
pyrrolidine	≥99.5%	Aldrich
$\text{RuCl}_3 \cdot x\text{H}_2\text{O}$	99.9%, 36% Ru	ABCR
silver nitrate	<i>puriss.</i>	VWR
sodium	–	Aldrich
tetrafluoroboric acid (in water)	50%	Fluka
tetrakis(dimethylamino) ethylene (tden)	≥95%	TCI
THF (dried over molecular sieve)	≥99.9%	Aldrich
toluene	technical	–
triphenyltin chloride	95%	ABCR
<i>p</i> -toluene sulfonic acid	≥98%	Aldrich

6.4 Syntheses of hexaaquaruthenium(II) salts

6.4.1 Preparation of "RuO₂·xH₂O"

Literature: C. Fellay, G. Laurency, S. M. Bischof, R. A. Periana, *Inorganic Syntheses, Vol. 35*, John Wiley & Sons, Inc., Hoboken, New Jersey, **2010**.

Starting materials: RuCl₃ · xH₂O, NaOH pellets, H₂O (de-ionized), AgNO₃ solution (2% in H₂O)

Procedure:

A solution of NaOH (1.23 mol, 49.2 g) in H₂O (250 mL) was prepared and heated up to 60 °C. The RuCl₃ · xH₂O (28.9 mmol, 6.00 g, statement abcr: 207.43 g/mol) was added and the suspension stirred for 1 h. After that, the solution was cooled down to room temperature and stirred again for 2 d. The black solid was filtered off and washed several times with H₂O until a test with AgNO₃ solution (2% in H₂O) was negative. The solid was dried at room temperature for 2 days.

Empirical formula: "RuO₂·xH₂O" (ill-defined)

Yield: ca. 9–10 g of black scales.

Please note: The product is ill-defined. The water content varies strongly depending on the drying process. The product was directly used without any further analytics. Nonetheless, following the route mentioned above the yield of the hexaaquaruthenium(II) salts stays nearly the same. Great care has to be taken in the washing process to avoid any chloride contamination, otherwise this will result in the formation of chlorine gas in the following syntheses and the subsequent decomposition of the ruthenium(II) species.

6.4.2 Setup for the synthesis of hexaaquaruthenium(II)

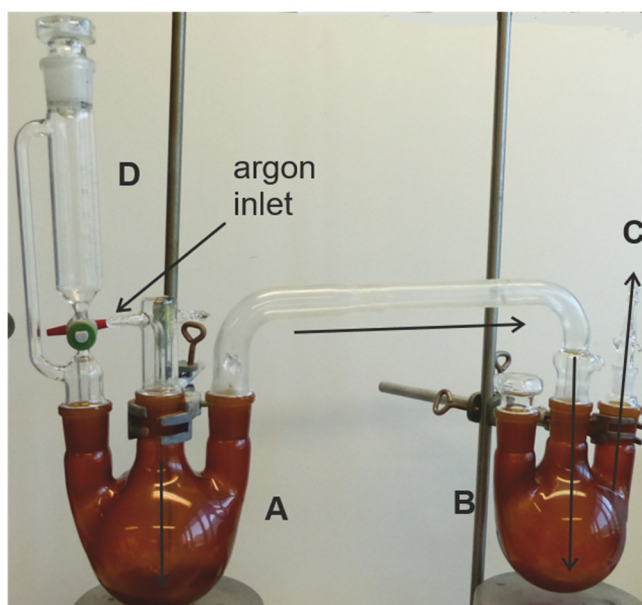


Figure 6.1: Set-up of the apparatus for the synthesis of the $[\text{Ru}(\text{H}_2\text{O})_6]^{2+}$ cation. Arrows indicate the way of the Ar flow. Washing flask C was omitted due to photographic limitations.

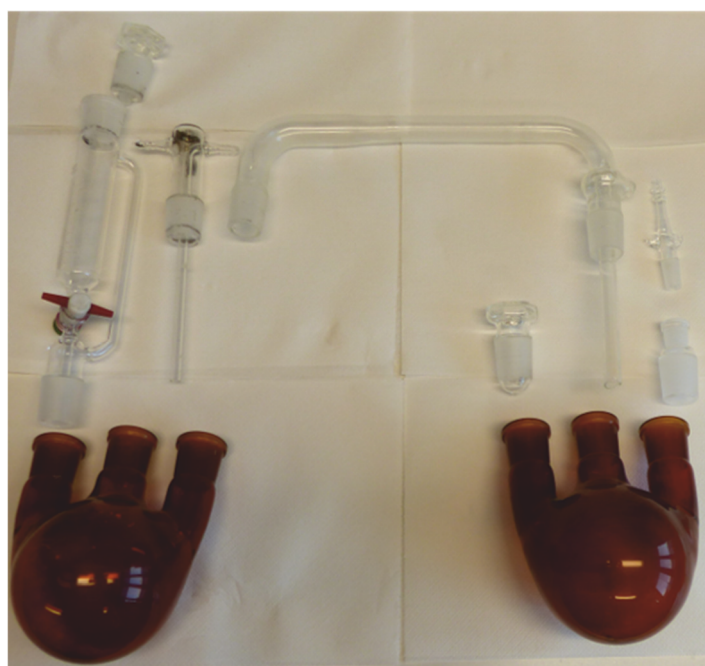
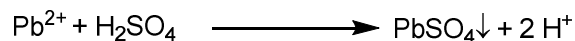
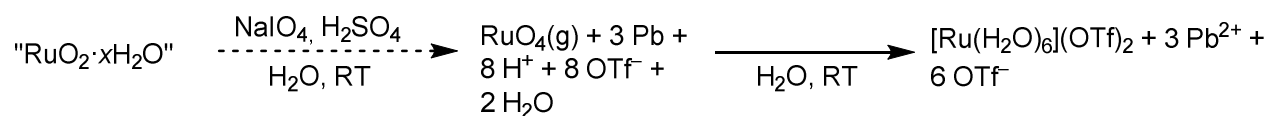


Figure 6.2: Set-up plan of the apparatus. The inlet tube is sealed at one side and the glass bridge has an integrated inlet tube to ensure a tightness of the apparatus. A stopcock with PTFE-key was used in the dropping funnel. Black residues, visible on the glass, occur, if organic impurities are on the glass or the surface is rough.

6.4.3 Hexa-aqua-ruthenium(II) tosylate (1)



1

According to: C. Fellay, G. Laurency, S. M. Bischof, R. A. Periana, *Inorganic Syntheses, Vol. 35*, John Wiley & Sons, Inc., Hoboken, New Jersey, **2010**.

Starting materials: RuO₂·xH₂O (ill-defined), NaIO₄, H₂SO₄ (50% a. 2.0 M), H₂O (de-ionized), Pb (dust), HOTf (98%), Htos (98%), neutralising solution (Pb in 1.0 M H₂SiF₆).

Procedure:

A solution of NaIO₄ (10.5 g, 49.0 mmol) (A) in water (85 ml), a suspension of Pb (20.0 g, 96.4 mmol) in HOTf (2.40 mM, 140 mL) (B) and a suspension Pb (3.00 g, 14.5 mmol) in H₂SiF₆ (1.0 M, 60 mL) (C) were prepared. After placing the solutions in the intended reaction flasks (Fig. 6.1 and 6.2), they were degassed with Ar for 1 h. After that, the H₂SO₄ solution (50%, 42 mL) (D) was prepared and degassed separately. The NaIO₄ solution was cooled to 0 °C, the RuO₂·xH₂O (2.1 g, ≈ 17 mmol) was added to solution A, the dropping funnel was filled with the H₂SO₄ solution and the apparatus was scrutinized to ensure leak tightness. The acid was dropped slowly (ca. 1 drop per second) into solution A and a constant flow of Ar (2 bubbles per second) was maintained. The ice bath was not removed and allowed to melt over time to ensure a slow emission of RuO₄ (please read instructions below). Stirring was continued for 3–4 d under constant Ar flow until solution A was clear. To the dark pink solution B H₂SO₄ (2.0 M, 42 mL) was added and stirred for 15 min. After sedimentation of the PbSO₄, the solution was filtered off with a Schlenk-frit with cotton wool (placed above the glass disc). To this solution Htos (35.0 g, 184 mmol) was added and immediately put in a rotary evaporator. The bath was heated to 45 °C and the pressure was reduced in small steps from 65 mbar to 30 mbar. The operational steps had to be done quickly otherwise the oxidation of Ru(II) to Ru(III) would result in preferential crystallisation of the Ru(III) product. When the first crystals appeared the evaporation was stopped, the crystal slurry was put under an Ar atmosphere and kept for 3 h at 4 °C in the refrigerator. The crystals were filtered off with a Schlenk-frit, washed with ethyl acetate (3 · 20 mL) and diethyl ether (3 · 20 mL) and dried in *vacuo*. The crystals were kept away from light and air.

Experimental Part

Empirical formula: $C_{14}H_{26}O_{12}RuS_2$ (551.55 g/mol)

Yield: 4.7 g (8.5 mmol, 61% of th. (14 mmol $RuCl_3$)) of pink platelets.

Elemental Analysis: (calcd. for $C_{14}H_{26}O_{12}RuS_2$, 551.55 g/mol) found (calcd.): C 30.43% (30.48%), H 4.85% (4.75%), S 11.76% (11.62%).

UV/VIS spectroscopy: 391.0, 533.0 (de-ionized water, pH 6); 392.5, 534.5 (H-tos solution, pH 1); 388.0, 521.0 (solid-state UV/VIS) nm

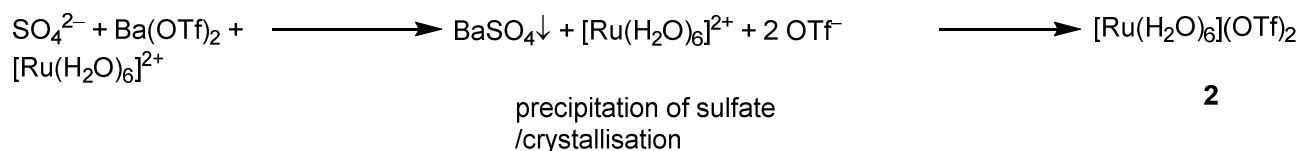
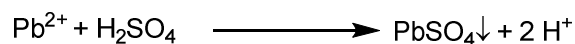
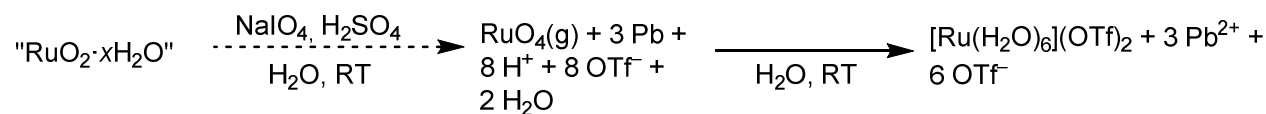
^{17}O NMR spectroscopy: (D_2O , 54 MHz): $\delta = 174.2$ (s) (*p*-toluene sulfonate), -189.9 (s) (hexaaquaruthenium(II)) ppm.

X-ray structure analysis: to008

Please note: RuO_4 is a toxic and highly reactive gas. Due to safety hazards proper instructions for the work with it was attached to the appendix. The ion-exchange chromatography—as suggested in the literature—could not be reproduced, therefore, the more expensive triflic acid (HOTf) was used to avoid this step.

6.4.4 Hexaaquaruthenium(II) triflate (2)

Variant I



Variant II



According to: C. Fellay, G. Laurency, S. M. Bischof, R. A. Periana, *Inorganic Syntheses, Vol. 35*, John Wiley & Sons, Inc., Hoboken, New Jersey, **2010**.

Starting materials: RuO₂·xH₂O (ill-defined), NaIO₄, H₂SO₄ (50% a. 2.0 M), H₂O (de-ionized), Pb (dust), HOTf (99%), neutralising solution (Pb in 1.0 M H₂SiF₆), Ba(OH)₂.

Procedure:

Variant I

A solution of NaIO₄ (10.5 g, 49.0 mmol) (A) in water (85 ml), a suspension of Pb (20.0 g, 96.4 mmol) in HOTf (2.40 M, 140 mL) (B) and a suspension Pb (3.00 g, 14.5 mmol) in H₂SiF₆ (1.0 M, 60 mL) (C) were prepared. After placing the solutions in the intended reaction flasks (Fig. 6.1 and 6.2), they were degassed with Ar for 1 h. After that, the H₂SO₄ solution (50%, 42 mL) (D) was prepared and degassed separately. The NaIO₄ solution was cooled to 0 °C, the RuO₂·xH₂O (2.1 g, ≈ 17 mmol) was added to solution A, the dropping funnel was filled with the H₂SO₄ solution and the apparatus was scrutinized to ensure leak tightness. The acid was dropped slowly (ca. 1 drop per second) into solution A and a constant flow of Ar (2 bubbles per second) was maintained. The ice bath was not removed and allowed to melt over time to ensure a slow emission of RuO₄. Stirring was continued for 3–4 d under constant Ar flow until solution A was clear. To the dark pink solution B H₂SO₄ (2.0 M, 42 mL) was added and stirred for 15 min. Separately, a solution of Ba(OH)₂ (753 mg, 4.39 mmol) in H₂O was neutralised with

Experimental Part

HOTf (2.0 mL, 23 mmol) and degassed with Ar. The other solution was titrated with the Ba(OTf)₂ solution until no visual precipitation of BaSO₄ occurred. The suspension was stirred for another 15 min. After sedimentation, the solution was filtered off with a Schlenk-frit with cotton wool (placed above the glass disc). The clear solution was reduced in a rotary evaporator. The bath was heated to 45 °C and the pressure was reduced in small steps from 65 mbar to 30 mbar. The evaporation had to be maintained until no further distillate could be collected. After that, the solution was put under Ar and cooled down to 4 °C in a refrigerator. After 1–2 days, the pink crystals were filtered off, cautiously (see below) and carefully washed with dry *n*-pentane (2 · 10 mL) and dried in *vacuo*. The crystals were kept away from air and light.

Empirical formula: C₂H₁₂F₆O₁₂RuS₂ (507,30 g/mol)

Yield: 1.83 g (3.60 mmol, 24.8% of th. (14.5 mmol RuCl₃)) of pink blocks.

Elemental Analysis: (calcd. for C₂H₁₂F₆O₁₂RuS₂, 507.30 g/mol) found (calcd.): C 4.88% (4.74%), H 2.65% (2.38%), S 12.85% (12.64%).

X-ray structure analysis: to024

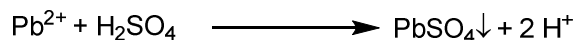
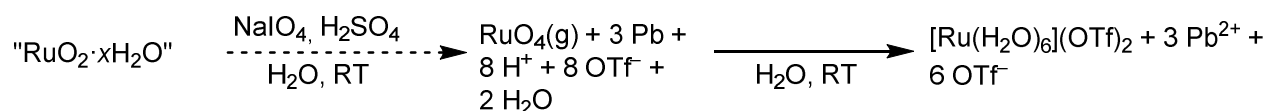
Variant II

A solution of [Ru(H₂O)₆]SO₄ (1.121 g, 3.7 mmol) in H₂O (20 mL) was prepared and treated with a neutralised solution of Ba(OH)₂ (750 mg, 4.0 mmol) with HOTf (2 mL, 22.6 mmol) in H₂O (10 mL). After sedimentation, the solution was filtered through a syringe filter, and evaporated in a rotary evaporator. The following work steps were identical to variant I.

Yield: 1.43 g (2.8 mmol, 76% of th.) of pink blocks.

Please note: The [Ru(H₂O)₆](OTf)₂ obtained in this synthesis is a highly soluble compound. Both ethyl acetate and diethyl ether are not suitable for the washing process. It is suspected that the solvent itself or trace impurities of water are enough to solve larger quantities of the product. Additionally, there is a possibility in variant I to obtain [Ru(H₂O)₆]SO₄, if a decent amount of sulfate remains. Due to the characteristics of the synthesis an exact determination of the Pb²⁺ concentration in solution is not possible. The method of titrating the solution was the most sensible way to solve this problem and also to avoid contamination with larger quantities of Ba(OTf)₂. Nonetheless, variant II offers the possibility to obtain a proper product.

6.4.5 Hexaaquaruthenium(II) sulfate (3)



According to: C. Fellay, G. Laurency, S. M. Bischof, R. A. Periana, *Inorganic Syntheses, Vol. 35*, John Wiley & Sons, Inc., Hoboken, New Jersey, **2010**.

Starting materials: RuO₂·xH₂O (ill-defined), NaIO₄, H₂SO₄ (50% a. 2.0 M), H₂O (de-ionized), Pb (dust), HOTf (99%), neutralising solution (Pb in 1.0 M H₂SiF₆)

Procedure:

A solution of NaIO₄ (10.5 g, 49.0 mmol) (A) in water (85 ml), a suspension of Pb (20.0 g, 96.4 mmol) in HOTf (2.40 M, 140 mL) (B) and a suspension Pb (3.00 g, 14.5 mmol) in H₂SiF₆ (1.0 M, 60 mL) (C) were prepared. After placing the solutions in the intended reaction flasks (Fig. 6.1 and 6.2), they were degassed with Ar for 1 h. After that, the H₂SO₄ solution (50%, 42 mL) (D) was prepared and degassed separately. The NaIO₄ solution was cooled to 0 °C, the RuO₂·xH₂O (2.1 g, ≈ 17 mmol) was added to solution A, the dropping funnel was filled with the H₂SO₄ solution and the apparatus was scrutinized to ensure leak tightness. The acid was dropped slowly (ca. 1 drop per second) into solution A and a constant flow of Ar (2 bubbles per second) was maintained. The ice bath was not removed and allowed to melt over time to ensure a slow emission of RuO₄. Stirring was continued for 3–4 d under constant Ar flow until solution A was clear. To the dark pink solution B H₂SO₄ (2.0 M, 42 mL) was added and stirred for 15 min. After sedimentation of the PbSO₄, the solution was filtered off with a Schlenk-frit with cotton wool (placed above the glass disc). To this solution an additional amount of H₂SO₄ (10 mL, 2.0 M) was added and immediately put in a rotary evaporator. The bath was heated to 45 °C and the pressure was reduced in small steps from 65 mbar to 30 mbar. The evaporation had to be maintained until no further distillate could be collected. After that, the solution was put under Ar and cooled down to 4 °C in a refrigerator. After 1–2 days, the pink crystals were filtered off, carefully washed with ethyl acetate (2 · 10 mL) and diethyl ether (2 · 10 mL) and dried in *vacuo*. The crystals were kept away from air and light.

Empirical formula: H₁₂O₁₀RuS (305.23 g/mol)

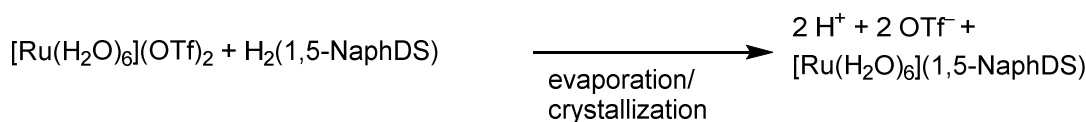
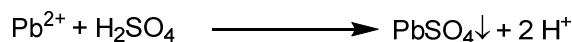
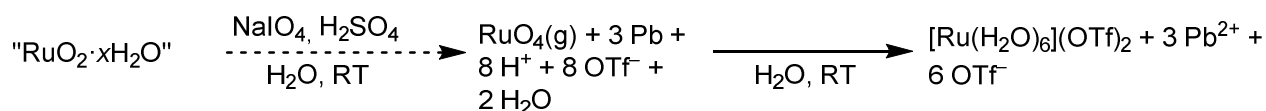
Experimental Part

Yield: 1.12 g (3.67 mmol, 25.3% of th. (14.5 mmol RuCl₃)) of red platelets.

Elemental Analysis: (calcd. for H₁₂O₁₀RuS, 305.23 g/mol) found (calcd.): H 3.83% (3.96%), S 10.45% (10.51%).

X-ray structure analysis: tv140

6.4.6 Hexa-aquaruthenium(II) naphthalenedisulfonate (4)



4

According to: C. Fellay, G. Laurency, S. M. Bischof, R. A. Periana, *Inorganic Syntheses*, Vol. 35, John Wiley & Sons, Inc., Hoboken, New Jersey, **2010**.

Starting materials: RuO₂·xH₂O (ill-defined), NaIO₄, H₂SO₄ (50% a. 2.0 M), H₂O (de-ionized), Pb (dust), HOTf (99%), neutralising solution (Pb in 1.0 M H₂SiF₆), H₂(1,5-NaphDS) (≥ 98%).

Procedure:

A solution of NaIO₄ (10.5 g, 49.0 mmol) (A) in water (85 ml), a suspension of Pb (20.0 g, 96.4 mmol) in HOTf (2.40 M, 140 mL) (B) and a suspension Pb (3.00 g, 14.5 mmol) in H₂SiF₆ (1.0 M, 60 mL) (C) were prepared. After placing the solutions in the intended reaction flasks (Fig. 6.1 and 6.2), they were degassed with Ar for 1 h. After that, the H₂SO₄ solution (50%, 42 mL) (D) was prepared and degassed separately. The NaIO₄ solution was cooled to 0 °C, the RuO₂·xH₂O (2.1 g, ≈ 17 mmol) was added to solution A, the dropping funnel was filled with the H₂SO₄ solution and the apparatus was scrutinized to ensure leak tightness. The acid was dropped slowly (ca. 1 drop per second) into solution A and a constant flow of Ar (2 bubbles per second) was maintained. The ice bath was not removed and allowed to melt over time to ensure a slow emission of RuO₄ (please read instructions below). Stirring was continued for 3–4 d under constant Ar flow until solution A was clear. To the dark pink solution B H₂SO₄ (2.0 M, 42 mL) was added and stirred for 15 min. After sedimentation of the PbSO₄, the solution was filtered off with a Schlenk-frit with cotton wool (placed above the glass disc). To this solution H₂(1,5-NaphDS) (2.88 g, 8.00 mmol) was added and immediately put in a rotary evaporator. The bath was heated to 45 °C and the pressure was reduced in small steps from 65 mbar to 30 mbar. When the first crystals appeared the evaporation was stopped, the crystal slurry was put under an Ar atmosphere and kept for 3 h at 4 °C in the refrigerator. The crystals were filtered off with a Schlenk-frit, washed with methanol (3 · 20 mL), ethyl acetate (3 · 20 mL) and diethyl ether (3 · 20 mL) and dried in *vacuo*. The crystals were kept away from light and air.

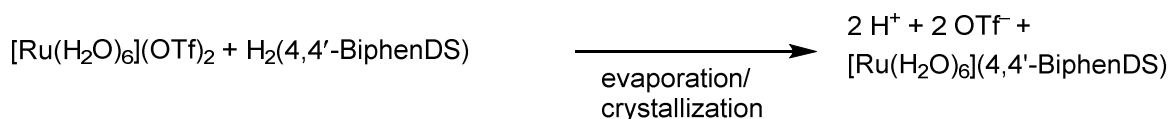
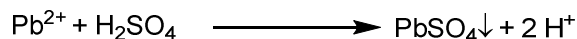
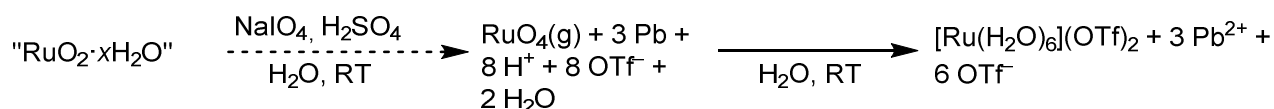
Empirical formula: C₁₀H₁₈O₁₂RuS₂ (495.45 g/mol)

Experimental Part

Yield: 3.13 g (6.32 mmol, 43.6% of th. (14.5 mmol RuCl₃)) of pink platelets.

Elemental Analysis: (calcd. for C₁₀H₁₈O₁₂RuS₂, 495.45 g/mol) found (calcd.): C 24.20% (24.24%), H 3.73% (3.66%), S 12.97% (12.94%).

X-ray structure analysis: tv449

6.4.7 Hexa-aquaruthenium(II) biphenyldisulfonate (5)**5**

According to: C. Fellay, G. Laurency, S. M. Bischof, R. A. Periana, *Inorganic Syntheses*, Vol. 35, John Wiley & Sons, Inc., Hoboken, New Jersey, **2010**.

Starting materials: RuO₂·xH₂O (ill-defined), NaIO₄, H₂SO₄ (50% a. 2.0 M), H₂O (de-ionized), Pb (dust), HOTf (99%), neutralising solution (Pb in 1.0 M H₂SiF₆), H₂(4,4'-BiphenDS) (≥ 98%).

Procedure:

A solution of NaIO₄ (10.5 g, 49.0 mmol) (A) in water (85 ml), a suspension of Pb (20.0 g, 96.4 mmol) in HOTf (2.40 mM, 140 mL) (B) and a suspension Pb (3.00 g, 14.5 mmol) in H₂SiF₆ (1.0 M, 60 mL) (C) were prepared. After placing the solutions in the intended reaction flasks (Fig. 6.1 and 6.2), they were degassed with Ar for 1 h. After that, the H₂SO₄ solution (50%, 42 mL) (D) was prepared and degassed separately. The NaIO₄ solution was cooled to 0 °C, the RuO₂·xH₂O (2.1 g, ≈ 17 mmol) was added to solution A, the dropping funnel was filled with the H₂SO₄ solution and the apparatus was scrutinized to ensure leak tightness. The acid was dropped slowly (ca. 1 drop per second) into solution A and a constant flow of Ar (2 bubbles per second) was maintained. The ice bath was not removed and allowed to melt over time to ensure a slow emission of RuO₄ (please read instructions below). Stirring was continued for 3–4 d under constant Ar flow until solution A was clear. To the dark pink solution B H₂SO₄ (2.0 M, 42 mL) was added and stirred for 15 min. After sedimentation of the PbSO₄, the solution was filtered off with a Schlenk-frit with cotton wool (placed above the glass disc). To this solution H₂(4,4'-BiphenDS) (3.14 g, 10.0 mmol) was added and immediately put in a rotary evaporator. The bath was heated to 45 °C and the pressure was reduced in small steps from 65 mbar to 30 mbar. When the first crystals appeared the evaporation was stopped, the crystal slurry was put under an Ar atmosphere and kept for 3 h at 4 °C in the refrigerator. The crystals were filtered off with a Schlenk-frit, washed with ethyl acetate (3 · 20 mL) and diethyl ether (3 · 20 mL) and dried in *vacuo*. The crystals were kept away from light and air.

Empirical formula: C₁₂H₂₄O₁₄RuS₂ (557.52 g/mol)

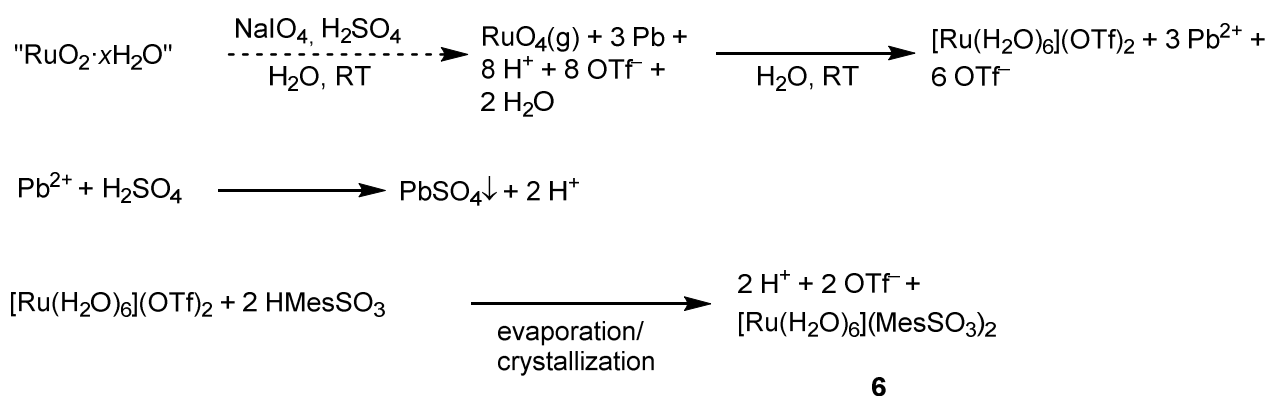
Experimental Part

Yield: 3.90 g (7.00 mmol, 48.2% of th. (14.5 mmol RuCl₃)) of pink platelets.

Elemental Analysis: (calcd. for C₁₂H₂₀O₁₂RuS₂, 521.49 g/mol) found (calcd.): C 27.43% (27.64%), H 3.83% (3.87%), S 12.28% (12.31%) (Loss of two water of crystallization in the drying process).

X-ray structure analysis: uo030

6.4.8 Hexa-aquaruthenium(II) mesitylsulfonate (6)



According to: C. Fellay, G. Laurency, S. M. Bischof, R. A. Periana, *Inorganic Syntheses, Vol. 35*, John Wiley & Sons, Inc., Hoboken, New Jersey, **2010**.

Starting materials: RuO₂·xH₂O (ill-defined), NaIO₄, H₂SO₄ (50% a. 2.0 M), H₂O (de-ionized), Pb (dust), HOTf (99%), neutralising solution (Pb in 1.0 M H₂SiF₆), HMesSO₃·2H₂O (97%).

Procedure:

A solution of NaIO₄ (10.5 g, 49.0 mmol) (A) in water (85 ml), a suspension of Pb (20.0 g, 96.4 mmol) in HOTf (2.40 mM, 140 mL) (B) and a suspension Pb (3.00 g, 14.5 mmol) in H₂SiF₆ (1.0 M, 60 mL) (C) were prepared. After placing the solutions in the intended reaction flasks (Fig. 6.1 and 6.2), they were degassed with Ar for 1 h. After that, the H₂SO₄ solution (50%, 42 mL) (D) was prepared and degassed separately. The NaIO₄ solution was cooled to 0 °C, the RuO₂·xH₂O (2.1 g, ≈ 17 mmol) was added to solution A, the dropping funnel was filled with the H₂SO₄ solution and the apparatus was scrutinized to ensure leak tightness. The acid was dropped slowly (ca. 1 drop per second) into solution A and a constant flow of Ar (2 bubbles per second) was maintained. The ice bath was not removed and allowed to melt over time to ensure a slow emission of RuO₄ (please read instructions below). Stirring was continued for 3–4 d under constant Ar flow until solution A was clear. To the dark pink solution B H₂SO₄ (2.0 M, 42 mL) was added and stirred for 15 min. After sedimentation of the PbSO₄, the solution was filtered off with a Schlenk-frit with cotton wool (placed above the glass disc). To this solution

Experimental Part

HMeSO₃·2H₂O (5.00 g, 20.6 mmol) was added and immediately put in a rotary evaporator. The bath was heated to 45 °C and the pressure was reduced in small steps from 65 mbar to 30 mbar. When the first crystals appeared the evaporation was stopped, the crystal slurry was put under an Ar atmosphere and kept for 3 h at 4 °C in the refrigerator. The crystals were filtered off with a Schlenk-frit, washed with ethyl acetate (3 · 20 mL) and diethyl ether (3 · 20 mL) and dried in *vacuo*. The crystals were kept away from light and air at 4 °C.

Empirical formula: C₁₈H₃₄O₁₂RuS₂ (607.64 g/mol)

Yield: 3.90 g (6.42 mmol, 44.3% of th. (14.5 mmol RuCl₃)) of pink platelets.

Elemental Analysis: (calcd. for C₁₈H₃₄O₁₂RuS₂, 607.64 g/mol) found (calcd.): C 34.24% (35.58%), H 5.51% (5.64%), S 10.25% (10.55%).

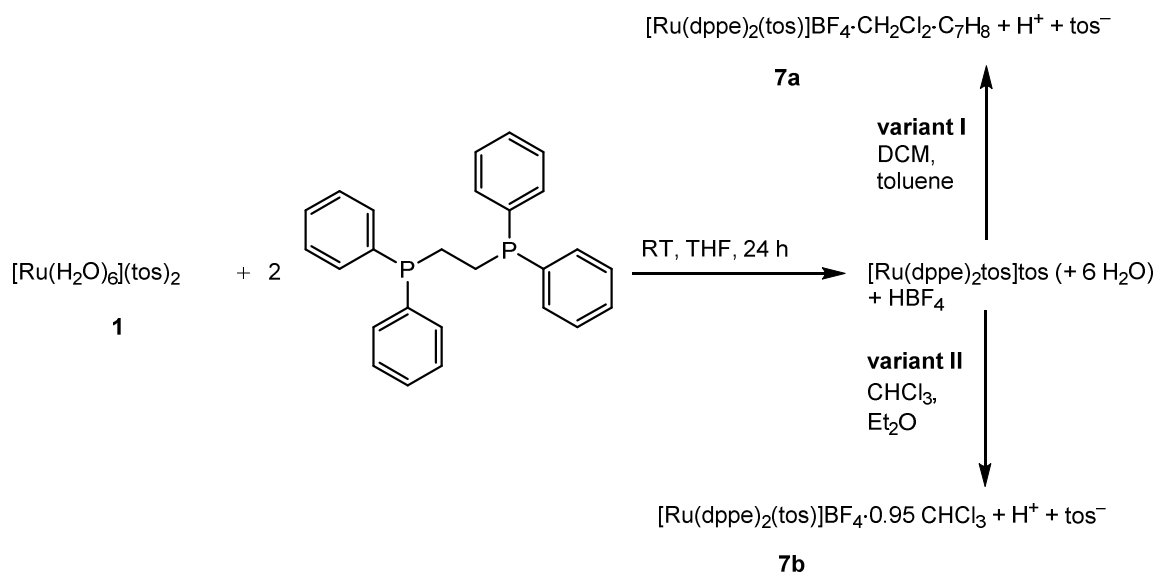
X-ray structure analysis: uo031

Please note: The [Ru(H₂O)₆](MeSO₃)₂ obtained in this synthesis is more sensitive to air and temperature than the other salts. The lifespan of the product can be prolonged by storing at 4 °C. Nonetheless, the product will decompose over time showing a tentative surface of elemental ruthenium.

6.5 Syntheses of phosphane precursor complexes

6.5.1 Phosphane complexes with κ^2O,O' -tosylato/mesitylsulfonato ligands

6.5.1.1 Bis{bis(diphenylphosphanyl)ethane}tosylatoruthenium(II) tetrafluoridoborate (7)



According to: O. H. Bailey, A. Ludi, *Inorg. Chem.* **1985**, *24*, 2582–2585. **Literature:** D. Beck, P. Klüfers, *Chem. Eur. J.* **2018**, *24*, 16019–16028.

Starting materials: $[\text{Ru}(\text{H}_2\text{O})_6](\text{tos})_2$, 1,2-bis(diphenylphosphanyl)ethane (99%, dppe), THF, tetrafluoroboric acid (50% in H_2O), DCM, chloroform, toluene, diethyl ether.

Procedure:

A mixture of $[\text{Ru}(\text{H}_2\text{O})_6](\text{tos})_2$ (275 mg, 0.498 mmol, 1.00 equiv.) and dppe (400 mg, 1.00 mmol, 2.01 equiv.) was prepared and suspended in THF (10 mL). The suspension was stirred for 1–2 d until a yellow-orange solution was formed. The solvent was removed in *vacuo*. The yellow crude product was resolved in DCM (3 mL), filtered off through a syringe filter and layered with diethyl ether. For the tetrafluoro-borate product HBF_4 (0.13 mL, 2.1 equiv., 50% in H_2O) was added to the DCM solution, filtered off and layered with toluene (variant I). To obtain crystals without intrinsic distortion a chloroform (4 mL) solution of the crude product was treated with HBF_4 (0.065 mL, 1.0 equiv., 50% in H_2O), filtered off through a syringe filter and layered with diethyl ether (variant II). In all cases orange crystals formed after few hours and after 1 d the crystallisation was finished. The solvent was removed, the crystals were washed with diethyl ether (10 mL) and dried in *vacuo*.

Empirical formula: $\text{C}_{59}\text{H}_{55}\text{BF}_4\text{O}_3\text{P}_4\text{RuS}$ (1155.92 g/mol)

Experimental Part

Yield (a): 570 mg (0.493 mmol, 99.0% of th.) of orange platelets.

Yield (b): 520 mg (0.449 mmol, 90.2% of th.) of orange platelets.

Variant I:

IR spectroscopy: (RT, solid), (intensity): $\tilde{\nu}$ = 1586vw, 1486w, 1435m, 1256s, 1192m, 1058s, 993s, 748m cm^{-1} .

UV/VIS spectroscopy: $\lambda_{\text{max}}/\text{nm}$ ($\epsilon_{\text{max}}[\text{M}^{-1} \text{cm}^{-1}]$) (DCM) 342 (1952), 380 (2030).

NMR spectroscopy:

$^{13}\text{C}\{^1\text{H}\}$ NMR spectroscopy (101 MHz, CD_2Cl_2): δ 142.3 ($\underline{\text{C}}\text{-CH}_3$), 139.3 ($\underline{\text{C}}\text{-SO}_3^-$), 128.2-135.1 (Ph + tos aromatic), 125.5 (C1 toluene), 31.3 (P- $\underline{\text{C}}\text{H}_2$), 25.4 (P- $\underline{\text{C}}\text{H}_2$), 21.6 (Ph- CH_3) ppm.

$^{31}\text{P}\{^1\text{H}\}$ NMR (162 MHz, CD_2Cl_2): δ 60.3 (t, dppe), 46.9 (t, dppe) ppm.

Elemental Analysis: (calcd. for $\text{C}_{61.53}\text{H}_{58.53}\text{BCl}_{1.5}\text{F}_4\text{O}_3\text{P}_4\text{RuS}$, 1211.65 g/mol, included DCM as crystal solvent) found (calcd.): C 58.90% (60.99%), H 4.84% (4.87%), S 2.90% (2.65%).^[161]

Variant II:^[39]

IR spectroscopy: (RT, solid), (intensity): $\tilde{\nu}$ = 3027vw, 1600vw, 1487w, 1436m, 1256s, 1192w, 1049s, 989s, 742m cm^{-1} .

UV/VIS spectroscopy: $\lambda_{\text{max}}/\text{nm}$ ($\epsilon_{\text{max}}[\text{M}^{-1} \text{cm}^{-1}]$) (DCM) 338 (1396), 379 (1178).

NMR spectroscopy:

$^{13}\text{C}\{^1\text{H}\}$ NMR spectroscopy (101 MHz, CD_2Cl_2): δ 142.3 ($\underline{\text{C}}\text{-CH}_3$), 128.3-134.8 (Ph + tos aromatic), 30.9 (P- $\underline{\text{C}}\text{H}_2$), 25.3 (P- $\underline{\text{C}}\text{H}_2$), 21.6 (Ph- CH_3) ppm.

$^{31}\text{P}\{^1\text{H}\}$ NMR (162 MHz, CD_2Cl_2): δ 60.3 (t, $^3J_{\text{PP}} = 18.3$ Hz), 46.9 (t, $^3J_{\text{PP}} = 18.3$ Hz) ppm.

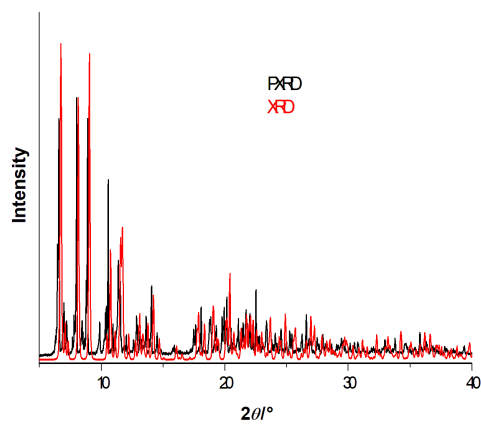
Elemental Analysis: (calcd. for $\text{C}_{60}\text{H}_{56}\text{BCl}_3\text{F}_4\text{O}_3\text{P}_4\text{RuS}$, 1275.28 g/mol, included CHCl_3 as crystal solvent) found (calcd.): C 56.38% (56.51%), H 4.57% (4.43%), S 2.88% (2.51%).

HRMS (ESI+): $m/z = 1069.11$ ($\text{C}_{59}\text{H}_{55}\text{O}_3\text{P}_4\text{RuS}$)

X-ray structure analysis: uv252

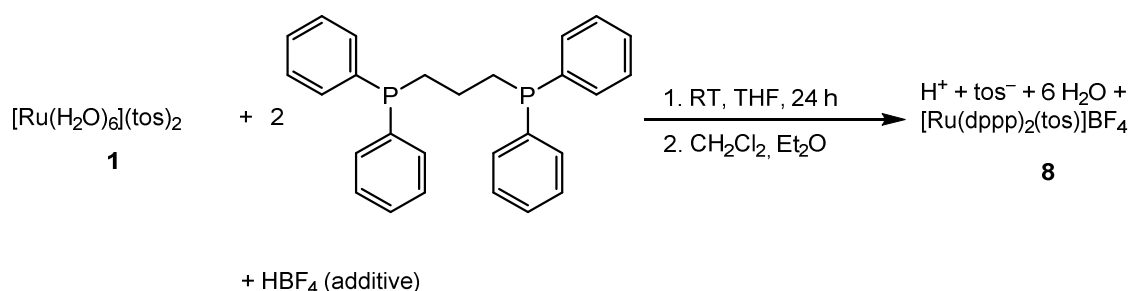
Experimental Part

PXRD:



Graph 1: Powder-X-ray diffraction of **7b**. Red: X-ray diffraction at 100 K, Black: Powder-X-ray diffraction at RT.^[39]

6.5.1.2 Bis{bis(diphenylphosphanyl)propane}tosylatoruthenium(II) tetrafluoridoborate (8)



According to: O. H. Bailey, A. Ludi, *Inorg. Chem.* **1985**, *24*, 2582–2585. **Literature:** D. Beck, P. Klüfers, *Chem. Eur. J.* **2018**, *24*, 16019–16028.

Starting materials: [Ru(H₂O)₆](tos)₂, 1,3-bis(diphenylphosphanyl)propane (98%, dppp), THF, tetrafluoroboric acid (50% in H₂O), DCM, diethyl ether.

Procedure:

A mixture of [Ru(H₂O)₆](tos)₂ (275 mg, 0.498 mmol, 1.00 equiv.) and dppp (413 mg, 1.00 mmol, 2.01 equiv.) was prepared and suspended in THF (10 mL). The suspension was stirred for 1–2 d until a red-orange solution was formed. The solvent was removed in *vacuo* and the orange crude product was washed with diethyl ether (10 mL). The compound was resolved in DCM (3 mL), HBF₄ (0.13 mL, 2.0 equiv., 50% in H₂O) was added, stirred again, filtered off and layered with diethyl ether. Red crystals formed after 3 d. The solvent was removed, the crystals were washed with diethyl ether (10 mL) and dried in *vacuo*.

Empirical formula: C₆₁H₅₉BF₄O₃P₄RuS (1183.97 g/mol)

Yield: 527 mg (0.445 mmol, 89.4%) of yellow-red rods.

IR spectroscopy: (RT, solid), (intensity): $\tilde{\nu}$ = 3059w, 2923w, 2878w, 1598vw, 1573vw, 1485w, 1433m, 1407w, 1317w, 1249s, 1191m, 1160m, 1117m, 1050s, 1025s, 992s, 972s, 921m, 837m, 777w, 790m, 744m cm⁻¹.

UV/VIS spectroscopy: λ_{max} /nm (DCM) 317 (sh), 400.

NMR spectroscopy:

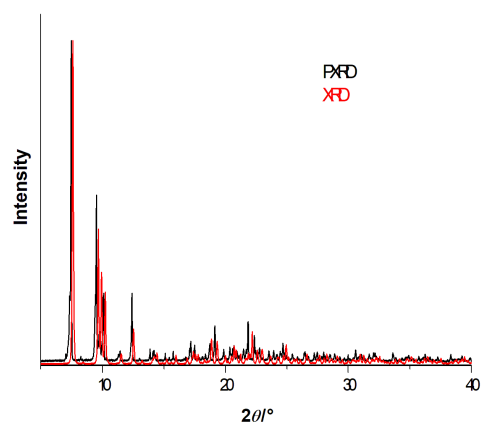
³¹P{¹H} NMR (162 MHz, CD₂Cl₂): δ 23.1 (t, ⁴J_{PP} = 33.7 Hz), -2.9 (t, ⁴J_{PP} = 33.7 Hz) ppm.

HRMS (ESI+): m/z = 1097.21 (C₆₁H₅₉O₃P₄RuS).

Experimental Part

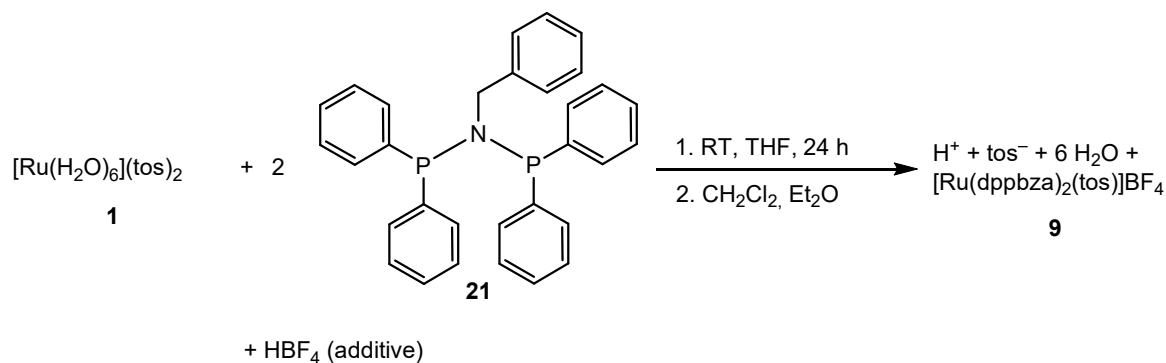
X-ray structure analysis: vv493

PXRD:



Graph 2: Powder-X-ray diffraction of **8**. Red: X-ray diffraction at 100 K, Black: Powder-X-ray diffraction at room temperature.^[39]

6.5.1.3 Bis{bis(diphenylphosphanyl)benzylamine}tosylatoruthenium(II) tetrafluoridoborate (9)



According to: O. H. Bailey, A. Ludi, *Inorg. Chem.* **1985**, *24*, 2582–2585.

Starting materials: [Ru(H₂O)₆](tos)₂, 1,1'-bis(diphenylphosphanyl)benzylamine (dppbza), THF, tetrafluoroboric acid (50% in H₂O), DCM, diethyl ether.

Procedure:

A mixture of [Ru(H₂O)₆](tos)₂ (275 mg, 0.498 mmol, 1.00 equiv.) and dppbza (476 mg, 1.00 mmol, 2.01 equiv.) was prepared and suspended in THF (10 mL). The suspension was stirred for 1–2 d until an orange-brown solution was formed. The solvent was removed in *vacuo* and the orange crude product was washed with diethyl ether (10 mL). The compound was resolved in DCM (3 mL), HBF₄ (0.13 mL, 2.0 equiv., 50% in H₂O) was added, stirred again, filtered off and layered with diethyl ether. Yellow crystals formed after 2 d. The solvent was removed, the crystals were washed with diethyl ether (10 mL) and dried in *vacuo*.

Empirical formula: C₆₉H₆₁BF₄N₂O₃P₄RuS (1310.09 g/mol).

Yield: 431 mg (0.328 mmol, 65.9%) of dark-yellow prisms.

IR spectroscopy: (RT, solid), (intensity): $\tilde{\nu}$ = 3061vw, 2921vw, 1483w, 1436m, 1274m, 112m, 1050s, 989m, 750m, 695s, 680s cm⁻¹.

UV/VIS spectroscopy: (DCM) Expected signals reside in the solvent cut-off region.

NMR spectroscopy:

¹³C{¹H} NMR spectroscopy (101 MHz, CDCl₃): δ 135.5 (C–CH₃), 135.0 (Ph), 134.7 (Ph), 132.4 (Ph), 131.8 (Ph), 131.3 (Ph), 129.6 (Ph), 129.1 (Ph), 128.6 (Ph), 125.9 (C–SO₃), 66.2 (CH₃–CH₂–O–Et), 53.2 (CH₂), 21.7 (tos–CH₃), 15.7 (CH₃–CH₂–O–Et) ppm.

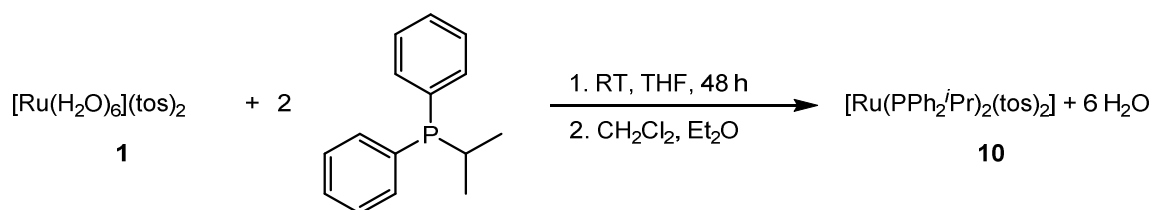
Experimental Part

$^{31}\text{P}\{^1\text{H}\}$ NMR (162 MHz, CDCl_3): δ 87.7 (t, $^2J_{\text{PP}} = 38.4$ Hz), 66.2 (t, $^2J_{\text{PP}} = 38.4$ Hz) ppm.

Elemental Analysis: (calcd. for $\text{C}_{69}\text{H}_{62}\text{BF}_4\text{N}_2\text{O}_3\text{P}_4\text{RuS}\cdot 1.31\text{C}_4\text{H}_{10}\text{O}$, 1408.20 g/mol, found (calcd.): C 62.19% (62.02%), H 4.82% (4.63%), N 2.18% (2.08%), S 2.84% (2.56%).

HRMS (ESI+): $m/z = 1310.30$ ($\text{C}_{69}\text{H}_{61}\text{BF}_4\text{N}_2\text{O}_3\text{P}_4\text{RuS}$).

X-ray structure analysis: uv279

6.5.1.4 Di(*iso*-propyldiphenylphosphane)ditosylatoruthenium(II) (10)

According to: O. H. Bailey, A. Ludi, *Inorg. Chem.* **1985**, *24*, 2582–2585.

Starting materials: $[\text{Ru}(\text{H}_2\text{O})_6](\text{tos})_2$, *i*-propyldiphenylphosphane (99%, PPh_2^iPr), THF, DCM, diethyl ether.

Procedure:

A mixture of $[\text{Ru}(\text{H}_2\text{O})_6](\text{tos})_2$ (275 mg, 0.498 mmol, 1.00 equiv.) and diphenyl-*iso*-propylphosphane PPh_2^iPr (229 mg, 1.00 mmol, 2.01 equiv.) was prepared and suspended in THF (10 mL). The suspension was stirred for 2 d until a dark violet solution was formed. The solvent was removed in *vacuo*. The compound was resolved in DCM (3 mL), filtered off and layered with diethyl ether. Violet crystals formed after 2 d. The solvent was removed, the crystals were washed with cool diethyl ether (3 mL) and dried in *vacuo*.

Empirical formula: $\text{C}_{44}\text{H}_{48}\text{O}_6\text{P}_2\text{RuS}_2$, 899.95 g/mol.

Yield: 368 mg (0.410 mmol, 82.3% of th.) of violet platelet.

IR spectroscopy: (RT, solid), (intensity): $\tilde{\nu} = 1598\text{vw}, 1485\text{w}, 1428\text{w}, 1267\text{m}, 982\text{s}, 672\text{vs cm}^{-1}$.

UV/VIS spectroscopy: $\lambda_{\text{max}}/\text{nm}$ ($\epsilon_{\text{max}}[\text{M}^{-1} \text{cm}^{-1}]$) (DCM) 383 (1028), 530 (467).

NMR spectroscopy:

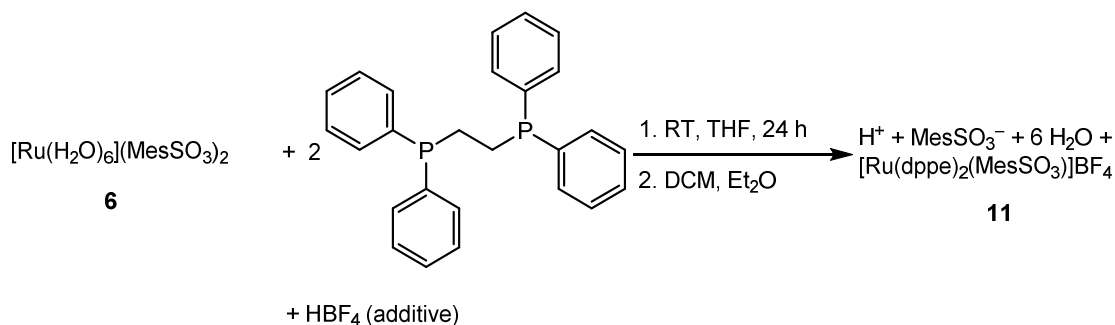
$^{13}\text{C}\{^1\text{H}\}$ NMR spectroscopy (101 MHz, CD_2Cl_2): δ 143.3 ($\underline{\text{C}}\text{-CH}_3$), 139.2 ($\underline{\text{C}}\text{-SO}_3^-$), 134.5 (P-C(Ph)), 129.6 (tos), 127.4 (tos), 27.5 ('d' , $\underline{\text{C}}\text{H-P}$), 21.9 (Ph- CH_3), 18.5 (PCH- $\underline{\text{C}}\text{H}_3$) ppm.

$^{31}\text{P}\{^1\text{H}\}$ NMR (162 MHz, CD_2Cl_2): δ 69.2 (s) ppm.

Elemental Analysis: (calcd. for $\text{C}_{44}\text{H}_{48}\text{O}_6\text{P}_2\text{RuS}_2$, 899.95 g/mol) found (calcd.): C 58.11% (58.72%), H 5.36% (5.38%), S 7.18% (7.13%).

HRMS (ESI+): $m/z = 811.18$. **X-ray structure analysis:** uv107

6.5.1.5 Bis{bis(diphenylphosphanyl)ethane}mesitylsulfonatoruthenium(II) tetrafluoridoborate (11)



According to: O. H. Bailey, A. Ludi, *Inorg. Chem.* **1985**, *24*, 2582–2585.

Starting materials: $[\text{Ru}(\text{H}_2\text{O})_6](\text{MesSO}_3)_2$, 1,2-bis(diphenylphosphanyl)ethane (99%, dppe), THF, tetrafluoroboric acid (50% in H_2O), DCM, diethyl ether.

Procedure:

A mixture of $[\text{Ru}(\text{H}_2\text{O})_6](\text{MesSO}_3)_2$ (304 mg, 0.500 mmol, 1.00 equiv.) and dppe (400 mg, 1.00 mmol, 2.00 equiv.) was prepared and suspended in THF (10 mL). The suspension was stirred for 2 d until an orange solution was formed. The solvent was removed in *vacuo*. The compound was resolved in DCM (3 mL), HBF_4 (0.13 mL, 2.0 equiv., 50% in H_2O) was added, filtered off and layered with diethyl ether. Orange crystals formed after 1 d. The solvent was removed, the crystals were washed with diethyl ether (3 mL) and dried in *vacuo*.

Empirical formula: $\text{C}_{61}\text{H}_{59}\text{BF}_4\text{O}_3\text{P}_4\text{RuS}$ (1183.97 g/mol)

Yield: 534 mg (0.451 mmol, 90.6% of th.) of orange platelets.

IR spectroscopy: (RT, solid), (intensity): $\tilde{\nu} = 3057\text{w}$, 2970w , 2931w , 1604w , 1573w , 1485m , 1470w , 1434s , 1379w , 1310m , 1247vs , 1191s , 1150s , 1081vs , 1051vs , 984vs , 958s , 886m , 872m , 849m , 821m , 797m , 749vs cm^{-1} .

UV/VIS spectroscopy: $\lambda_{\text{max}}/\text{nm}$ (DCM) 341, 379.

NMR spectroscopy:

$^{13}\text{C}\{^1\text{H}\}$ NMR spectroscopy (101 MHz, CD_2Cl_2): δ 140.9 ($\underline{\text{C}}\text{-CH}_3$), 138.5 ($\underline{\text{C}}\text{-SO}_3^-$), 134.4–127.9 (MesSO_3), 66.2, 22.2 ($\underline{\text{C}}\text{H-P}$), 21.0 ($\text{Ph-}\underline{\text{C}}\text{H}_3$), 15.6 ($\text{PCH-}\underline{\text{C}}\text{H}_3$) ppm.

$^{31}\text{P}\{^1\text{H}\}$ NMR (162 MHz, CD_2Cl_2 , RT): δ 60.5 (bs) ppm (additional signals 50.8 (bs), 44.7 (bs) ppm) (bad signal-to-noise ratio).

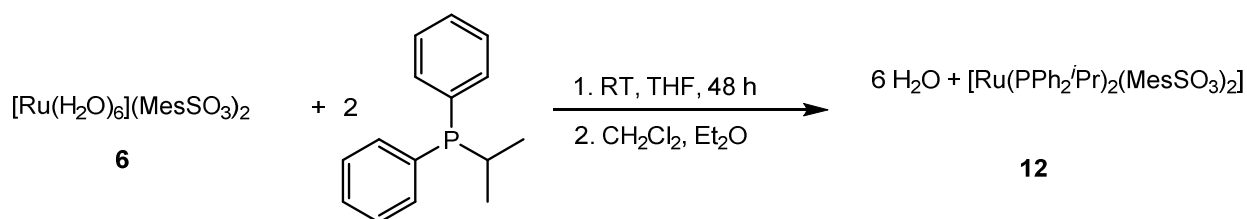
Experimental Part

$^{31}\text{P}\{^1\text{H}\}$ NMR (162 MHz, CD_2Cl_2 , 0 °C): δ 60.6 (br s), 57.8 (br s); 52.0, 50.1 ($\nu_{\text{A}} = 51.0$); 43.4, 41.6 ($\nu_{\text{B}} = 42.6$) ppm.

Elemental Analysis: (calcd. for $\text{C}_{44}\text{H}_{48}\text{O}_6\text{P}_2\text{RuS}_2$, 899.95 g/mol) found (calcd.): C 59.25% (61.83%), H 5.08% (5.10%), S 2.38% (2.71%).

HRMS (ESI+): $m/z = 1183.28$ (added BF_4^-).

X-ray structure analysis: vv826

6.5.1.6 Di(*iso*-propyldiphenylphosphane)dimesitylsulfonatoruthenium(II) (12)

According to: O. H. Bailey, A. Ludi, *Inorg. Chem.* **1985**, *24*, 2582–2585.

Starting materials: $[\text{Ru}(\text{H}_2\text{O})_6](\text{MesSO}_3)_2$, *iso*-propyldiphenylphosphane (99%, PPh_2^iPr), THF, DCM, diethyl ether.

Procedure:

A mixture of $[\text{Ru}(\text{H}_2\text{O})_6](\text{MesSO}_3)_2$ (304 mg, 0.50 mmol, 1.00 equiv.) and PPh_2^iPr (229 mg, 1.00 mmol, 2.00 equiv.) was prepared and suspended in THF (10 mL). The suspension was stirred for 2 d until a dark violet solution was formed. The solvent was removed in *vacuo*. The compound was resolved in DCM (3 mL), filtered off and layered with diethyl ether. Violet crystals formed after 2 d. The solvent was removed, the crystals were washed with cool diethyl ether (3 mL) and dried in *vacuo*.

Empirical formula: $\text{C}_{48}\text{H}_{56}\text{O}_6\text{P}_2\text{RuS}_2$ (956.12 g/mol)

Yield: 313 mg (0.327 mmol, 65.7% of th.) of violet needles.

IR spectroscopy: (RT, solid), (intensity): $\tilde{\nu} = 3047\text{w}$, 2955w , 2928w , 2867w , 1604w , 1566w , 1486w , 1460w , 1435m , 1404w , 1379w , 1362w , 1249vs , 1189w , 1157w , 1084m , 1055m , 1034m , 979vs , 952s , 882w , 857m , 843m , 737m , 707m cm^{-1} .

UV/VIS spectroscopy: $\lambda_{\text{max}}/\text{nm}$ (DCM) 379, 519.

NMR spectroscopy:

$^{13}\text{C}\{^1\text{H}\}$ NMR spectroscopy (101 MHz, CD_2Cl_2): δ 141.0 ($\underline{\text{C}}\text{-CH}_3$), 138.5 ($\underline{\text{C}}\text{-SO}_3^-$), 137.3 (MesSO_3), 134.3 (P-C(Ph)), 131.0 (MesSO_3), 129.6 (MesSO_3), 127.4 ("t", MesSO_3), 27.8 (m, $\underline{\text{C}}\text{H-P}$), 22.37 (tos), 21.3 (Ph-CH_3), 18.6 (PCH-CH_3) ppm.

$^{31}\text{P}\{^1\text{H}\}$ NMR (162 MHz, CD_2Cl_2): δ 70.2 (s) ppm.

Elemental Analysis: (calcd. for $\text{C}_{48}\text{H}_{56}\text{O}_6\text{P}_2\text{RuS}_2$, 956.12 g/mol g/mol) found (calcd.): C 59.90% (60.17%), H 5.93% (6.10%), S 6.47% (6.69%).

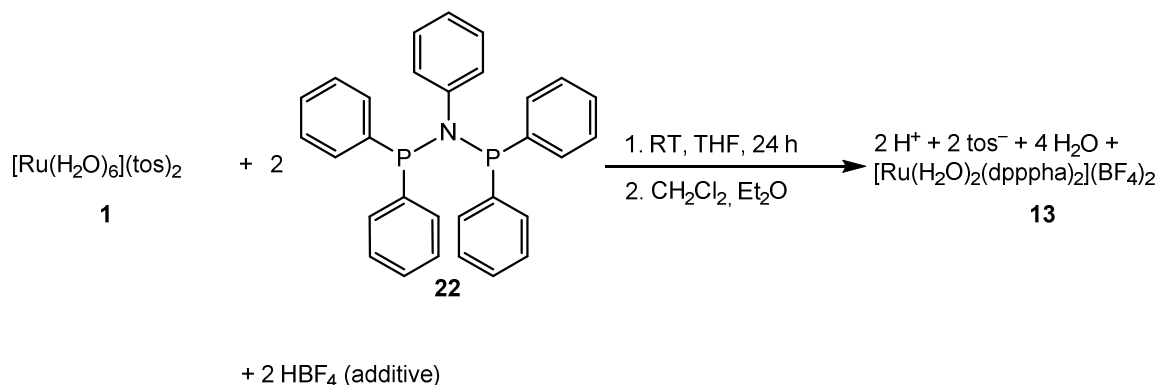
Experimental Part

HRMS (ESI+): $m/z = 839.21$.

X-ray structure analysis: vv833

6.5.2 Phosphane complexes with aqua ligands

6.5.2.1 Diaqua-bis{bis(diphenylphosphanyl)phenylamine}ruthenium(II) tetrafluoridoborate (13)



According to: O. H. Bailey, A. Ludi, *Inorg. Chem.* **1985**, *24*, 2582–2585.

Starting materials: [Ru(H₂O)₆](tos)₂, 1,1'-bis(diphenylphosphanyl)phenylamine (dpppha), THF, tetrafluoroboric acid (50% in H₂O), DCM, diethyl ether.

Procedure:

A mixture of [Ru(H₂O)₆](tos)₂ (275 mg, 0.498 mmol, 1.00 equiv.) and dpppha (462 mg, 1.00 mmol, 2.01 equiv.) was prepared and suspended in THF (10 mL). The suspension was stirred for 1–2 d until a yellow-brown solution was formed. The solvent was removed in *vacuo* and the orange crude product was washed with diethyl ether (10 mL). The compound was resolved in DCM (3 mL), HBF₄ (0.13 mL, 2.0 equiv., 50% in H₂O) was added, stirred again, filtered off and layered with diethyl ether. Yellow crystals formed after 4 d. The solvent was removed, the crystals were washed with *n*-hexane (3 · 10 mL), diethyl ether (10 mL) and dried in *vacuo*.

Empirical formula: C₆₀H₅₄B₂F₈N₂O₂P₄Ru (1233.68 g/mol)

Yield: 297 mg (0.241 mmol, 48.4% of th.) of yellow crystal agglomerates.

IR spectroscopy: (RT, solid), (intensity): $\tilde{\nu}$ = 1590vw, 1495w, 1436w, 1212m, 1158m, 1100m, 928m, 876w, 814w, 741m, 689m cm⁻¹.

UV/VIS spectroscopy: λ_{max} /nm (DCM) 349.0, 423.1.

NMR spectroscopy:

Experimental Part

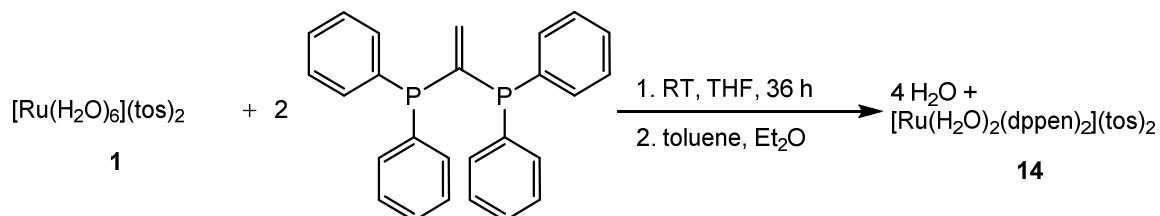
$^{13}\text{C}\{^1\text{H}\}$ NMR spectroscopy (101 MHz, CD_2Cl_2): δ 132.3–122.5 (Ph) ppm.

$^{31}\text{P}\{^1\text{H}\}$ NMR (162 MHz, CD_2Cl_2): δ 78.7 (s) (main signal), 90.1, 88.8, 87.4, 63.4, 52.9, 35.8 (several subsidiary signals) ppm.

HRMS (ESI+): m/z = 1082.20.

X-ray structure analysis: uv275

6.5.2.2 Diaqua-bis{1,1'-bis(diphenylphosphanyl)ethene}ruthenium(II) tetrafluoroborate (14)



According to: O. H. Bailey, A. Ludi, *Inorg. Chem.* **1985**, *24*, 2582–2585.

Starting materials: $[\text{Ru}(\text{H}_2\text{O})_6](\text{tos})_2$, 1,1'-bis(diphenylphosphanyl)ethene (99%, dppen), THF, tetrafluoroboric acid (50% in H_2O), DCM, diethyl ether.

Procedure:

A mixture of $[\text{Ru}(\text{H}_2\text{O})_6](\text{tos})_2$ (275 mg, 0.498 mmol, 1.00 equiv.) and dppen (397 mg, 1.00 mmol, 2.01 equiv.) was prepared and suspended in THF (10 mL). The suspension was stirred for 1–2 d until an orange solution was formed. The solvent was removed in *vacuo* and the orange crude product was washed with diethyl ether (10 mL). The compound was resolved in toluene (3 mL) was added, stirred again, filtered off and layered with diethyl ether. Yellow crystals formed after 5 d. The solvent was removed, the crystals were washed with *n*-hexane (3 · 10 mL) and dried in *vacuo*.

Empirical formula: $\text{C}_{66}\text{H}_{64}\text{O}_8\text{P}_4\text{RuS}_2$ (1274.33 g/mol)

Yield: 343 mg (0.269 mmol, 54.0% of th.) of dark yellow crystal agglomerates.

IR spectroscopy: (RT, solid), (intensity): $\tilde{\nu} = 3056\text{vw}, 2084\text{vw}, 1653\text{w}, 1435\text{m}, 1055\text{m}, 729\text{m cm}^{-1}$.

UV/VIS spectroscopy: $\lambda_{\text{max}}/\text{nm}$ (DCM) 364.2, 427.5.

NMR spectroscopy:

$^{13}\text{C}\{^1\text{H}\}$ NMR spectroscopy (101 MHz, CD_2Cl_2): δ 142.7 (Ph), 134.3–126.18 (m) (Ph + $\text{C}=\text{CH}_2$), subsidiary species: 66.2, 21.7, 15.7, 1.33 ppm.

$^{31}\text{P}\{^1\text{H}\}$ NMR (162 MHz, CD_2Cl_2): δ 23.1 (s), 3.14 (s) (main species), 61.5, 33.8, 8.6, 6.5 (subsidiary species) ppm.

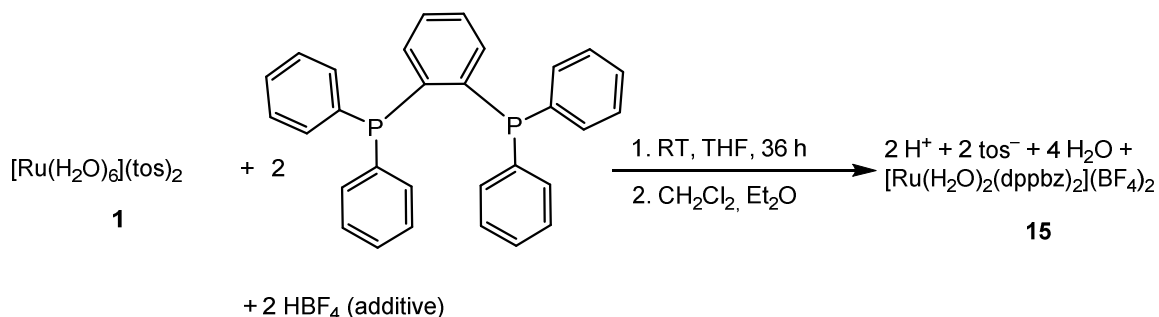
Elemental Analysis: (calcd. for $\text{C}_{66}\text{H}_{64}\text{O}_8\text{P}_4\text{RuS}_2(\text{BF}_4)(\text{tos})$, 956.12 g/mol g/mol) found (calcd.): C 59.78% (59.55%), H 4.92% (4.83%), S 2.16% (2.69%).

Experimental Part

HRMS (ESI+): $m/z = 1082.22$.

X-ray structure analysis: uv186

6.5.2.3 Diaqua-bis{1,2-bis(diphenylphosphanyl)benzene}ruthenium(II) tetrafluoridoborate (15)



According to: O. H. Bailey, A. Ludi, *Inorg. Chem.* **1985**, *24*, 2582–2585.

Starting materials: [Ru(H₂O)₆](tos)₂, 1,2-bis(diphenylphosphanyl)benzene (99%, dppbz), THF, tetrafluoroboric acid (50% in H₂O), DCM, diethyl ether.

Procedure:

A mixture of [Ru(H₂O)₆](tos)₂ (275 mg, 0.498 mmol, 1.00 equiv.) and dppbz (224 mg, 1.00 mmol, 2.01 equiv.) was prepared and suspended in THF (10 mL). The suspension was stirred for 1–2 d until a light-yellow solution was formed. The solvent was removed in *vacuo* and the yellow crude product was washed with diethyl ether (4 mL). The compound was resolved in DCM (3 mL), HBF₄ (0.13 μL, 2.0 equiv., 50% in H₂O) was added, stirred again, filtered off and layered with diethyl ether. Yellow crystals formed after 3 d. The solvent was removed, the crystals were washed with *n*-hexane (3 · 10 mL) and dried in *vacuo*.

Empirical formula: C₆₀H₅₂B₂F₈O₂P₄Ru (1203.65 g/mol)

Yield: 370 mg (0.307 mmol, 61.6% of th.) of yellow rods.

IR spectroscopy: (RT, solid), (intensity): $\tilde{\nu}$ = 3524w, 3555br, 3066vw, 1636m, 1482m, 1434m, 1314w, 1277w, 1255w, 1189m, 1165m, 1146m, 1099vs, 1061vs, 983vs, 851m, 777s, 754vs, 742vs cm⁻¹.

UV/VIS spectroscopy: λ_{max} /nm (DCM) 434.1.

NMR spectroscopy:

³¹P{¹H} NMR (162 MHz, CD₂Cl₂): δ 50.66 (s) ppm.

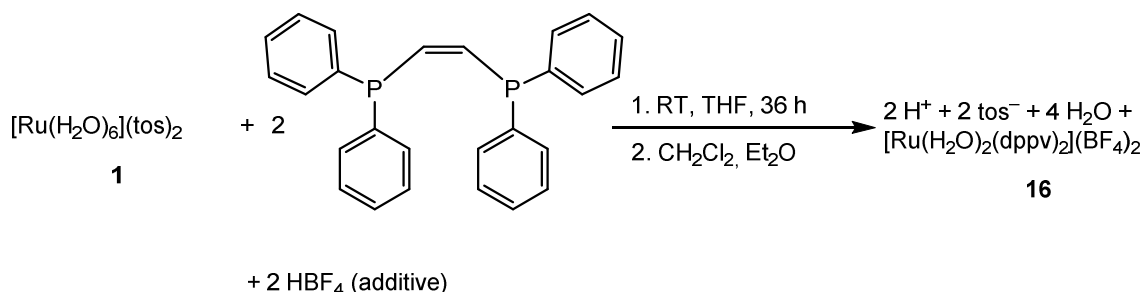
Experimental Part

Elemental Analysis: (calcd. for $C_{60}H_{52}O_2P_4Ru$, 1030.04 g/mol) found (calcd.): C 56.82% (59.87%), H 4.36% (4.35%).^[161]

HRMS (ESI+): $m/z = 1054.20$.

X-ray structure analysis: vv399

6.5.2.4 Diaqua-bis{*cis*-1,2-bis(diphenylphosphanyl)ethene}ruthenium(II) tetrafluoridoborate (16)



According to: O. H. Bailey, A. Ludi, *Inorg. Chem.* **1985**, *24*, 2582–2585. **Literature:** D. Beck, P. Klüfers, *Chem. Eur. J.* **2018**, *24*, 16019–16028.

Starting materials: $[\text{Ru}(\text{H}_2\text{O})_6](\text{tos})_2$, 1,2-bis(diphenylphosphanyl)ethene (99%, dppv), THF, tetrafluoroboric acid (50% in H_2O), DCM, diethyl ether.

Procedure:

A suspension of $[\text{Ru}(\text{H}_2\text{O})_6](\text{tos})_2$ (275 mg, 0.498 mmol, 1.00 equiv.) and dppv (397 mg, 1.00 mmol, 2.01 equiv.) in THF (10 mL) was stirred for 24 h. The solvent was removed and the crude product was suspended in DCM (3 mL). To this suspension, HBF_4 (126 μL , 2.00 equiv., 50% in water) was added. After filtration through a syringe filter, the solution was layered with diethyl ether. After crystallization and removal of the residual solvent, the crystals were washed three times with cyclohexane (10 mL each) and dried *in vacuo*.

Empirical formula: $\text{C}_{52}\text{H}_{48}\text{B}_2\text{F}_8\text{O}_2\text{P}_4\text{Ru}$ (1103.53 g/mol)

Yield: 125 mg (0.113 mmol, 22.7% of th.) of yellow crystal agglomerates.

IR spectroscopy: (RT, solid), (intensity): $\tilde{\nu} = 3059\text{w}, 1633\text{w}, 1599\text{w}, 1483\text{m}, 1433\text{s}, 1404\text{w}, 1316\text{m}, 1267\text{m}, 1253\text{s}, 1190\text{m}, 1139\text{m}, 1098\text{s}, 1050\text{vs}, 1030\text{vs}, 1001\text{vs}, 921\text{w}, 847\text{w}, 816\text{m}, 740\text{vs}, 718\text{m cm}^{-1}$.

UV/VIS spectroscopy: $\lambda_{\text{max}}/\text{nm}$ (DCM) 274.0, 360.4

NMR spectroscopy:

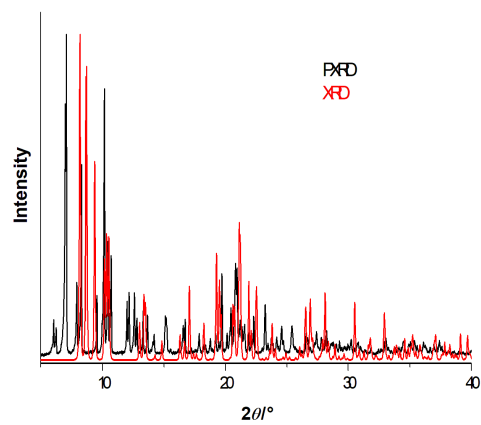
$^{31}\text{P}\{^1\text{H}\}$ NMR (162 MHz, CD_2Cl_2): δ 69.2 (t, $^3J_{\text{PP}} = 15$ Hz), 54.2 (t, $^3J_{\text{PP}} = 15$ Hz) ppm (additional signals 66.47 (t), 58.9 (br), 55.7 (s) ppm).

HRMS (ESI+): $m/z = 929.91$ ($\text{C}_{52}\text{H}_{58}\text{O}_2\text{P}_4\text{Ru}$).

Experimental Part

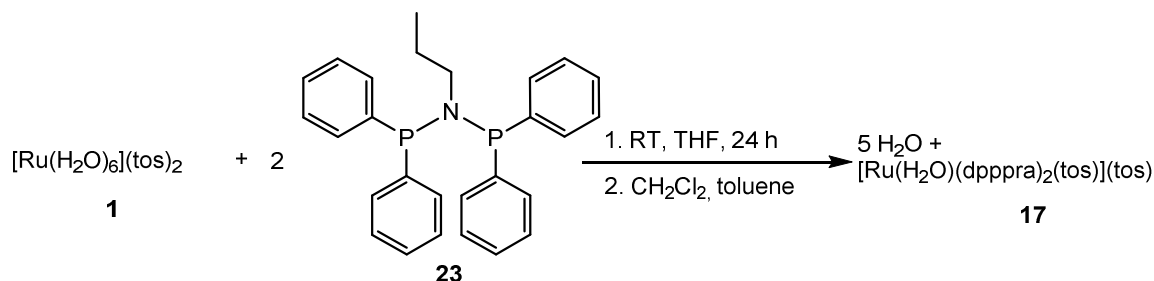
X-ray structure analysis: vv418

PXRD:



Graph 3: Powder-X-ray diffraction of **16**. Red: X-ray diffraction at 100 K, Black: Powder-X-ray diffraction at RT.^[39]

6.5.3 Borderline complexes between chelate and diaqua coordination

6.5.3.1 Aqua-bis{bis(diphenylphosphanyl)-*n*-propylamine}tosylatoruthenium(II) tetrafluoridoborate (17)

According to: O. H. Bailey, A. Ludi, *Inorg. Chem.* **1985**, *24*, 2582–2585.

Starting materials: $[\text{Ru}(\text{H}_2\text{O})_6](\text{tos})_2$, 1,2-bis(diphenylphosphanyl)propylamine, THF, DCM, toluene.

Procedure:

A suspension of $[\text{Ru}(\text{H}_2\text{O})_6](\text{tos})_2$ (275 mg, 0.498 mmol, 1.00 equiv.) and dppv (428 mg, 1.00 mmol, 2.01 equiv.) in THF (10 mL) was stirred for 24 h. The solvent was removed and the crude product was suspended in DCM (3 mL). After filtration through a syringe filter, the solution was layered with toluene. After crystallization and removal of the residual solvent, the crystals were washed three times with *n*-hexane (5 mL each), three times with diethyl ether (5 mL each) and dried *in vacuo*.

Empirical formula: $\text{C}_{68}\text{H}_{72}\text{N}_2\text{O}_7\text{P}_4\text{RuS}_2$ (1318.42 g/mol)

Yield: 288 mg (0.218 mmol, 43.8% of th.) of yellow platelets.

IR spectroscopy: (RT, solid), (intensity): $\tilde{\nu} = \approx 3350, \approx 3200, 3057\text{w}, 2997\text{w}, 2084\text{vw}, 1623\text{w}, 1485\text{m}, 1435\text{m}, 1282\text{w}, 1172\text{--}1036, 816\text{m}, 668\text{vs cm}^{-1}$.

UV/VIS spectroscopy: $\lambda_{\text{max}}/\text{nm}$ (DCM) 305.5, 362.0.

NMR spectroscopy:

$^{13}\text{C}\{^1\text{H}\}$ NMR spectroscopy (101 MHz, CD_2Cl_2): δ 143.1 ($\underline{\text{C}}\text{-CH}_3$), 138.9 (C-SO₃), 135.2–128.7 (m, Ph), 126.0 (Ph), 53.2 ($\underline{\text{C}}\text{H}_2\text{-CH}_2\text{-CH}_3$), 21.7 ($\text{CH}_2\text{-}\underline{\text{C}}\text{H}_2\text{-CH}_3$), 11.5 ($\text{CH}_2\text{-CH}_2\text{-}\underline{\text{C}}\text{H}_3$) ppm.

$^{31}\text{P}\{^1\text{H}\}$ NMR (162 MHz, CD_2Cl_2): δ 83.6 (t, $^2J_{\text{PP}} = 37.6$ Hz), 62.2 (t, $^2J_{\text{PP}} = 37.6$ Hz) ppm.

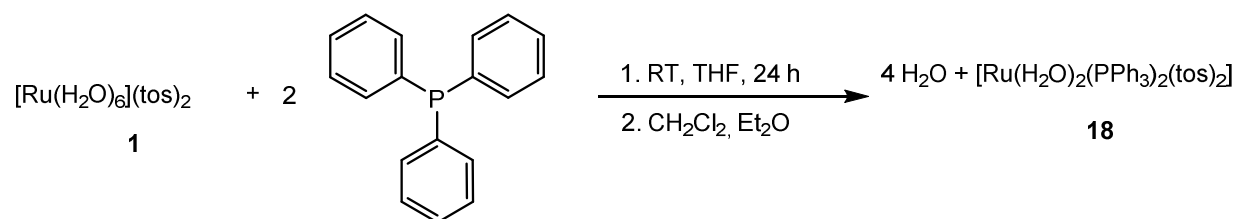
Elemental Analysis: (calcd. for $\text{C}_{68}\text{H}_{72}\text{N}_2\text{O}_7\text{P}_4\text{RuS}_2 \cdot 1.89 \text{ C}_7\text{H}_8$, 1492.57 g/mol) found (calcd.): C 67.91% (65.60%), H 5.62% (5.50%), N 1.98% (2.12%), S 3.76% (3.50%).^[161]

Experimental Part

HRMS (ESI+): $m/z = 1127.24$ or 1209.29 .

X-ray structure analysis: uv148

6.5.3.2 Diaqua-bis(triphenylphosphane)ditosylatoruthenium(II) (18)



According to: O. H. Bailey, A. Ludi, *Inorg. Chem.* **1985**, *24*, 2582–2585.

Starting materials: $[\text{Ru}(\text{H}_2\text{O})_6](\text{tos})_2$, triphenylphosphane (PPh_3) (99%), THF, diethyl ether, DCM.

Procedure:

To a suspension of $[\text{Ru}(\text{H}_2\text{O})_6](\text{tos})_2$ (275 mg, 0.498 mmol, 1.00 equiv.) in THF (5 mL) triphenylphosphane (PPh_3) (263 mg, 1.00 mmol, 2.01 equiv.) was added. The mixture was stirred for 72 h, whereby the solution turned orange. The solvent was removed *in vacuo*, the solid was dried and resolved in DCM (2 mL). The solution was filtered through a syringe filter and the filtrate was layered with diethyl ether (4 mL) and stored at -20°C . The obtained crystals were washed with *n*-hexane (3 · 2.5 mL) and dried *in vacuo*.

Empirical formula: $\text{C}_{50}\text{H}_{48}\text{O}_8\text{P}_2\text{RuS}_2$, 1004.06 g/mol.

Yield: 279 mg (0.278 mmol, 55.8% of th.) of red blocks.

IR spectroscopy: (RT, solid), (intensity): $\tilde{\nu} = 3060\text{vw}$, 1599w , 1483m , 1436m , 1220m , 1145s , 979vs , 693vs cm^{-1} .

UV/VIS spectroscopy: $\lambda_{\text{max}}/\text{nm}$ ($\epsilon_{\text{max}}[\text{M}^{-1} \text{cm}^{-1}]$) (DCM) 372 (1030), 474 (181).

NMR spectroscopy:

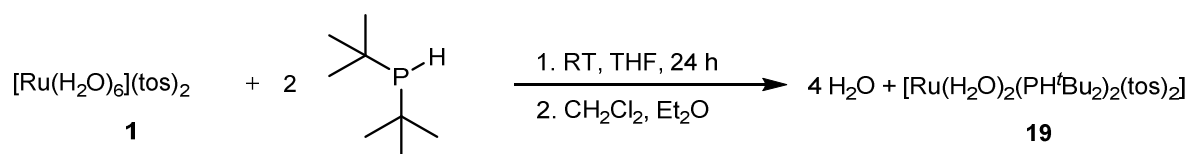
$^{13}\text{C}\{^1\text{H}\}$ NMR spectroscopy (101 MHz, CD_2Cl_2): δ 142.3 ($\underline{\text{C}}-\text{CH}_3$), 140.0 ($\underline{\text{C}}-\text{SO}_3^-$), 134.9 ($\underline{\text{C}}-\text{SO}_3^-$), 133.4 (m, $\text{P}-\underline{\text{C}}_1$), 126.2–129.9 (Ph – tos), 21.7 (tos– CH_3) ppm.

$^{31}\text{P}\{^1\text{H}\}$ NMR (162 MHz, CD_2Cl_2): δ 52.6 (s) ppm.

Elemental Analysis: (calcd. for $\text{C}_{30}\text{H}_{56}\text{O}_8\text{P}_2\text{RuS}_2$, 771.87 g/mol) found (calcd.): C 59.75% (59.82%), H 4.87% (4.82%), S 6.50% (6.39%).

HRMS (ESI+): $m/z = 838.12$ **X-ray structure analysis:** vv088

6.5.3.3 Diaqua-bis(di-tert-butylphosphane)ditosylatoruthenium(II) (19)



According to: O. H. Bailey, A. Ludi, *Inorg. Chem.* **1985**, *24*, 2582–2585.

Starting materials: $[\text{Ru}(\text{H}_2\text{O})_6](\text{tos})_2$, di-tert-butylphosphane (PH^tBu_2) (98%), THF, diethyl ether, DCM.

Procedure:

To a suspension of $[\text{Ru}(\text{H}_2\text{O})_6](\text{tos})_2$ (275 mg, 0.498 mmol, 1.00 equiv.) in THF (5 mL) di-tert-butylphosphane (PH^tBu_2) (292 mg, 370 μL , 1.00 mmol, 2.01 equiv.) was added. The mixture was stirred for 24 h. The colour changed from yellowish to orange-red. The solvent was removed *in vacuo*, the solid was dried and resolved in DCM (2 mL). The solution was filtered through a syringe filter and the filtrate was layered with diethyl ether. The obtained crystals were washed with cyclohexane (3 · 10 mL) and dried *in vacuo*.

Empirical formula: $\text{C}_{30}\text{H}_{56}\text{O}_8\text{P}_2\text{RuS}_2$, 771.87 g/mol.

Yield: 210 mg (0.272 mmol, 54.6% of th.) of red platelets.

IR spectroscopy: (RT, solid), (intensity): $\tilde{\nu} = 2902\text{br}, 2314\text{w}, 1601\text{vw}, 1496\text{vw}, 1366\text{m}, 1150\text{vs}, 1221\text{s}, 984 \text{ cm}^{-1}$.

UV/VIS spectroscopy: $\lambda_{\text{max}}/\text{nm}$ ($\epsilon_{\text{max}}[\text{M}^{-1} \text{ cm}^{-1}]$) (DCM) 377 (1467), 516 (215).

NMR spectroscopy:

$^{13}\text{C}\{^1\text{H}\}$ NMR spectroscopy (101 MHz, CD_2Cl_2): δ 142.2 ($\underline{\text{C}}\text{-CH}_3$), 139.9 ($\underline{\text{C}}\text{-SO}_3^-$), 129.3 (tos aromatic), 126.2 (tos), 36.6 ("t", $\text{C}(\text{CH}_3)_3$), 32.3 (P-CCH₃), 21.7 (Ph-CH₃) ppm.

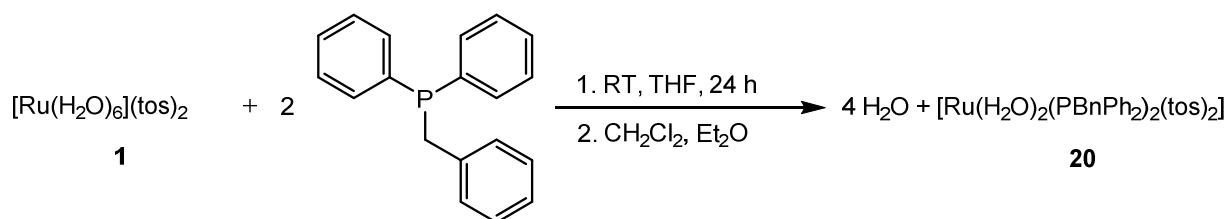
$^{31}\text{P}\{^1\text{H}\}$ NMR (162 MHz, CD_2Cl_2): δ 75.0 (s) ppm.

Elemental Analysis: (calcd. for $\text{C}_{30}\text{H}_{56}\text{O}_8\text{P}_2\text{RuS}_2$, 771.87 g/mol) found (calcd.): C 46.80% (46.68%), H 7.24% (7.31%), S 8.40% (8.31%).

HRMS (ESI+): $m/z = 606.19$.

X-ray structure analysis: vv035

6.5.3.4 Diaqua-di(benzylidiphenylphosphane)ditosylatoruthenium(II) (20)



According to: O. H. Bailey, A. Ludi, *Inorg. Chem.* **1985**, *24*, 2582–2585.

Starting materials: $[\text{Ru}(\text{H}_2\text{O})_6](\text{tos})_2$, benzylidiphenylphosphane (PPh_2Bn) (98%), THF, diethyl ether, DCM.

Procedure:

To a suspension of $[\text{Ru}(\text{H}_2\text{O})_6](\text{tos})_2$ (275 mg, 0.498 mmol, 1.00 equiv.) in THF (5 mL) benzylidiphenylphosphane (PPh_2Bn) (277 mg, 1.00 mmol, 2.00 equiv.) was added. The mixture was stirred for 36 h. The solvent was removed *in vacuo*, the solid was dried and resolved in DCM (2 mL). The solution was filtered through a syringe filter and the filtrate was layered with diethyl ether (8 mL). The obtained crystals were washed with diethyl ether (3 · 2.5 mL) and dried *in vacuo*.

Empirical formula: $\text{C}_{52}\text{H}_{52}\text{O}_8\text{P}_2\text{RuS}_2$, 1032.13 g/mol.

Yield: 133 mg (0.129 mmol, 25.9% of th.) of dark-yellow blocks.

IR spectroscopy: (RT, solid), (intensity): $\tilde{\nu} = 3059\text{vw}$, 1600vw , 1494w , 1438w , 1452vw , 1216m , 1151s , 1103 , 989vs , 694vs cm^{-1} .

UV/VIS spectroscopy: $\lambda_{\text{max}}/\text{nm}$ ($\epsilon_{\text{max}}[\text{M}^{-1} \text{cm}^{-1}]$) (DCM) 360 (3478), 463 (805).

NMR spectroscopy: $^{13}\text{C}\{^1\text{H}\}$ NMR spectroscopy (101 MHz, CD_2Cl_2): δ 142.4 ($\underline{\text{C}}\text{-CH}_3$), 139.9 ($\underline{\text{C}}\text{-SO}_3^-$), 135.8 (Bn-C1), 134.2, 131.8 (Ph-C1), 126.9–131.4 (tos aromatic), 66.8 (Et-O- $\underline{\text{C}}\text{H}_2\text{-CH}_3$), 35.3 (“t”, (P- $\underline{\text{C}}\text{H}_2$)), 21.7 (tos- $\underline{\text{C}}\text{H}_3$), 15.7 (Et-O- $\underline{\text{C}}\text{H}_2\text{-CH}_3$) ppm.

$^{31}\text{P}\{^1\text{H}\}$ NMR (162 MHz, CD_2Cl_2): δ 59.8 (s) ppm.

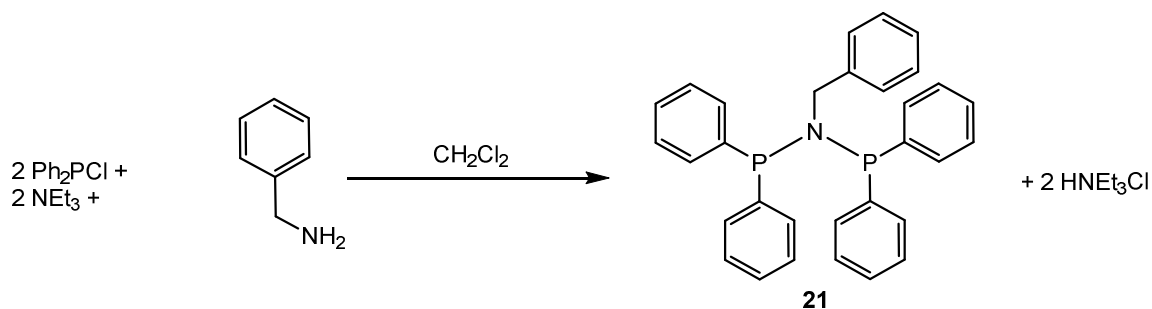
Elemental Analysis: (calcd. for $\text{C}_{56}\text{H}_{62}\text{O}_9\text{P}_2\text{RuS}_2$, 1106.19 g/mol) found (calcd.): C 60.80% (60.94%), H 5.65% (5.48%), S 5.80% (5.81%).

HRMS (ESI+): $m/z = 866.16$.

X-ray structure analysis: vv193

6.5.4 Syntheses of bisphosphanes

6.5.4.1 dppbza, bis(diphenylphosphanyl)benzylamine (21)



Literature: Y. Wang, Z. Li, X. Zeng, X. Wang, C. Zhan, Y. Liu, Q. Luo, X. Liu, *New J. Chem.* **2009**, *33*, 1780.

Starting materials: acetonitrile, benzylamine, DCM, chlorodiphenylphosphane, magnesium sulfate, sodium hydroxide, triethylamine.

Procedure:

Benzylamine (2.44 mL, 22.4 mmol) was solved in DCM (100 mL). An equivalent chlorodiphenylphosphane (4.02 mL, 22.4 mmol) and triethylamine (30 mL) were added and the solution was stirred for 30 min at RT. Then, another equivalent of chlorodiphenylphosphane was added and stirred for 18 h. The solvent was removed *in vacuo* and the residue was resolved in DCM (50 mL). The solution was washed with saturated NaOH solution and dried over MgSO₄. The solid was filtered off, the solvent removed *in vacuo* and the residue was recrystallised from DCM/acetonitrile (1:2) at 4 °C. The solvent was decanted and the crystals were washed with acetonitrile (5 mL) and dried *in vacuo*.

Empirical formula: C₃₁H₂₇NP₂, 475.50 g/mol.

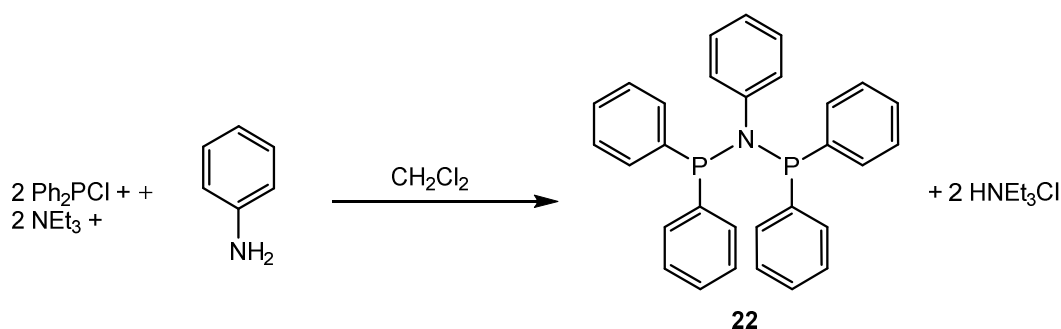
Yield: 3.84 g (8.07 mmol, 36.0% of th.) of colourless blocks.

NMR spectroscopy: ¹³C{¹H} NMR spectroscopy (101 MHz, THF-d₈): δ 141.2 (Ph), 141.0 (Ph), 140.8 (Ph), 134.1 (Ph), 134.0 (Ph), 133.9 (Ph), 130.0 (Ph), 129.6 (Ph), 128.7 (Ph), 127.6 (Ph), 57.1 (CH₂) ppm.

³¹P{¹H} NMR (162 MHz, THF-d₈): δ 61.2 (s) ppm.

Elemental Analysis: (calcd. for C₃₁H₂₇NP₂, 475.50 g/mol) found (calcd.): C 78.12% (78.30%), H 5.73% (5.72%), N 2.96% (2.95%).

6.5.4.2 dpppha, bis(diphenylphosphanyl)phenylamine (22)



Literature: W. Seidel, M. Alexiev, *Z. Anorg. Allg. Chem.* **1978**, 438, 68–74. Mayer Tobias, *Dinukleare Nitrosyl- und Hyponitrito-Komplexe*, Ph.D. thesis, LMU München, **2012**.

Starting materials: aniline, acetonitrile, DCM, chlorodiphenylphosphane, magnesium sulfate, sodium hydroxide, triethylamine.

Procedure:

Aniline (1.00 mL, 11.2 mmol) was solved in DCM (30 mL). An equivalent chlorodiphenylphosphane (2.07 mL, 11.2 mmol) and triethylamine (15 mL) were added and the solution was stirred for 30 min at RT. Then, another equivalent of chlorodiphenylphosphane was added and stirred for 18 h. The solvent was removed *in vacuo* and the residue was resolved in DCM (30 mL). The solution was washed with saturated NaOH solution and dried over MgSO₄. The solid was filtered off, the solvent removed *in vacuo* and the residue was recrystallised from DCM/acetonitrile (1:2) at 4 °C. The solvent was decanted and the crystals were washed with acetonitrile (5 mL) and dried *in vacuo*.

Empirical formula: C₃₀H₂₅NP₂, 461.48 g/mol.

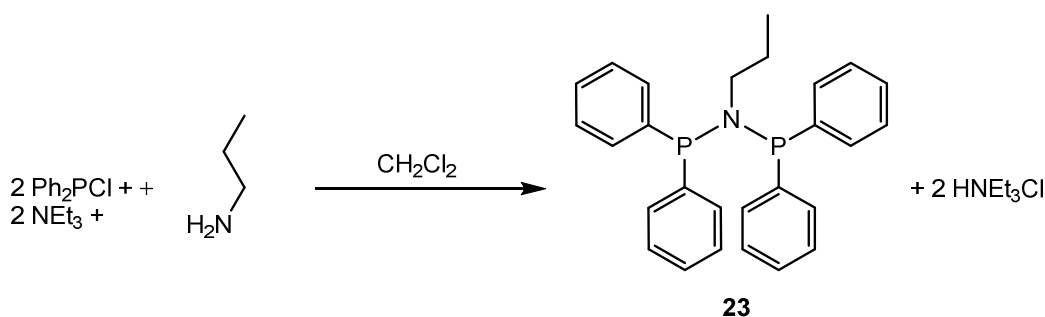
Yield: 3.68 g (7.97 mmol, 71.1% of th.) of colourless powder.

NMR spectroscopy: ¹³C{¹H} NMR spectroscopy (101 MHz, THF-d₈): δ 149.0 (Ph), 140.8 (Ph), 134.2 (Ph), 130.0 (Ph), 129.0 (Ph), 125.9 (Ph), 111.1 (Ph) ppm.

³¹P{¹H} NMR (162 MHz, THF-d₈): δ 69.1 (s) ppm.

Elemental Analysis: (calcd. for C₃₀H₂₅NP₂, 461.48 g/mol) found (calcd.): C 77.93% (78.08%), H 5.46% (5.46%), N 3.07% (3.04%).

6.5.4.3 dpppra, bis(diphenylphosphanyl)propylamine (23)



According to: T. Mayer, H.-C. Böttcher, *Z. Naturforsch. B* **2012**, 67, 504–506.

Starting materials: *n*-propylamine, acetonitrile, DCM, chlorodiphenylphosphane, magnesium sulfate, sodium hydroxide, triethylamine.

Procedure:

n-Propylamine (0.90 mL, 11.2 mmol) was solved in DCM (30 mL). An equivalent chlorodiphenylphosphane (2.07 mL, 11.2 mmol) and triethylamine (15 mL) were added and the solution was stirred for 30 min at RT. Then, another equivalent of chlorodiphenylphosphane was added and stirred for 18 h. The solvent was removed *in vacuo* and the residue was resolved in DCM (30 mL). The solution was washed with saturated NaOH solution and dried over MgSO₄. The solid was filtered off, the solvent removed *in vacuo* and the residue was recrystallised from DCM/acetonitrile (1:2) at –20 °C. The solvent was decanted and the crystals were washed with ice-cold acetonitrile (5 mL) and dried *in vacuo*.

Empirical formula: C₂₇H₂₇NP₂, 427.47 g/mol

Yield: 2.93 g (6.85 mmol, 61.1% of th.) of colourless blocks.

NMR spectroscopy: ¹³C{¹H} NMR spectroscopy (101 MHz, THF-d₈): δ 140.4 (Ph), 140.3 (Ph), 133.4 (Ph), 133.3 (Ph), 133.1 (Ph), 129.3 (Ph), 128.6 (Ph), 128.5 (Ph), 55.4 (CH₂–CH₂–CH₃), 25.2 (CH₂–CH₂–CH₃), 11.2 (CH₂–CH₂–CH₃) ppm.

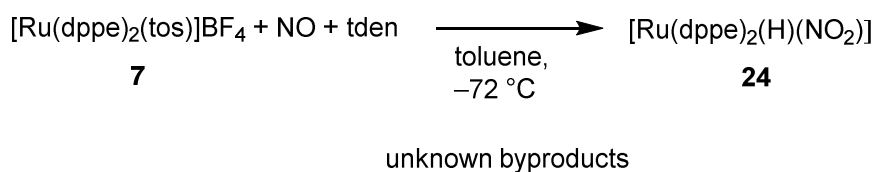
³¹P{¹H} NMR (162 MHz, THF-d₈): δ 63.2 (s) ppm.

Elemental Analysis: (calcd. for C₃₀H₂₅NP₂, 461.48 g/mol) found (calcd.): C 75.67% (75.86%), H 6.37% (6.35%), N 3.28% (3.28%).

HRMS (ESI+): m/z = 428.16 ([M–H]⁺, C₂₇H₂₈NP₂).

6.6 Reactions with gaseous nitric oxide

6.6.1 Bis{bis(diphenylphosphanyl)ethane}hydridonitritoruthenium(0) (24)



Starting materials: $[\text{Ru}(\text{dppe})_2(\text{tos})]\text{BF}_4$, toluene, tetrakisdiamino ethylene, nitrogen monoxide, DCM, diethyl ether.

Procedure:

The previously synthesised product $[\text{Ru}(\text{dppe})_2(\text{tos})](\text{BF}_4)$ (**7**) was solved in refluxing toluene (40 mL). tetrakis(dimethylamino)ethylene (tden; 200 μL , excess) was added. After cooling the solution to -72°C using a dry-ice/*i*-propanol cooling bath, the solution was treated with nitrogen monoxide for 1.5 h. The solution turned red. The solution was brought to room temperature whereby the colour changed from red to ocher. The solvent was decanted, the solid dried and resolved in DCM. The solution was filtered through a syringe filter and layered with diethyl ether. The obtained yellow-red crystal agglomerates were analysed without further work-up because of their sensitivity.

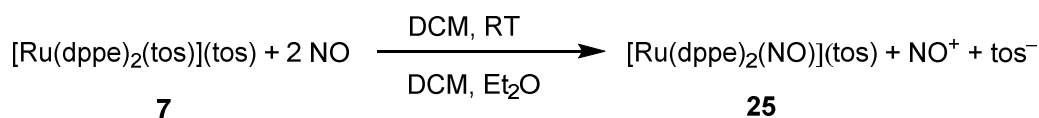
Empirical formula: $\text{C}_{52}\text{H}_{49}\text{NO}_2\text{P}_4\text{Ru}$, 944.93 g/mol.

Yield: Few agglomerates of yellow platelets.

X-ray structure analysis: vv099

Please note: The compound is water and oxygen sensitive. Therefore, successful analytics were not possible due to fast decomposition (melting of the crystals within few minutes). Nonetheless, the synthesis is repeatable.

6.6.2 Bis{bis(diphenylphosphanyl)ethane}nitrosylruthenium tosylate (25)



tentative byproducts

Starting materials: [Ru(dppe)₂(tos)](tos), DCM, nitrogen monoxide, diethyl ether.

Procedure:

The previously synthesised product [Ru(dppe)₂(tos)](tos) (**7**) was solved in DCM (20 mL). The solution was treated with nitrogen monoxide for 1.5 h at RT. The solution turned brown-red. The solution was filtered through a syringe filter and layered with diethyl ether. The obtained brown-red crystals were filtered off and dried *in vacuo*.

Empirical formula: C₅₉H₅₅NO₄P₄RuS, 1099.12 g/mol

Yield: Few agglomerates of red blocks (≈ 100 mg).

IR spectroscopy: (RT, solid), (intensity): $\tilde{\nu}$ = 3054 vw, 1665 (NO-stretch vib.) m, 1598vw, 1573 vw, 1483w, 1434s, 1252m, 1173s, 1158s, 1119vs, 1096vs, 1027m, 991s, 814s, 741vs cm⁻¹.

UV/VIS spectroscopy: λ_{max} /nm (DCM) ≈ 350 (sh), ≈ 425 (sh)

NMR spectroscopy:

³¹P{¹H} NMR (162 MHz, CD₂Cl₂): δ 61.4, 31.8. ppm.

HRMS (FAB+): m/z = 928.17 (¹²C₅₂H₄₈ONP₄¹⁰²Ru).

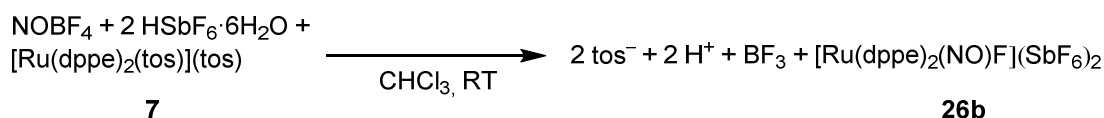
X-ray structure analysis: vv142

6.6.3 Bis{bis(diphenylphosphanyl)ethane}fluoridonitrosylruthenium tetrafluoridoborate (26a)

variant I



variant II



Starting materials: [Ru(dppe)₂(tos)]BF₄, nitric oxide, DCM, CHCl₃, NOBF₄, diethyl ether, HSbF₆·6H₂O.

Procedure:

Variant I

The previously synthesised product [Ru(dppe)₂(tos)](BF₄) (**7**) was solved in DCM (20 mL). To this solution crystalline HSbF₆ · xH₂O (ca. 250 mg) was added. The solution was treated with nitrogen monoxide for 1 h at RT. The solution turned brown-orange. The solution was stirred overnight, filtered through a syringe filter and layered with diethyl ether. The obtained yellow crystals were filtered off and dried *in vacuo*.

Variant II

The previously synthesised product [Ru(dppe)₂(tos)](tos) (**7**) was solved in CHCl₃ (5 mL). To this solution crystalline HSbF₆ · xH₂O (ca. 400 mg) was added. The solution was treated with NOBF₄ (175 mg, 1.5 mmol). The solution turned brown-orange. The solution was stirred overnight, filtered through a syringe filter and layered with diethyl ether. The obtained yellow crystals were filtered off and dried *in vacuo*.

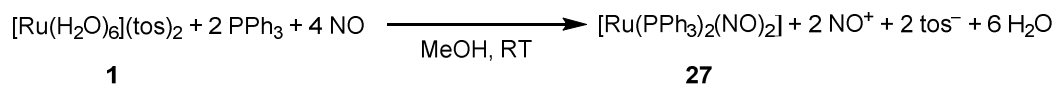
Empirical formula: C₅₂H₄₈F₁₃NOP₄RuSb₂, 1418.40 g/mol.

Yield: 320 mg (0.225 mmol, 45.1% of th.) of yellow platelets.

IR spectroscopy: (RT, solid), (intensity): $\tilde{\nu}$ = 3059w, 1846m, 1585w, 1485w, 1436m, 1417w, 1315w, 1273w, 1193w, 1098m, 1025m, 997m, 916m, 877m, 808 s, 758s cm⁻¹.

NMR spectroscopy: ³¹P{¹H} NMR (162 MHz, CD₂Cl₂): δ 41.5 (d, J = 34.6 Hz) ppm.

HRMS (ESI+): m/z = 1052.15 (C₅₁H₅₈OP₄RuSb). **X-ray structure analysis:** uv352

6.6.4 Dinitrosylbis(triphenylphosphane)ruthenium(0) (**27**) (using NO)

tentative byproducts

Starting materials: $[\text{Ru}(\text{H}_2\text{O})_6](\text{tos})_2$, nitrogen monoxide, EtOH, triphenylphosphane.

Procedure:

The previously synthesised product $[\text{Ru}(\text{H}_2\text{O})_6](\text{tos})_2$ (**1**) (275 mg, 0.498 mmol) was suspended in EtOH (10 mL). The solution was treated with nitrogen monoxide for 1.5 h at RT whereby the solution turned brown-red. To this solution PPh_3 (263 mg, 1.00 mmol, 2.01 equiv.) was added and the suspension was treated with NO for another 20 min. The solution was filtered through a syringe filter and layered with diethyl ether. The obtained brown-red crystals were filtered off and dried *in vacuo*.

Empirical formula: $\text{C}_{36}\text{H}_{30}\text{N}_2\text{O}_2\text{P}_2\text{Ru}$, 685.66 g/mol.

Yield: 101 mg (0.147 mmol, 29.5% of th.) of red blocks.

IR spectroscopy: (RT, solid), (intensity): $\tilde{\nu}$ = 3200vw, 3250vw, 1651s (NO), 1605vs (NO), 1569sh, 1478s, 1432s, 1305m, 1184w, 1156w, 1091vs, 1027w, 997w, 846w, 740vs cm^{-1} .

NMR spectroscopy:

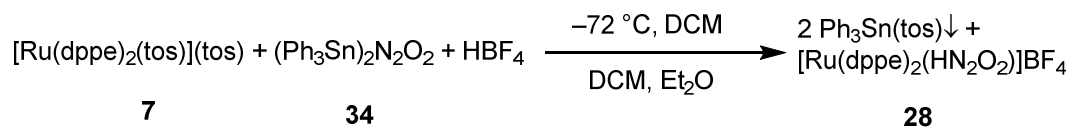
$^{31}\text{P}\{^1\text{H}\}$ NMR (162 MHz, CD_2Cl_2): δ 54.8 (s) ppm.

Elemental Analysis: (calcd. for $\text{C}_{36}\text{H}_{30}\text{N}_2\text{O}_2\text{P}_2\text{Ru}$, 685.66 g/mol) found (calcd.): C 62.71% (63.06%), H 4.39% (4.41%), N 4.13% (4.09%).

X-ray structure analysis: vv487

6.7 Hydrogenhyponitrito ruthenium complexes and hyponitrite derivatives

6.7.1 Bis{bis(diphenylphosphanyl)ethane}hydrogenhyponitritoruthenium(II) tetrafluoridoborate (**28**)



Literature: D. Beck, P. Klüfers, *Chem. Eur. J.* **2018**, *24*, 16019–16028.

Starting materials: [Ru(dppe)₂(tos)](tos), triphenylstannyl hyponitrite, DCM, tetrafluoroboric acid (50% in H₂O), diethyl ether.

Procedure:

a)

Crude [Ru(dppe)₂(tos)](tos) (**7**) was dissolved in DCM (15 mL) and cooled to -72 °C. Bis(triphenylstannyl) hyponitrite (**34**) was dissolved in DCM (20 mL) and added dropwise to the solution of (**7**). The light-yellow solution was stirred for 2 h and brought to room temperature afterwards. To the well-stirred solution, 600 µL HBF₄ (excess, 50% in water) was added and stirred until the solution became a suspension (ca. 15 min). The suspension was concentrated to 4 mL. The colourless solid was removed by filtration through a syringe filter, the solution was layered with diethyl ether and stored in the absence of any disturbance. Within 5 days, red blocks of **28** have formed as well as colourless precipitate of, tentatively, tin-containing side-products. The mother liquor was pipetted off and the colourless solid was removed by washing with diethyl ether (3 × 10 mL). The crystals were recrystallized with the same composition of DCM and diethyl ether, washed and dried *in vacuo*.

b) solvent-free crystals

The crystals were recrystallized with DCM and toluene, washed with diethyl ether and dried *in vacuo*.

Empirical formula: C₅₆H₅₉BF₄N₂O₃P₄Ru (1119.81 g/mol)

Yield 28a: 439 mg (0.392 mmol, 78.7% of th.) of yellow blocks.

IR spectroscopy: (ATR, solid-state): 3059w, 2971w, 1572w, 1484s, 1450shp, 1433vst, 1411w, 1383w, 1345w, 1311w, 1278 w, 1242w, 1192 w, 1100shp, 1050vst, 1032vs, 1002s, 928w, 871m, 841m, 815 m, 802m, 744vs, 715m cm⁻¹.

UV/VIS spectroscopy: λ_{max}/nm (DCM) 357.6.

UV/VIS spectroscopy: λ_{max}/nm (solid-state): 378.0, 532.9.

Experimental Part

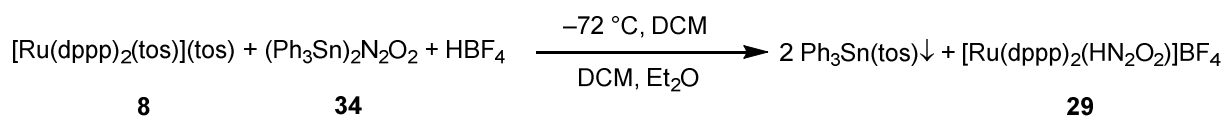
NMR spectroscopy:

$^{31}\text{P}\{^1\text{H}\}$ NMR (MAS, 202 MHz): δ 63.7 (s), 62.8 (s), 55.8 (s), 54.6 (s) ppm.

HRMS (FAB+): $m/z = 959.18$ ($\text{C}_{52}\text{H}_{49}\text{N}_2\text{O}_2\text{P}_4^{102}\text{Ru}$)

X-ray structure analysis: uv616 (with solvent), vv389 (without crystal-solvent)

6.7.2 Bis{bis(diphenylphosphanyl)propane}hydrogenhyponitridoruthenium(II) tetrafluoridoborate (**29**)



Literature: D. Beck, P. Klüfers, *Chem. Eur. J.* **2018**, *24*, 16019–16028.

Starting materials: [Ru(dppp)₂(tos)](tos), triphenylstannyl hyponitrite, DCM, tetrafluoroboric acid (50% in H₂O), diethyl ether.

Procedure:

Crude [Ru(dppp)₂(tos)](tos) (**8**) was dissolved in DCM (15 mL) and cooled to -72 °C. Bis(triphenylstannyl) hyponitrite (**34**) was dissolved in DCM (20 mL) and added dropwise to the solution of **7**. The light-yellow solution was stirred for 2 h and brought to room temperature afterwards. To the well-stirred solution, 600 µL HBF₄ (excess, 50% in water) was added and stirred until the solution became a suspension (ca. 15 min). The suspension was concentrated to 4 mL. The colourless solid was removed by filtration through a syringe filter, the solution was layered with diethyl ether and stored in the absence of any disturbance. Within 5 days, brown blocks of **29** have formed as well as colourless precipitate of, tentatively, tin-containing side-products. The mother liquor was pipetted off and the colourless solid was removed by washing with diethyl ether (3 × 10 mL). The crystals were recrystallized with the same composition of DCM and diethyl ether, washed and dried *in vacuo*.

Empirical formula: C₅₄H₅₃BF₄N₂O₂P₄Ru (1073.80 g/mol)

Yield: 482 mg (0.449 mmol, 90.2% of th.) of dark-red blocks.

IR spectroscopy: (ATR, solid-state): 3052w, 2019vw, 1572w, 1483m, 1453vw, 1433.82s, 1377m, 1313w, 1271w, 1245w, 1189w, 1163w, 1115w, 1090s, 1048vs, 1034vs, 1023shp, 999s, 970s, 935w, 834m, 791m, 742s, 730m cm⁻¹.

UV/VIS spectroscopy : λ_{max}/nm (DCM): 371.5, 453.2 (sh).

UV/VIS spectroscopy: λ_{max}/nm (solid-state): 386.0, 445.3, 545.3.

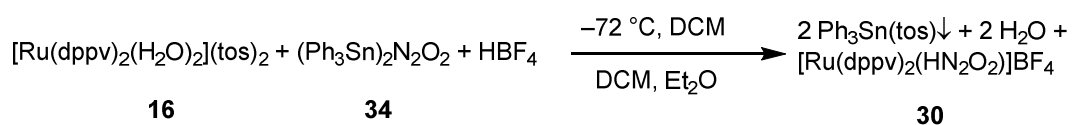
NMR spectroscopy:

³¹P{¹H} NMR (MAS, 202 MHz): δ 29.85 (s), 26.04 (s), 6.83 (s), -4.79 (s) ppm.

HRMS (FAB+): m/z = 987.21 (C₅₄H₅₃N₂O₂P₄¹⁰²Ru)

X-ray structure analysis: vv413

6.7.3 Bis{bis(diphenylphosphanyl)ethene}hydrogenhyponitridoruthenium(II) tetrafluoridoborate (**30**)



Literature: D. Beck, P. Klüfers, *Chem. Eur. J.* **2018**, *24*, 16019–16028.

Starting materials: [Ru(dppv)₂(H₂O)₂](tos)₂, triphenylstannyl hyponitrite, DCM, tetrafluoroboric acid (50% in H₂O), diethyl ether.

Procedure:

Crude [Ru(dppv)₂(H₂O)₂](tos)₂ **16** was dissolved in DCM (15 mL) and cooled to –72 °C. Bis(triphenylstannyl) hyponitrite (**34**) was dissolved in DCM (20 mL) and added dropwise to the solution of **16**. The light-yellow solution was stirred for 2 h and brought to room temperature afterwards. To the well-stirred solution, 600 µL HBF₄ (excess, 50% in water) was added and stirred until the solution became a suspension (ca. 15 min). The suspension was concentrated to 4 mL. The colourless solid was removed by filtration through a syringe filter, the solution was layered with diethyl ether and stored in the absence of any disturbance. Within 5 days, yellow rods of **31** have formed as well as colourless precipitate of, tentatively, tin-containing side-products. The mother liquor was pipetted off and the colourless solid was removed by washing with diethyl ether (3 × 10 mL). The crystals were recrystallized with the same composition of DCM and diethyl ether, washed and dried *in vacuo*.

Empirical formula: C₅₂H₄₅BF₄N₂O₂P₄Ru (1041.71 g/mol).

Yield: 145 mg (0.139 mmol, 27.9% of th.) of yellow rods.

IR spectroscopy: (ATR, solid-state): 3054w, 1633vw, 1483m, 1453vw, 1434st, 1379w, 1313m, 1286w, 1189w, 1164w, 1112shp, 1087vs, 1051vs, 1035shp, 997vs, 847w, 787w, 741w, 718m cm⁻¹.

UV/VIS spectroscopy: λ_{max}/nm (DCM) 358.

UV/VIS spectroscopy: λ_{max}/nm (solid-state): ≈ 388.

NMR spectroscopy:

³¹P{¹H} NMR (MAS, 202 MHz): δ 64.93 (s), 63.36 (s), 59.63 (s), 53.62 (s) ppm.

HRMS (FAB+): m/z = 955.15 (C₅₂H₄₅N₂O₂P₄¹⁰²Ru)

X-ray structure analysis: vv423

6.7.4 Bis{bis(diphenylphosphanyl)ethane}hyponitritoruthenium(II) (31)

Literature: D. Beck, P. Klüfers, *Chem. Eur. J.* **2018**, *24*, 16019–16028.

Starting materials: $[\text{Ru}(\text{dppe})_2(\text{N}_2\text{O}_2\text{H})](\text{BF}_4)$, imidazole, DCM, diethyl ether.

Procedure:

Crystals of $[\text{Ru}(\text{dppe})_2(\text{N}_2\text{O}_2\text{H})](\text{BF}_4)$ (**28**) (432 mg, 0.386 mmol) were dissolved in DCM (5 mL) and imidazole (100 mg, excess) was added. The solution was filtered and layered with diethyl ether. After the colour of the mother liquor remained constant (ca. 4 days), the mother liquor was pipetted off and the product was washed with diethyl ether (3 × 10 mL).

Empirical formula: $\text{C}_{55}\text{H}_{53}\text{N}_4\text{O}_2\text{P}_4\text{Ru}$ (1027.02 g/mol).

Yield: 361 mg (0.352 mmol, 91.2% of th.) of light-yellow blocks.

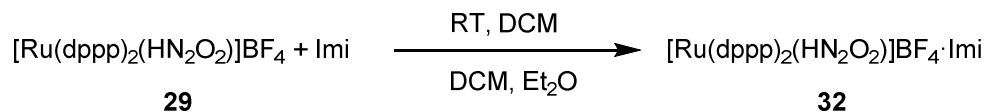
IR spectroscopy: (ATR, solid-state): 3066w, 2358w, 2333w, 1572w, 1485m, 1433s, 1413m, 1390shp, 1315w, 1272w, 1252vw, 1189w, 1161w, 1053vs, 997s, 974s, 943shp, 917w, 872m, 814m, 802m, 749s, 717m cm^{-1} .

UV/VIS spectroscopy: $\lambda_{\text{max}}/\text{nm}$ (DCM) 367.4.

HRMS (FAB+): $m/z = 961.18$ ($\text{C}_{52}\text{H}_{49}\text{N}_2\text{O}_2\text{P}_4^{102}\text{Ru}$) $[\text{M}+\text{H}]^+$

X-ray structure analysis: vv017

6.7.5 Bis{bis(diphenylphosphanyl)propane}hydrogenhyponitritoruthenium(II) tetrafluoridoborate (**32**)



Literature: D. Beck, P. Klüfers, *Chem. Eur. J.* **2018**, *24*, 16019–16028.

Starting materials: [Ru(dppp)₂(N₂O₂H)](BF₄), imidazole, DCM, diethyl ether.

Procedure:

Crystals of [Ru(dppp)₂(N₂O₂H)](BF₄) **29** (131 mg, 0.121 mmol) were dissolved in DCM (5 mL) and imidazole (100 mg, excess) was added. The solution was filtered and layered with diethyl ether. After the colour of the mother liquor remained constant (ca. 4 days), the mother liquor was pipetted off and the product was washed with diethyl ether (3 × 10 mL).

Empirical formula: C₅₄H₅₃BF₄N₂O₂P₄Ru (1073.80 g/mol).

Yield: 95 mg (0.089 mmol, 74% of th.) of yellow platelets.

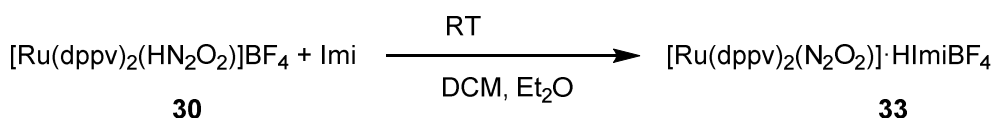
Please note: Regarding the crystal structure, no deprotonation occurred.

IR spectroscopy: (ATR, solid-state): 3288w, 3054w, 2360m, 1531w, 1484m, 1453vw, 1433s, 1386w, 1323w, 1313w, 1269w, 1269w, 1196w, 1166w, 1131vw, 1115w, 1051vs, 1020s, 974s, 935m, 842s, 797m, 745vs, 734m cm⁻¹.

UV/VIS spectroscopy: λ_{max}/nm (DCM) 312.0 (shoulder), 373.5.

HRMS (FAB+): m/z = 987.21 (C₅₄H₅₃N₂O₂P₄¹⁰²Ru) [M+H]⁺

X-ray structure analysis: vv427

6.7.6 Bis{bis(diphenylphosphanyl)ethene}hyponitritoruthenium(II) (33)

Literature: D. Beck, P. Klüfers, *Chem. Eur. J.* **2018**, *24*, 16019–16028.

Starting materials: $[\text{Ru}(\text{dppv})_2(\text{N}_2\text{O}_2\text{H})](\text{BF}_4)$, imidazole, DCM, diethyl ether.

Procedure:

Crystals of $[\text{Ru}(\text{dppv})_2(\text{N}_2\text{O}_2\text{H})](\text{BF}_4)$ **30** (125 mg, 0.120 mmol) were dissolved in DCM (5 mL) and imidazole (100 mg, excess) was added. The solution was filtered and layered with diethyl ether. After the colour of the mother liquor remained constant (ca. 4 days), the mother liquor was pipetted off and the product was washed with diethyl ether (3 × 10 mL).

Empirical formula: $\text{C}_{52}\text{H}_{44}\text{N}_2\text{O}_2\text{P}_4\text{Ru}$ (953.90 g/mol)

Yield: 100 mg (0.104 mmol, 86.7% of th.) of light-yellow rods.

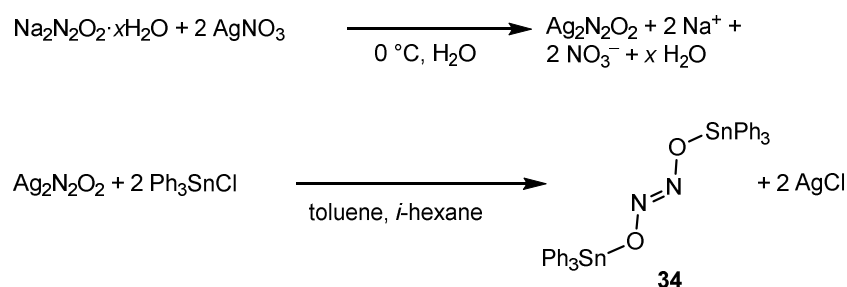
IR spectroscopy (ATR, solid-state): 3326w, 3146w, 3049w, 1587w, 1535w, 1483w, 1433s, 1385w, 1325w, 1285w, 1253shp, 1190w, 1159w, 1090s, 1051vs, 999s, 935m, 844w, 822w, 737vs, 716m cm^{-1} .

UV/VIS spectroscopy: λ_{max} /nm (DCM) 305.5 (shoulder), 362.0.

HRMS (ESI+): $m/z = 957.14$ ($\text{C}_{52}\text{H}_{48}\text{O}_2\text{P}_4\text{Ru}$) $[\text{M}+\text{H}]^+$

X-ray structure analysis: vv772

6.7.7 Bis(triphenylstannyl) hyponitrite (34)



Literature: G. Brauer, *Handbuch der präparativen Anorganischen Chemie*, Vol. 1, Stuttgart, **1960**, W. Beck, H. Engelmann, H. S. Smedal, *Z. Anorg. Allg. Chem.* **1968**, 357, 134–138. T. Mayer, W. Beck, H.-C. Böttcher, *Z. Anorg. Allg. Chem.* **2011**, 637, 345–347.

Starting materials: *i*-hexane, silver nitrate, $\text{Na}_2\text{N}_2\text{O}_2 \cdot x\text{H}_2\text{O}$, water, toluene, triphenyltin chloride.

Procedure: **$\text{Ag}_2\text{N}_2\text{O}_2$**

The work has to be done in absence of light. A solution of sodium *trans*-hyponitrite· $x\text{H}_2\text{O}$ (4.00 g, 37.7 mmol) was solved in 150 mL H_2O and cooled to 1 °C. To this solution AgNO_3 (7.70 g, 45.3 mmol) solved in H_2O (10 mL) was dropped. The bright green-yellow precipitate was sucked off, washed with ethanol (2 · 10 mL) and diethyl ether (3 · 10 mL) and dried in vacuo.

Empirical formula: $\text{Ag}_2\text{N}_2\text{O}_2$ (275.75 g/mol)

Yield: 7.28 g (26.4 mmol, 70.0% of th.) of green-yellow scales.

Please note: $\text{Ag}_2\text{N}_2\text{O}_2$ was used for the following set-up without further analytics.

 $\text{Ph}_3\text{Sn}(\text{N}_2\text{O}_2)\text{SnPh}_3$ (34)

A suspension of $\text{Ag}_2\text{N}_2\text{O}_2$ (1.01 g, 3.67 mmol) and Ph_3SnCl (2.94 g, 7.63 mmol) in toluene (60 mL) was stirred for 24 h. The AgCl precipitate was filtered off through a filter paper with cotton wool. The clear solution was reduced using an rotary evaporator, resolved in toluene (40 mL) and layered with *i*-hexane (80 mL). The colourless solid was washed with *i*-hexane (3 · 10 mL), dried *in vacuo* and resolved in DCM (20 mL). The amount of triphenyltin hyponitrite was directly used for the previous syntheses of **28–30**.

Empirical formula: $\text{C}_{36}\text{H}_{30}\text{N}_2\text{O}_2\text{Sn}_2$ (760,07 g/mol)

Experimental Part

Yield: \approx 350 mg of colourless crystals. The product was resolved and directly used for syntheses of the products **28–30**.

IR spectroscopy (ATR, solid-state): 3065w, 3020w, 1578w, 1479m, 1428s, 1332m, 1303m, 1263m, 1178m, 1159m, 1076s, 1023w, 996vs, 914m, 894m, 850m, 727vs cm^{-1} .

NMR spectroscopy:

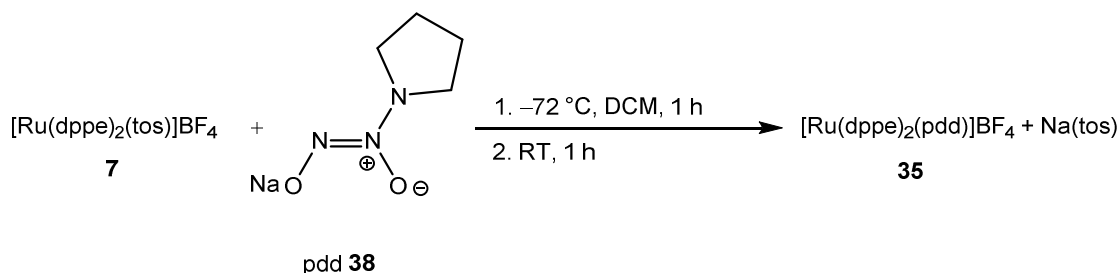
$^{119}\text{Sn}\{^1\text{H}\}$ NMR spectroscopy (149 MHz, toluene- d_8): δ -87.9 (s) ppm.

Elemental Analysis: (calcd. for $\text{C}_{36}\text{H}_{30}\text{N}_2\text{O}_2\text{Sn}_2$, 760,07 g/mol) found (calcd.): C 56.95% (56.89%), H 4.07% (3.98%), N 3.42% (3.69%).

HRMS (EI+): $m/z = 715.9$ [$\text{M}^+ - \text{N}_2\text{O}$] $^+$

6.8 Diazoniumdiolato complexes as models for *cis*-hyponitrito complexes

6.8.1 Bis{bis(diphenylphosphanyl)ethane}pyrrolidinediazoniumdiolatoruthenium(II) tetrafluoridoborate (35)



Starting materials: $[\text{Ru}(\text{dppe})_2(\text{tos})]\text{BF}_4$, pdd, DCM, diethyl ether.

Procedure:

Crystallised $[\text{Ru}(\text{dppe})_2(\text{tos})]\text{BF}_4$ (**7**) was dissolved in DCM (5 mL) and cooled to $-72 \text{ }^\circ\text{C}$. A solution of sodium pyrrolidinediazoniumdiolate (85 mg, 0.56 mmol) in MeOH (5 mL) was prepared and dropped in the other solution. The solution was stirred for 1 h at $-72 \text{ }^\circ\text{C}$ and 1 h at RT. The colour changes from red to red brown. After that, the volume of the solution was reduced to 2.5 mL, filtered through a syringe filter and layered with diethyl ether. The mother liquor was decanted and the crystals were dried *in vacuo*.

Empirical formula: $\text{C}_{56}\text{H}_{56}\text{BF}_4\text{N}_3\text{O}_2\text{P}_4\text{Ru}$ (1114.85 g/mol)

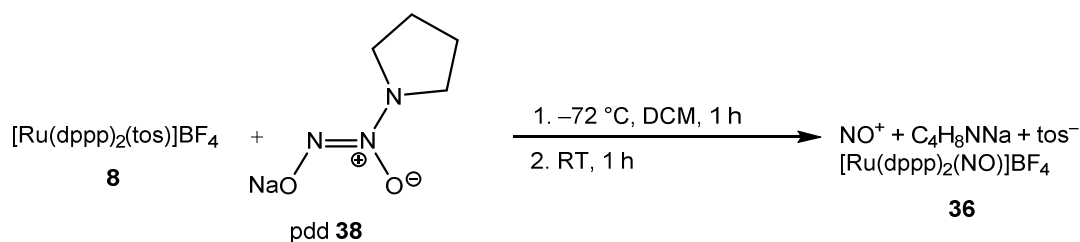
Yield: 264 mg (0.237 mmol, 48.1% of th.) of yellow crystals.

IR spectroscopy: (RT, solid), (intensity): $\tilde{\nu} = 3057\text{vw}, 2939\text{vw}, 1682\text{vw}, 1586\text{w}, 1573\text{w}, 1484\text{m}, 1433\text{s}, 1409\text{m}, 1378\text{w}, 1313\text{w}, 1282\text{w}, 1257\text{w}, 1190\text{w}, 1167\text{m}, 1083\text{s}, 1053\text{vs}, 1026\text{vs}, 999\text{vs}, 874\text{m}, 810\text{m}, 745\text{s cm}^{-1}$.

UV/VIS spectroscopy: $\lambda_{\text{max}}/\text{nm}$ (DCM) 371.

HRMS (ESI+): $m/z = 944.17$ ($\text{C}_{52}\text{H}_{48}\text{O}_2\text{NP}_4\text{Ru}$)

6.8.2 Bis{bis(diphenylphosphanyl)propane}nitrosylruthenium(II) tetrafluoridoborate (36)



Starting materials: $[\text{Ru}(\text{dppp})_2(\text{tos})]\text{BF}_4$, pdd, DCM, diethyl ether.

Procedure:

Crystallised $[\text{Ru}(\text{dppp})_2(\text{tos})]\text{BF}_4$ (**8**) was dissolved in DCM (5 mL) and cooled to -72 °C. A solution of sodium pyrrolidinediazonioldiolate (85 mg, 0.56 mmol) in MeOH (5 mL) was prepared and dropped in the other solution. The solution was stirred for 1 h at -72 °C and 1 h at RT. The colour changes from red to dark brown. After that, the volume of the solution was reduced to 2.5 mL, filtered through a syringe filter and layered with diethyl ether. The mother liquor was decanted and the crystals were dried *in vacuo*.

Empirical formula: $\text{C}_{54}\text{H}_{52}\text{BF}_4\text{NOP}_4\text{Ru}$ (1042.78 g/mol)

Yield: 120 mg (0.115 mmol, 23.3% of th.) of yellow blocks.

IR spectroscopy: (RT, solid), (intensity): $\tilde{\nu} = 3054\text{vw}, 2669\text{vw}, 2869\text{vw}, 1656\text{s} (\text{NO}), 1586\text{w}, 1573\text{w}, 1484\text{m}, 1433\text{s}, 1406\text{w}, 1379\text{w}, 1344\text{w}, 1309\text{w}, 1277\text{w}, 1184\text{w}, 1162\text{m}, 1087\text{s}, 1045\text{vs}, 998\text{s}, 970\text{s}, 914\text{m}, 831\text{s}, 793\text{s}, 757\text{s} \text{ cm}^{-1}$.

UV/VIS spectroscopy: $\lambda_{\text{max}}/\text{nm}$ (DCM) 373, 432, 573.

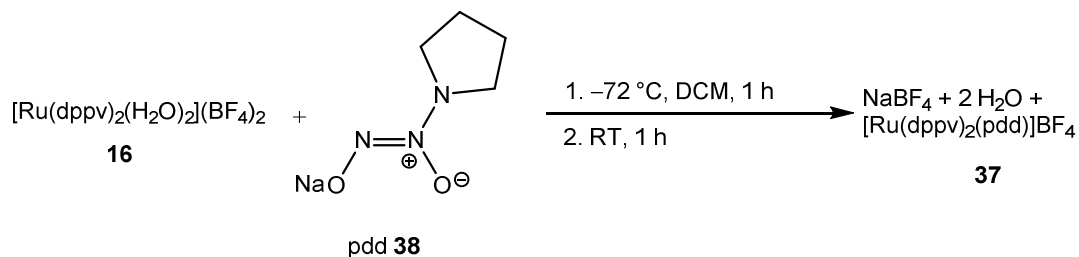
NMR spectroscopy:

$^{31}\text{P}\{^1\text{H}\}$ NMR (162 MHz, CD_2Cl_2): δ 16.0, 10.6 ($^3J_{\text{PP}} = 39.1$ Hz, first isomer), 29.2, 0.8 ($^3J_{\text{PP}} = 31.0$ Hz, second isomer), 34.0, 1.4 ($^3J_{\text{PP}} = 32.4$ Hz, third isomer) ppm.

HRMS (ESI+): $m/z = 956.20$ ($\text{C}_{54}\text{H}_{52}\text{ONP}_4\text{Ru}$)

X-ray structure analysis: wv165

6.8.3 Bis{bis(diphenylphosphanyl)ethene}pyrrolidinediazoniumdiolatoruthenium(II) tetrafluoridoborate (**37**)



Starting materials: $[\text{Ru}(\text{dppv})_2(\text{H}_2\text{O})_2](\text{BF}_4)_2$, pdd, DCM, diethyl ether.

Procedure:

Crystallised $[\text{Ru}(\text{dppv})_2(\text{H}_2\text{O})_2](\text{BF}_4)_2$ (**16**) was dissolved in DCM (5 mL) and cooled to $-72 \text{ }^\circ\text{C}$. A solution of sodium pyrrolidinediazonioldiolate (85 mg, 0.56 mmol) in MeOH (5 mL) was prepared and dropped in the other solution. The solution was stirred for 1 h at $-72 \text{ }^\circ\text{C}$ and 1 h at RT. The colour changes from yellow to pale yellow. After that, the volume of the solution was reduced to 2.5 mL, filtered through a syringe filter and layered with diethyl ether. The mother liquor was decanted and the crystals were dried *in vacuo*.

Empirical formula: $\text{C}_{56}\text{H}_{52}\text{BF}_4\text{N}_3\text{O}_2\text{P}_4\text{Ru}$ (1110.82 g/mol)

Yield: 182 mg (0.164 mmol, 33.3% of th.) of yellow rods.

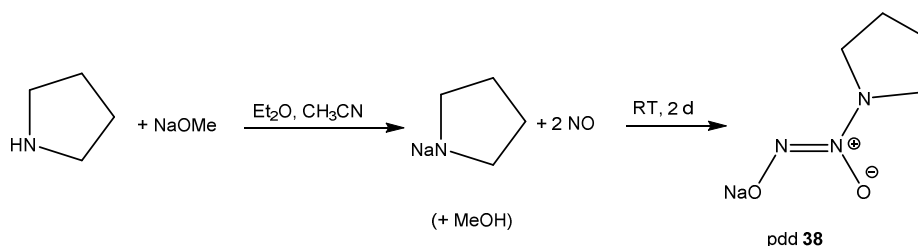
IR spectroscopy: (RT, solid), (intensity): $\tilde{\nu} = 3055\text{w}, 2969\text{w}, 1707\text{m}, 1587\text{w}, 1572\text{w}, 1482\text{m}, 1459\text{m}, 1434\text{m}, 1308\text{w}, 1217\text{m}, 1187\text{m}, 1090\text{s}, 1046\text{vs}, 997\text{s}, 885\text{w}, 848\text{w}, 813\text{w}, 741\text{vs cm}^{-1}$.

UV/VIS spectroscopy: $\lambda_{\text{max}}/\text{nm}$ (DCM) 364.

HRMS (ESI+): $m/z = 1024.21$ ($\text{C}_{56}\text{H}_{52}\text{O}_2\text{N}_3\text{P}_4\text{Ru}$)

X-ray structure analysis: ww182

6.8.4 pdd, pyrrolidinediazoniumdiolate (38)



Literature: J. E. Saavedra, T. R. Billiar, D. L. Williams, Y.-M. Kim, S. C. Watkins, L. K. Keefer, *J. Med. Chem.* **1997**, *40*, 1947–1954.

Starting materials: sodium, methanol, pyrrolidine, diethyl ether, acetonitrile, nitric oxide.

Procedure:

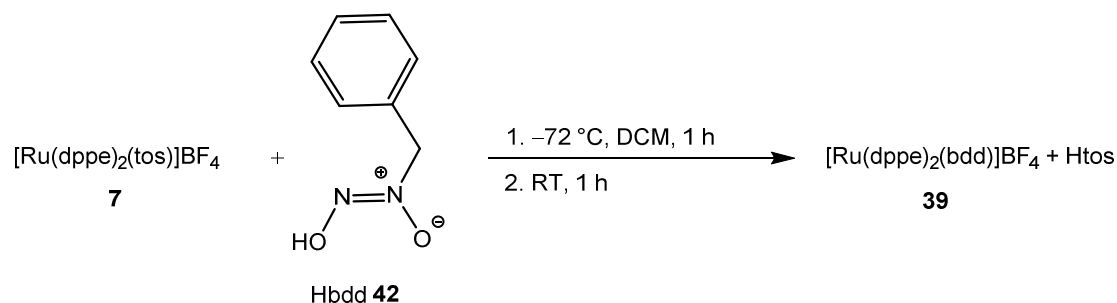
To sodium (0.92 g, 0.040 mol) methanol (14.5 mL) was dropped under constant stirring using a metal-reflux condenser under an argon atmosphere. The developing hydrogen was removed by a constant argon flow. In a high-pressure bottle pyrrolidine (2.82 g, 3.31 mL, 0.04 mol) was solved in diethyl ether (10 mL) and acetonitrile (10 mL). The NaOMe solution was dropped slowly into the other solution and the flask was sealed. The bottle was flushed with nitric oxide (1 h, without pressure) after appearance of the colourless precipitate the outlet of the bottle was closed and the NO flow was kept at around 1.5 bar for 2 h. After formation of a colourless slurry, the inlet was closed, the apparatus flushed with Ar and the suspension was stirred for 2 further days under NO atmosphere. The solid was sucked off, washed with diethyl ether and dried *in vacuo*.

Empirical formula: C₄H₈N₃NaO₂ (153.12 g/mol)

Yield: 3.10 g (20.2 mmol, 50.5% of th.) of colourless crystals (ill-defined).

Please note: The product is stable for a short time. Steady decomposition is visible in brown fumes and yellow discolouration. Therefore, the yield described for **35–37** is estimated.

6.8.5 Bis{bis(diphenylphosphanyl)ethane}benzylidiazoniumdiolatoruthenium(II) tetrafluoridoborate (39)



Starting materials: $[\text{Ru}(\text{dppe})_2(\text{tos})]\text{BF}_4$, bdd, DCM, diethyl ether.

Procedure:

Crystallised $[\text{Ru}(\text{dppe})_2(\text{tos})]\text{BF}_4$ (**7**) was dissolved in DCM (5 mL) and cooled to $-72\text{ }^\circ\text{C}$. A solution of hydrogen benzylidiazoniumdiolate (Hbdd (**42**)) (100 mg, 0.657 mmol) in DCM (5 mL) was prepared and dropped in the other solution. The solution was stirred for 1 h at $-72\text{ }^\circ\text{C}$ and 1 h at RT. After that, the volume of the solution was reduced to 2.5 mL, filtered through a syringe filter and layered with diethyl ether. The mother liquor was decanted and the crystals were dried *in vacuo*.

Empirical formula: $\text{C}_{59}\text{H}_{55}\text{BF}_4\text{N}_2\text{O}_2\text{P}_4\text{Ru}$ (1135.87 g/mol)

Yield: 420 mg (0.370 mmol, 75.1% of th.) of yellow platelets.

IR spectroscopy: (RT, solid), (intensity): $\tilde{\nu} = 3058\text{vw}, 1584\text{vw}, 1571\text{vw}, 1498\text{w}, 1483\text{w}, 1460\text{w}, 1433\text{s}, 1345\text{w}, 1322\text{w}, 1274\text{w}, 1238\text{w}, 1217\text{s}, 1192\text{m}, 1162\text{w}, 1146\text{w}, 1084\text{s}, 1048\text{vs}, 997\text{s}, 948\text{w}, 923\text{m}, 868\text{m}, 848\text{m}, 810\text{m}, 793\text{w}, 748\text{vs cm}^{-1}$.

UV/VIS spectroscopy: $\lambda_{\text{max}}/\text{nm}$ (DCM) 370.

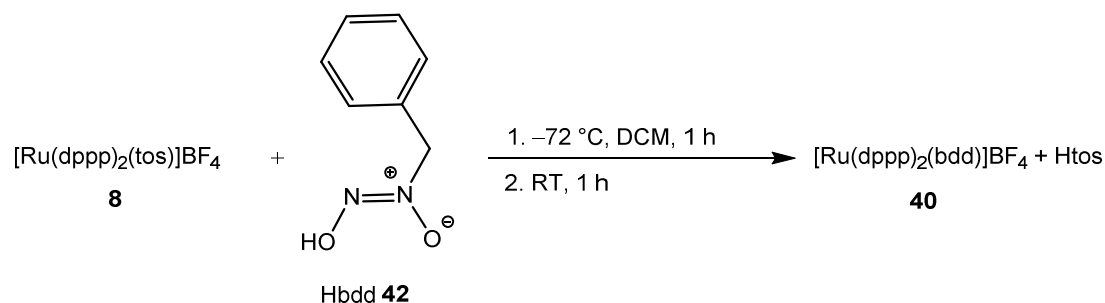
NMR spectroscopy:

$^{31}\text{P}\{^1\text{H}\}$ NMR (162 MHz, CD_2Cl_2): δ 55.8, 55.6 (dd, 11.6 Hz, 21.1 Hz), 55.1, 54.9 (dd, 13.3 Hz, 21.1 Hz), 50.3, 48.3 (dd, 11.7 Hz, 21.9 Hz), 44.6 (dd, 13.3 Hz, 21.2 Hz) ppm.

HRMS (ESI+): $m/z = 1049.23$ ($\text{C}_{59}\text{H}_{55}\text{O}_2\text{N}_2\text{P}_4\text{Ru}$)

X-ray structure analysis: wv167

6.8.6 Bis{bis(diphenylphosphanyl)propane}benzylidiazoniumdiolatoruthenium(II) tetrafluoridoborate (**40**)



Starting materials: $[\text{Ru}(\text{dppp})_2(\text{tos})]\text{BF}_4$, bdd, DCM, diethyl ether.

Procedure:

Crystallised $[\text{Ru}(\text{dppp})_2(\text{tos})]\text{BF}_4$ (**8**) was dissolved in DCM (5 mL) and cooled to $-72\text{ }^{\circ}\text{C}$. A solution of hydrogen benzylidiazoniumdiolate (Hbdd (**42**)) (100 mg, 0.657 mmol) in DCM (5 mL) was prepared and dropped in the other solution. The solution was stirred for 1 h at $-72\text{ }^{\circ}\text{C}$ and 1 h at RT. After that, the volume of the solution was reduced to 2.5 mL, filtered through a syringe filter and layered with diethyl ether. The mother liquor was decanted and the crystals were dried *in vacuo*.

Empirical formula: $\text{C}_{61}\text{H}_{59}\text{BF}_4\text{N}_2\text{O}_2\text{P}_4\text{Ru}$ (1163.92 g/mol)

Yield: 471 mg (0.405 mmol, 82.2% of th.) of yellow prisms.

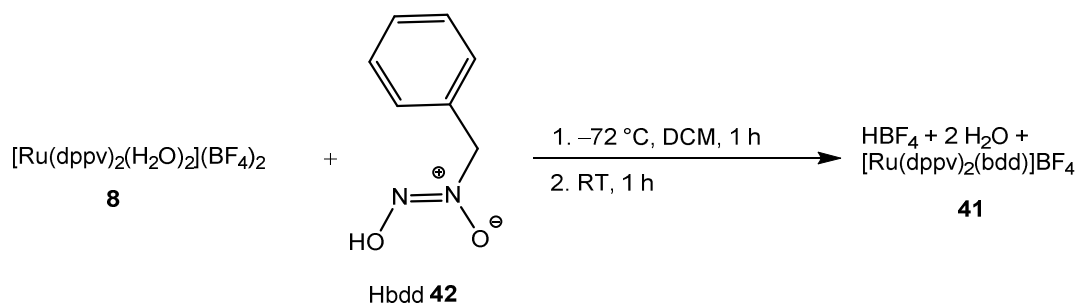
IR spectroscopy: (RT, solid), (intensity): $\tilde{\nu} = 3059\text{w}$, 2921w , 2868w , 1572w , 1484w , 1455w , 1433m , 1347w , 1305m , 1230vs , 1197vs , 1153vs , 1092vs , 1049vs , 997s , 980vs , 920m , 836m , 793m , 749s cm^{-1} .

UV/VIS spectroscopy: $\lambda_{\text{max}}/\text{nm}$ (DCM) 379.

HRMS (ESI+): $m/z = 1077.26$ ($\text{C}_{61}\text{H}_{59}\text{O}_2\text{N}_2\text{P}_4\text{Ru}$)

X-ray structure analysis: wv172

6.8.7 Bis{bis(diphenylphosphanyl)ethene}benzylidiazoniumdiolatoruthenium(II) tetrafluoridoborate (41)



Starting materials: $[\text{Ru}(\text{dppp})_2(\text{H}_2\text{O})_2](\text{BF}_4)_2$, bdd, DCM, diethyl ether.

Procedure:

Crystallised $[\text{Ru}(\text{dppp})_2(\text{H}_2\text{O})_2](\text{BF}_4)_2$ (**8**) was dissolved in DCM (5 mL) and cooled to $-72\text{ }^\circ\text{C}$. A solution of hydrogen benzylidiazoniumdiolate (Hbdd (**42**)) (100 mg, 0.657 mmol) in DCM (5 mL) was prepared and dropped in the other solution. The solution was stirred for 1 h at $-72\text{ }^\circ\text{C}$ and 1 h at RT. After that, the volume of the solution was reduced to 2.5 mL, filtered through a syringe filter and layered with diethyl ether. The mother liquor was decanted and the crystals were dried *in vacuo*.

Empirical formula: $\text{C}_{59}\text{H}_{51}\text{BF}_4\text{N}_2\text{O}_2\text{P}_4\text{Ru}$ (1131.84 g/mol)

Yield: 320 mg (0.283 mmol, 57.4% of th.) of yellow platelets.

IR spectroscopy: (RT, solid), (intensity): $\tilde{\nu} = 3057\text{w}$, 1599w , 1572w , 1483w , 1457w , 1433s , 1415m , 1340w , 1313w , 1209w , 1191s , 1146m , 1119m , 1090s , 1051vs , 1036vs , 998s , 910m , 846w , 814m , 786m , 740vs cm^{-1} .

UV/VIS spectroscopy: $\lambda_{\text{max}}/\text{nm}$ (DCM) 365.

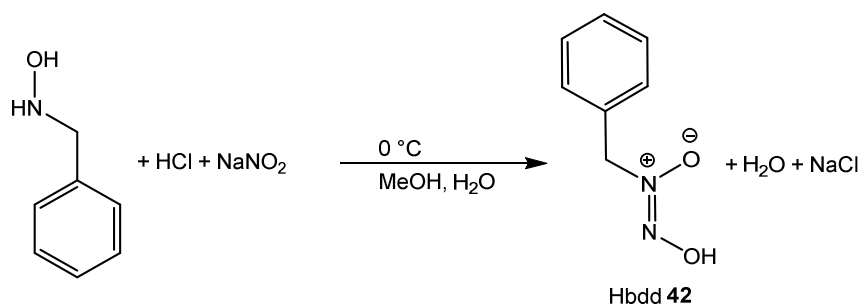
NMR spectroscopy:

$^{31}\text{P}\{^1\text{H}\}$ NMR (162 MHz, CD_2Cl_2): δ 66.1, 65.9 (dd, 7.0 Hz, 19.6 Hz), 65.5, 65.3 (dd, 8.3 Hz, 20.3 Hz), 56.3, 54.1 (dd, 6.9 Hz, 20.2 Hz), 53.3, 51.2 (dd, 8.1 Hz, 19.8 Hz) ppm.

HRMS (ESI+): $m/z = 1045.20$ ($\text{C}_{59}\text{H}_{51}\text{O}_2\text{N}_2\text{P}_4\text{Ru}$)

X-ray structure analysis: wv179

6.8.8 bdd, benzyldiazoniumdiolate (42)



Literatur: H. Maskill, W. P. Jencks, *J. Am. Chem. Soc.* **1987**, *109*, 2062–2070.

Starting materials: NaNO₂, *N*-benzyloxyamine hydrochloride, HCl (2 M), methanol, water.

Procedure:

An ice-cold solution of NaNO₂ (0.960 g, 13.9 mmol) in H₂O (2.4 mL) was added to a solution of benzyloxyamine hydrochloride (1.00 g, 6.27 mmol) in HCl (2.0 M, 6.6 mL) and MeOH (3.6 mL) over a time of 5 min. A foaming suspension was obtained. The solid was sucked off, washed with ice-cold water (3 · 10 mL) and dried *in vacuo*.

Empirical formula: C₇H₈N₂O₂ (152.15 g/mol)

Yield: 749 mg (4.93 mmol, 78.6% of th.) of colourless crystals.

IR spectroscopy: (RT, solid), (intensity): $\tilde{\nu}$ = 3034w, 1807vw, 1632vw, 1493m, 1471m, 1454m, 1429m, 1395m, 1348m, 1330m, 1312m, 1268s, 1211m, 1186w, 1159w, 1101w, 1078s, 1057s, 1029m, 1002m, 970m, 947m, 911m, 829 m, 775m, 702s cm⁻¹.

Elemental Analysis: (calcd. for C₇H₈N₂O₂, 152.15 g/mol g/mol) found (calcd.): 55.32% (55.26%), H 5.11% (5.30%), N 18.13% (18.41).

HRMS (ESI⁻): m/z = 151.05 (C₇H₇O₂N₂).

7 Appendix

7.1 Packing diagrams of the molecular structures

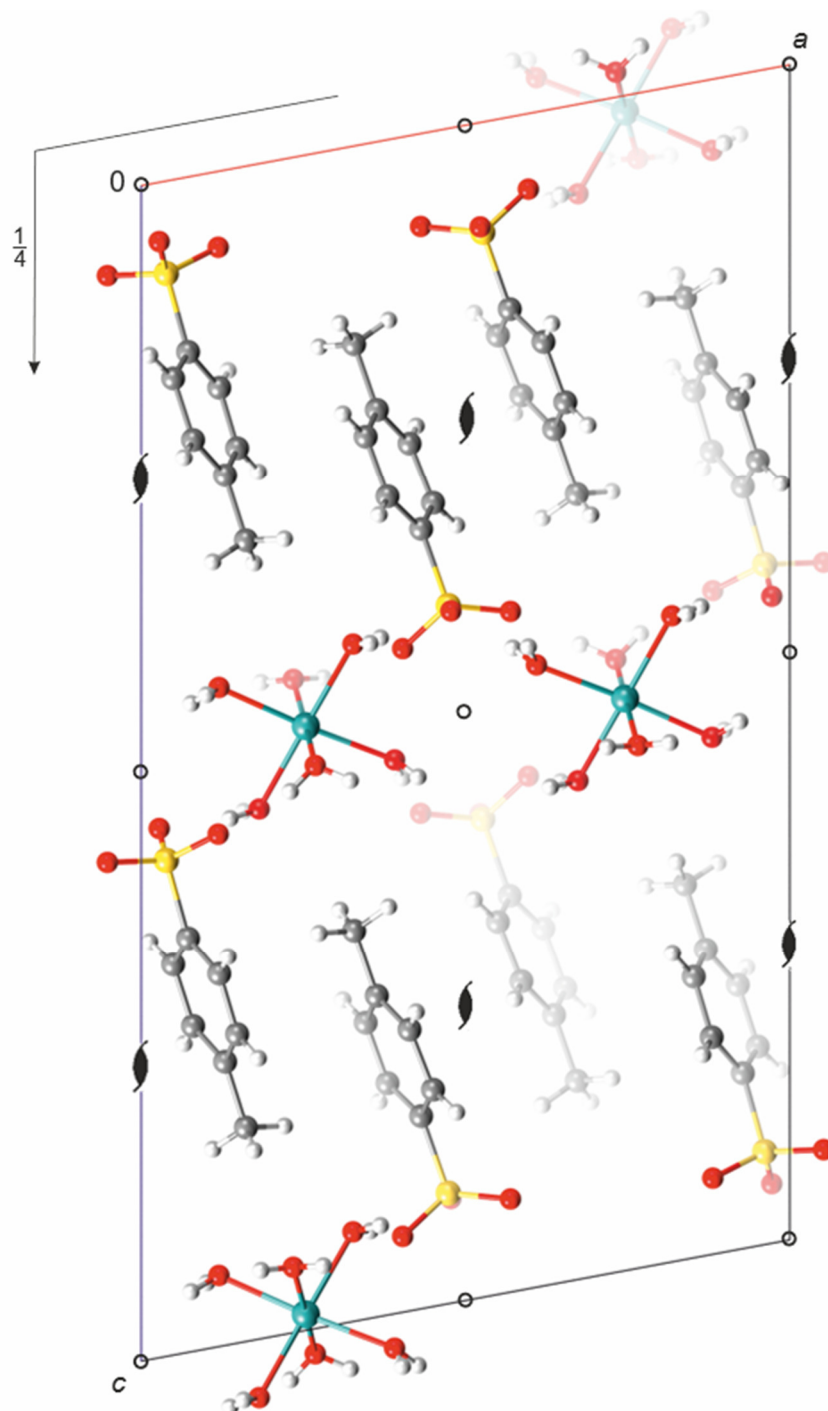


Figure 7.1: Mercury packing diagram of $[\text{Ru}(\text{H}_2\text{O})_6](\text{tos})_2$ (**1**) in the monoclinic space group $P2_1/c$ with view along $[0 \bar{1} 0]$. The symmetry elements of the space group are overlaid. Atoms: carbon (grey), hydrogen (white), oxygen (red), ruthenium (turquoise), sulphur (yellow).

Appendix

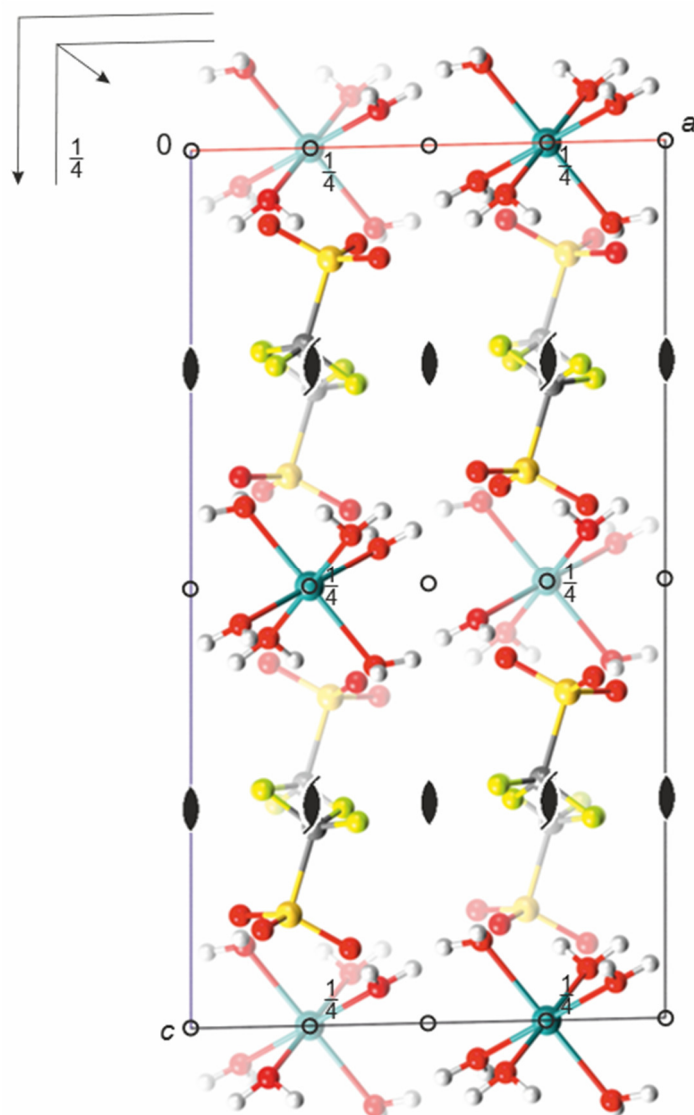


Figure 7.2: Mercury packing diagram of $[\text{Ru}(\text{H}_2\text{O})_6](\text{OTf})_2$ (**2**) in the monoclinic space group $C2/c$ with view along $[0 \bar{1} 0]$. The symmetry elements of the space group are overlaid. Atoms: carbon (grey), hydrogen (white), fluorine (light green), oxygen (red), ruthenium (turquoise), sulphur (yellow).

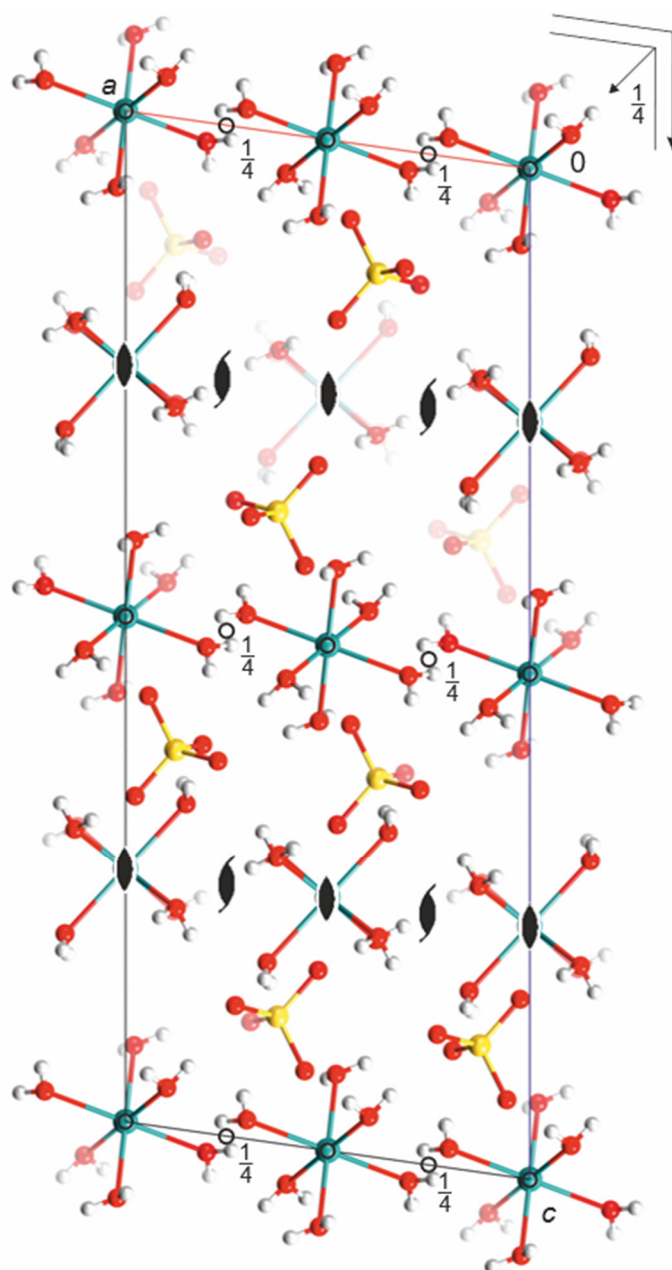


Figure 7.3: Mercury packing diagram of $[\text{Ru}(\text{H}_2\text{O})_6]\text{SO}_4$ (**3**) in the monoclinic space group $C2/c$ with view along $[0\ 1\ 0]$. The symmetry elements of the space group are overlaid. Atoms: hydrogen (white), oxygen (red), ruthenium (turquoise), sulphur (yellow).

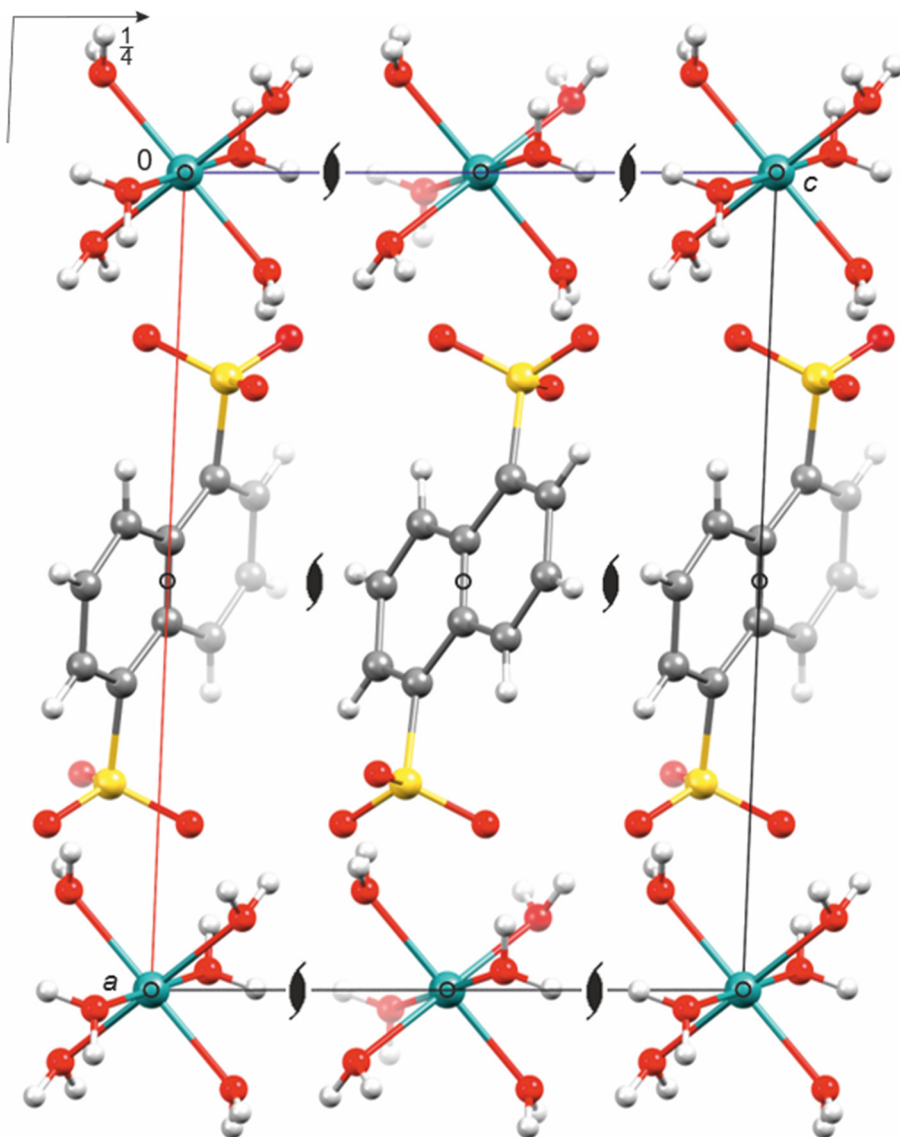


Figure 7.4: Mercury packing diagram of $[\text{Ru}(\text{H}_2\text{O})_6](1,5\text{-NaphDS})$ (**4**) in the monoclinic space group $P2_1/c$ with view along $[0\ 1\ 0]$. The symmetry elements of the space group are overlaid. Atoms: carbon (grey), hydrogen (white), oxygen (red), ruthenium (turquoise), sulphur (yellow).

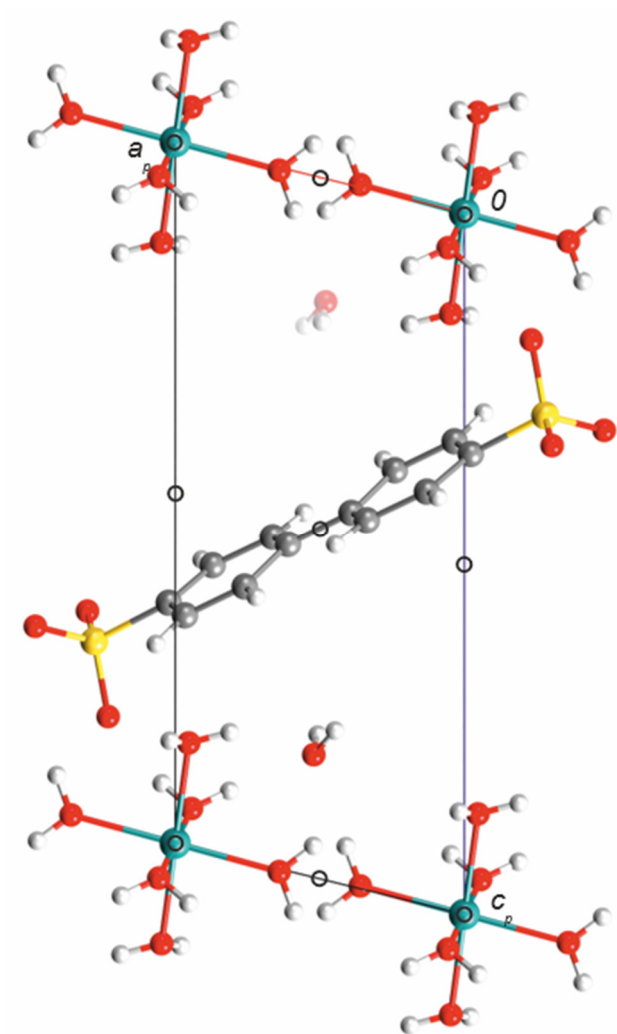


Figure 7.5: Mercury packing diagram of $[\text{Ru}(\text{H}_2\text{O})_6](4,4'\text{-BiphenDS}) \cdot 2\text{H}_2\text{O}$ (5) in the triclinic space group $P\bar{1}$ with view along $[0\ 1\ 0]$. The symmetry elements of the space group are overlaid. Atoms: carbon (grey), hydrogen (white), oxygen (red), ruthenium (turquoise), sulphur (yellow). The disorder of the biphenyl moiety is omitted.

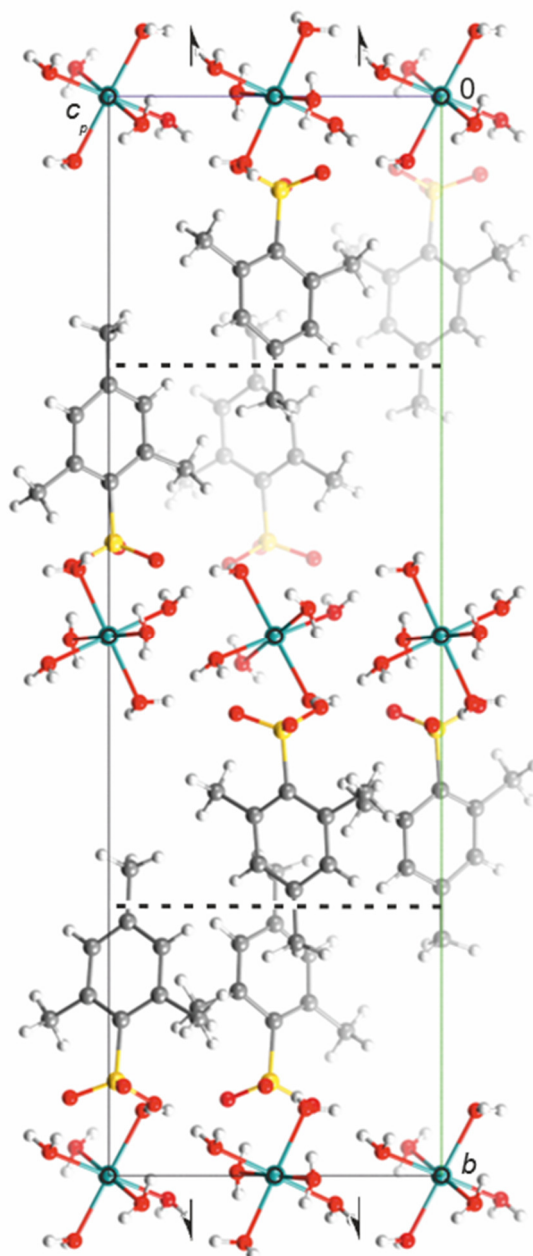


Figure 7.6: Mercury packing diagram of $[\text{Ru}(\text{H}_2\text{O})_6](\text{MesSO}_3)_2$ (**6**) in the monoclinic space group $P2_1/c$ with view along $[1\ 0\ 0]$. The symmetry elements of the space group are overlaid. Atoms: carbon (grey), hydrogen (white), oxygen (red), ruthenium (turquoise), sulphur (yellow).

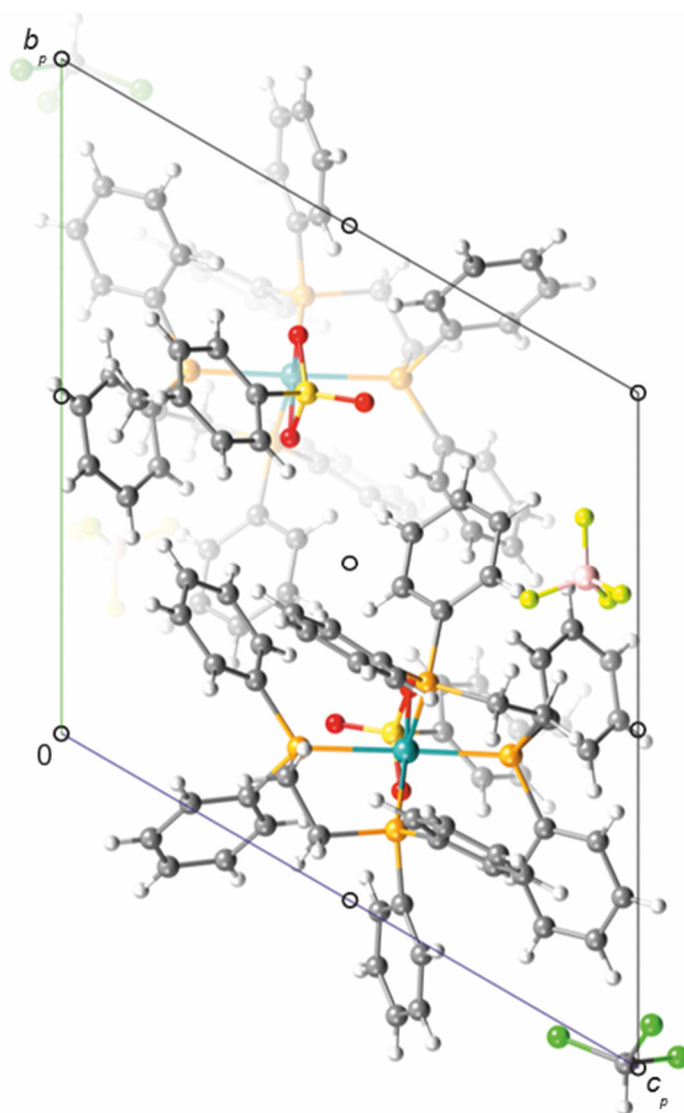


Figure 7.7: Mercury packing diagram of [Ru(dppe)₂(tos)(BF₄)]·0.985CHCl₃ (**7**) in the triclinic space group $P\bar{1}$ with view along [1 0 0]. The symmetry elements of the space group are overlaid. Atoms: carbon (grey), hydrogen (white), boron (rose), chlorine (green), fluorine (green-yellow), oxygen (red), phosphorus (orange), ruthenium (turquoise), sulphur (yellow).

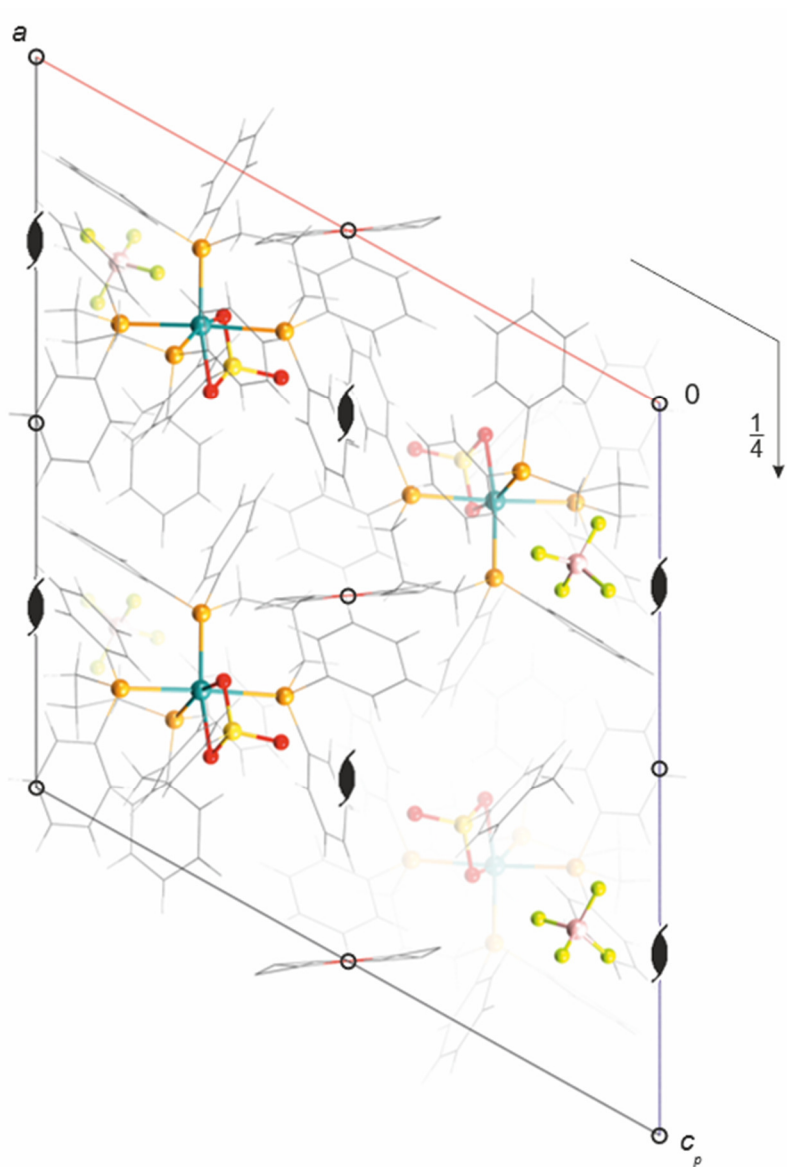


Figure 7.8: Mercury packing diagram of $[\text{Ru}(\text{dppp})_2(\text{tos})(\text{BF}_4)] \cdot x\text{Et}_2\text{O}$ (**8**) in the monoclinic space group $P2_1/c$ with view along $[0\ 1\ 0]$. The symmetry elements of the space group are overlaid. Atoms: carbon (grey), hydrogen (white), boron (rose), fluorine (green-yellow), oxygen (red), phosphorus (orange), ruthenium (turquoise), sulphur (yellow). Phenyl-groups and diethyl ether were illustrated as wireframe.

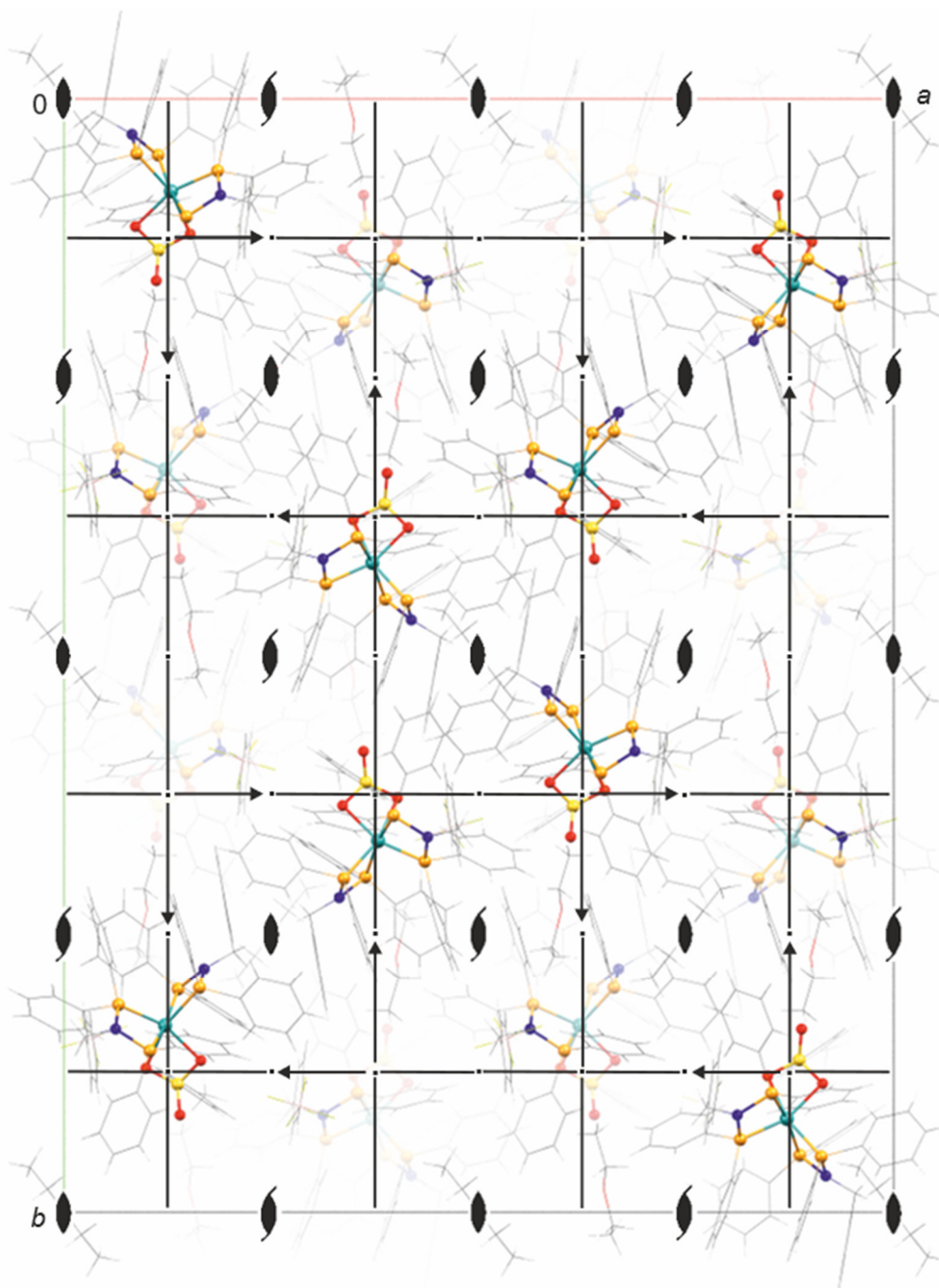


Figure 7.9: Mercury packing diagram of $[\text{Ru}(\text{dppbza})_2(\text{tos})(\text{BF}_4)] \cdot 2.9\text{Et}_2\text{O}$ (9) in the orthorhombic space group $Fdd2$ with view along $[001]$. The symmetry elements of the space group are overlaid. Atoms: carbon (grey), hydrogen (white), boron (rose), fluorine (green-yellow), nitrogen (blue), oxygen (red), phosphorus (orange), ruthenium (turquoise), sulphur (yellow). Phenyl-groups, diethyl ether and tetrafluoride borate were illustrated as wireframe.

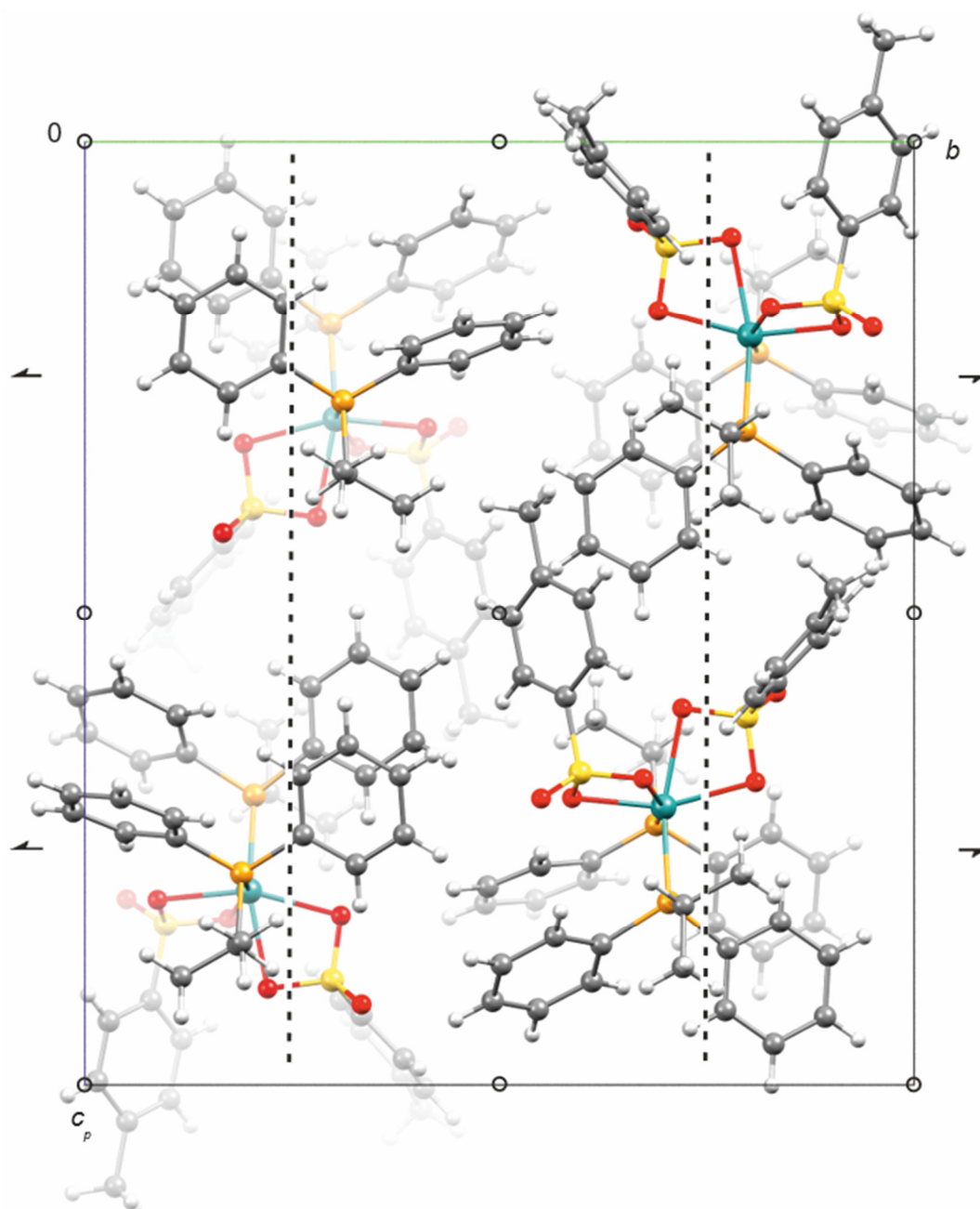


Figure 7.10: Mercury packing diagram of $[\text{Ru}(\text{P}'\text{PrPh}_2)_2(\text{tos})_2]$ (**10**) in the monoclinic space group $P2_1/c$ with view along $[1\ 0\ 0]$. The symmetry elements of the space group are overlaid. Atoms: carbon (grey), hydrogen (white), oxygen (red), phosphorus (orange), ruthenium (turquoise), sulphur (yellow).

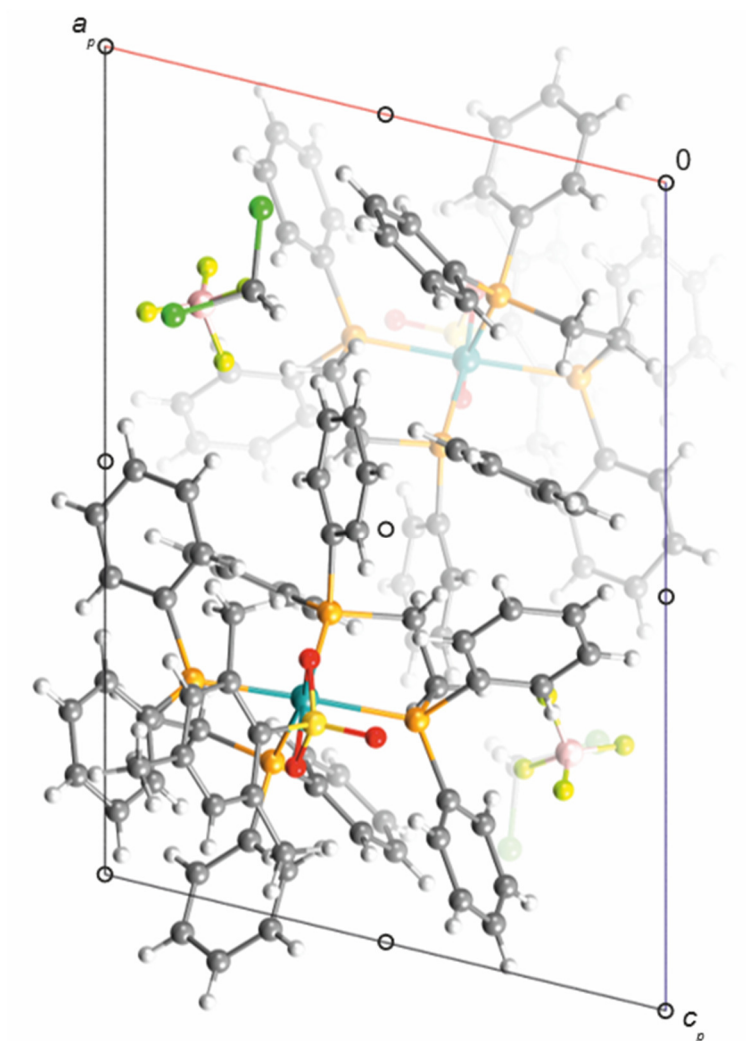


Figure 7.11: Mercury packing diagram of [Ru(dppe)₂(MesSO₃)(BF₄)]·DCM (**11**) in the triclinic space group $P\bar{1}$ with view along $[0\ 1\ 0]$. The symmetry elements of the space group are overlaid. Atoms: carbon (grey), hydrogen (white), boron (rose), chlorine (green), fluorine (green-yellow), oxygen (red), phosphorus (orange), ruthenium (turquoise), sulphur (yellow).

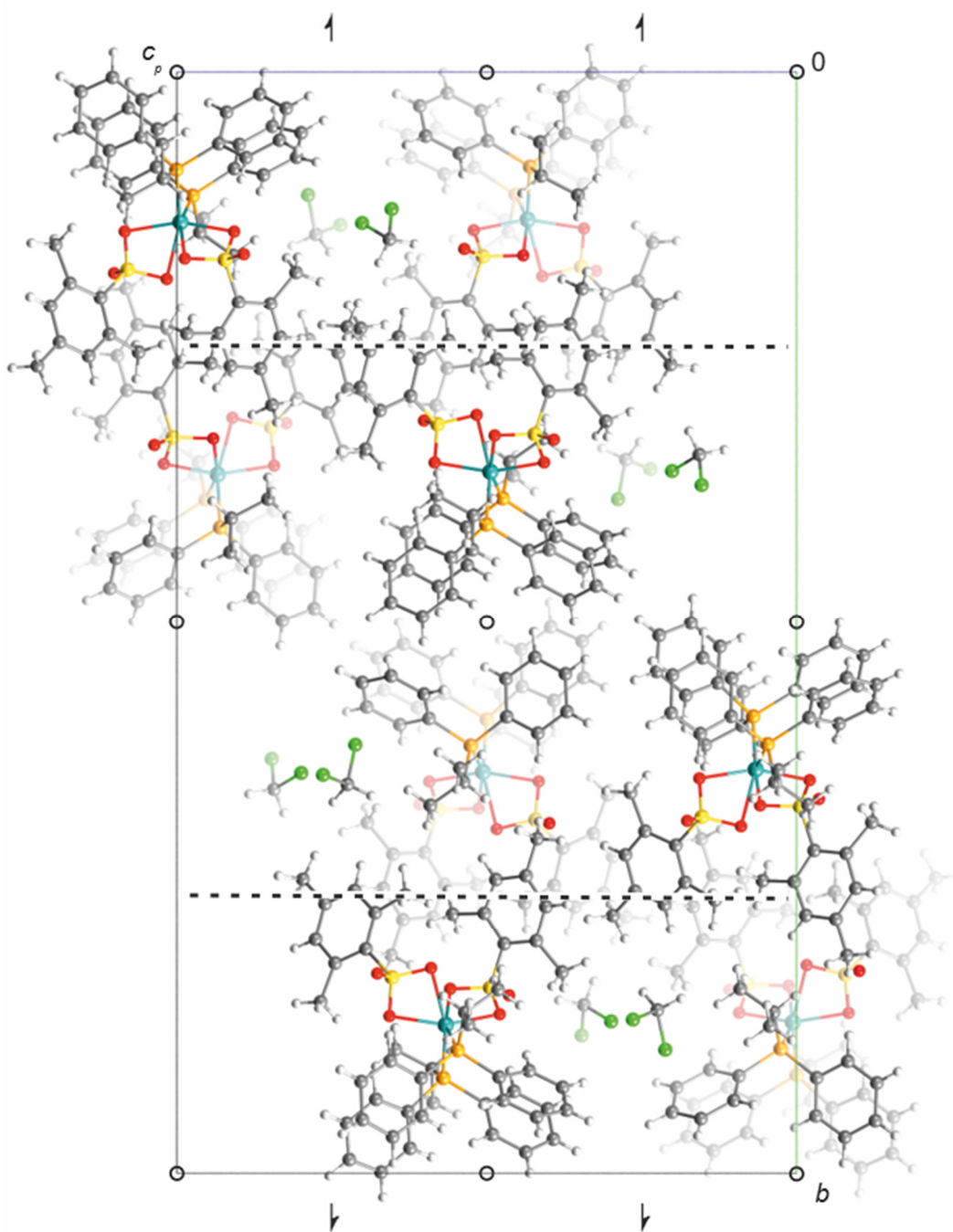


Figure 7.12: Mercury packing diagram of [Ru(PⁱPrPh₂)₂(MesSO₃)₂]·0.826DCM (**12**) in the monoclinic space group *P*₂₁/*c* with view along [1 0 0]. The symmetry elements of the space group are overlaid. Atoms: carbon (grey), hydrogen (white), chlorine (green), oxygen (red), phosphorus (orange), ruthenium (turquoise), sulphur (yellow).

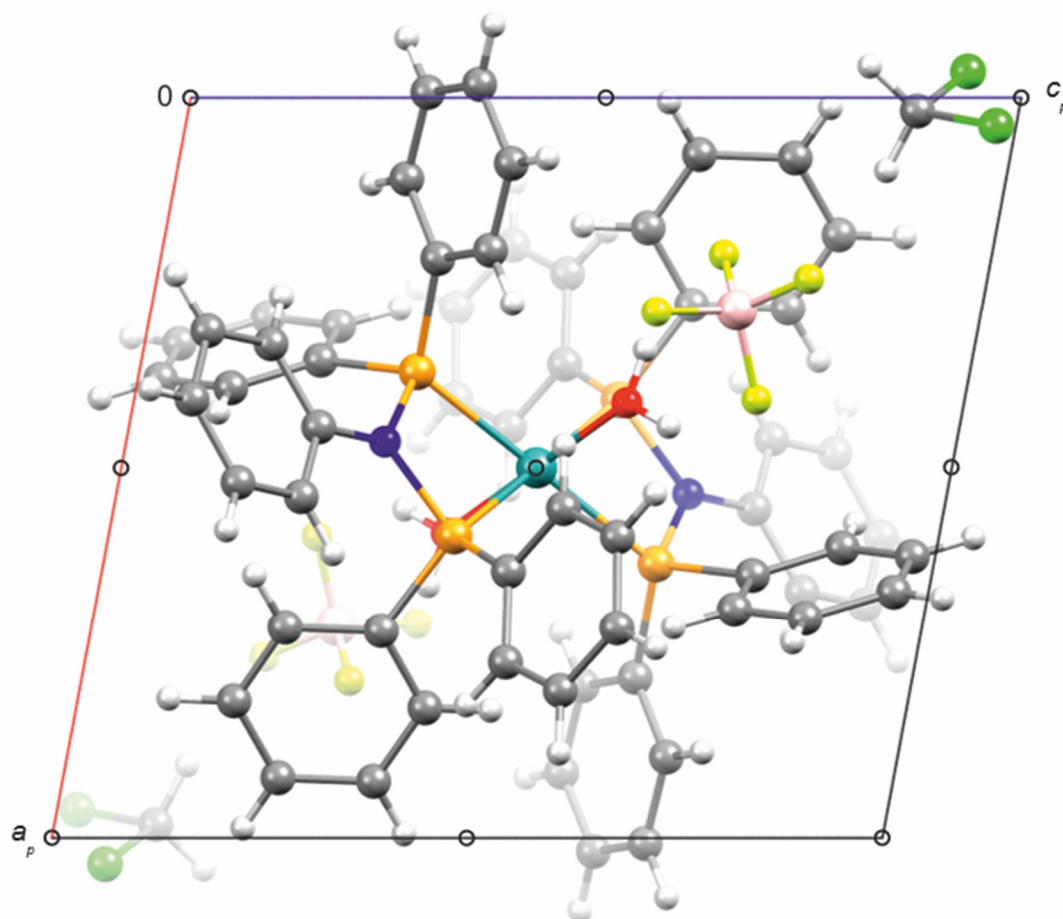


Figure 7.13: Mercury packing diagram of [Ru(dpppha)₂(H₂O)₂](BF₄)₂·1.948DCM (**13**) in the triclinic space group *P* $\bar{1}$ with view along [0 1 0]. The symmetry elements of the space group are overlaid. Atoms: carbon (grey), hydrogen (white), boron (rose), chlorine (green), fluorine (green-yellow), nitrogen (blue), oxygen (red), phosphorus (orange), ruthenium (turquoise).

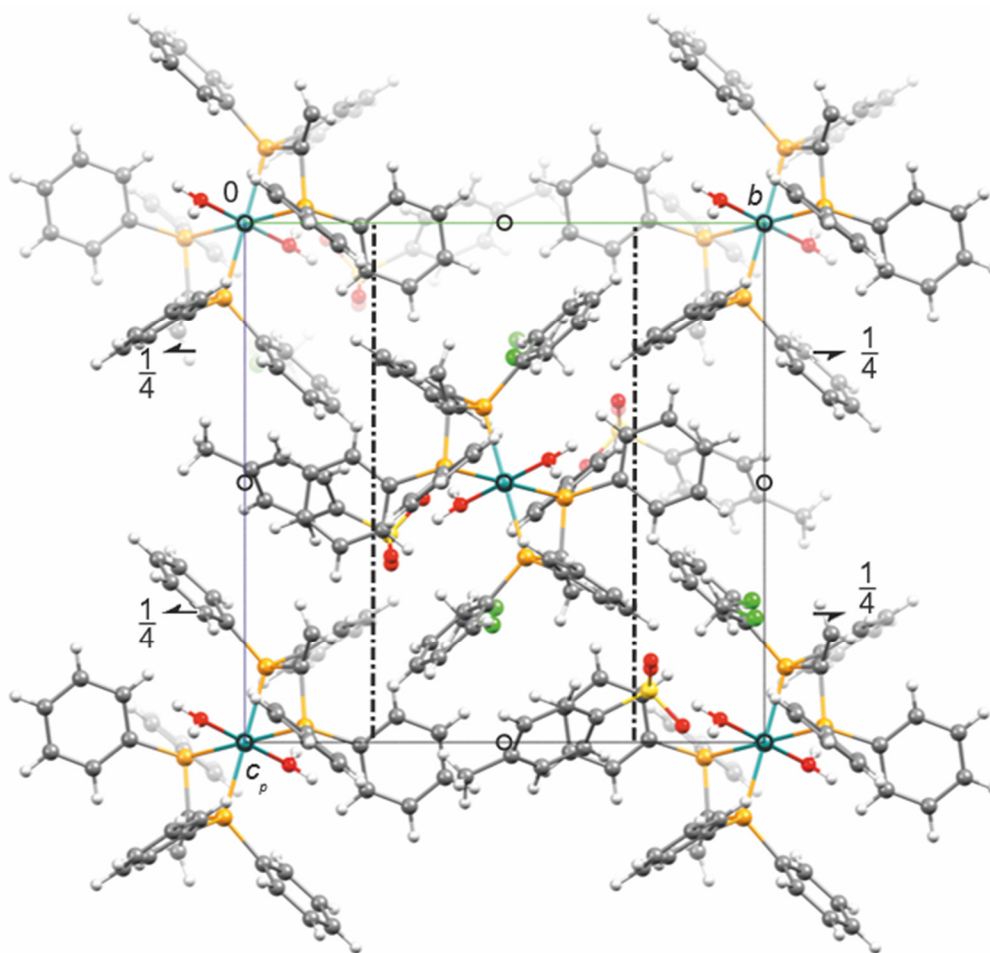


Figure 7.14: Mercury packing diagram of $[\text{Ru}(\text{dppen})_2(\text{H}_2\text{O})_2](\text{tos})_2 \cdot 1.506\text{DCM}$ (**14**) in the monoclinic space group $P2_1/n$ with view along $[1\ 0\ 0]$. The symmetry elements of the space group are overlaid. Atoms: carbon (grey), hydrogen (white), chlorine (green), oxygen (red), phosphorus (orange), ruthenium (turquoise), sulphur (yellow).

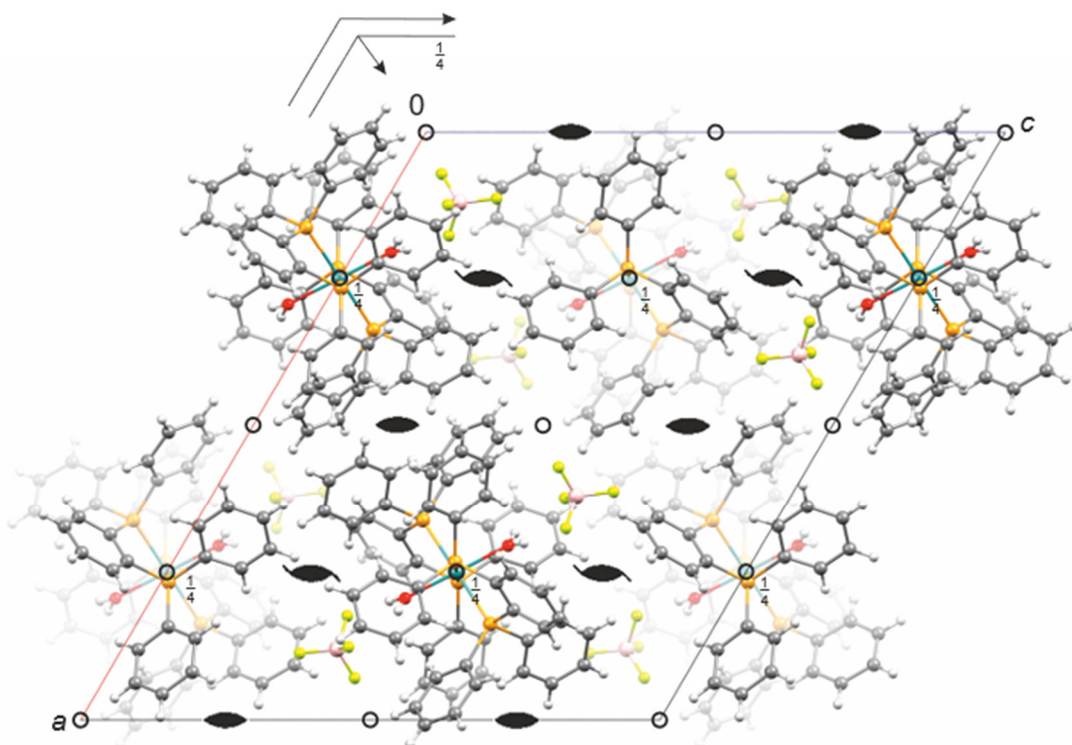


Figure 7.15: Mercury packing diagram of $[\text{Ru}(\text{dppbz})_2(\text{H}_2\text{O})_2](\text{BF}_4)_2$ (**15**) in the monoclinic space group $C2/c$ with view along $[0\ 1\ 0]$. The symmetry elements of the space group are overlaid. Atoms: carbon (grey), hydrogen (white), boron (rose), fluorine (green-yellow), oxygen (red), phosphorus (orange), ruthenium (turquoise).

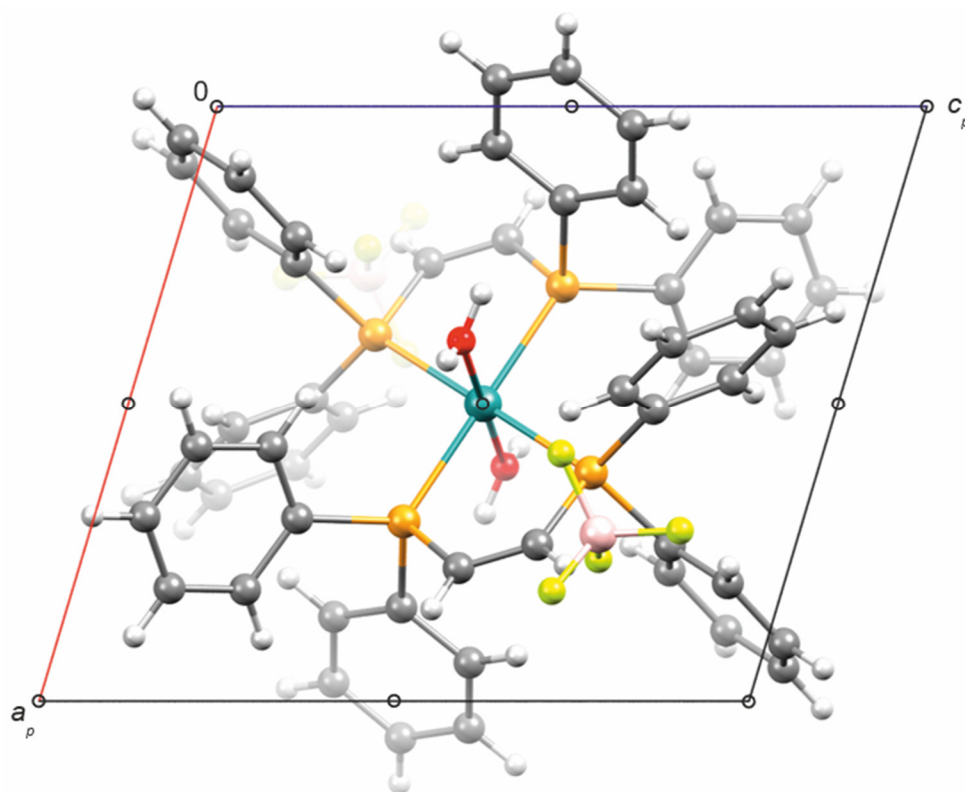


Figure 7.16: Mercury packing diagram of $[\text{Ru}(\text{dppv})_2(\text{H}_2\text{O})_2](\text{BF}_4)_2$ (**16**) in the triclinic space group $P\bar{1}$ with view along $[0\ 1\ 0]$. The symmetry elements of the space group are overlaid. Atoms: carbon (grey), hydrogen (white), boron (rose), fluorine (green-yellow), oxygen (red), phosphorus (orange), ruthenium (turquoise).

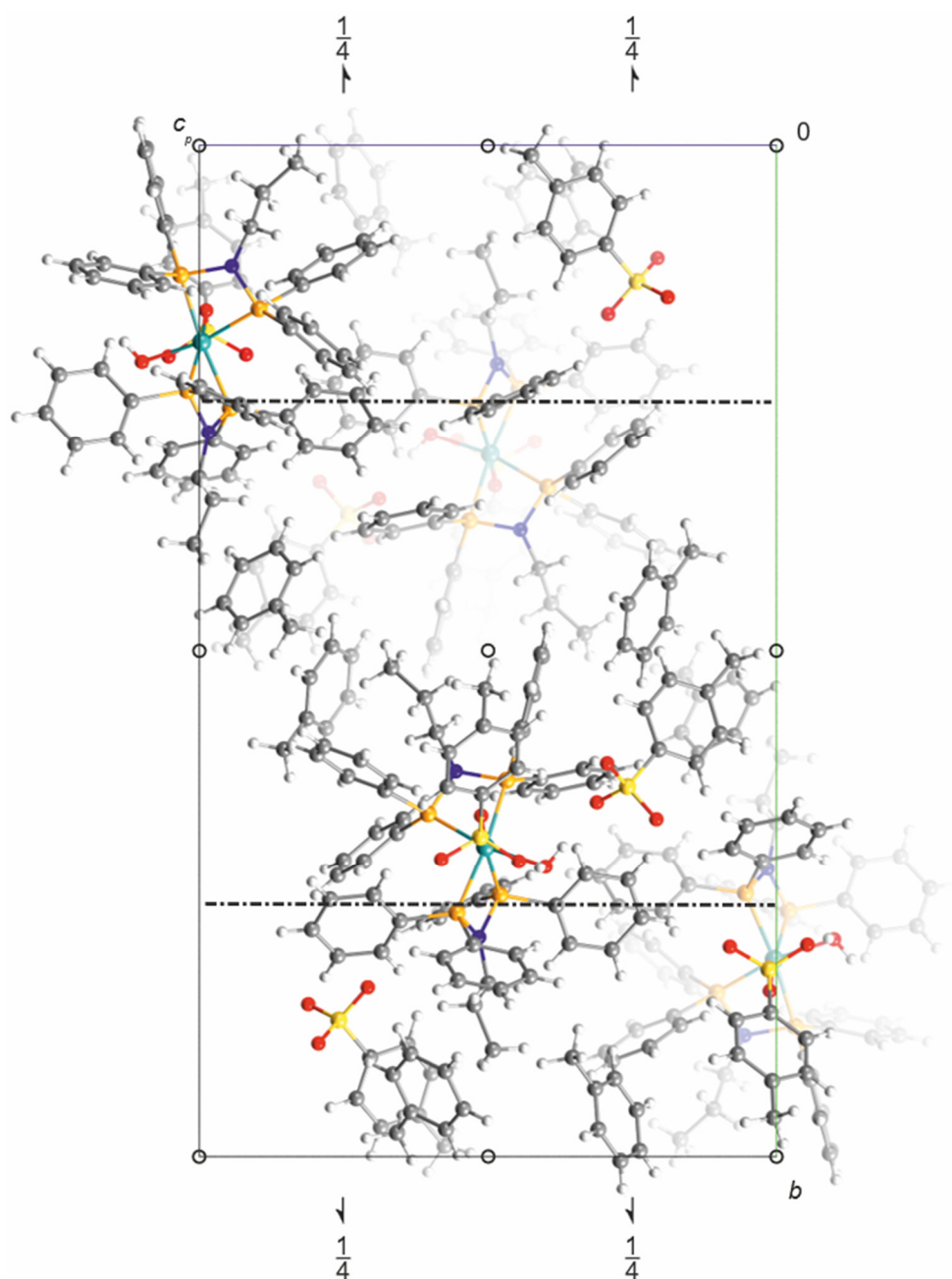


Figure 7.17: Mercury packing diagram of $[\text{Ru}(\text{dpppra})_2(\text{H}_2\text{O})(\text{tos})](\text{tos}) \cdot 1.891\text{C}_7\text{H}_8$ (**17**) in the monoclinic space group $P2_1/n$ with view along $[1\ 0\ 0]$. The symmetry elements of the space group are overlaid. Atoms: carbon (grey), hydrogen (white), nitrogen (blue), oxygen (red), phosphorus (orange), ruthenium (turquoise), sulphur (yellow).

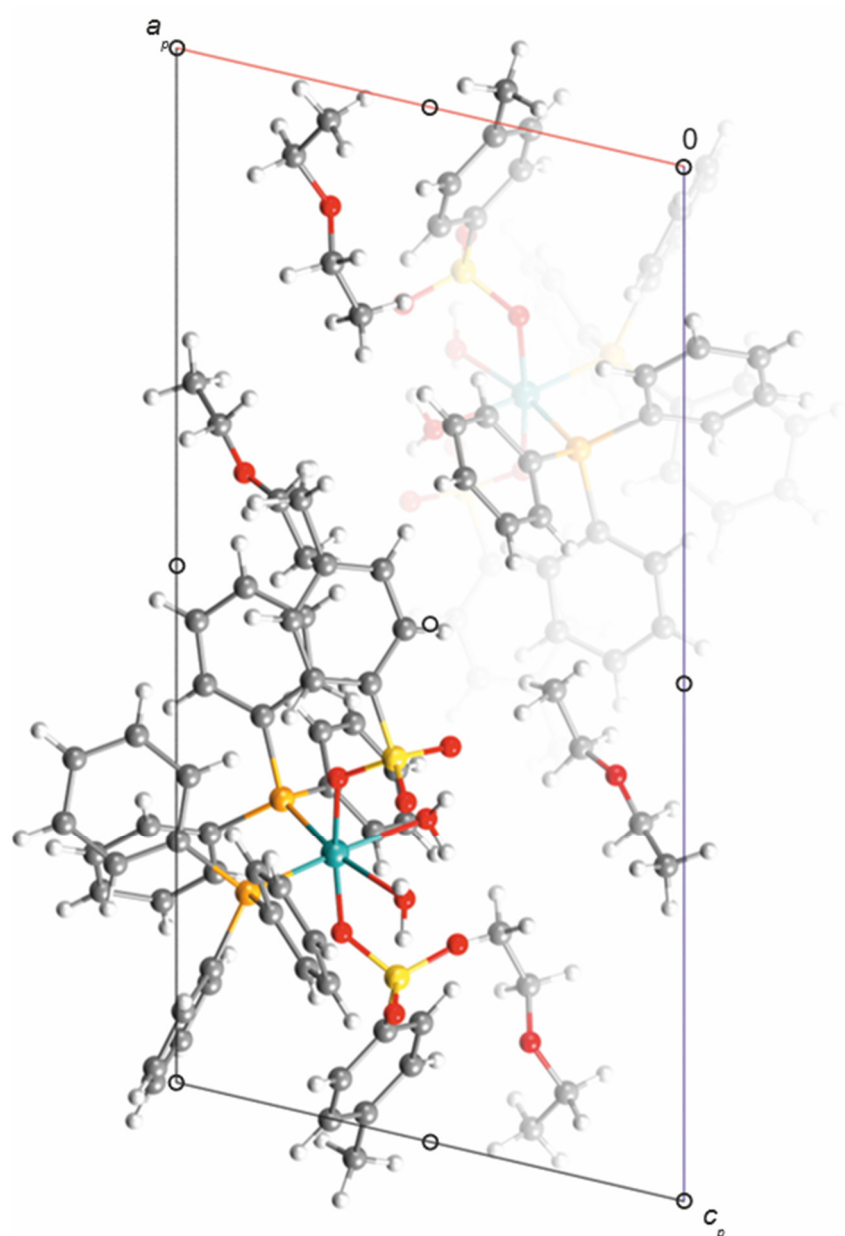


Figure 7.18: Mercury packing diagram of [Ru(PPh₃)₂(H₂O)₂(tos)₂]·2C₄H₁₀O (**18**) in the triclinic space group $P\bar{1}$ with view along $[0\ 1\ 0]$. The symmetry elements of the space group are overlaid. Atoms: carbon (grey), hydrogen (white), oxygen (red), phosphorus (orange), ruthenium (turquoise), sulphur (yellow).

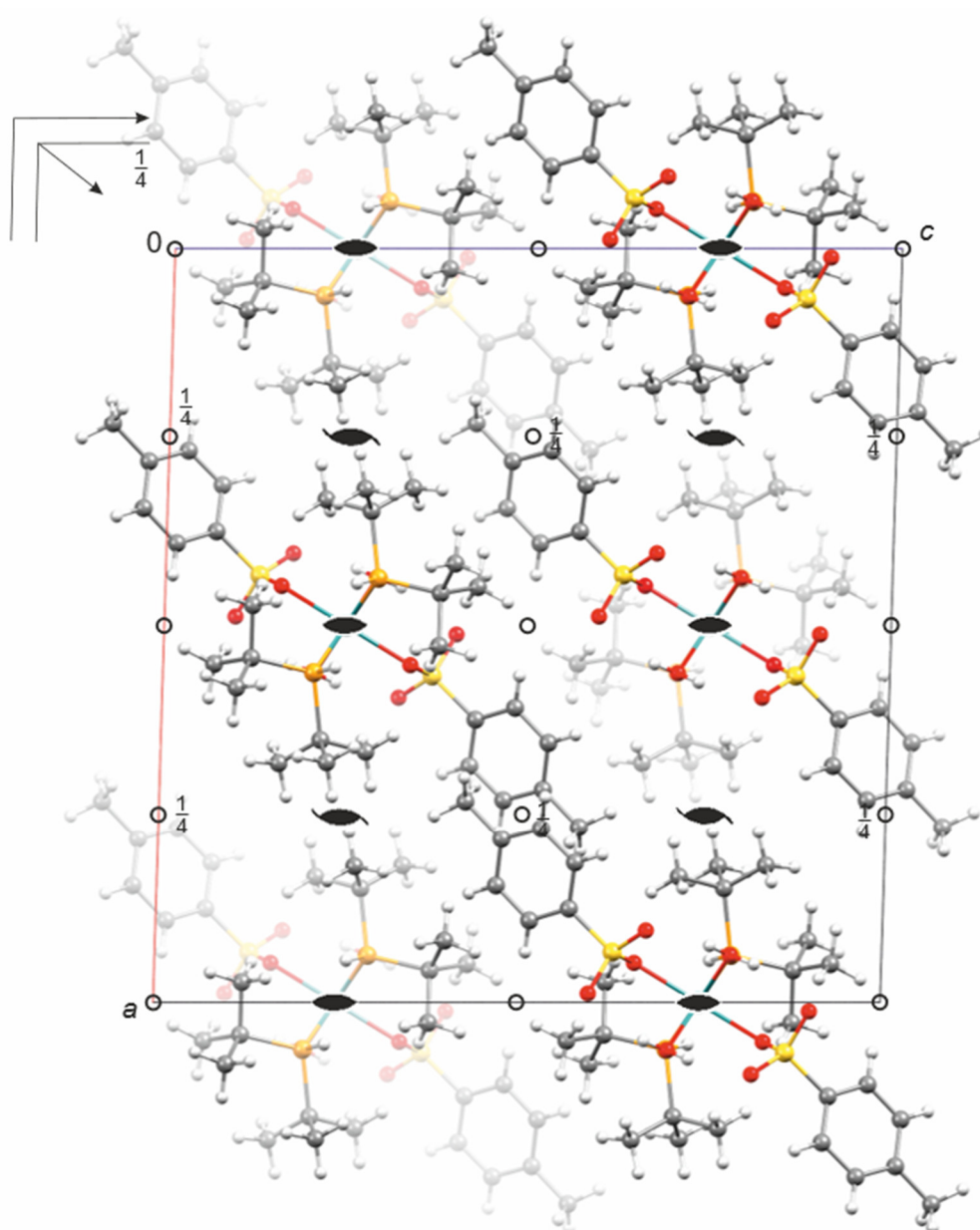


Figure 7.19: Mercury packing diagram of $[\text{Ru}(\text{PH}^t\text{Bu}_2)_2(\text{H}_2\text{O})_2(\text{tos})_2]$ (**19**) in the monoclinic space group $C2/c$ with view along $[0\ 1\ 0]$. The symmetry elements of the space group are overlaid. Atoms: carbon (grey), hydrogen (white), oxygen (red), phosphorus (orange), ruthenium (turquoise), sulphur (yellow).

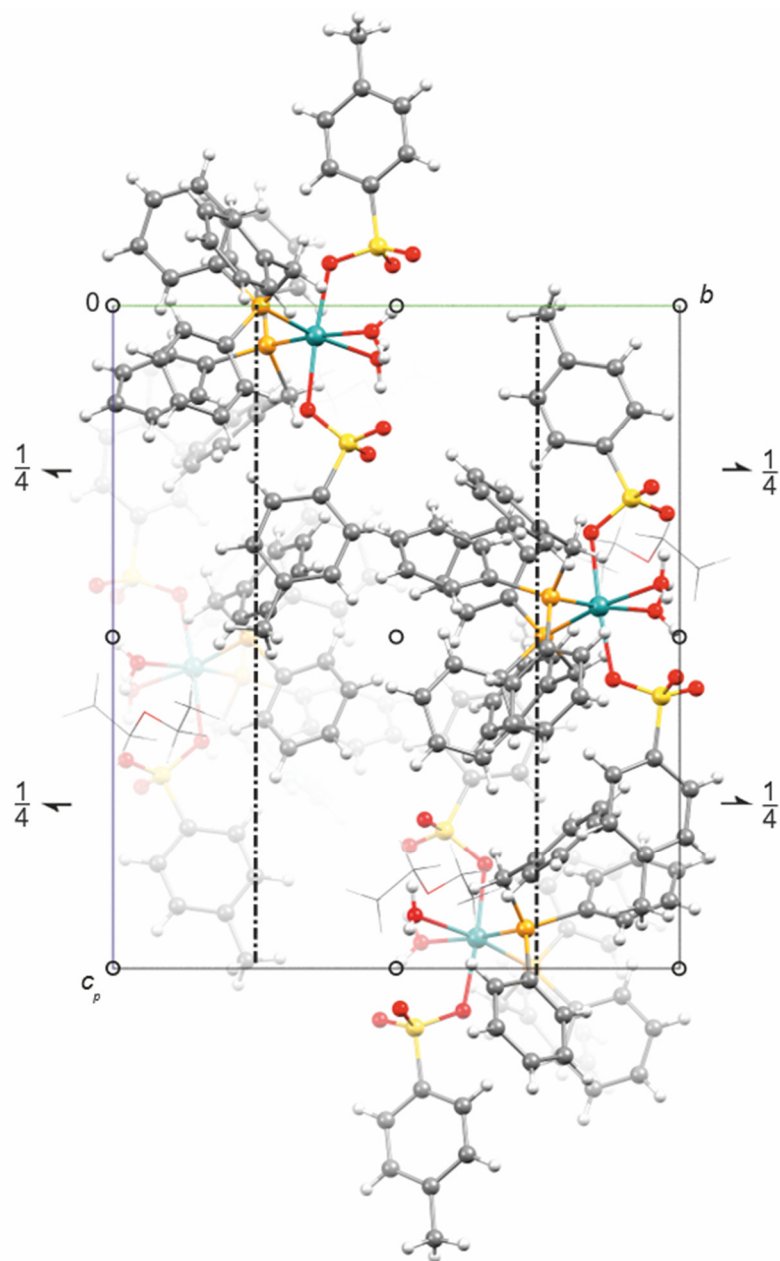


Figure 7.20: Mercury packing diagram of $[\text{Ru}(\text{PPh}_2\text{Bn})_2(\text{H}_2\text{O})_2(\text{tos})_2] \cdot \text{C}_4\text{H}_{10}\text{O}$ (**20**) in the monoclinic space group $P2_1/n$ with view along $[1\ 0\ 0]$. The symmetry elements of the space group are overlaid. Atoms: carbon (grey), hydrogen (white), oxygen (red), phosphorus (orange), ruthenium (turquoise), sulphur (yellow). Diethyl ether was illustrated as wireframe.

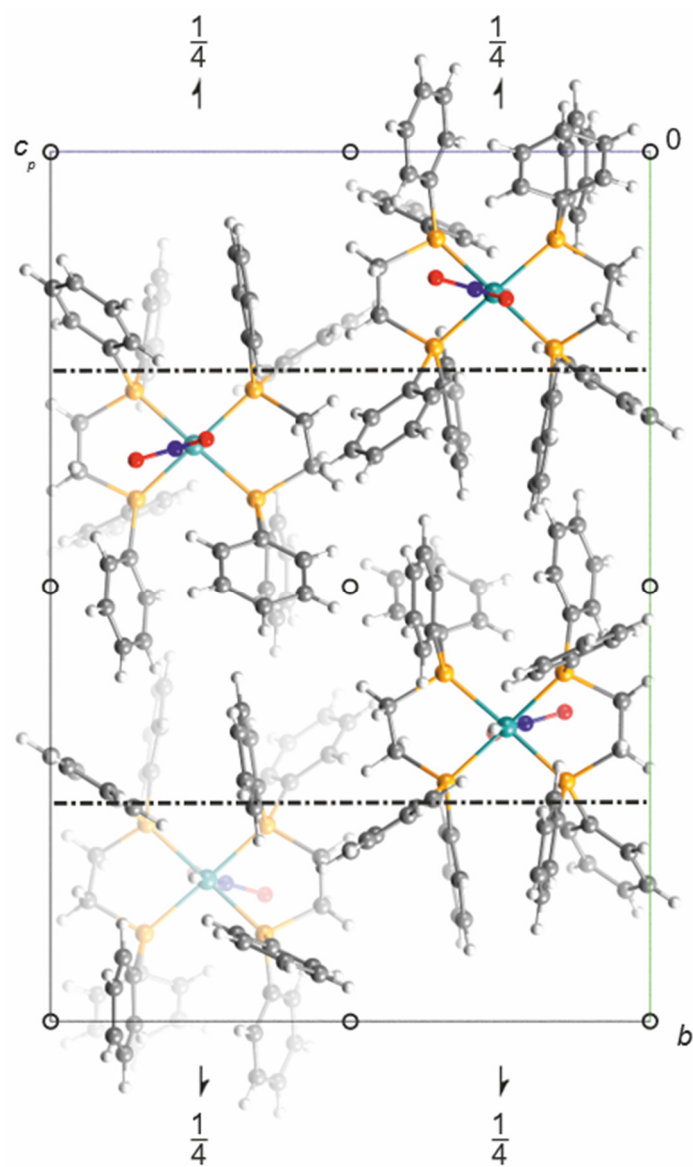


Figure 7.21: Mercury packing diagram of $[\text{Ru}(\text{dppe})_2(\text{H})(\text{NO}_2)]$ (**24**) in the monoclinic space group $P2_1/n$ with view along $[1\ 0\ 0]$. The symmetry elements of the space group are overlaid. Atoms: carbon (grey), hydrogen (white), nitrogen (blue), oxygen (red), phosphorus (orange), ruthenium (turquoise).

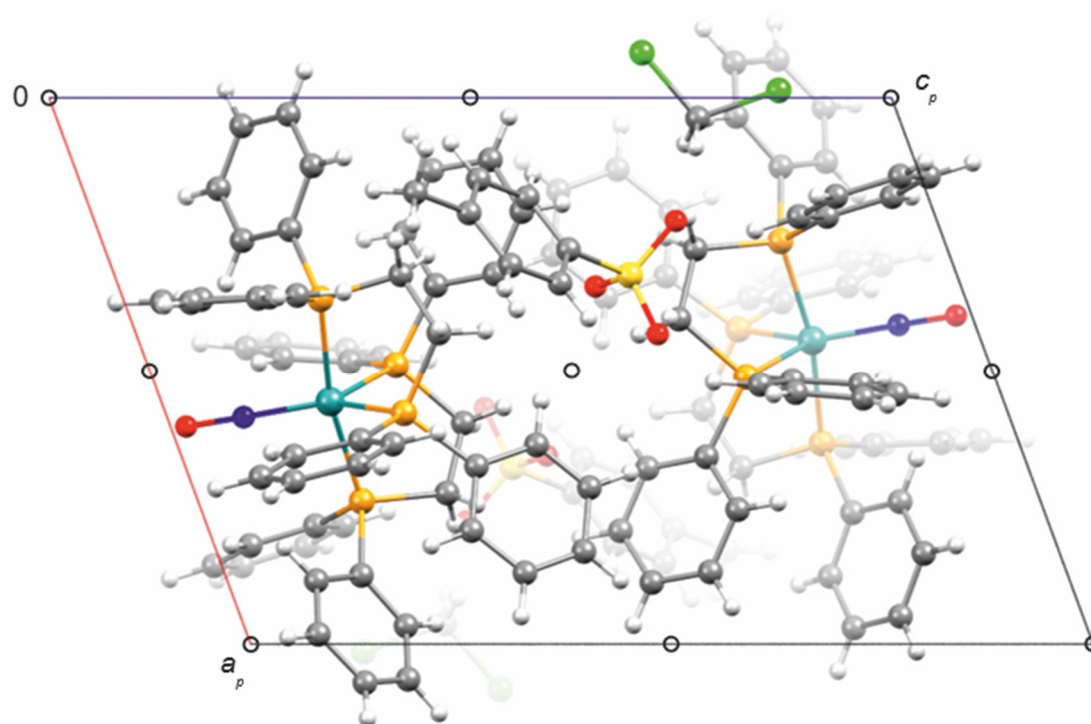


Figure 7.22: Mercury packing diagram of $[\text{Ru}(\text{dppe})_2(\text{NO})](\text{tos})\cdot 0.955\text{DCM}$ (**25**) in the triclinic space group $P\bar{1}$ with view along $[0\ 1\ 0]$. The symmetry elements of the space group are overlaid. Atoms: carbon (grey), hydrogen (white), chlorine (green), nitrogen (blue), oxygen (red), phosphorus (orange), ruthenium (turquoise), sulphur (yellow).

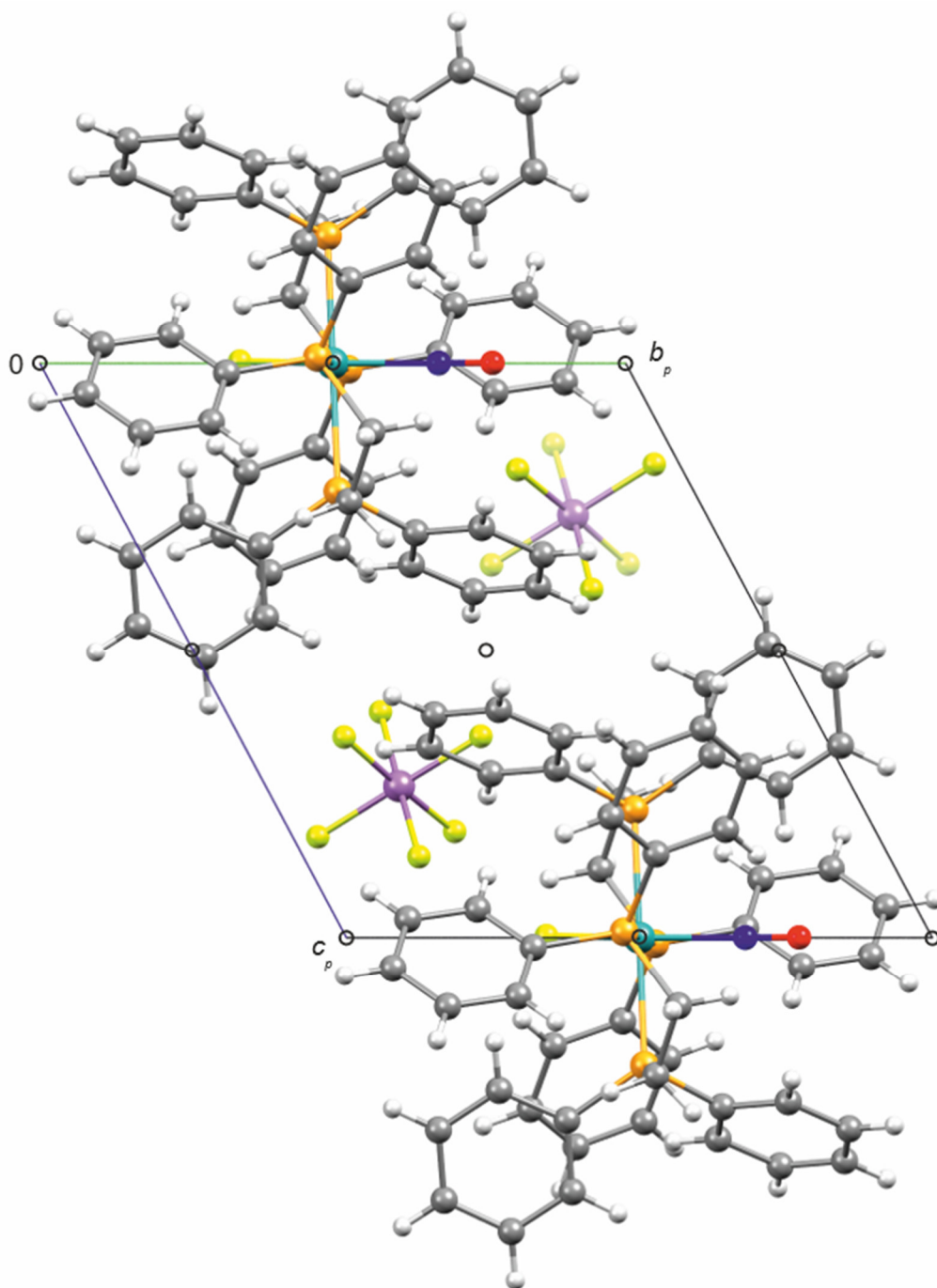


Figure 7.23: Mercury packing diagram of $[\text{Ru}(\text{dppe})_2(\text{NO})\text{F}](\text{SbF}_6)$ (**26**) in the triclinic space group $P\bar{1}$ with view along $[1\ 0\ 0]$. The symmetry elements of the space group are overlaid. Atoms: carbon (grey), hydrogen (white), nitrogen (blue), oxygen (red), phosphorus (orange), ruthenium (turquoise), antimony (lavender).

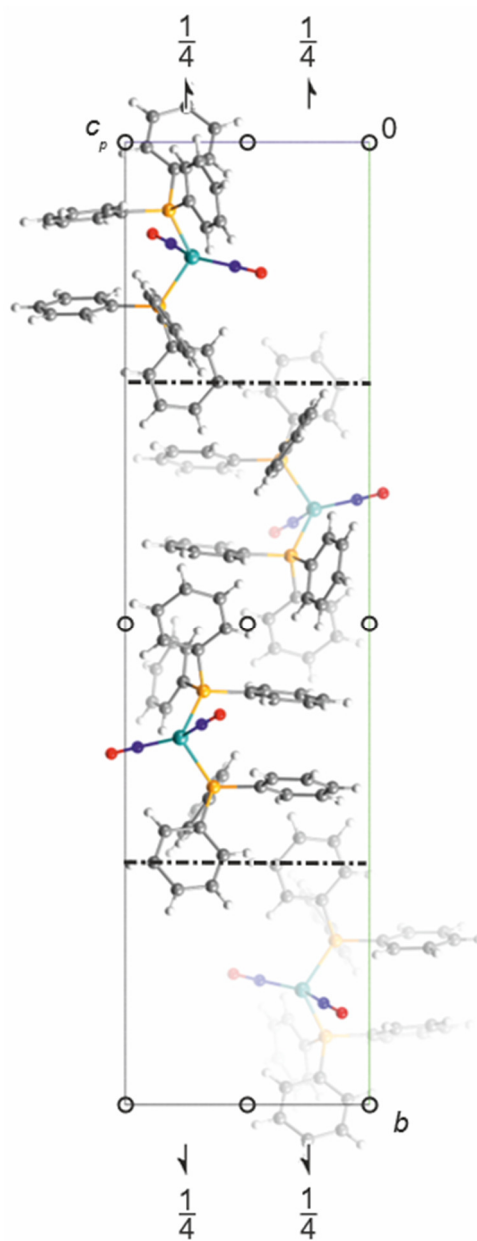


Figure 7.24: Mercury packing diagram of $[\text{Ru}(\text{PPh}_3)_2(\text{NO})_2]$ (**27**) in the monoclinic space group $P2_1/n$ with view along $[1\ 0\ 0]$. The symmetry elements of the space group are overlaid. Atoms: carbon (grey), hydrogen (white), nitrogen (blue), oxygen (red), phosphorus (orange), ruthenium (turquoise).

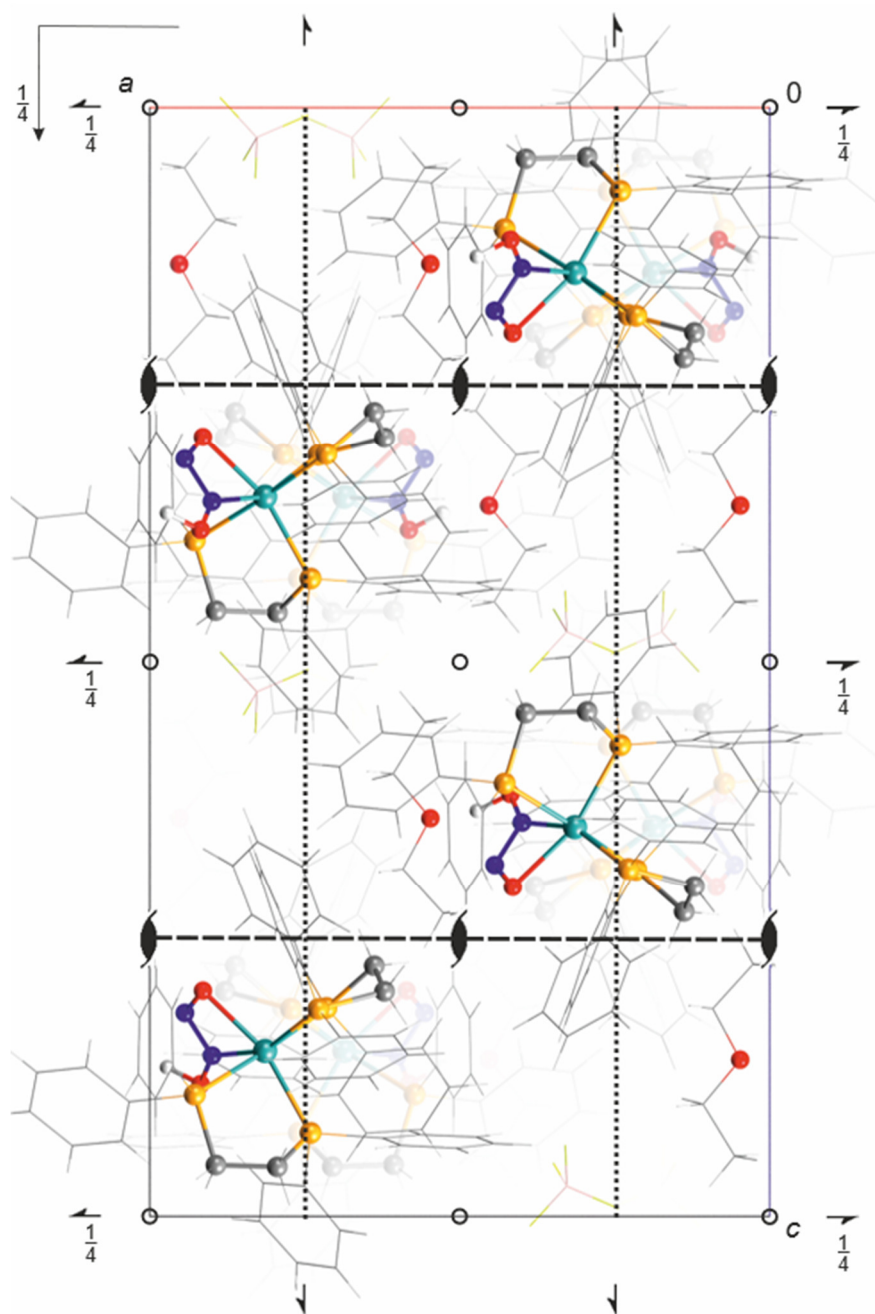


Figure 7.25: Mercury packing diagram of $[\text{Ru}(\text{dppe})_2(\text{N}_2\text{O}_2\text{H})]\text{BF}_4 \cdot \text{Et}_2\text{O}$ (**28a**) in the orthorhombic space group $Pbca$ with view along $[0\ 1\ 0]$. The symmetry elements of the space group are overlaid. Atoms: carbon (grey), hydrogen (white), boron (rose), fluorine (green-yellow), nitrogen (blue), oxygen (red), phosphorus (orange), ruthenium (turquoise). Phenyl groups, diethyl ether (except oxygen) and tetrafluorido borate were illustrated as wireframe.

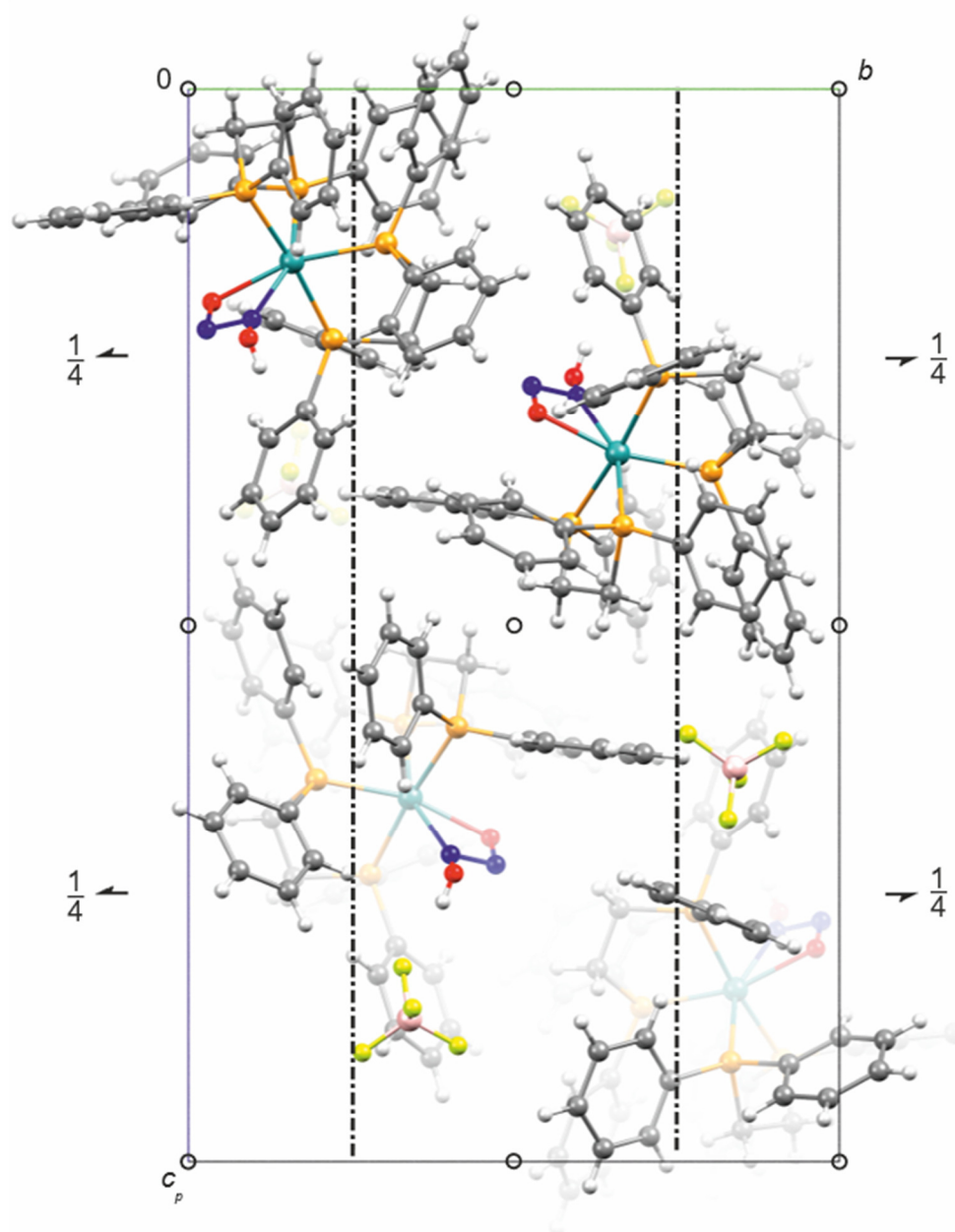


Figure 7.26: Mercury packing diagram of $[\text{Ru}(\text{dppe})_2(\text{N}_2\text{O}_2\text{H})]\text{BF}_4$ (**28b**) in the monoclinic space group $P2_1/n$ with view along $[1\ 0\ 0]$. The symmetry elements of the space group are overlaid. Atoms: carbon (grey), hydrogen (white), boron (rose), fluorine (green-yellow), nitrogen (blue), oxygen (red), phosphorus (orange), ruthenium (turquoise).

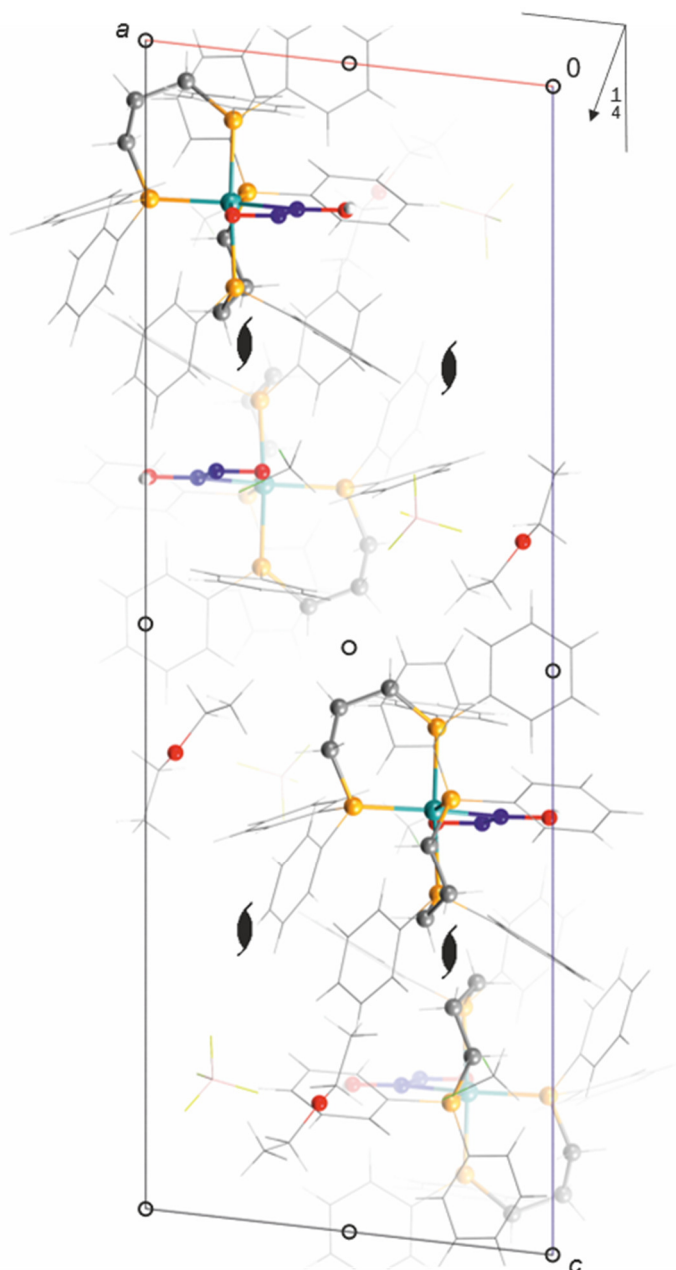


Figure 7.27: Mercury packing diagram of $[\text{Ru}(\text{dppp})_2(\text{N}_2\text{O}_2\text{H})]\text{BF}_4 \cdot \text{Et}_2\text{O} \cdot \text{DCM}$ (**29**) in the monoclinic space group $P2_1/n$ with view along $[0\ 1\ 0]$. The symmetry elements of the space group are overlaid. Atoms: carbon (grey), hydrogen (white), boron (rose), chlorine (green), fluorine (green-yellow), nitrogen (blue), oxygen (red), phosphorus (orange), ruthenium (turquoise). Phenyl groups, diethyl ether (except oxygen), dichloromethane and tetrafluorido borate were illustrated as wireframe.

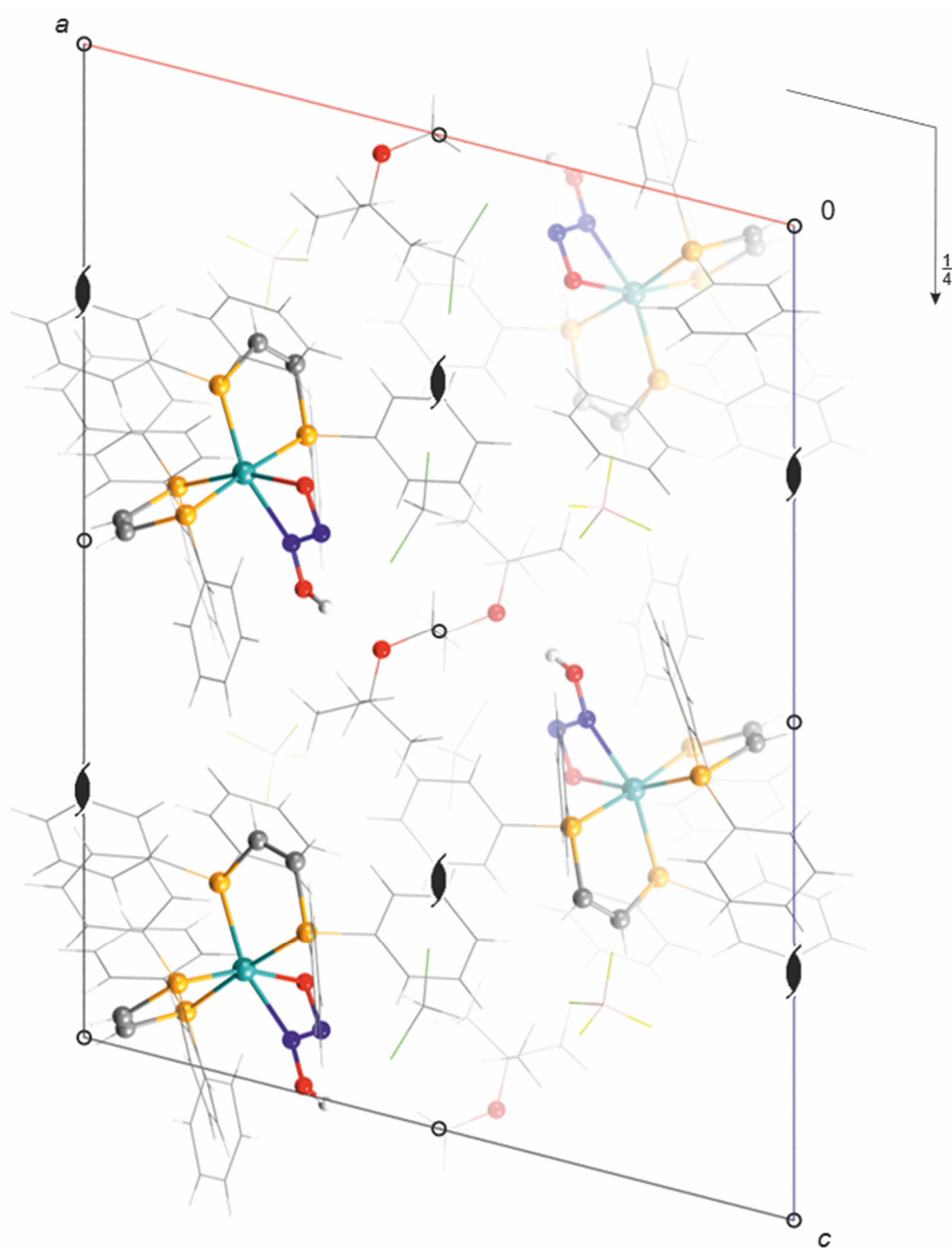


Figure 7.28: Mercury packing diagram of $[\text{Ru}(\text{dppv})_2(\text{N}_2\text{O}_2\text{H})]\text{BF}_4 \cdot 0.81\text{TBME} \cdot \text{DCM}$ (**30**) in the monoclinic space group $P2_1/c$ with view along $[0\ 1\ 0]$. The symmetry elements of the space group are overlaid. Atoms: carbon (grey), hydrogen (white), boron (rose), chlorine (green), fluorine (green-yellow), nitrogen (blue), oxygen (red), phosphorus (orange), ruthenium (turquoise). Phenyl groups, TBME (except oxygen), dichloromethane and tetrafluorido borate were illustrated as wireframe.

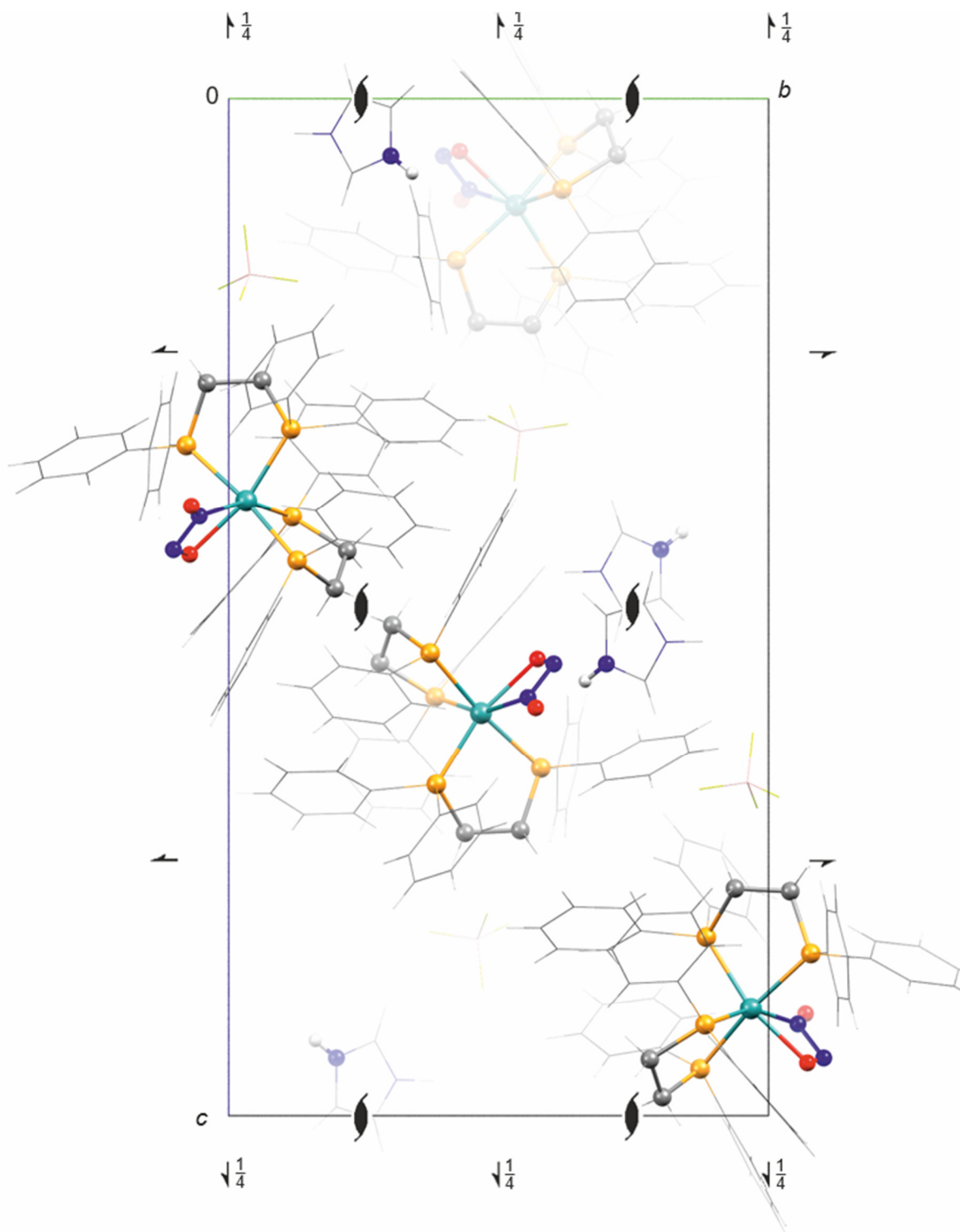


Figure 7.29: Mercury packing diagram of $[\text{Ru}(\text{dppe})_2(\text{N}_2\text{O}_2)] \cdot \text{HImiBF}_4$ (**31**) in the orthorhombic space group $P2_12_12_1$ with view along $[1\ 0\ 0]$. The symmetry elements of the space group are overlaid. Atoms: carbon (grey), hydrogen (white), boron (rose), fluorine (green-yellow), nitrogen (blue), oxygen (red), phosphorus (orange), ruthenium (turquoise). Phenyl groups, imidazole (except the protonated nitrogen) and tetrafluorido borate were illustrated as wireframe.

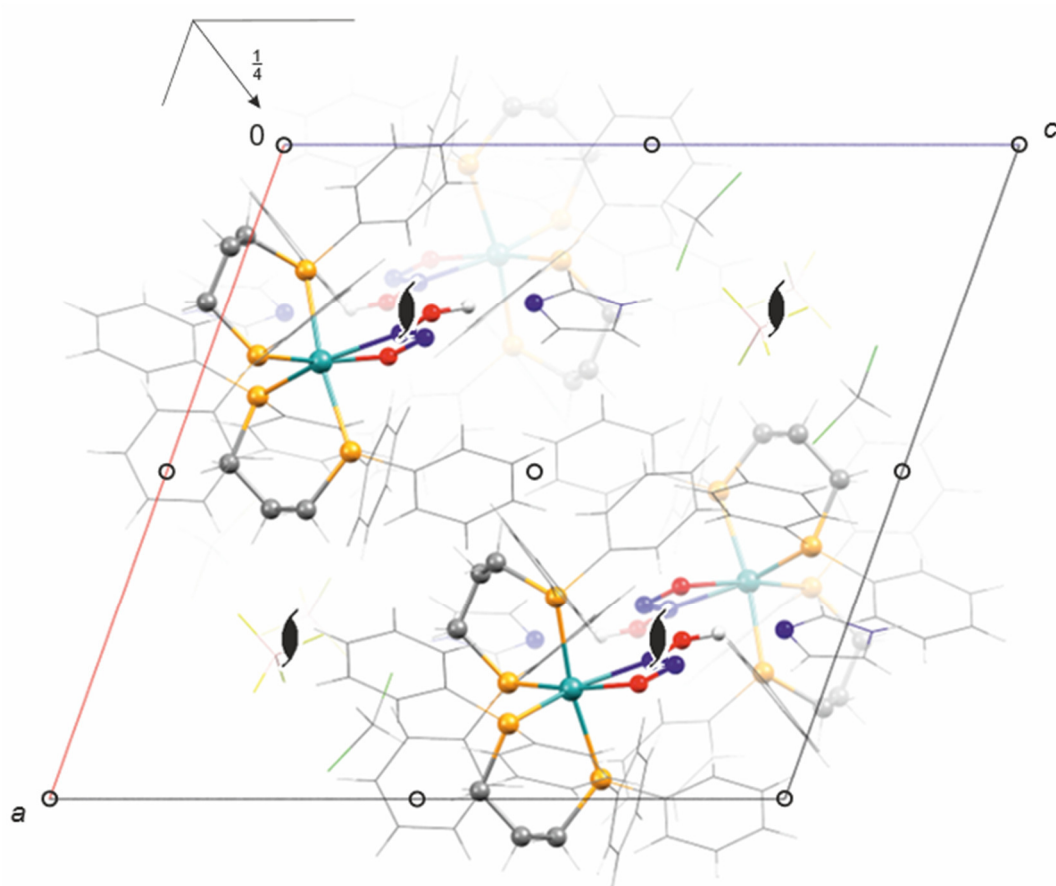


Figure 7.30: Mercury packing diagram of $[\text{Ru}(\text{dppp})_2(\text{N}_2\text{O}_2\text{H})]\text{BF}_4 \cdot \text{Imi} \cdot 0.856\text{DCM}$ (**32**) in the monoclinic space group $P2_1/n$ with view along $[0\ 1\ 0]$. The symmetry elements of the space group are overlaid. Atoms: carbon (grey), hydrogen (white), boron (rose), chlorine (green), fluorine (green-yellow), nitrogen (blue), oxygen (red), phosphorus (orange), ruthenium (turquoise). Phenyl groups, imidazole (except the basic nitrogen), dichloromethane and tetrafluorido borate were illustrated as wireframe.

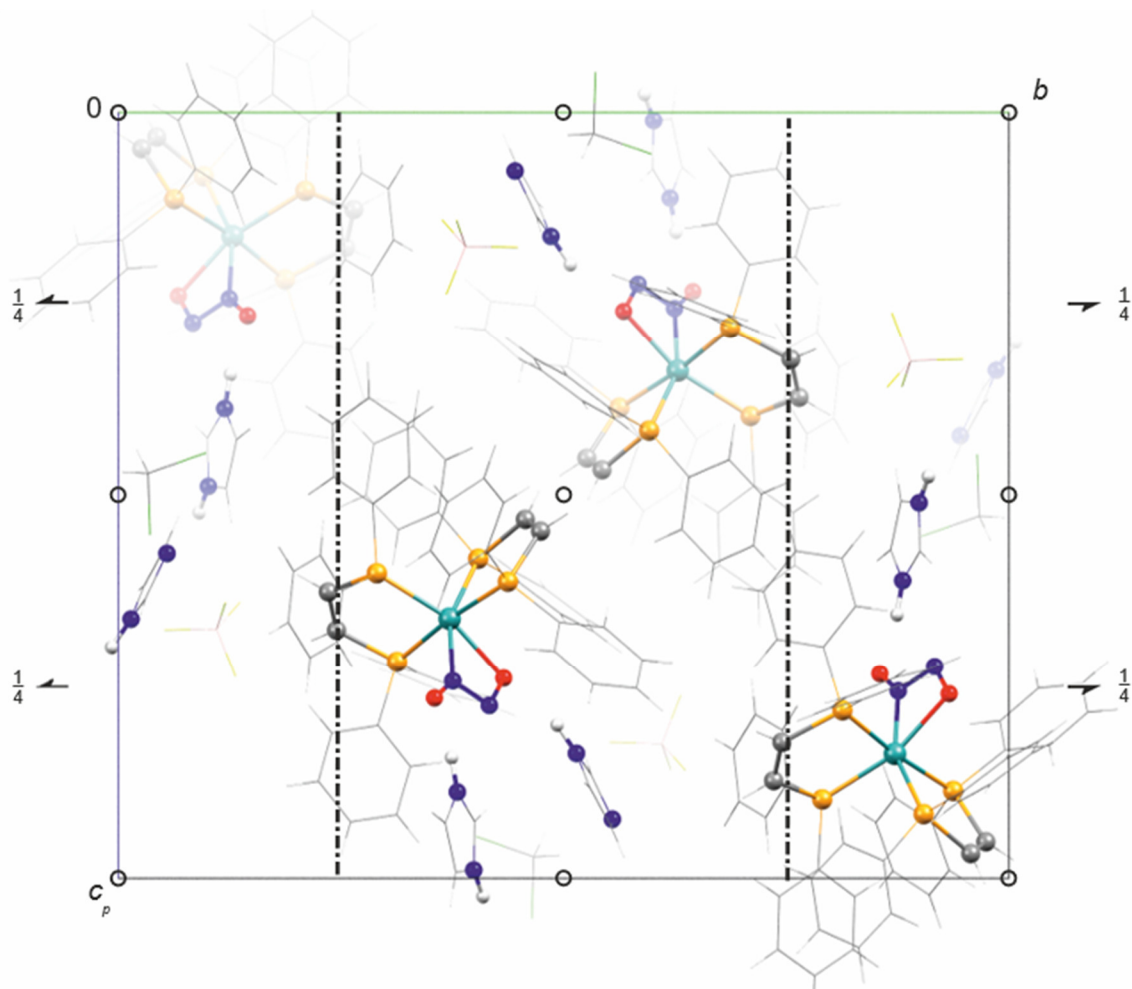


Figure 7.31: Mercury packing diagram of $[\text{Ru}(\text{dppv})_2(\text{N}_2\text{O}_2)] \cdot \text{HImiBF}_4 \cdot \text{Imi} \cdot 0.804\text{DCM}$ (**33**) in the monoclinic space group $P2_1/n$ with view along $[1\ 0\ 0]$. The symmetry elements of the space group are overlaid. Atoms: carbon (grey), hydrogen (white), boron (rose), chlorine (green), fluorine (green-yellow), nitrogen (blue), oxygen (red), phosphorus (orange), ruthenium (turquoise). Phenyl groups, imidazole (except both nitrogens), dichloromethane and tetrafluorido borate were illustrated as wireframe.

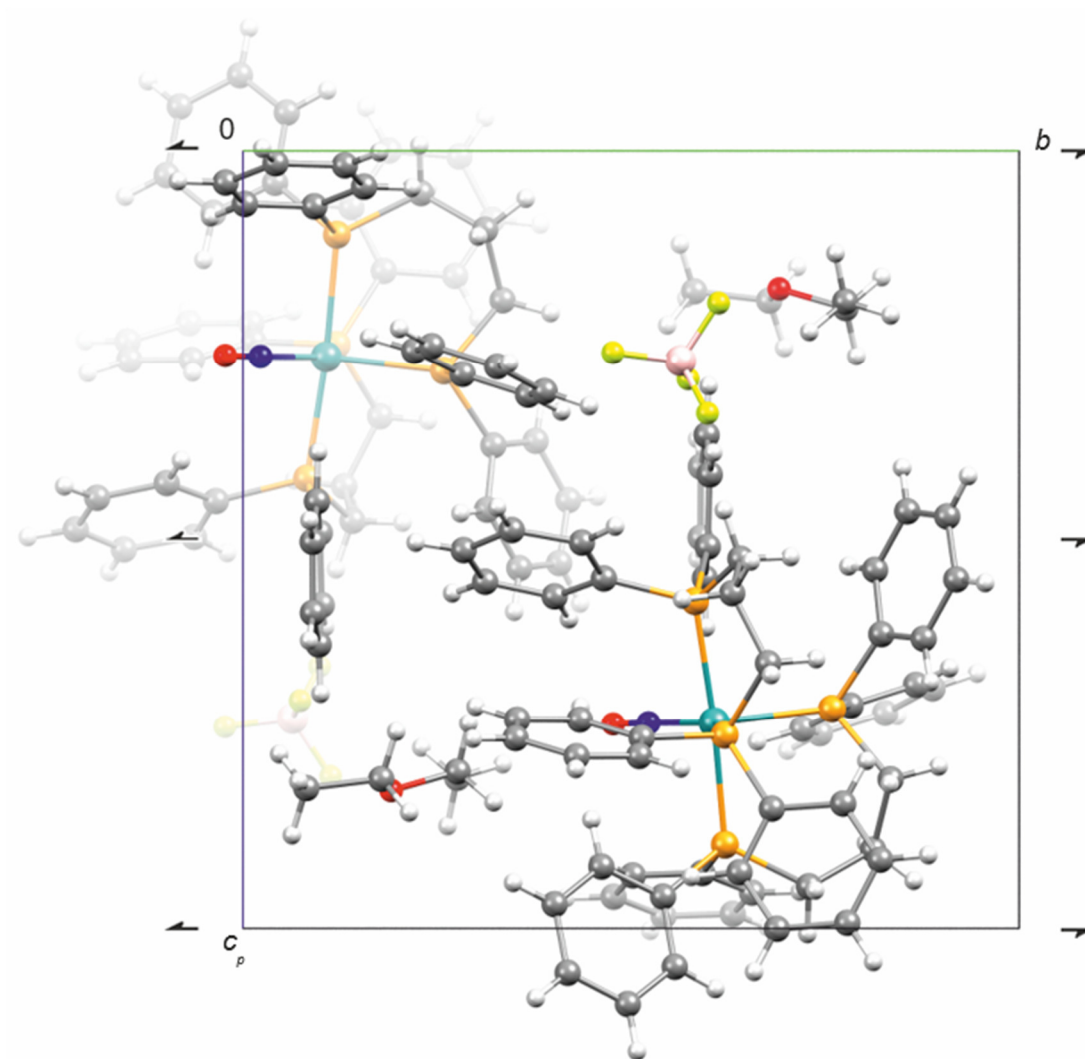


Figure 7.32: Mercury packing diagram of $[\text{Ru}(\text{dppp})_2(\text{NO})]\text{BF}_4 \cdot \text{Et}_2\text{O}$ (**36**) in the monoclinic space group $P2_1$ with view along $[1\ 0\ 0]$. The symmetry elements of the space group are overlaid. Atoms: carbon (grey), hydrogen (white), boron (rose), fluorine (green-yellow), nitrogen (blue), oxygen (red), phosphorus (orange), ruthenium (turquoise).

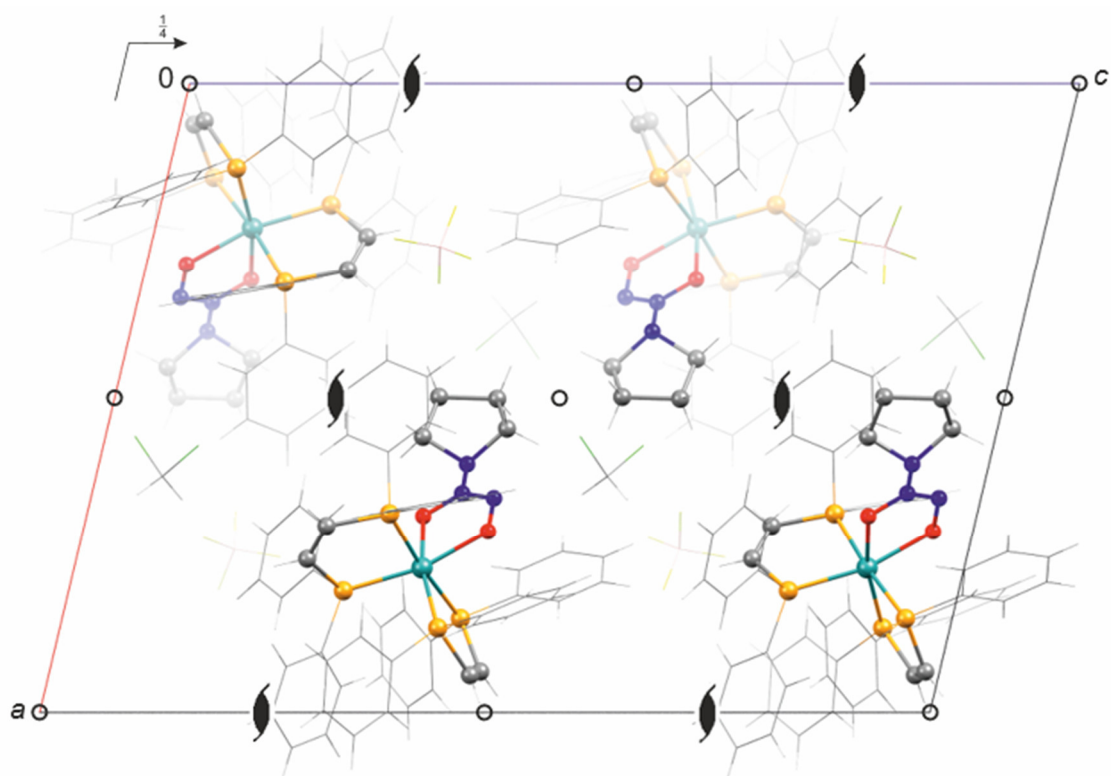


Figure 7.33: Mercury packing diagram of [Ru(dppv)₂(pdd)]BF₄·0.601DCM (**37**) in the monoclinic space group *P*2₁/*c* with view along [0 1 0]. The symmetry elements of the space group are overlaid. Atoms: carbon (grey), hydrogen (white), boron (rose), chlorine (green), fluorine (green-yellow), nitrogen (blue), oxygen (red), phosphorus (orange), ruthenium (turquoise). Phenyl groups, dichloromethane and tetrafluorido borate were illustrated as wireframe.

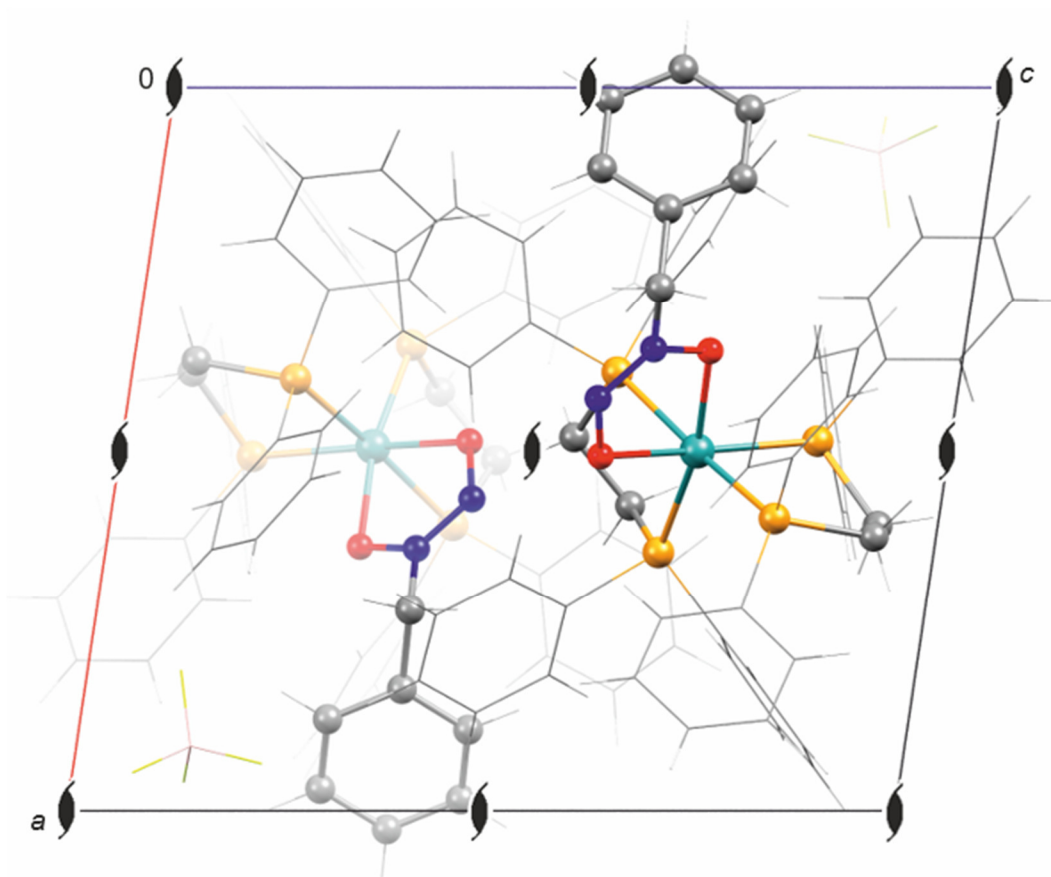


Figure 7.34: Mercury packing diagram of [Ru(dppe)₂(bdd)]BF₄ (**39**) in the monoclinic space group *P*2₁ with view along [0 1 0]. The symmetry elements of the space group are overlaid. Atoms: carbon (grey), hydrogen (white), boron (rose), fluorine (green-yellow), nitrogen (blue), oxygen (red), phosphorus (orange), ruthenium (turquoise). Phenyl groups and tetrafluorido borate were illustrated as wireframe.

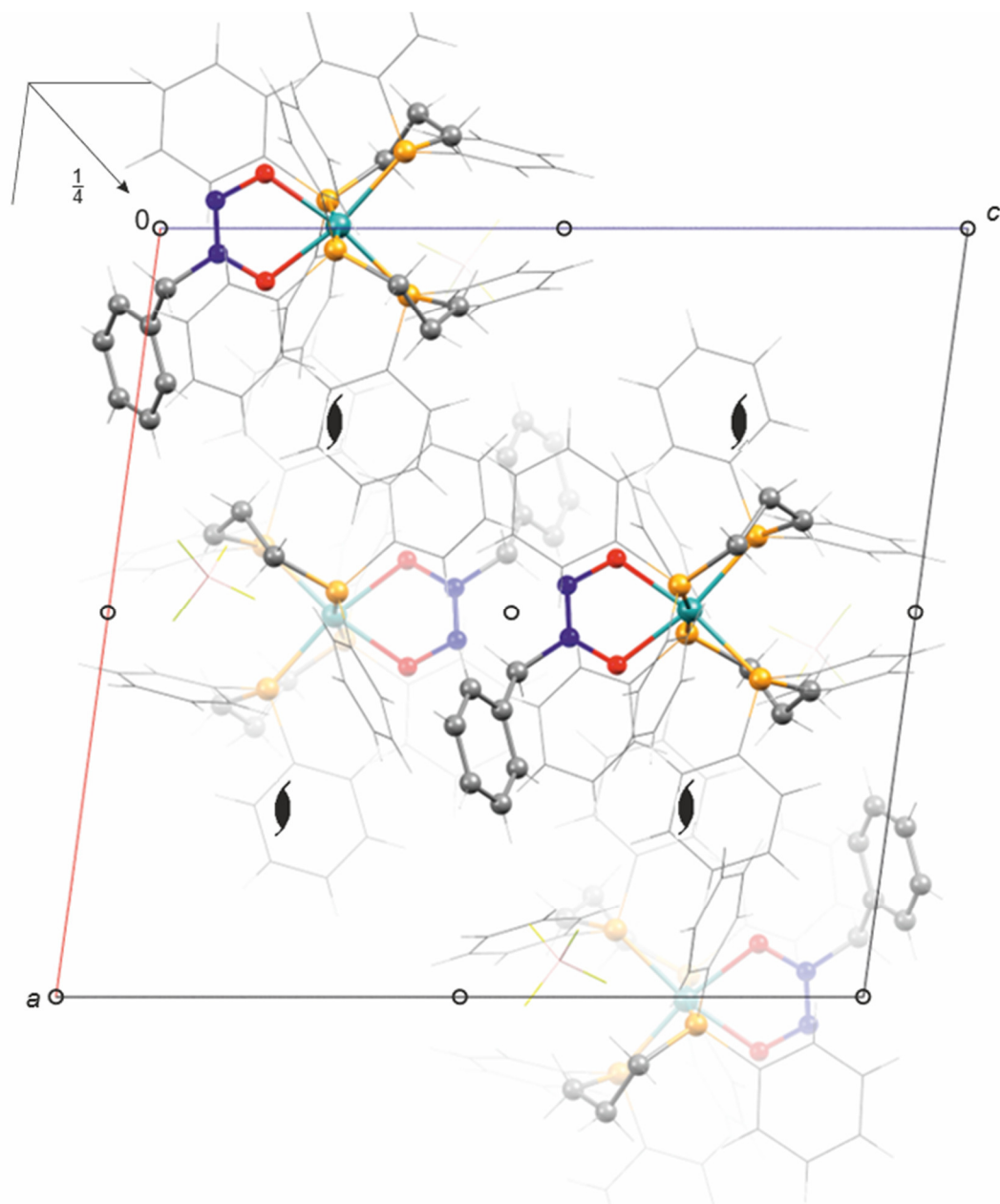


Figure 7.35: Mercury packing diagram of $[\text{Ru}(\text{dppp})_2(\text{bdd})]\text{BF}_4$ (**40**) in the monoclinic space group $P2_1/n$ with view along $[0\ 1\ 0]$. The symmetry elements of the space group are overlaid. Atoms: carbon (grey), hydrogen (white), boron (rose), fluorine (green-yellow), nitrogen (blue), oxygen (red), phosphorus (orange), ruthenium (turquoise). Phenyl groups and tetrafluorido borate were illustrated as wireframe.

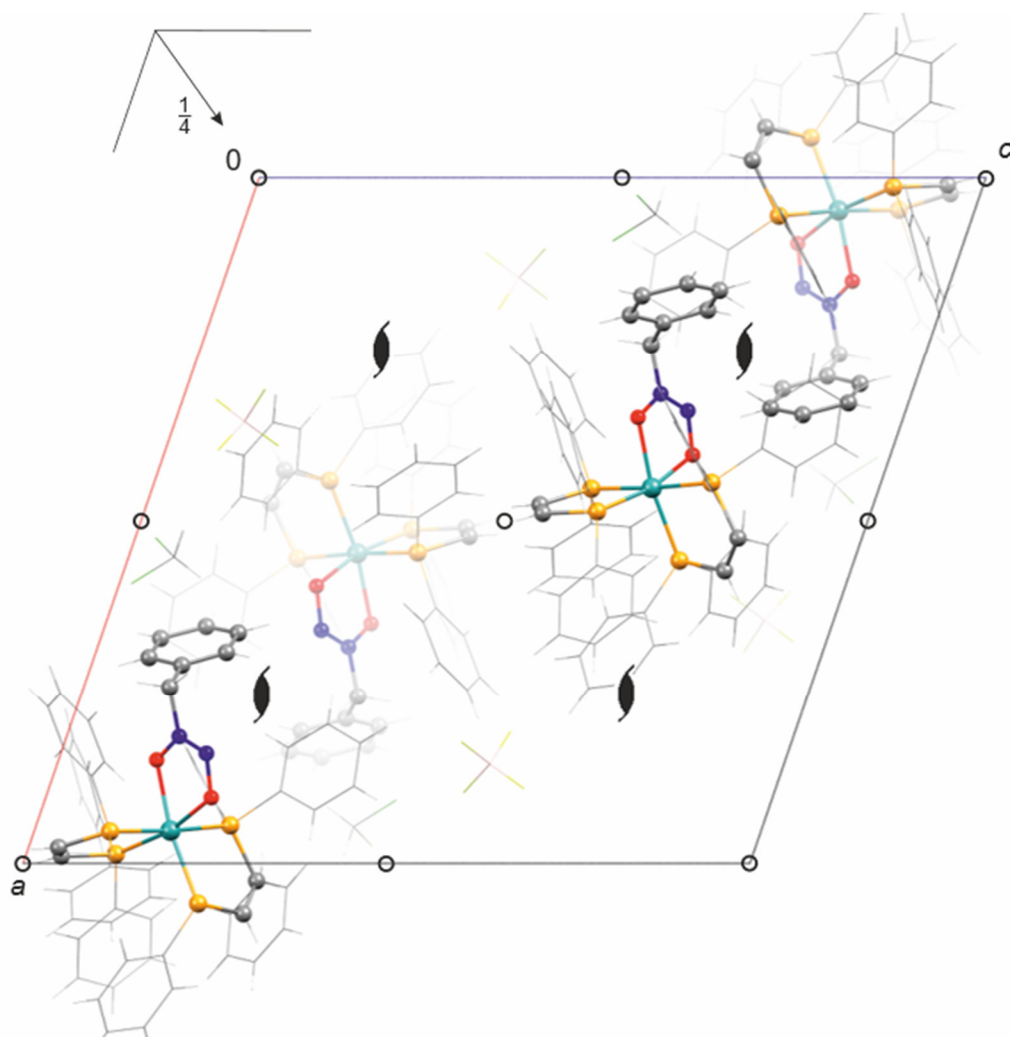


Figure 7.36: Mercury packing diagram of $[\text{Ru}(\text{dppv})_2(\text{bdd})]\text{BF}_4 \cdot 0.867\text{DCM}$ (**41**) in the monoclinic space group $P2_1/n$ with view along $[0\ 1\ 0]$. The symmetry elements of the space group are overlaid. Atoms: carbon (grey), hydrogen (white), boron (rose), chlorine (green), fluorine (green-yellow), nitrogen (blue), oxygen (red), phosphorus (orange), ruthenium (turquoise). Phenyl groups, dichloromethane and tetrafluorido borate were illustrated as wireframe.

7.2 Crystallographic Tables

Table 7.1: Crystallographic data of [Ru(H₂O)₆](tos)₂ (**1**), [Ru(H₂O)₆](OTf)₂ (**2**), [Ru(H₂O)₆](SO₄) (**3**).

	1 ^{*)} , ^{**)}	2 ^{*)} , ^{**)}	3 ^{**)}
sum formula	C ₁₄ H ₂₆ O ₁₂ RuS ₂	C ₂ H ₁₂ F ₆ O ₁₂ RuS ₂	H ₁₂ O ₁₀ RuS
<i>M_r</i> /g mol ⁻¹	551.54	507.31	305.23
color and habit	pink platelet	pink block	red platelet
crystal system	monoclinic	monoclinic	monoclinic
space group	<i>P</i> 2 ₁ / <i>c</i>	<i>C</i> 2/ <i>c</i>	<i>C</i> 2/ <i>c</i>
<i>a</i> /Å	14.0088(7)	9.5224(4)	9.6832(4)
<i>b</i> /Å	6.2999(3)	9.2316(4)	7.3250(3)
<i>c</i> /Å	24.9685(14)	17.6491(9)	24.0235(10)
<i>β</i> /°	100.545(5)	91.299(4)	98.1130(10)
<i>V</i> /Å ³	2166.3(2)	1551.08(12)	1686.92(12)
<i>Z</i>	4	4	8
<i>ρ</i> /g cm ⁻³	1.691	2.172	2.404
<i>μ</i> (MoKα)/mm ⁻¹	0.973	1.401	2.136
crystal size/mm	0.16 × 0.10 × 0.04	0.18 × 0.11 × 0.1	0.10 × 0.09 × 0.05
temperature/K	100(2)	293(2)	293(2)
<i>θ</i> range/°	4.36–28.66	4.56–28.47	3.50–27.15
refls. measured	8005	2737	9660
independent refls.	4829	1718	1862
<i>R</i> _{int}	0.0430	0.0242	0.0207
mean <i>σ</i> (<i>I</i>)/ <i>I</i>	0.0901	0.0396	0.0156
diffractometer	Oxford XCalibur		Bruker D8Venture
reflexes with <i>I</i> ≥ 2 <i>σ</i> (<i>I</i>)	3224	1521	1752
parameters	300	125	148
<i>R</i> (<i>F</i> _{obs})	0.0547	0.0316	0.0192
<i>R</i> _w (<i>F</i> ²)	0.1317	0.0785	0.0471
<i>S</i>	1.046	1.032	1.076
max. shift/error	0.001	0.001	0.001
max. electron density in e Å ⁻³	1.320 (1.056 Å from Ru1)	0.519	0.662
min. electron density in e Å ⁻³	-1.027	-0.762	-0.714
<i>x</i> , <i>y</i> (weighting scheme)	0.0409, 0.000	0.0363, 1.1818	0.0199, 4.4904

^{*)} C-bonded H: constrained, ^{**)} O-bonded H: O–H fixed to 0.82 Å, H...H fixed to 1.31 Å

Appendix

Table 7.2: Crystallographic data of [Ru(H₂O)₆](1,5-NaphDS) (**4**), [Ru(H₂O)₆](4,4'-BiphenDS)·2H₂O (**5**), [Ru(H₂O)₆](MesSO₃)₂ (**6**).

	4 ^{*)} , ^{**)}	5 ^{*)} , ^{**)} , ^{***)}	6 ^{*)} , ^{**)}
sum formula	C ₁₀ H ₁₈ O ₁₂ RuS ₂	C ₁₂ H ₂₄ O ₁₄ RuS ₂	C ₁₈ H ₃₄ O ₁₂ RuS ₂
<i>M_r</i> /g mol ⁻¹	495.43	557.50	607.64
color and habit	pink platelet	pink platelet	pink platelet
crystal system	monoclinic	triclinic	monoclinic
space group	<i>P</i> 2 ₁ / <i>c</i>	<i>P</i> $\bar{1}$	<i>P</i> 2 ₁ / <i>c</i>
<i>a</i> /Å	13.2776(6)	6.3148(4)	8.4108(3)
<i>b</i> /Å	6.5560(3)	6.7346(3)	30.6658(13)
<i>c</i> /Å	9.5892(4)	13.5126(9)	9.4564(4)
α /°	90	90.475(4)	90
β /°	92.344(2)	102.302(5)	93.023(3)
γ /°	90	114.935(5)	90
<i>V</i> /Å ³	834.02(6)	506.00(6)	2435.64(17)
<i>Z</i>	2	1	4
ρ /g cm ⁻³	1.973	1.830	1.657
μ (MoK α)/mm ⁻¹	1.252	1.050	0.874
crystal size/mm	0.08 × 0.05 × 0.02	0.46 × 0.25 × 0.02	0.42 × 0.21 × 0.04
temperature/K	100(2)	100(2)	100(2)
θ range/°	3.07–27.13	4.20–27.48	4.13–26.37
refls. measured	16757	3211	13426
independent refls.	1821	2266	4970
<i>R</i> _{int}	0.0614	0.0226	0.0289
mean $\sigma(I)/I$	0.0429	0.0424	0.0348
diffractometer	Bruker D8Venture	Oxford XCalibur	Oxford XCalibur
reflexes with $I \geq 2\sigma(I)$	1553	2134	3978
parameters	133	194	343
<i>R</i> (<i>F</i> _{obs})	0.0411	0.0313	0.0334
<i>R</i> _w (<i>F</i> ²)	0.0918	0.0730	0.0818
<i>S</i>	1.130	1.032	1.084
max. shift/error	0.001	0.001	0.001
max. electron density in e Å ⁻³	0.728	0.993	0.826
min. electron density in e Å ⁻³	-1.043	-0.872	-0.693
<i>x</i> , <i>y</i> (weighting scheme)	0.0081, 6.3318	0.0306, 0.5339	0.0267, 3.5678

^{*)} C-bonded H: constrained, ^{**)} O-bonded H: O–H fixed to 0.82 Å, H...H fixed to 1.31 Å, ^{***)} Disordered biphenyl moiety

Appendix

Table 7.3: Crystallographic data of [Ru(dppe)₂(tos)]BF₄·0.985CHCl₃ (**7**), [Ru(dppp)₂(tos)]BF₄·xEt₂O (**8**), [Ru(dppbza)₂(tos)]BF₄·2.9Et₂O (**9**).

	7 ^{*)}	8 ^{*)}	9 ^{*)}
sum formula	C _{59.97} H _{55.97} BCl _{2.97} F ₄ O ₃ P ₄ Ru	C _{126.28} H ₁₁₈ B ₂ F ₈ O ₇ P ₈ Ru ₂ S ₂	C _{149.66} H _{151.14} B ₂ F ₈ N ₄ O ₉ P ₈ Ru ₂ S ₂
<i>M_r</i> /g mol ⁻¹	1273.90	2435.22	2837.39
color and habit	orange platelet	yellow rod	dark-yellow prism
crystal system	triclinic	monoclinic	orthorhombic
space group	<i>P</i> $\bar{1}$	<i>P</i> 2 ₁ / <i>c</i>	<i>F</i> dd2
<i>a</i> /Å	13.9552(5)	20.4360(9)	34.8309(19)
<i>b</i> /Å	15.4053(5)	15.3302(6)	46.815(3)
<i>c</i> /Å	16.1482(6)	20.9705(8)	16.9247(10)
α /°	115.552(1)	90	90
β /°	110.580(1)	119.062(1)	90
γ /°	95.805(1)	90	90
<i>V</i> /Å ³	2797.8(2)	5742.6(4)	27598(3)
<i>Z</i>	2	2	8
ρ /g cm ⁻³	1.512	1.408	1.366
μ (MoK α)/mm ⁻¹	0.634	0.481	0.413
crystal size/mm	0.1 × 0.05 × 0.02	0.10 × 0.02 × 0.02	0.10 × 0.10 × 0.05
temperature/K	100(2)	97(2)	100(2)
θ range/°	2.937–26.44	2.892–27.12	3.043–25.72
refls. measured	50568	116853	181917
independent refls.	11326	12657	13146
<i>R</i> _{int}	0.0421	0.0647	0.0288
mean $\sigma(I)/I$	0.0513	0.0442	0.0181
diffractometer	Bruker D8Venture	Bruker D8Venture	Bruker D8Venture
refls. with $I \geq 2\sigma(I)$	9636	10215	12957
parameters	715	696	820
Flack parameter	–	–	–0.017(3)
<i>R</i> (<i>F</i> _{obs})	0.0389	0.0447	0.0319
<i>R</i> _w (<i>F</i> ²)	0.0966	0.0973	0.0838
<i>S</i>	1.114	1.048	1.049
max. shift/error	0.001	0.001	0.002
max. electron density in e Å ⁻³	0.847	2.375 (1.180 Å from Ru1)	0.734
min. electron density in e Å ⁻³	–0.726	–1.410	–0.446
<i>x</i> , <i>y</i> (weighting scheme)	0.0000, 9.0622	0.0276, 13.0291	0.0375, 77.1749

^{*)} C-bonded H: constrained

Appendix

Table 7.4: Crystallographic data of [Ru(PⁱPrPh₂)₂(tos)₂] (**10**), [Ru(dppe)₂(MesSO₃)]BF₄·DCM (**11**), [Ru(PⁱPrPh₂)₂(MesSO₃)₂]·0.826DCM (**12**).

	10 ^{*)}	11 ^{*)}	12 ^{*)}
sum formula	C ₄₄ H ₄₈ O ₆ P ₂ RuS ₂	C ₆₂ H ₆₁ BCl ₂ F ₄ O ₃ P ₄ RuS	C _{48.83} H _{57.65} Cl _{1.65} O ₆ P ₂ RuS ₂
<i>M_r</i> /g mol ⁻¹	899.95	1268.82	1026.21
color and habit	violet platelet	orange platelet	violet needle
crystal system	monoclinic	triclinic	monoclinic
space group	<i>P</i> 2 ₁ / <i>c</i>	<i>P</i> $\bar{1}$	<i>P</i> 2 ₁ / <i>c</i>
<i>a</i> /Å	10.1812(8)	12.2709(5)	10.5758(3)
<i>b</i> /Å	18.8518(13)	13.6469(5)	40.3791(10)
<i>c</i> /Å	21.5726(16)	17.5092(7)	22.7217(6)
α /°	90	93.876(2)	90
β /°	95.855(3)	102.976(2)	90.8920(10)
γ /°	90	97.578(2)	90
<i>V</i> /Å ³	4118.9(5)	2817.88(19)	9701.9(4)
<i>Z</i>	4	2	8
ρ /g cm ⁻³	1.451	1.495	1.405
μ (MoK α)/mm ⁻¹	0.607	0.584	0.613
crystal size/mm	0.08 × 0.06 × 0.03	0.10 × 0.08 × 0.01	0.10 × 0.01 × 0.01
temperature/K	100(2)	100(2)	100(2)
θ range/°	2.84–26.40	3.00–27.91	2.17–27.88
refls. measured	160645	58544	190730
independent refls.	8407	13423	23074
<i>R</i> _{int}	0.0498	0.0622	0.0437
mean $\sigma(I)/I$	0.0240	0.0720	0.0371
diffractometer	Bruker D8Venture	Bruker D8Venture	Bruker D8Venture
reflexes with $I \geq 2\sigma(I)$	7698	9772	19296
parameters	502	725	1139
<i>R</i> (<i>F</i> _{obs})	0.0244	0.0439	0.0397
<i>R</i> _w (<i>F</i> ²)	0.0603	0.1101	0.0825
<i>S</i>	1.044	1.010	1.071
max. shift/error	0.002	0.001	0.004
max. electron density in e Å ⁻³	0.407	1.120 (1.231 Å from B1)	1.505 (0.947 Å from Cl2)
min. electron density in e Å ⁻³	-0.499	-0.875	-0.563
<i>x</i> , <i>y</i> (weighting scheme)	0.0202, 4.3592	0.0473, 1.7856	0.0231, 15.3053

^{*)} C-bonded H: constrained

Appendix

Table 7.5: Crystallographic data of [Ru(dpppha)₂(H₂O)₂](BF₄)₂·1.948DCM (**13**), [Ru(dppen)₂(H₂O)₂](BF₄)₂·1.506DCM (**14**), [Ru(dppbz)₂(H₂O)₂](BF₄)₂ (**15**).

	13 ^{*)} , ^{**)}	14 ^{*)} , ^{**)}	15 ^{*)} , ^{**)}
sum formula	C _{61.95} H _{57.90} B ₂ Cl _{3.90} F ₈ N ₂ O ₂ P	C _{67.51} H _{65.01} Cl _{3.01} O ₈ P ₄ RuS ₂	C ₆₀ H ₅₂ B ₂ F ₈ O ₂ P ₄ Ru
<i>M_r</i> /g mol ⁻¹	1399.09	1400.02	1203.58
color and habit	yellow rod	dark-yellow block	yellow block
crystal system	triclinic	monoclinic	monoclinic
space group	<i>P</i> $\bar{1}$	<i>P</i> 2 ₁ / <i>n</i>	<i>C</i> 2/ <i>c</i>
<i>a</i> /Å	11.2628(3)	13.2765(5)	24.9957(10)
<i>b</i> /Å	11.6441(3)	15.5607(5)	11.5994(4)
<i>c</i> /Å	12.8451(4)	15.6970(6)	21.2476(9)
α /°	110.2550(10)	90	90
β /°	94.9400(10)	96.9190(10)	120.4480(10)
γ /°	103.6610(10)	90	90
<i>V</i> /Å ³	1509.43(7)	3219.3(2)	5310.8(4)
<i>Z</i>	1	2	4
ρ /g cm ⁻³	1.539	1.444	1.505
μ (MoK α)/mm ⁻¹	0.609	0.588	0.489
crystal size/mm	0.1 × 0.05 × 0.02	0.50 × 0.40 × 0.10	0.02 × 0.02 × 0.01
temperature/K	100(2)	100(2)	100(2)
θ range/°	3.093–26.39	2.509–27.13	1.994–26.37
refls. measured	37740	85474	49632
independent refls.	6117	7096	5427
<i>R</i> _{int}	0.0258	0.1171	0.0751
mean $\sigma(I)/I$	0.0239	0.0661	0.0429
diffractometer	Bruker D8Venture	Bruker D8Venture	Bruker D8Venture
reflexes with $I \geq 2\sigma(I)$	5796	5694	0.0572
parameters	392	402	355
<i>R</i> (<i>F</i> _{obs})	0.0264	0.0684	0.0446
<i>R</i> _w (<i>F</i> ²)	0.0738	0.1292	0.0849
<i>S</i>	1.253	1.114	1.042
max. shift/error	0.001	0.001	0.001
max. electron density in e Å ⁻³	0.623	0.753	0.586
min. electron density in e Å ⁻³	-0.715	-0.827	-0.870
<i>x</i> , <i>y</i> (weighting scheme)	0.0450, 0.9798	0.0211, 13.6085	0.0192, 17.8828

^{*)} C-bonded H: constrained, ^{**)} O-bonded H: O–H fixed to 0.82 Å, H...H fixed to 1.31 Å

Appendix

Table 7.6: Crystallographic data of [Ru(dppv)₂(H₂O)₂](BF₄)₂ (**16**), [Ru(dpppra)₂(H₂O)(tos)](tos)·1.891C₇H₈ (**17**), [Ru(PPh₃)₂(H₂O)₂(tos)]·2C₄H₁₀O (**18**).

	16 ^{*)} , ^{**)}	17 ^{*)} , ^{**)}	18 ^{*)} , ^{**)}
sum formula	C ₅₂ H ₄₈ B ₂ F ₈ O ₂ P ₄ Ru	C _{81.24} H _{85.13} N ₂ O ₇ P ₄ RuS ₂	C ₅₈ H ₆₈ O ₁₀ P ₂ RuS ₂
<i>M_r</i> /g mol ⁻¹	1103.47	1490.53	1152.25
color and habit	yellow block	yellow platelet	red block
crystal system	triclinic	monoclinic	triclinic
space group	<i>P</i> $\bar{1}$	<i>P</i> 2 ₁ / <i>n</i>	<i>P</i> $\bar{1}$
<i>a</i> /Å	10.3088(3)	12.8014(7)	10.8950(5)
<i>b</i> /Å	11.0702(4)	31.8789(17)	12.1360(5)
<i>c</i> /Å	11.5073(4)	18.3168(8)	22.2528(11)
α /°	101.346(1)	90	103.563(2)
β /°	102.254(1)	96.778(2)	101.945(2)
γ /°	106.826(1)	90	93.294(2)
<i>V</i> /Å ³	1180.64(7)	7422.7(7)	2780.9(2)
<i>Z</i>	1	4	2
ρ /g cm ⁻³	1.552	1.334	1.376
μ (MoK α)/mm ⁻¹	0.542	0.409	0.472
crystal size/mm	0.10 × 0.08 × 0.05	0.12 × 0.06 × 0.03	0.20 × 0.15 × 0.10
temperature/K	100(2)	100(2)	100(2)
θ range/°	2.994–28.74	2.67–27.13	3.02–26.39
refls. measured	37607	297562	53787
independent refls.	6095	16357	11331
<i>R</i> _{int}	0.0378	0.0565	0.0481
mean σ (<i>I</i>)/ <i>I</i>	0.0305	0.0272	0.0517
diffractometer	Bruker D8Venture	Bruker D8Venture	Bruker D8Venture
reflexes with <i>I</i> ≥ 2 σ (<i>I</i>)	5457	14470	9454
parameters	319	867	713
<i>R</i> (<i>F</i> _{obs})	0.0275	0.0420	0.0398
<i>R</i> _w (<i>F</i> ²)	0.0640	0.1095	0.0886
<i>S</i>	1.090	1.036	1.044
max. shift/error	0.001	0.001	0.001
max. electron density in e Å ⁻³	0.507	2.080 (1.000 Å from C71)	0.702
min. electron density in e Å ⁻³	-0.674	-1.111	-0.664
<i>x</i> , <i>y</i> (weighting scheme)	0.0141, 1.2618	0.0433, 18.5327	0.0245, 3.9358

^{*)} C-bonded H: constrained, ^{**)} O-bonded H: O–H fixed to 0.82 Å, H...H fixed to 1.31 Å

Appendix

Table 7.7: Crystallographic data of [Ru(PH^tBu)₂(H₂O)₂(tos)₂] (**19**), [Ru(PPh₂Bn)₂(H₂O)₂(tos)₂]·C₄H₁₀O (**20**), [Ru(dppe)₂(H)(NO₂)] (**24**).

	19 ^{*)} , ^{**)}	20 ^{*)} , ^{**)}	24 ^{*)} , ^{***)}
sum formula	C ₃₀ H ₅₆ O ₈ P ₂ RuS ₂	C ₅₆ H ₆₂ O ₉ P ₂ RuS ₂	C ₅₂ H ₄₉ NO ₂ P ₄ Ru
<i>M_r</i> /g mol ⁻¹	771.87	1106.18	944.87
color and habit	red platelet	dark-yellow block	yellow platelet
crystal system	monoclinic	monoclinic	monoclinic
space group	<i>C2/c</i>	<i>P2₁/n</i>	<i>P2₁/n</i>
<i>a</i> /Å	21.1944(10)	17.8180(14)	10.5618(3)
<i>b</i> /Å	8.3783(4)	15.9422(12)	24.5648(8)
<i>c</i> /Å	20.4169(10)	18.7631(14)	17.1283(6)
<i>α</i> /°	90	90	90
<i>β</i> /°	91.703(2)	96.778(2)	99.2210(10)
<i>γ</i> /°	90	90	90
<i>V</i> /Å ³	3623.9(3)	5299.3(7)	4386.5(2)
<i>Z</i>	4	4	4
<i>ρ</i> /g cm ⁻³	1.415	1.387	1.431
<i>μ</i> (MoKα)/mm ⁻¹	0.680	0.491	0.547
crystal size/mm	0.09 × 0.08 × 0.06	0.10 × 0.09 × 0.04	0.10 × 0.08 × 0.01
temperature/K	100(2)	293(2)	100(2)
<i>θ</i> range/°	3.27–27.16	2.94–30.53	2.925–25.73
refls. measured	70609	110510	114840
independent refls.	4002	16129	8325
<i>R</i> _{int}	0.0430	0.0738	0.0829
mean <i>σ</i> (<i>I</i>)/ <i>I</i>	0.0169	0.0620	0.0454
diffractometer	Bruker D8Venture	Bruker D8Venture	Bruker D8Venture
reflexes with <i>I</i> ≥ 2 <i>σ</i> (<i>I</i>)	3861	13091	6605
parameters	212	645	545
<i>R</i> (<i>F</i> _{obs})	0.0207	0.0449	0.0552
<i>R</i> _w (<i>F</i> ²)	0.0769	0.1178	0.1008
<i>S</i>	1.296	1.011	1.129
max. shift/error	0.001	0.001	0.001
max. electron density in e Å ⁻³	0.571	1.310 (0.890 Å from C54b)	0.798
min. electron density in e Å ⁻³	-0.585	-0.690	-0.950
<i>x</i> , <i>y</i> (weighting scheme)	0.0396, 3.7975	0.0450, 6.4209	0.0203, 12.9942

^{*)} C-bonded H: constrained, ^{**)} O-bonded H: O–H fixed to 0.82 Å, H...H fixed to 1.31 Å, ^{***)} Ru-bonded H: *x*, *y*, *z* and *U*_{iso} refined freely

Appendix

Table 7.8: Crystallographic data of [Ru(dppe)₂(NO)](tos)·0.955DCM (**25**), [Ru(dppe)₂(NO)F](SbF₆) (**26**), [Ru(PPh₃)₂(NO)₂] (**27**).

	25 ^{*)}	26 ^{*)} , 26 ^{**)}	27 ^{*)}
sum formula	C _{59.96} H _{56.91} Cl _{1.91} NO ₄ P ₄ RuS	C ₅₂ H ₄₈ F _{13.02} N _{0.98} O _{0.98} P ₄ RuSb	C ₃₆ H ₃₀ N ₂ O ₂ P ₂ Ru
<i>M_r</i> /g mol ⁻¹	1180.12	1418.11	685.63
color and habit	red block	yellow platelet	red platelet
crystal system	triclinic	triclinic	monoclinic
space group	<i>P</i> $\bar{1}$	<i>P</i> $\bar{1}$	<i>P</i> 2 ₁ / <i>n</i>
<i>a</i> /Å	12.3785(3)	10.8263(3)	9.2255(5)
<i>b</i> /Å	14.2057(4)	11.3656(4)	36.5078(18)
<i>c</i> /Å	17.2074(5)	12.1778(4)	9.9088(5)
α /°	86.8550(10)	62.6220(10)	90
β /°	69.6940(10)	88.4480(10)	111.201(2)
γ /°	73.6980(10)	74.2360(10)	90
<i>V</i> /Å ³	2720.66(13)	1272.14(7)	3111.4(3)
<i>Z</i>	2	1	4
ρ /g cm ⁻³	1.441	1.851	1.464
μ (MoK α)/mm ⁻¹	0.587	1.562	0.642
crystal size/mm	0.10 × 0.08 × 0.04	0.10 × 0.05 × 0.01	0.10 × 0.08 × 0.01
temperature/K	98(2)	100(2)	100(2)
θ range/°	2.991–26.40	3.119–26.44	3.082–26.42
refls. measured	100712	55262	28609
independent refls.	11129	5225	6271
<i>R</i> _{int}	0.0331	0.0447	0.0348
mean $\sigma(I)/I$	0.0192	0.0265	0.0545
diffractometer	Bruker D8Venture	Bruker D8Venture	Bruker D8Venture
reflexes with $I \geq 2\sigma(I)$	9994	4687	5430
parameters	660	335	388
<i>R</i> (<i>F</i> _{obs})	0.0277	0.0532	0.0733
<i>R</i> _w (<i>F</i> ²)	0.0668	0.1209	0.1423
<i>S</i>	1.070	1.148	1.333
max. shift/error	0.004	0.001	0.001
max. electron density in e Å ⁻³	0.748	1.275 (0.373 Å from Ru1)	1.495 (0.935 Å from Ru1)
min. electron density in e Å ⁻³	-0.545	-1.611	-1.625
<i>x</i> , <i>y</i> (weighting scheme)	0.0194, 3.4304	0.0232, 12.0432	0.0000, 18.4555

^{*)} C-bonded H: constrained, ^{**) disorder of NO and F (inversion centre)}

Appendix

Table 7.9: Crystallographic data of [Ru(dppe)₂(N₂O₂H)]BF₄·Et₂O (**28a**), [Ru(dppe)₂(N₂O₂H)]BF₄ (**28b**), [Ru(dppp)₂(N₂O₂H)]BF₄·Et₂O·DCM (**29**).

	28a ^{*)} , ^{**)}	28b ^{*)} , ^{**)}	29 ^{*)} , ^{**)}
sum formula	C ₅₆ H ₅₉ BF ₄ N ₂ O ₃ P ₄ Ru	C ₅₂ H ₄₉ BF ₄ N ₂ O ₂ P ₄ Ru	C ₅₉ H ₆₅ BCl ₂ F ₄ N ₂ O ₃ P ₄ Ru
<i>M_r</i> /g mol ⁻¹	1119.81	1045.69	1232.79
color and habit	red block	yellow block	dark-red block
crystal system	orthorhombic	monoclinic	monoclinic
space group	<i>Pbca</i>	<i>P2₁/n</i>	<i>P2₁/n</i>
<i>a</i> /Å	15.2572(6)	12.0831(4)	11.5983(3)
<i>b</i> /Å	24.3348(10)	15.3194(4)	14.5177(4)
<i>c</i> /Å	27.3115(11)	25.2725(7)	33.0980(8)
α /°	90	90	90
β /°	90	91.250(1)	96.484(1)
γ /°	90	90	90
<i>V</i> /Å ³	10140.2(7)	4677.0(2)	5537.4(2)
<i>Z</i>	8	4	4
ρ /g cm ⁻³	1.467	1.485	1.479
μ (MoK α)/mm ⁻¹	0.498	0.532	0.557
crystal size/mm	0.10 × 0.05 × 0.01	0.10 × 0.04 × 0.03	0.10 × 0.06 × 0.05
temperature/K	100(2)	100(2)	100(2)
θ range/°	2.794–25.73	2.978–25.78	3.048–27.15
refls. measured	291839	98288	76948
independent refls.	9634	8853	12241
<i>R</i> _{int}	0.0836	0.0497	0.0356
mean $\sigma(I)/I$	0.0249	0.0289	0.0313
diffractometer	Bruker D8Venture	Bruker D8Venture	Bruker D8Venture
reflexes with $I \geq 2\sigma(I)$	8281	7668	10665
parameters	644	598	684
<i>R</i> (<i>F</i> _{obs})	0.0318	0.0344	0.0506
<i>R</i> _w (<i>F</i> ²)	0.0834	0.0809	0.1267
<i>S</i>	1.074	1.082	1.081
max. shift/error	0.002	0.001	0.001
max. electron density in e Å ⁻³	0.550	1.657 (2.391 Å from O2)	1.402 (1.186 Å from C56)
min. electron density in e Å ⁻³	-0.531	-0.474	-0.849
<i>x</i> , <i>y</i> (weighting scheme)	0.0308, 16.714	0.0266, 8.5015	0.0424, 18.9393

^{*)} C-bonded H: constrained, ^{**)} O-bonded H: *x*, *y*, *z* refined, *U*_{iso} constrained

Appendix

Table 7.10: Crystallographic data of [Ru(dppv)₂(N₂O₂H)]BF₄·0.81TBME·DCM (**30**), [Ru(dppe)₂(N₂O₂)·H]ImiBF₄ (**31**), [Ru(dppp)₂(N₂O₂H)]BF₄·Imi·0.856DCM (**32**).

	30 ^{*)} , ^{**)}	31 ^{*)} , ^{****)}	32 ^{*)} , ^{***)} , ^{****)}
sum formula	C _{57.05} H _{56.72} BCl ₂ F ₄ N ₂ O _{2.81} P	C ₅₅ H ₅₃ BF ₄ N ₄ O ₂ P ₄ Ru	C _{57.86} H _{58.71} BCl _{1.71} F ₄ N ₄ O ₂ P
<i>M_r</i> /g mol ⁻¹	1197.99	1113.77	1214.54
color and habit	yellow rod	yellow block	yellow platelet
crystal system	monoclinic	orthorhombic	monoclinic
space group	<i>P</i> 2 ₁ / <i>c</i>	<i>P</i> 2 ₁ 2 ₁ 2 ₁	<i>P</i> 2 ₁ / <i>n</i>
<i>a</i> /Å	18.3784(9)	12.0407(3)	17.2207(5)
<i>b</i> /Å	12.6393(6)	14.7601(4)	18.7259(6)
<i>c</i> /Å	24.9339(12)	27.8330(8)	18.2062(5)
α /°	90	90	90
β /°	104.375(2)	90	109.701(1)
γ /°	90	90	90
<i>V</i> /Å ³	5610.6(5)	4946.5(2)	5527.3(3)
<i>Z</i>	4	4	4
ρ /g cm ⁻³	1.418	1.496	1.459
μ (MoK α)/mm ⁻¹	0.547	0.510	0.543
crystal size/mm	0.10 × 0.03 × 0.02	0.10 × 0.08 × 0.02	0.10 × 0.08 × 0.01
temperature/K	100(2)	100(2)	100(2)
θ range/°	2.96–27.18	2.86–26.38	3.15–27.89
refls. measured	104640	157844	123188
independent refls.	12336	10089	13124
<i>R</i> _{int}	0.0802	0.0541	0.0445
mean σ (<i>I</i>)/ <i>I</i>	0.0632	0.0241	0.0320
diffractometer	Bruker D8Venture	Bruker D8Venture	Bruker D8Venture
reflexes with <i>I</i> ≥ 2 σ (<i>I</i>)	9423	9800	10989
parameters	678	642	694
Flack parameter	–	–0.012(6)	–
<i>R</i> (<i>F</i> _{obs})	0.0589	0.0221	0.0393
<i>R</i> _w (<i>F</i> ²)	0.1540	0.0519	0.0951
<i>S</i>	1.057	1.059	1.047
max. shift/error	0.001	0.003	0.001
max. electron density in e Å ⁻³	1.515 (1.267 Å from O1)	0.372	1.688 (0.983 Å from Cl1)
min. electron density in e Å ⁻³	–1.421	–0.318	–0.820
<i>x</i> , <i>y</i> (weighting scheme)	0.0633, 19.9090	0.0224, 2.2851	0.0334, 11.5784

^{*)} C-bonded H: constrained, ^{**)} O-bonded H: *x*, *y*, *z* refined, *U*_{iso} constrained, ^{***)} O-bonded H: *x*, *y*, *z* and *U*_{iso} refined freely, ^{****)} N-bonded H: constrained

Appendix

Table 7.11: Crystallographic data of [Ru(dppv)₂(N₂O₂)]·HImiBF₄·Imi·0.804DCM (**33**), [Ru(dppp)₂(NO)]BF₄·Et₂O (**36**), [Ru(dppv)₂(pdd)]BF₄·0.601DCM (**37**).

	33 ^{*)} , 36 ^{*)} , 37 ^{*)}	36 ^{*)}	37 ^{*)}
sum formula	C _{58.80} H _{54.61} BCl _{1.61} F ₄ N ₆ O ₂ P ₄ Ru	C ₅₈ H ₆₂ BF ₄ NO ₂ P ₄ Ru	C _{56.5} H ₅₄ BCl ₂ F ₄ N ₃ O ₂ P ₄ Ru
<i>M_r</i> /g mol ⁻¹	1246.10	1116.84	1183.73
color and habit	yellow rod	yellow block	yellow rod
crystal system	monoclinic	monoclinic	monoclinic
space group	<i>P2₁/n</i>	<i>P2₁</i>	<i>P2₁/c</i>
<i>a</i> /Å	11.8299(5)	11.5161(4)	18.0796(11)
<i>b</i> /Å	23.4827(9)	14.9621(5)	12.3722(7)
<i>c</i> /Å	20.3765(8)	15.1677(5)	24.8831(15)
α /°	90	90	90
β /°	97.709(2)	98.6130(10)	103.400(2)
γ /°	90	90	90
<i>V</i> /Å ³	5609.4(4)	2584.00(15)	5414.4(6)
<i>Z</i>	4	2	2
ρ /g cm ⁻³	1.476	1.435	1.425
μ (MoK α)/mm ⁻¹	0.533	0.486	0.526
crystal size/mm	0.10 × 0.03 × 0.02	0.10 × 0.08 × 0.04	0.10 × 0.03 × 0.01
temperature/K	97(2)	100(2)	100(2)
θ range/°	3.129–27.90	3.258–26.45	3.012–26.41
refls. measured	89602	38193	104617
independent refls.	13362	10462	11042
<i>R</i> _{int}	0.0442	0.0266	0.0677
mean $\sigma(I)/I$	0.0386	0.0412	0.0484
diffractometer	Bruker D8Venture	Bruker D8Venture	Bruker D8Venture
reflexes with $I \geq 2\sigma(I)$	10854	9968	8812
parameters	725	642	668
Flack parameter	–	0.000(8)	–
<i>R</i> (<i>F</i> _{obs})	0.0354	0.0288	0.0567
<i>R</i> _w (<i>F</i> ²)	0.0900	0.0621	0.1469
<i>S</i>	1.027	1.064	1.059
max. shift/error	0.001	0.002	0.001
max. electron density in e Å ⁻³	0.959	0.459	2.120 (1.140 Å from C3)
min. electron density in e Å ⁻³	-0.487	-0.367	-0.850
<i>x</i> , <i>y</i> (weighting scheme)	0.0361, 6.7539	0.0198, 1.3745	0.0590, 21.1059

^{*)} C-bonded H: constrained, ^{**)} N-bonded H: N–H fixed to 0.88 Å (hydrogen between hyponitrite and imidazole), ^{***)} N-bonded H: constrained

Appendix

Table 7.12: Crystallographic data of [Ru(dppe)₂(bdd)]BF₄ (**39**), [Ru(dppp)₂(bdd)]BF₄ (**40**), [Ru(dppv)₂(bdd)]BF₄·0.867DCM (**41**).

	39	40	41
sum formula	C ₅₉ H ₅₅ BF ₄ N ₂ O ₂ P ₄ Ru	C ₆₁ H ₅₉ BF ₄ N ₂ O ₂ P ₄ Ru	C _{59.87} H _{52.73} BCl _{1.73} F ₄ N ₂ O ₂ P
<i>M_r</i> /g mol ⁻¹	1135.81	1163.86	1205.41
color and habit	yellow platelet	yellow prism	yellow platelet
crystal system	monoclinic	monoclinic	monoclinic
space group	<i>P</i> 2 ₁	<i>P</i> 2 ₁ / <i>n</i>	<i>P</i> 2 ₁ / <i>n</i>
<i>a</i> /Å	12.4187(4)	18.1272(4)	21.2955(5)
<i>b</i> /Å	14.7256(4)	15.6549(3)	12.5255(3)
<i>c</i> /Å	14.0644(4)	18.8405(4)	21.3100(5)
α /°	90	90	90
β /°	98.5210(10)	97.7170(10)	108.9640(10)
γ /°	90	90	90
<i>V</i> /Å ³	2543.61(13)	5298.13(19)	5375.6(2)
<i>Z</i>	2	4	4
ρ /g cm ⁻³	1.483	1.459	1.489
μ (MoK α)/mm ⁻¹	0.496	0.478	0.558
crystal size/mm	0.10 × 0.05 × 0.01	0.10 × 0.06 × 0.03	0.10 × 0.08 × 0.02
temperature/K	100(2)	100(2)	100(2)
θ range/°	3.130–27.89	2.614–27.93	2.870–26.40
refls. measured	53672	83988	114636
independent refls.	12142	12618	10988
<i>R</i> _{int}	0.0323	0.0522	0.0648
mean σ (<i>I</i>)/ <i>I</i>	0.0374	0.0470	0.0359
diffractometer	Bruker D8Venture	Bruker D8Venture	Bruker D8Venture
reflexes with $I \geq 2\sigma(I)$	11502	9950	9043
parameters	658	676	680
Flack parameter	-0.026(7)	–	–
<i>R</i> (<i>F</i> _{obs})	0.0303	0.0400	0.0484
<i>R</i> _w (<i>F</i> ²)	0.0725	0.0969	0.1167
<i>S</i>	1.040	1.032	1.032
max. shift/error	0.001	0.001	0.002
max. electron density in e Å ⁻³	0.669	0.749	2.656 (0.715 Å from C60)
min. electron density in e Å ⁻³	-0.536	-0.771	-1.382
<i>x</i> , <i>y</i> (weighting scheme)	0.0341, 1.2765	0.0322, 7.8096	0.0373, 21.3304

^a) C-bonded H: constrained

7.3 Safety data sheets (in german)

Betriebsanweisung für die Herstellung von $[\text{Ru}(\text{H}_2\text{O})_6]\text{tos}_2$

Daniel Beck, Datum: 27.11.2015

Arbeitssicherheit, Chemikalien, Geräte

Die allgemeine Betriebsanweisung des Arbeitskreises sowie die Betriebsanweisungen und/oder Sicherheitsdatenblätter der einzelnen Gefahrstoffe müssen gelesen, beachtet und bereitgehalten werden.

Spezifikation der Ausgangsstoffe, Formel (Synonyme; Abkürzungen):

(C. Fellay, G. Laurency, *Inorg. Synth.* **2010**, *35*, 152-155.)

- $\text{RuCl}_3 \cdot x\text{H}_2\text{O}$ (99.9%, ABCR, 40%)
- NaOH (Plätzchen, Chemikalienausgabe)
- NaIO_4 (Chemikalienausgabe, 99%)
- RuO_2 (Darstellung s. Publikation)
- Pb (Sigma-Aldrich, 99%)
- RuO_4 (Einstufung fehlt: R: 8-36/38; S: 7/8-26-28-37/39)
- H_2SO_4 (Chemikalienausgabe)
- H_2SiF_6 (1L, Sigma-Aldrich, 33.5-35%)
- KHSO_4 (Chemikalienausgabe, 99%)
- **Nur perfluoriertes Schliiffett verwenden**

Gefahren für Mensch und Umwelt:

H: 314, 335, 290, 319, 360D, 360F, 332, 302, 373, 410

P: 201, 273, 308+313, 280, 305+351+338, 310, 301+330+331, 309+310

Ruthenium(III)-chlorid $\cdot x\text{H}_2\text{O}$: **gesundheitsschädlich, verursacht Verätzungen**

NaOH, KHSO_4 , H_2SO_4 : **ätzend**

Hexafluorokieselsäure: **ätzend, giftig (geringe Mengen HF)**

Natriumperiodat: **brandfördernd**

Rutheniumtetraoxid: **sehr giftig beim Einatmen, beim Verschlucken und bei Berührung mit der Haut; leichtflüchtig; entwickelt bereits unter 100°C sehr giftige Dämpfe; verursacht schwerste Verätzungen; brandfördernd; stark wassergefährdend, in Kontakt mit organischen Stoffen explosiv.**

Pb (Staub): giftig, teratogen, steht im Verdacht nachhaltig das Nervensystem zu schädigen, umweltgefährdend



Bereitzuhaltende persönliche Schutzausrüstung:

Nitrilhandschuhe, Atemschutzmaske für Stäube, Schutzbrille, Laborkittel

Bereitzuhaltende Löschmittel:

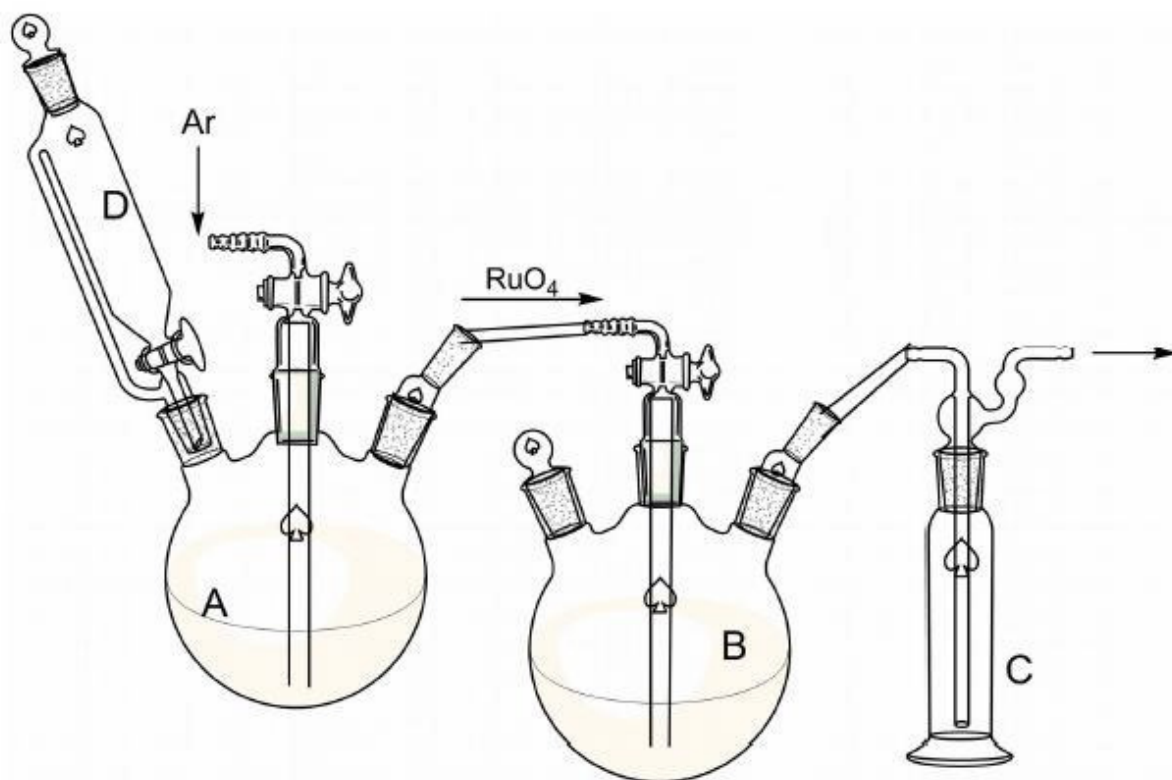
■ Wasser im Sprühstrahl einsetzen und Druckknopfmelder betätigen!

Feuerwehr auf giftige Gase aufmerksam machen. Atemschutz: Kombinationsfilter ABEK

Ansatzgröße:

■ 2,1 g (■ ≈17 mmol) RuO₂ auf 11 g (0.049 mol) NaIO₄

Apparatur:



Die Reaktion muss im Abzug durchgeführt werden! Der Fortgang der Reaktion ist mit Zeitangaben im Laborjournal zu dokumentieren!

Entsorgung:

■ nach 4 Tagen Reaktionslösung A in separatem Müllkanister entsorgen (als „sauer“ kennzeichnen), sollte Flüssigkeit weiterhin gelben Stich haben: Zugabe von Methanol (Nebenprodukt: elementares Iod)

Blei nach Filtration (Granalienform) in Feststofftonne entsorgen.

Verhalten im Gefahrfall:

■ Behälter dicht geschlossen an einem gut gelüfteten Ort aufbewahren.

Bei Berührung mit den Augen sofort gründlich mit Wasser abspülen und Arzt konsultieren.

Bei Unfall oder Unwohlsein sofort Arzt hinzuziehen und diese Betriebsanweisung vorzeigen.

Immer im Abzug arbeiten (spezieller Platz Nachtlabor)

Bei Gefahr des Hautkontaktes Neopren- bzw. Nitril-Schutzhandschuhe benutzen.

Beschäftigungsverbot für Jugendliche unter 16 Jahren.

Beschäftigungserlaubnis für Jugendliche über 16 Jahren nur, wenn das Ausbildungsziel den

Umgang notwendig macht und eine fachkundige Aufsicht gewährleistet ist.

Erste Hilfe Immer:

Notarzt holen: siehe Alarmplan und diese Betriebsanweisung vorzeigen

Nach Einatmen:

Frischlucht zuführen, Atemwege freihalten, ggf. Atemspende

Nach Verschlucken:

Wiederholt reichlich Wasser mit A-Kohle-Zusatz trinken lassen. Als Laxans Na₂SO₄

(1 Esslöffel auf 1 Glas Wasser) verabreichen. Kein Erbrechen!

Nach Hautkontakt:

Sofort mit viel Wasser abwaschen, dann mit PEG 400 abtupfen und mit sterilem Verbandmaterial abdecken. Mit viel Wasser und Seife abwaschen.

Nach Kleidungskontakt:

Kleidung entfernen und Haut wie oben behandeln.

Nach Augenkontakt:

10–15 Minuten bei geöffnetem Lidspalt unter fließendem Wasser spülen.

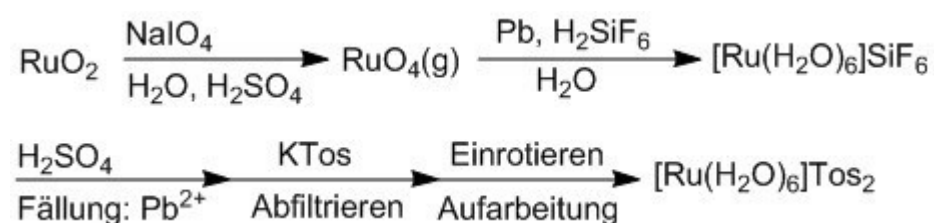
Danach lockeren Verband anlegen. Sofort Augenarzt hinzuziehen!

Ersthelfer:

siehe Alarmplan Gefährliche Reaktionen Allgemeines: mit leichtoxidierbaren Stoffen, z.B. organischen Lösungsmitteln heftige bis explosive Reaktion möglich; kräftiges Oxidationsmittel: setzt aus Salzsäure Chlor (giftiges Gas) frei; leichtflüchtig Explosive Reaktion mit Ammoniak, Ethanol und Iodwasserstoff

Arbeitsvorschrift

Reaktionsgleichung:



M_r: 4.5 g, 8.2 mmol, 48% (551.55 g/mol)

Literatur:

C. Fellay, G. Laurency, *Inorg. Synth.* **2010**, *35*, 152–155.

Achtung:

RuO₄ zersetzt sich am Magnetrührstab, Teflonfett, Silikonstopfen und Silikon-Schlauch zu schwarzem RuO₂ (Ru).

Ausführung:

Die Anlage wird mit Ar auf Dichtigkeit geprüft. Zugabe von Rutheniumdioxid (2.1 g) zu einer Lösung aus Natriumperodat (11 g) in Wasser (85 mL). Vorsicht: Bereits leichte Gelbverfärbung durch Rutheniumtetroxid. Zutropfen von H_2SO_4 (42 mL) mittels Tropftrichter. Überleitung durch Argonstrom (1 Tropfen in der Waschflasche pro Sekunde). Reduktion des Tetroxids durch anwesendes Blei (20 g) in 1M H_2SiF_6 (140 mL). Die Reaktion für 4 Tage unter zuverlässigem Rühren laufen lassen. Reaktion wird erst gestoppt, wenn im 1. Kolben keine Gelbverfärbung zu erkennen ist (nach 4 Tagen meistens keine Gefahr mehr). Aufarbeitung: Entweder Zugabe von Kaliumtosylat (aus KOH (280 mmol, 15.71 g) und HTos (280 mmol, 53.26 g) oder Zugabe von KHSO_4 (280 mmol, 38,12 g) und 1.5 eq. der gewünschten Sulfonsäure. Fritten unter Argon (zwei Wattebäusche auf den Frittenboden, ansonsten dauert die Filtration mind. 5 Stunden). Einrotieren und im Kühlschrank kristallisieren.

(Weitere Informationen in der Publikation).

Betriebsanweisung für die Herstellung von *cis*-Natriumhyponitrit, *cis*- $\text{Na}_2\text{N}_2\text{O}_2$

Beck Daniel, Datum: 15.05.2017

Arbeitssicherheit, Chemikalien, Geräte

Die allgemeine Betriebsanweisung des Arbeitskreises sowie die Betriebsanweisungen und/oder Sicherheitsdatenblätter der einzelnen Gefahrstoffe müssen gelesen, beachtet und bereitgehalten werden.

Spezifikation der Ausgangsstoffe, Formel (Synonyme; Abkürzungen):

Natrium (Na): H: [260- 314](#); P: [223- 231+232- 280- 305+351+338- 370+378- 422](#)

Ammoniak (gasförmig): H: [221- 280- 331- 314- 400](#); P: [210- 260- 280- 273- 304+340303+361+353- 305+351+338- 315- 377- 381- 405- 403](#)

Stickstoffmonoxid (gasförmig): H: [270- 280- 330- 314](#); P: [260- 280- 244- 220- 304+340303+361+353- 305+351+338- 370+376- 315- 405- 403](#)

Gefahren für Mensch und Umwelt:

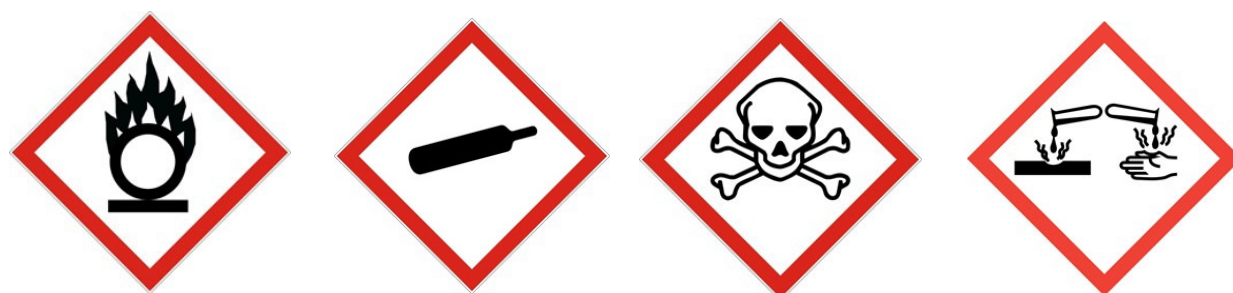
Ammoniak (gasförmig):



Natrium (Na):



Stickstoffmonoxid (gasförmig):



Bereitzuhaltende persönliche Schutzausrüstung:

Schutzbrille, Labormantel, Gesichtsvisionier, Nitrilhandschuhe, Kevlarhandschuhe, Gehörschutz



Bereitzuhaltende Löschmittel:

Sand bei Metallbrand.



Maximale Ansatzgröße: bei größerem Ansatz muss eine neue BA verfasst werden.

122 mg (5.5 mmol) Natrium.



Apparatur:

Trockeneiskühler, Dreihalsrundkolben 100 mL, Blasenähler mit zwei abschließbaren Hähnen-Schlaucholive-Schliffkern, zweifach geklammert (bei der Einkondensierung NH_3 und Einleitung NO); Hahnaufsatz 14.5, Standard- NO -Apparatur.

Die Reaktion muss im Abzug durchgeführt werden! Der Fortgang der Reaktion ist mit Zeitangaben im Laborjournal zu dokumentieren! Umsetzung bei erhöhtem Luftzug durchführen (Abzug 10 cm geöffnet). Ersthelfer bitten dabei zu sein (bei Zugabe des Lösungsmittels), dass er im Falle eines Unfalls direkt eingreifen kann.

Entsorgung:

Falls Produkt nicht vollständig mit Eduktkomplex abreagiert hat, dann die Reste mit Wasser quenchen und Entsorgung im wässrigen Metallsalzkanister.

Verhalten im Gefahrfall:

Da das Produkt explosive Eigenschaften besitzt, muss generell mit Schutzscheibe und Schutzschild gearbeitet werden. Im trockenen Zustand ist Produkt generell gefährlich. Vermutung: Der ursprüngliche Ansatz (3g Natrium) ist schlagempfindlich. Deswegen dürfen nur geringe Mengen für einen Ansatz verwenden (5.5 mmol Natrium hat sich als brauchbar herausgestellt)

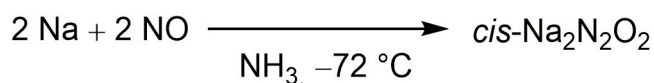
Bei Freiwerden von Gasen und Dämpfen umgehend den Raum verlassen **Erste-Hilfe-Maßnahmen:**

Verbandskasten bereit stellen.

Bei Explosion: Unter fließendem Wasser (Augendusche, Notdusche) abwaschen, Blutung stillen, Arzt rufen.

Austritt NO: Raum verlassen und warten bis NO/NO₂ Atmosphäre verschwunden.

Austritt NH₃: In Abzug ausgasen lassen und Raum verlassen.

Arbeitsvorschrift**Reaktionsgleichung:****Literatur:**

Claus Feldmann, Martin Jansen, *Z. Anorg. Allg. Chem.* **1997**, 623, 1803–1809.

J. Goubeau, K. Laitenberger, *Z. Anorg. Allg. Chem.* **1963**, 320, 78–85.

Ausführung:

Wichtig direkt weiterverwenden:

Natrium (122 mg) vorlegen und mit verflüssigtem Ammoniak (50 mL) lösen. Dazu wird das Ammoniakgas bei –72°C einkondensiert (Zugang über den Schlenkstopfen am Kolben). Die Lösung wird mit Überschuss an gasförmigem Stickstoffmonoxid behandelt (–72 °C). Die Lösung entfärbt sich ca. nach einer dreiviertel Stunde. Vor der Reaktionsanlage befindet sich dabei grundsätzlich ein Schutzschild (wie für Autoklaven zu positionieren), zusätzlich ist die Schutzscheibe des Abzuges heruntergelassen. Man arbeitet durch geöffnete Seitenschieber. Der Ammoniak wird bei RT abdestilliert, **wobei unbedingt der Rührer ausgeschaltet sein muss** (Stecker muss gezogen werden). Der Hahn des Blasenzählers wird leicht geöffnet, so dass Ammoniak mit Argon (Zuleitung über Schlaucholive) in den Abzug ausgetragen wird.

Nach 2 Stunden ist das Lösungsmittel abdestilliert und kleine farblose Schuppen von cisNatriumhyponitrit liegen im Gefäß (ab hier besonders aufpassen). Zu dem trockenen Produkt wird nun unter Trockeneis-Kühlung (+ iso-Propanol) der gewünschte Eduktkomplex gegeben (hier gelöst in DCM (20 mL)) (danach kann der Rührer wieder in Betrieb genommen werden,

(-72 °C)). Sobald das Hyponitrit von Flüssigkeit umgeben ist, sollte keine Explosionsgefahr mehr bestehen (trotzdem Vorsicht). Die Schutzscheibe bleibt weiter positioniert. Eine Farbänderung zeigt die Komplexierung und damit eine Inaktivierung von Hyponitrit an. Beim Einengen des DCM ist darauf zu achten, dass kein farbloser Feststoff sichtbar ist. (Falls Rückstände sichtbar sind mit Wasser quenchen!)

Generell sollte die oben angegebene Schutzkleidung von Anfang an verwendet werden.

Ausbeute: –

Analyse: direkt weiterverwenden! (Ist am sichersten)

Eigenschaften: weißer bzw. farbloser Feststoff.

8 Bibliography

- [1] S. Alvarez, P. Alemany, D. Casanova, J. Cirera, M. Llunell, D. Avnir, *Coord. Chem. Rev.* **2005**, *249*, 1693–1708.
- [2] S. M. Holmes, S. G. McKinley, G. S. Girolami, P. S. Szalay, K. R. Dunbar, *Inorganic Syntheses, Vol. 33*, John Wiley & Sons, Inc., Hoboken, New Jersey, **2002**.
- [3] E. Becker, K. Kirchner, K. Mereiter, *Acta Crystallogr., Sect. E: Struct. Rep. Online* **2009**, *65*, i71.
- [4] L. W. Zimmermann, T. Schleid, *Z. Kristallogr. - Cryst. Mater.* **2013**, *228*, 558–564.
- [5] D. Yang, F. L. Yang, *Acta Crystallogr., Sect. E: Struct. Rep. Online* **2014**, *70*, m169.
- [6] A. Capobianchi, G. Campi, M. Camalli, C. Veroli, *Z. Kristallogr.* **2009**, *224*, 384–388.
- [7] H. Euler, B. Barbier, A. Meents, A. Kirfel, *Z. Kristallogr. - New Cryst. Struct.* **2009**, *224*, 171–173.
- [8] S. Yahyaoui, W. Rekik, H. Naili, T. Mhiri, T. Bataille, *J. Solid State Chem.* **2007**, *180*, 3560–3570.
- [9] M. Taimisto, R. Oilunkaniemi, S. Laitinen Risto, M. Ahlgrén, *Z. Naturforsch., B: J. Chem. Sci.*, **2003**, *58*, 959–964.
- [10] P. Bernhard, H. B. Büergi, J. Hauser, H. Lehmann, A. Ludi, *Inorg. Chem.* **1982**, *21*, 3936–3941.
- [11] P. Bernhard, M. Biner, A. Ludi, *Polyhedron* **1990**, *9*, 1095–1097.
- [12] C. Fellay, G. Laurenczy, S. M. Bischof, R. A. Periana, *Inorganic Syntheses, Vol. 35*, John Wiley & Sons, Inc., Hoboken, New Jersey, **2010**.
- [13] S. Dolder, D. Spichiger, P. L. W. Tregenna-Piggott, *Inorg. Chem.* **2003**, *42*, 1343–1349.
- [14] N. Aebischer, R. Churlaud, L. Dolci, U. Frey, A. E. Merbach, *Inorg. Chem.* **1998**, *37*, 5915–5924.
- [15] L. Shen, W. Yang, *J. Chem. Theory Comput.* **2016**, *12*, 2017–2027.
- [16] P. Jaque, A. V. Marenich, C. J. Cramer, D. G. Truhlar, *J. Phys. Chem. C* **2007**, *111*, 5783–5799.
- [17] C. Fellay, N. Yan, P. J. Dyson, G. Laurenczy, *Chem. Eur. J.* **2009**, *15*, 3752–3760.

Bibliography

- [18] P. J. Ferko, J. R. Withers, H. Nguyen, J. Ema, T. Ema, C. Allison, C. Dornhoefer, N. P. Rath, S. M. Holmes, *J. Chem. Educ.* **2017**, *94*, 95–100.
- [19] J. G. Hamilton, J. J. Rooney, J. M. DeSimone, C. Mistele, *Macromolecules* **1998**, *31*, 4387–4389.
- [20] L. Y. Kuo, F. E. Delaney, *Inorg. Chim. Acta* **2015**, *435*, 335–339.
- [21] T. Karlen, A. Ludi, *Helv. Chim. Acta* **1992**, *75*, 1604–1606.
- [22] A. Thevenon, E. Frost-Pennington, G. Weijia, A. F. Dalebrook, G. Laurency, *ChemCatChem* **2014**, *6*, 3146–3152.
- [23] O. H. Bailey, A. Ludi, *Inorg. Chem.* **1985**, *24*, 2582–2585.
- [24] P. V. Grundler, O. V. Yazyev, N. Aebischer, L. Helm, G. Laurency, A. E. Merbach, *Inorg. Chim. Acta* **2006**, *359*, 1795–1806.
- [25] U. C. Meier, R. Scopelliti, E. Solari, A. E. Merbach, *Inorg. Chem.* **2000**, *39*, 3816–3822.
- [26] C. Creutz, H. Taube, *Inorg. Chem.* **1971**, *10*, 2664–2667.
- [27] P. Bernhard, H. Lehmann, A. Ludi, *J. Chem. Soc., Chem. Commun.* **1981**, 1216–1217.
- [28] M. Stebler-Roethlisberger, W. Hummel, P. A. Pittet, H. B. Buergi, A. Ludi, A. E. Merbach, *Inorg. Chem.* **1988**, *27*, 1358–1363.
- [29] U. Kölle, G. Flunkert, R. Görissen, M. U. Schmidt, U. Englert, *Angew. Chem., Int. Ed. Engl.* **1992**, *31*, 440–442. *Angew. Chem.* **1992**, *104*, 445–447.
- [30] J. Kovacs, F. Joo, A. C. Benyei, G. Laurency, *Dalton Trans.* **2004**, 2336–2340.
- [31] G. A. Lawrance, *Chem. Rev.* **1986**, *86*, 17–33.
- [32] W. Beck, K. Suenkel, *Chem. Rev.* **1988**, *88*, 1405–1421.
- [33] P. A. Lay, R. H. Magnuson, H. Taube, J. Sen, *J. Am. Chem. Soc.* **1982**, *104*, 7658–7659.
- [34] N. E. Dixon, G. A. Lawrance, P. A. Lay, A. M. Sargeson, *Inorg. Chem.* **1983**, *22*, 846–847.
- [35] N. E. Dixon, G. A. Lawrance, P. A. Lay, A. M. Sargeson, *Inorg. Chem.* **1984**, *23*, 2940–2947.
- [36] B. Anderes, S. T. Collins, D. K. Lavalley, *Inorg. Chem.* **1984**, *23*, 2201–2203.
- [37] P. A. Harding, S. D. Robinson, *J. Chem. Soc., Dalton Trans.* **1987**, 947–952.

Bibliography

- [38] J. F. Bickley, A. A. La Pensée, S. J. Higgins, C. A. Stuart, *Dalton Trans.* **2003**, 4663–4668.
- [39] D. Beck, P. Klüfers, *Chem. Eur. J.* **2018**, *24*, 16019–16028.
- [40] W. Smit, V. Koudriavtsev, G. Occhipinti, K. W. Törnroos, V. R. Jensen, *Organometallics* **2016**, *35*, 1825–1837.
- [41] F. Jiang, K. Yuan, M. Achard, C. Bruneau, *Chem. Eur. J.* **2013**, *19*, 10343–10352.
- [42] O. Bashir, L. Piche, J. P. Claverie, *Organometallics* **2014**, *33*, 3695–3701.
- [43] G. Rheinwald, H. Stoeckli-Evans, G. Süss-Fink, *J. Organomet. Chem.* **1992**, *441*, 295–308.
- [44] C. K. Hill, J. F. Hartwig, *Nat. Chem.* **2017**, *9*, 1213–1221.
- [45] L. J. Farrugia, *J. Appl. Crystallogr.* **2012**, *45*, 849–854.
- [46] H. Werner, G. Fries, B. Weberndörfer, *J. Organomet. Chem.* **2000**, *607*, 182–193.
- [47] J. F. Bickley, S. J. Higgins, C. A. Stuart, A. Steiner, *Inorg. Chem. Commun.* **2000**, *3*, 211–213.
- [48] O. Tissot, M. Gouygou, J.-C. Daran, G. G. A. Balavoine, *Organometallics* **1998**, *17*, 5927–5930.
- [49] T. A. Peganova, N. V. Vologdin, P. V. Petrovskii, I. D. Nesterov, K. A. Lyssenko, O. V. Gusev, *Russ. Chem. Bull.* **2006**, *55*, 683–686.
- [50] M. F. Mahon, M. K. Whittlesey, P. T. Wood, *Organometallics* **1999**, *18*, 4068–4074.
- [51] T. Funaioli, C. Cavazza, F. Marchetti, G. Fachinetti, *Inorg. Chem.* **1999**, *38*, 3361–3368.
- [52] P. A. Harding, S. D. Robinson, K. Henrick, *J. Chem. Soc., Dalton Trans.* **1988**, 415–420.
- [53] P. Alexander Harding, M. Preece, S. D. Robinson, K. Henrick, *Inorg. Chim. Acta* **1986**, *118*, L31–L33.
- [54] J. Coetzee, D. L. Dodds, J. Klankermayer, S. Brosinski, W. Leitner, A. M. Slawin, D. J. Cole-Hamilton, *Chem. Eur. J.* **2013**, *19*, 11039–11050.
- [55] C. Schotes, M. Ranocchiari, A. Mezzetti, *Organometallics* **2011**, *30*, 3596–3602.
- [56] U. Koelle, *Coord. Chem. Rev.* **1994**, *135-136*, 623–650.
- [57] C. K. Jorgensen, *Inorg. Chem.* **1964**, *3*, 1201–1202.
- [58] R. G. Pearson, *J. Am. Chem. Soc.* **1963**, *85*, 3533–3539.
- [59] J. Bjerrum, *Chem. Rev.* **1950**, *46*, 381–401.

Bibliography

- [60] P. W. Blosser, J. C. Gallucci, A. Wojcicki, *Inorg. Chem.* **1992**, *31*, 2376–2384.
- [61] O. V. Gusev, A. M. Kal'sin, T. A. Peganova, P. V. Petrovskii, G. P. Belov, E. V. Novikova, *Russ. Chem. Bull.* **2000**, *49*, 1113–1115.
- [62] A. C. Bényei, S. Lehel, F. Joó, *J. Mol. Catal. A: Chem.* **1997**, *116*, 349–354.
- [63] P. Knochel, *Modern Solvents in Organic Synthesis*, Springer-Verlag, Berlin Heidelberg, **1999**.
- [64] W. A. Herrmann, C. W. Kohlpaintner, *Angew. Chem., Int. Ed. Engl.* **1993**, *32*, 1524–1544; *Angew. Chem.* **1993**, *105*, 1588–1609.
- [65] R. Mason, D. W. Meek, *Angew. Chem., Int. Ed. Engl.* **1978**, *17*, 183–194; *Angew. Chem.* **1978**, *90*, 195–206.
- [66] C. A. Tolman, W. C. Seidel, L. W. Gosser, *J. Am. Chem. Soc.* **1974**, *96*, 53–60.
- [67] C. A. Tolman, *Chem. Rev.* **1977**, *77*, 313–348.
- [68] G. J. Palenik, M. Mathew, W. L. Steffen, G. Beran, *J. Am. Chem. Soc.* **1975**, *97*, 1059–1066.
- [69] B. R. James, D. Mahajan, *Can. J. Chem.* **1979**, *57*, 180–187.
- [70] D. E. Berning, A. Miedaner, C. J. Curtis, B. C. Noll, M. C. Rakowski DuBois, D. L. DuBois, *Organometallics* **2001**, *20*, 1832–1839.
- [71] D. L. DuBois, D. M. Blake, A. Miedaner, C. J. Curtis, M. R. DuBois, J. A. Franz, J. C. Linehan, *Organometallics* **2006**, *25*, 4414–4419.
- [72] J. W. Raebiger, A. Miedaner, C. J. Curtis, S. M. Miller, O. P. Anderson, D. L. DuBois, *J. Am. Chem. Soc.* **2004**, *126*, 5502–5514.
- [73] P. C. J. Kamer, P. W. N. M. van Leeuwen, J. N. H. Reek, *Acc. Chem. Res.* **2001**, *34*, 895–904.
- [74] C. P. Casey, G. T. Whiteker, *Isr. J. Chem.* **1990**, *30*, 299–304.
- [75] K. Angermund, W. Baumann, E. Dinjus, R. Fornika, H. Görls, M. Kessler, C. Krüger, W. Leitner, F. Lutz, *Chem. Eur. J.* **1997**, *3*, 755–764.
- [76] A. Mannu, G. Vlahopoulou, C. Kubis, H.-J. Drexler, *J. Organomet. Chem.* **2019**, *885*, 59–64.
- [77] N. Lehnert, J. C. Peters, *Inorg. Chem.* **2015**, *54*, 9229–9233.
- [78] J. Wang, D. R. Chadwick, Y. Cheng, X. Yan, *Sci. Total Environ.* **2017**, *616-617*, 908–917.

Bibliography

- [79] D. E. Canfield, A. N. Glazer, P. G. Falkowski, *Science* **2010**, *330*, 192–196.
- [80] T. Hino, S. Nagano, H. Sugimoto, T. Tosha, Y. Shiro, *Biochim. Biophys. Acta* **2012**, *1817*, 680–687.
- [81] Y. Shiro, *Biochim. Biophys. Acta* **2012**, *1817*, 1907–1913.
- [82] S. Khatua, A. Majumdar, *J. Inorg. Biochem.* **2015**, *142*, 145–153.
- [83] J. ter Beek, N. Krause, J. Reimann, P. Lachmann, P. Adelroth, *J. Biol. Chem.* **2013**, *288*, 30626–30635.
- [84] A. Crow, Y. Matsuda, H. Arata, A. Oubrie, *Biochemistry* **2016**, *55*, 3198–3203.
- [85] J. D. M. Kurtz, *Dalton Trans.* **2007**, 4115–4121.
- [86] C. Van Stappen, N. Lehnert, *Inorg. Chem.* **2018**, *57*, 4252–4269.
- [87] T. C. Householder, E. M. Fozo, J. A. Cardinale, V. L. Clark, *Infect. Immun.* **2000**, *68*, 5241–5246.
- [88] M. F. Anjum, T. M. Stevanin, R. C. Read, J. W. B. Moir, *J. Bacteriol.* **2002**, *184*, 2987–2993.
- [89] S. McNicholas, E. Potterton, K. S. Wilson, M. E. Noble, *Acta Crystallogr., Sect. D: Biol. Crystallogr.* **2011**, *67*, 386–394.
- [90] M. R. Blomberg, *Biochemistry* **2017**, *56*, 120–131.
- [91] H. Kumita, K. Matsuura, T. Hino, S. Takahashi, H. Hori, Y. Fukumori, I. Morishima, Y. Shiro, *J. Biol. Chem.* **2004**, *279*, 55247–55254.
- [92] M. R. A. Blomberg, P. Adelroth, *Biochim. Biophys. Acta, Bioenerg.* **2018**, *1859*, 1223–1234.
- [93] R. W. Ye, B. A. Averill, J. M. Tiedje, *Appl. Environ. Microbiol.* **1994**, *60*, 1053–1058.
- [94] A. M. Wright, T. W. Hayton, *Inorg. Chem.* **2015**, *54*, 9330–9341.
- [95] D. Lionetti, G. de Ruiter, T. Agapie, *J. Am. Chem. Soc.* **2016**, *138*, 5008–5011.
- [96] S. Kundu, P. N. Phu, P. Ghosh, S. A. Kozimor, J. A. Bertke, S. C. E. Stieber, T. H. Warren, *J. Am. Chem. Soc.* **2019**, *141*, 1415–1419.
- [97] E. Ferretti, S. Dechert, S. Demeshko, M. C. Holthausen, F. Meyer, *Angew. Chem. Int. Ed. Engl.* **2019**, *58*, 1705–1709; *Angew. Chem.* **2019**, *131*, 1719–1723.

Bibliography

- [98] S. Bhaduri, B. F. G. Johnson, A. Pickard, P. R. Raithby, G. M. Sheldrick, C. I. Zuccaro, *J. Chem. Soc., Chem. Commun.* **1977**, 354–355.
- [99] H.-C. Böttcher, M. Graf, K. Mereiter, K. Kirchner, *Organometallics* **2004**, *23*, 1269–1273.
- [100] W. J. Evans, M. Fang, J. E. Bates, F. Furche, J. W. Ziller, M. D. Kiesz, J. I. Zink, *Nat. Chem.* **2010**, *2*, 644–647.
- [101] R. Bau, I. H. Sabherwal, A. B. Burg, *J. Am. Chem. Soc.* **1971**, *93*, 4926–4928.
- [102] A. M. Wright, G. Wu, T. W. Hayton, *J. Am. Chem. Soc.* **2012**, *134*, 9930–9933.
- [103] G. B. Wijeratne, S. Hematian, M. A. Siegler, K. D. Karlin, *J. Am. Chem. Soc.* **2017**, *139*, 13276–13279.
- [104] N. Xu, E. G. Abucayon, D. R. Powell, G. B. Richter-Addo, *Nitric Oxide* **2016**, *52*, 16–20.
- [105] T. Mayer, P. Mayer, H.-C. Böttcher, *J. Organomet. Chem.* **2012**, *700*, 41–47.
- [106] H.-C. Böttcher, C. Wagner, K. Kirchner, *Inorg. Chem.* **2004**, *43*, 6294–6299.
- [107] J. A. Hrabie, L. K. Keefer, *Chem. Rev.* **2002**, *102*, 1135–1154.
- [108] N. Xu, J. H. Christian, N. S. Dalal, E. G. Abucayon, C. Lingafelt, D. R. Powell, G. B. Richter-Addo, *Dalton. Trans.* **2015**, *44*, 20121–20130.
- [109] L. K. Keefer, J. L. Flippen-Anderson, C. George, A. P. Shanklin, T. M. Dunams, D. Christodoulou, J. E. Saavedra, E. S. Sagan, D. S. Bohle, *Nitric Oxide* **2001**, *5*, 377–394.
- [110] B. Wang, M. Nishiura, J. Cheng, Z. Hou, *Dalton. Trans.* **2014**, *43*, 14215–14218.
- [111] M. Shiino, Y. Watanabe, K. Umezawa, *Biorg. Med. Chem.* **2001**, *9*, 1233–1240.
- [112] H. Iinuma, M. Matsuzaki, T. Nagatsu, T. Takeuchi, H. Umezawa, *Agric. Biol. Chem.* **1974**, *38*, 2107–2111.
- [113] M. Nishio, K. S. M. Hasegawa, Y. Sawada, D. J. Hook, T. Oki, *J. Antibiot.* **1993**, *46*, 193–195.
- [114] S. B. Ahuja, U. Kiran, U. Sudershan, *Indian J. Biochem. Biophys.* **1981**, 86.
- [115] Y. K. S. Murthy, J. E. Thiemann, C. Coronelli, P. Sensi, *Nature* **1966**, *211*, 1198–1199.
- [116] H. N. Jayaram, A. K. Tyagi, S. Anandaraj, J. A. Montgomery, J. A. Kelley, J. Kelley, R. H. Adamson, D. A. Cooney, *Biochem. Pharmacol.* **1979**, *28*, 3551–3566.

Bibliography

- [117] H. A. J. Hibbard, M. M. Reynolds, *J. Mater. Chem. B* **2019**, *7*, 2009–2018.
- [118] A. H. A. Heyn, N. G. Dave, *Talanta* **1966**, *13*, 27–32.
- [119] H. H. Willard, E. L. Martin, R. Feltham, *Anal. Chem.* **1953**, *25*, 1863–1865.
- [120] G. E. F. Lundell, H. B. Knowles, *J. Ind. Eng. Chem.* **1920**, *12*, 344–350.
- [121] R. Hermenau, K. Ishida, S. Gama, B. Hoffmann, M. Pfeifer-Leeg, W. Plass, J. F. Mohr, T. Wichard, H. P. Saluz, C. Hertweck, *Nat. Chem. Biol.* **2018**, *14*, 841–843.
- [122] S.-C. So, W.-M. Cheung, G.-C. Wang, E. Kwan Huang, M.-K. Lau, Q.-F. Zhang, H. H. Y. Sung, I. D. Williams, W.-H. Leung, *Organometallics* **2014**, *33*, 4497–4502.
- [123] Z. Huang, J. Fu, Y. Zhang, *J. Med. Chem.* **2017**, *60*, 7617–7635.
- [124] S. Wiese, P. Kapoor, K. D. Williams, T. H. Warren, *J. Am. Chem. Soc.* **2009**, *131*, 18105–18111.
- [125] O. Kovalchukova, A. S. Bostanabad, V. Sergienko, I. Polyakova, I. Zyuzin, S. Strashnova, *Open J. Inorg. Chem.* **2013**, *3*, 1–6.
- [126] M. Ahmed, A. J. Edwards, C. J. Jones, J. A. McCleverty, A. S. Rothin, J. P. Tate, *J. Chem. Soc., Dalton Trans.* **1988**, 257–263.
- [127] A. Deák, L. Radics, A. Kálmán, L. Párkányi, I. Haiduc, *Eur. J. Inorg. Chem.* **2001**, *2001*, 2849–2856.
- [128] H. W. S. J. Bucher, H. Berke, *CSC Communication CCDC 621198*, **2016**.
- [129] M. Ziche, S. Donnini, L. Morbidelli, E. Monzani, R. Roncone, R. Gabbini, L. Casella, *ChemMedChem* **2008**, *3*, 1039–1047.
- [130] S. C. Puiu, T. H. Warren, *Organometallics* **2003**, *22*, 3974–3976.
- [131] S. Amirkhalili, P. B. Hitchcock, J. D. Smith, J. G. Stamper, *J. Chem. Soc., Dalton Trans.* **1980**, 2493–2497.
- [132] W. S. Horton, *J. Am. Chem. Soc.* **1956**, *78*, 897–899.
- [133] M. Guo, Y. Xu, J. Wu, L. Zhao, J. Tang, *Dalton Trans.* **2017**, *46*, 8252–8258.
- [134] P. Edwards, K. Mertis, G. Wilkinson, M. B. Hursthouse, K. M. A. Malik, *J. Chem. Soc., Dalton Trans.* **1980**, 334–344.

Bibliography

- [135] G. Fochi, C. Floriani, A. Chiesi-Villa, C. Guastini, *J. Chem. Soc., Dalton Trans.* **1986**, 445–447.
- [136] Y. F. Liu, H. T. Xia, D. Q. Wang, X. L. Gong, *Acta Crystallogr., Sect. E: Struct. Rep. Online* **2009**, *65*, m1526–1527.
- [137] M. H. Abraham, J. I. Bullock, J. H. N. Garland, A. J. Golder, G. J. Harden, L. F. Larkworthy, D. C. Povey, M. J. Riedl, G. W. Smith, *Polyhedron* **1987**, *6*, 1375–1381.
- [138] K. Sardar, C. N. R. Rao, *Adv. Mater.* **2004**, *16*, 425–429.
- [139] L. Párkányi, A. Kálmán, A. Deák, M. Venter, I. Haiduc, *Inorg. Chem. Commun.* **1999**, *2*, 265–268.
- [140] G. Mohammadnezhad, F. Nasimpour, M. M. Amini, E. Najafi, H. Görls, W. Plass, M. R. Sabzalian, *J. Mol. Struct.* **2019**, *1175*, 471–480.
- [141] A. N. Belay, R. Koen, J. A. Venter, R. M. Drost, *Z. Kristallogr. - New Cryst. Struct.* **2016**, *231*, 513–515.
- [142] I. J. Casely, Y. Suh, J. W. Ziller, W. J. Evans, *Organometallics* **2010**, *29*, 5209–5214.
- [143] A. Deák, M. Venter, A. Kálmán, L. Párkányi, L. Radics, I. Haiduc, *Eur. J. Inorg. Chem.* **2000**, *2000*, 127–132.
- [144] S. V. Evans, P. Legzdins, S. J. Rettig, L. Sánchez, J. Trotter, *Acta Crystallogr., Sect. C* **1995**, *51*, 584–586.
- [145] J. D. Wilkins, M. G. B. Drew, *J. Organomet. Chem.* **1974**, *69*, 111–119.
- [146] K. Tamaki, N. Okabe, *Acta Crystallogr., Sect. C* **1998**, *54*, 195–197.
- [147] E. Najafi, M. M. Amini, S. W. Ng, *Acta Crystallogr., Sect. E: Struct. Rep. Online* **2012**, *68*, m791.
- [148] F. Ferretti, M. Rimoldi, F. Ragaini, P. Macchi, *Inorg. Chim. Acta* **2018**, *470*, 284–289.
- [149] T. Wang, L. Wang, C. G. Daniliuc, K. Samigullin, M. Wagner, G. Kehr, G. Erker, *Chem. Sci.* **2017**, *8*, 2457–2463.
- [150] C. Chuy, L. R. Falvello, E. Libby, J. C. Santa-María, M. Tomás, *Inorg. Chem.* **1997**, *36*, 2004–2009.

Bibliography

- [151] J. L. Schneider, J. A. Halfen, V. G. Young, W. B. Tolman, W. B. Tolman, *New J. Chem.* **1998**, *22*, 459–466.
- [152] E. H. G. Klebe, K. H. Boehn, W. Reuther, E. Hickman *Z. Kristallogr. - Cryst. Mater.* **1996**, *211*, 798–803.
- [153] K. Tamaki, N. Okabe, *Acta Crystallogr., Sect. C* **1996**, *52*, 1612–1614.
- [154] C. Pretorius, J. A. Venter, A. Roodt, *Z. Kristallogr. - Cryst. Mater.* **2014**, *229*, 437–439.
- [155] I. Rapaport, L. Helm, A. E. Merbach, P. Bernhard, A. Ludi, *Inorg. Chem.* **1988**, *27*, 873–879.
- [156] G. Kortüm, G. Schreyer, *Angew. Chem.* **1955**, *67*, 694–698.
- [157] J. Bernstein, R. E. Davis, L. Shimoni, N.-L. Chang, *Angew. Chem., Int. Ed. Engl.* **1995**, *34*, 1555–1573; *Angew. Chem.* **1995**, *107*, 1689–1708.
- [158] A. Belz, Dissertation, LMU München (München), **2017**.
- [159] M. Khodaei, K. Bahrami, J. Abbasi, *Synthesis* **2011**, *2012*, 316–322.
- [160] S. G. J. B. Lambert, H. F. Shurvell, D. A. Lighter, *Spektroskopie - Strukturaufklärung in der organischen Chemie, Vol. 2*, Pearson, Munich, **2012**.
- [161] W. Kopycki, J. Binkowski, *Microchim. Acta* **1984**, *84*, 149–157.
- [162] Y. Wang, Z. Li, X. Zeng, X. Wang, C. Zhan, Y. Liu, X. Zeng, Q. Luo, X. Liu, *New J. Chem.* **2009**, *33*, 1780–1789.
- [163] T. Mayer, H.-C. Böttcher, *Z. Naturforsch., B* **2012**, *67*, 504–506.
- [164] T. Jiang, S. Zhang, X. Jiang, C. Yang, B. Niu, Y. Ning, *J. Mol. Catal. A: Chem.* **2008**, *279*, 90–93.
- [165] T. Mayer, Dissertation, LMU München, **2012**.
- [166] C. G. Pierpont, R. Eisenberg, *Inorg. Chem.* **1973**, *12*, 199–205.
- [167] A. P. Gaughan, B. J. Corden, R. Eisenberg, J. A. Ibers, *Inorg. Chem.* **1974**, *13*, 786–791.
- [168] J. H. Enemark, R. D. Feltham, *Coord. Chem. Rev.* **1974**, *13*, 339–406.
- [169] A. Zangl, Dissertation, LMU München (München), **2009**.
- [170] S. Bhaduri, G. M. Sheldrick, *Acta Crystallogr., Sect. B* **1975**, *31*, 897–899.
- [171] N. Arulsamy, D. S. Bohle, J. A. Imonigie, E. S. Sagan, *Inorg. Chem.* **1999**, *38*, 2716–2725.

Bibliography

- [172] M. B. Esler, D. W. T. Griffith, S. R. Wilson, L. P. Steele, *Anal. Chem.* **2000**, *72*, 206–215.
- [173] D. F. Smith, J. Overend, R. C. Spiker, L. Andrews, *Spectrochim. Acta, Part A* **1972**, *28*, 87–93.
- [174] T. Mayer, W. Beck, H.-C. Böttcher, *Z. Anorg. Allg. Chem.* **2011**, *637*, 345–347.
- [175] W. Beck, H. Engelmann, H. S. Smedal, *Z. Anorg. Allg. Chem.* **1968**, *357*, 134–138.
- [176] O. V. Kovalchukova, N. Namichemazi, A. S. Bostanabad, A. I. Stash, S. B. Strashnova, I. N. Zuzin, *Russ. J. Inorg. Chem.* **2016**, *61*, 718–725.
- [177] G. Bombieri, E. Forsellini, R. Graziani, G. Zotti, *Transition Met. Chem.* **1977**, *2*, 264–267.
- [178] G. Pilloni, G. Zotti, C. Corvaja, M. Martelli, *J. Electroanal. Chem. Interfacial Electrochem.* **1978**, *91*, 385–392.
- [179] G. Zotti, G. Pilloni, M. Bressan, M. Martelli, *J. Electroanal. Chem. Interfacial Electrochem.* **1977**, *75*, 607–612.
- [180] J. E. Saavedra, T. R. Billiar, D. L. Williams, Y.-M. Kim, S. C. Watkins, L. K. Keefer, *J. Med. Chem.* **1997**, *40*, 1947–1954.
- [181] H. Maskill, W. P. Jencks, *J. Am. Chem. Soc.* **1987**, *109*, 2062–2070.
- [182] E. E. Mercer, R. R. Buckley, *Inorg. Chem.* **1965**, *4*, 1692–1695.
- [183] J. E. Earley, T. W. Kallen, *Inorg. Chem.* **1971**, *10*, 1149–1151.
- [184] W. Bottcher, G. M. Brown, N. Sutin, *Inorg. Chem.* **1979**, *18*, 1447–1451.
- [185] C. Hee Ng, S. Guan Teoh, N. Moris, S. Yang Yap, *J. Coord. Chem.* **2004**, *57*, 1037–1046.
- [186] N. Aebischer, G. Laurencyzy, A. Ludi, A. E. Merbach, *Inorg. Chem.* **1993**, *32*, 2810–2814.
- [187] J. E. Hueey, E. A. Keiter, R. L. Keiter, *Anorganische Chemie, Prinzipien von Struktur und Reaktivität*, 4. ed., Walter de Gruyter GmbH & Co. KG, Berlin/Boston, **2012**.
- [188] N. Aebischer, E. Sidorenkova, M. Ravera, G. Laurencyzy, D. Osella, J. Weber, A. E. Merbach, *Inorg. Chem.* **1997**, *36*, 6009–6020.
- [189] L. Helm, A. E. Merbach, *Coord. Chem. Rev.* **1999**, *187*, 151–181.
- [190] E. K. J. Huheey, R. Keiter, *Anorganische Chemie Prinzipien von Struktur und Reaktivität*, 3 ed., Walter de Gruyter & Co. KG, Berlin, **2003**.

Bibliography

- [191] A. Zalkin, H. Ruben, D. H. Templeton, *Acta Crystallogr.* **1964**, *17*, 235–240.
- [192] Y. Elerman, *Acta Crystallogr., Sect. C* **1988**, *44*, 599–601.
- [193] R. E. Gerkin, W. J. Reppart, *Acta Crystallogr., Sect. C* **1988**, *44*, 1486–1488.
- [194] M. Spiess, R. Gruehn, *Z. Anorg. Allg. Chem.* **1979**, *456*, 222–240.
- [195] F. A. Cotton, L. R. Falvello, R. Llusar, E. Libby, C. A. Murillo, W. Schwotzer, *Inorg. Chem.* **1986**, *25*, 3423–3428.
- [196] V. V. Vlasov, A. V. Kuznetsov, *Zap. Vses. Mineral. Ob.* **1962**, *91*, 490–492.
- [197] A. Abdul-Rahman, *J. Comput. Chem.* **2011**, *32*, 174–182.
- [198] Y. Arikawa, M. Onishi, *Coord. Chem. Rev.* **2012**, *256*, 468–478.
- [199] M. Gama Sauaia, R. Santana da Silva, *Transition Met. Chem.* **2003**, *28*, 254–259.
- [200] T. Mayer, W. Beck, H.-C. Böttcher, *Z. Anorg. Allg. Chem.* **2011**, *637*, 345–347.
- [201] J. Zevallos, A. Toro-Labbé, O. Mó, M. Yáñez, *Struct. Chem.* **2005**, *16*, 295–303.
- [202] M. E. Chacón Villalba, C. A. Franca, J. A. Güida, *Spectrochim. Acta, Part A* **2017**, *176*, 189–196.
- [203] C. M. Pavlos, H. Xu, J. P. Toscano, *Free Radical Biol. Med.* **2004**, *37*, 745–752.
- [204] X. Wu, X. Tang, M. Xian, P. G. Wang, *Tetrahedron Lett.* **2001**, *42*, 3779–3782.
- [205] N. Shaikh, M. Valiev, S. V. Lymar, *J. Inorg. Biochem.* **2014**, *141*, 28–35.
- [206] R. Behrend, E. König, *Justus Liebigs Ann. Chem.* **1891**, *263*, 175–223.
- [207] G. R. Fulmer, A. J. M. Miller, N. H. Sherden, H. E. Gottlieb, A. Nudelman, B. M. Stoltz, J. E. Bercaw, K. I. Goldberg, *Organometallics* **2010**, *29*, 2176–2179.
- [208] G. M. Sheldrick, *Acta Crystallogr., Sect. A: Found. Adv.* **2015**, *71*, 3–8.
- [209] G. M. Sheldrick, *Acta Crystallogr., Sect. C: Struct. Chem.* **2015**, *71*, 3–8.
- [210] F. Neese, *Wiley Interdiscip. Rev.: Comput. Mol. Sci.* **2012**, *2*, 73–78.

Danksagung

Herrn Prof. Dr. Peter Klüfers danke ich für die Aufnahme in seinen Arbeitskreis, die anspruchsvolle Themenstellung, die ich selbst weiterentwickeln durfte, und die grenzenlose akademische Freiheit gepaart mit hervorragenden Arbeitsbedingungen.

Herrn Prof. Dr. Hans-Christian Böttcher danke ich für die Erstellung des Zweitgutachtens für die vorliegende Arbeit, sowie für die Ratschläge bezüglich meiner Chemie und für ein stets offenes Ohr für alle möglichen Probleme.

Für Ihre Mitwirkung in der Promotionskommission danke ich Prof. Dr. Lena Daumann, Prof. Dr. Karlheinz Sünkel, Prof. Dr. Oliver Trapp, und Prof. Dr. Wolfgang Beck.

Lida Holowaty-den Toom danke ich für jegliche Hilfe bei sämtlichen organisatorischen Dingen, das Korrekturlesen dieser Arbeit und die positive Art, die stets die dunklen Wolken vertrieben hat.

Christine Neumann danke ich für die stete Versorgung mit Gerät und Material und die zuverlässige Messung meiner NMR-Proben.

Dr. Peter Mayer danke ich für die geduldige Einführung in die Röntgenkristallographie und die ebenso geduldige Beantwortung meiner Fragen zu diesem Thema. Dafür möchte ich Sandra Albrecht, Christine Sturm und Anja Belz ebenfalls danken.

Für die Einführung in die wunderbare und verwirrende Welt der DFT-Rechnungen danke ich Markus Wolf und Anja Belz.

Vielen Dank an all die Kollegen, die meine Arbeit Korrektur gelesen haben: Sezen Hollweck, Jens Popp, Helen Funk und Tobias Riggermann.

Vielen Dank an meine F-Praktikanten und Bacheloranden: Ich habe euch gleich gesagt, dass ich kein schwieriger Assistent bin.

Dankesworte gehen auch an meine engsten Freunde: Florian Graßl, der die Realität so sieht wie sie ist. Benedikt Schukwerk, der mir den Wert des Kämpfens gezeigt hat. Elija Wiedemann, der Arbeit viel zu ernst nimmt und Philipp Bielec, der tatsächlich immer noch davon überzeugt ist, dass ich intelligent wäre.

Besonderer Dank geht an meine liebsten Kollegen Areenan In-lam, Jens Popp, Anja Belz und Christine Sturm. Danke auch an den AK Klüfers, dass das Einende meistens stärker war als das Trennende. Auf eine schöne, freundschaftliche und produktive Atmosphäre.